



University
of Glasgow

Kelleher, Patrick (2015) Random access spectral imaging. PhD thesis.

<http://theses.gla.ac.uk/6889/>

Copyright and moral rights for this thesis are retained by the author

A copy can be downloaded for personal non-commercial research or study, without prior permission or charge

This thesis cannot be reproduced or quoted extensively from without first obtaining permission in writing from the Author

The content must not be changed in any way or sold commercially in any format or medium without the formal permission of the Author

When referring to this work, full bibliographic details including the author, title, awarding institution and date of the thesis must be given.

Random Access Spectral Imaging

Patrick Kelleher

**A thesis submitted in fulfillment of the requirements for the degree of
Doctor of Philosophy**

**School of Physics and Astronomy
University of Glasgow
G12 8QQ, UK**

September 2015

Abstract

A salient goal of spectral imaging is to record a so-called hyperspectral data-cube, consisting of two spatial and one spectral dimension. Traditional approaches are based on either time-sequential scanning in either the spatial or spectral dimension: spatial scanning involves passing a fixed aperture over a scene in the manner of a raster scan and spectral scanning is generally based on the use of a tuneable filter, where typically a series of narrow-band images of a fixed field of view are recorded and assembled into the data-cube. Such techniques are suitable only when the scene in question is static or changes slower than the scan rate.

When considering dynamic scenes a time-resolved (snapshot) spectral imaging technique is required. Such techniques acquire the whole data-cube in a single measurement, but require a trade-off in spatial and spectral resolution. These trade-offs prevent current snapshot spectral imaging techniques from achieving resolutions on par with time-sequential techniques. Any snapshot device needs to have an optical architecture that allows it to gather light from the scene and map it to the detector in a way that allows the spatial and spectral components can be de-multiplexed to reconstruct the data-cube. This process results in the decreased resolution of snapshot devices as it becomes a problem of mapping a 3D data-cube onto a 2D detector. The sheer volume of data present in the data-cube also presents a processing challenge, particularly in the case of real-time processing.

This thesis describes a prototype snapshot spectral imaging device that employs a random-spatial-access technique to record spectra only from the regions of interest in the scene, thus enabling maximisation of integration time and minimisation of data volume and recording rate. The aim of this prototype is to demonstrate how a particular optical architecture will allow for the effect of some of the above mentioned bottlenecks to be removed. Underpinning the basic concept is the fact that in all practical scenes most of the spectrally interesting information is contained in relatively few pixels. The prototype system uses random-spatial-access to multiple points in the scene considered to be of greatest interest. This enables time-resolved high resolution spectrometry to be made simultaneously at points across the full field of view.

The enabling technology for the prototype was a digital micromirror device (DMD), which is an array of switchable mirrors that was used to create a two channel system. One channel was to a conventional imaging camera, while the other was to a spectrometer. The DMD acted as a dynamic aperture to the spectrometer and could be used to open and close slits in any part of the spectrometer aperture. The imaging channel was used to guide the selection of points of interest from the scene. An extensive geometric calibration was performed to determine the relationships between the DMD and two channels of the system.

Two demonstrations of the prototype are given in this thesis: a dynamic biological scene and a static scene sampled using statistical sampling methods enabled by the dynamic aperture of the system. The dynamic scene consisted of red blood cells in motion and also undergoing a process of de-oxygenation which resulted in a change in the spectrum. Ten red blood cells were tracked across the scene and the expected change in spectrum was observed. For the second example the prototype was modified for Raman spectroscopy by adding laser illumination, a mineral sample was scanned and used to test statistical sampling methods. These methods exploited the re-configurable aperture of the system to sample the scene using blind random sampling and a grid based sampling approach. Other spectral imaging systems have a fixed aperture and cannot operate such sampling schemes.

Contents

List of Figures	v
List of Tables	viii
List of Acronyms	ix
Acknowledgments	x
Declaration	xi
1 Introduction	1
1.1 Introduction	1
1.2 Spectral Imaging Overview	3
1.2.1 Spectral Imaging: Limitations and Bottlenecks	4
1.3 Hyperspectral Data Acquisition	7
1.3.1 Time-sequential Spectral Imaging	8
1.3.2 Time-resolved Spectral Imaging	10
1.4 Hyperspectral Data Analysis	19
1.4.1 Hyperspectral Image Classification	20
1.4.2 Spectral Unmixing	21
1.5 Motivation for Random Access Spectral Imaging	25
1.6 Random-access sampling	25
1.7 Multi-object spectrometers	26
1.8 Digital Micromirror device	29
1.8.1 DMD Applications	30
1.8.2 DMD Multi-object spectrometers	32
1.9 RASI Design Parameters	33
1.10 Thesis Outline	34
2 Instrument Concept and Design	35
2.1 Introduction	35
2.2 System overview	35

2.3	Specular reflection properties	37
2.4	Field of View and Etendue	39
2.5	Telecentric lenses, off-axis alignment and system layout	42
2.5.1	Telecentric lenses	42
2.5.2	Off-axis imaging and the Scheimpflug condition	43
2.5.3	On-axis vs. off-axis illumination layouts	45
2.6	DMD diffraction	46
2.7	Spectrometer	47
2.8	Optical throughput	50
2.9	Zemax model	50
2.10	Chapter Summary	53
3	Experimental realisation	54
3.1	Introduction	54
3.2	System overview	54
3.2.1	Digital micromirror device	55
3.2.2	Telecentric lenses	56
3.2.3	Spectroscopy components	57
3.3	Core RASI construction	58
3.3.1	Custom Microscope for RASI	58
3.4	Imaging arm parameters	60
3.4.1	Geometric calibration	60
3.4.2	Image orientation, correction and contrast	62
3.5	Spectroscopy channel parameters	64
3.5.1	Geometric and wavelength calibration	64
3.5.2	Spectral linewidth	75
3.6	Stray light analysis	77
3.6.1	Sources of scatter	77
3.6.2	Stray light analysis	78
3.6.3	Spectral crosstalk	79
3.6.4	Stray light correction	79
3.7	Signal to noise considerations	80
3.8	Chapter summary	82

4	Demonstration of RASI	83
4.1	Introduction	83
4.2	Core operation	83
4.3	Red blood cell experiment	85
4.3.1	Red blood cell background	86
4.3.2	RBC absorption	87
4.4	Dynamic spectral imaging of RBCs	91
4.4.1	Tracking algorithm	91
4.4.2	De-oxygenating RBCs	93
4.4.3	Aperture consideration	93
4.4.4	Sample preparation	95
4.4.5	Experimental procedure	96
4.4.6	Data post processing	96
4.4.7	Spectral unmixing analysis	100
4.4.8	Discussion of red blood cell experiment	103
4.5	Spectral overlap in the spectrometer detector plane	104
4.5.1	Subtraction	106
4.5.2	Linear mixing model	106
4.5.3	Demonstration of spectral overlap correction	108
4.5.4	Spectral Overlap discussion	109
4.6	Chapter summary	110
5	Raman spectroscopy and alternative spatial sampling methods	112
5.1	Introduction	112
5.2	The Raman effect	112
5.2.1	Background of the Raman effect	112
5.2.2	Description of the Raman effect	113
5.2.3	Raman spectrometers	115
5.3	Raman hyperspectral imaging	116
5.4	Raman RASI	117
5.4.1	Modeling of the global illumination	119
5.4.2	Filters	124

Contents

5.4.3	Experimental alignment	125
5.5	Example Raman spectrum	126
5.6	Different Sampling approaches	128
5.6.1	Test case overview	129
5.6.2	Blind random sampling	131
5.6.3	Systematic sampling approach	133
5.6.4	Overview of sampling methods	135
5.7	Chapter summary	135
6	Conclusions	137
6.1	Thesis Summary	137
6.2	Recommendations for future work	139
	References	140

List of Figures

1.1	Overview of spectral imaging data-cubes	3
1.2	Mapping a 3D cube to a 2D detector	5
1.3	Spectral Imaging resolution trade-offs	6
1.4	Time-sequential scanning hyperspectral imagers	9
1.5	Computed Tomographic Imaging Spectrometer optical layout	11
1.6	Image Replicating Imaging spectrometer layout	13
1.7	Coded aperture spectral imaging	14
1.8	Integral field spectroscopy examples	16
1.9	Multi-aperture and filter array cameras	18
1.10	Sequential access and Random access	26
1.11	Multi-object spectrometers	27
1.12	Digital Micromirror Devices	30
2.1	Optical architecture of RASI	36
2.2	Single micromirror	37
2.3	Divergence between two DMD states	38
2.4	Etendue of a single micromirror	40
2.5	System etendue schematic	41
2.6	Telecentric and non-telecentric lenses	42
2.7	Scheimpflug condition	43
2.8	Scheimpflug orientation of telecentric lenses	44
2.9	Illumination layouts	45
2.10	Spectrometer schematic	48
2.11	Spectrometer distortions	49
2.12	Zemax raytrace for the spectrometer channel	51
2.13	Zemax raytrace for the imaging channel	52
3.1	RASI layout	54
3.2	DMD window transmission	55
3.3	Kaiser Holospec spectrometer	57

3.4	3D CAD model of RASI system	59
3.5	Breadboard view of RASI setup	60
3.6	Koehler illumination	61
3.7	Pictures of constructed system	62
3.8	Image correction example	63
3.9	Test images	63
3.10	Reference Neon spectrum	65
3.11	912 nm Neon line detector position	67
3.12	Fits to the horizontal coordinates of the camera and wavelength, each fit is associated with a particular DMD pixel of coordinates (i,j).	68
3.13	Fits to the vertical coordinates of the camera and wavelength, each fit is associated with a particular DMD pixel of coordinates (i,j).	68
3.14	Fits to the horizontal coordinates of the camera and wavelength, each fit is associated with a particular DMD pixel of coordinates (i,j) for the infrared grating.	69
3.15	Fits to the vertical coordinates of the camera and wavelength, each fit is associated with a particular DMD pixel of coordinates (i,j) for the infrared grating.	69
3.16	The fitting parameters fit to a third order polynomial for the broadband grating calibration in the horizontal direction.	70
3.17	The fitting parameters fit to a third order polynomial for the broadband grating calibration in the vertical direction.	70
3.18	The fitting parameters fit to a third order 2D polynomial for the infrared grating calibration in the horizontal direction.	71
3.19	The fitting parameters fit to a third order 2D polynomial for the infrared grating calibration in the vertical direction.	71
3.20	Broadband grating calibration error boxplots	72
3.21	IR grating calibration error boxplots	73
3.22	Calibration demonstration	75
3.23	Spectral linewidth for Neon example	76
3.24	Background stray light	78
3.25	Spectral track cross talk	79
3.26	Stray light correction	80

4.1	Example application of RASI	84
4.2	Dispersed light on the CCD	85
4.3	Transmission profiles from sample	85
4.4	Spectral absorption profile of blood from 500 to 630 nm [103]	88
4.5	Spectra for multiple states of de-oxygenation	89
4.6	Multiple states of oxygenation	90
4.7	Slit averaging overview	94
4.8	RBCs at beginning of tracking process	97
4.9	Measured absorption spectra	98
4.10	3D plot of change in absorption profile	98
4.11	Absorption spectra from 9 tracked RBCs	99
4.12	Spectral unmixing of a single RBC	100
4.13	Spectral unmixing from 9 RBCs	101
4.14	Spectral overlap	104
4.15	Spectral overlap correction via subtraction	108
4.16	Spectral overlap via linear spectral unmixing	109
5.1	Rayleigh and Raman excitation	114
5.2	Spectral output of Raman laser	118
5.3	Laser diode collimation	120
5.4	Ray trace of laser illumination	122
5.5	Laser intensity distribution in the object plane	123
5.6	Intensity distribution change with position	123
5.7	Optical filter profiles	124
5.8	RASI modified for Raman spectroscopy layout	126
5.9	Reference Raman spectra	127
5.10	Polystyrene Raman spectrum	127
5.11	Test case overview	130
5.12	Spectral classifier	131
5.13	Blind random sampling classification reconstruction	132
5.14	Grid sampling classification reconstruction	134

List of Tables

3.1	Telecentric lens parameters	56
3.2	Diffraction grating parameters	57
3.3	Spectroscopy camera parameters	58
3.4	Imaging channel geometric calibration	62
3.5	Measured Neon spectral line wavelengths	66

List of acronyms

RASI - Random Access Spectral Imaging
2D - two dimensional
3D - three dimensional
DMD - Digital micromirror device
MOS - Multi-object spectroscopy
FOV - Field of view
FTIS - Fourier transform imaging spectroscopy
CTIS - Computed tomographic imaging spectrometer
CGH - Computer generated hologram
IRIS - Image replicating imaging spectrometer
CASSI - Coded aperture snapshot spectral imager
DD CASSI - Dual disperser coded aperture snapshot spectral imager
SD CASSI - Single disperser coded aperture snapshot spectral imager
ISS - Image slicing spectrometer
LMM - Linear mixing model
CMOS - Complementary metal-oxide semiconductor (used in detectors)
CCD - Charge-coupled device (used in detectors)
RITMOS - Rochester Institute of Technology Multi-object spectrometer
NA - Numerical aperture
CAD - Computer aided design
LED - Light emitting diode
RBC - Red blood cell

Acknowledgments

This work has been funded by EPSRC and I'd like to my express my gratitude to these organisations for making this research possible.

I'd like to thanks my supervisor, Professor Andy Harvey for his support and guidance in this endeavor. I'd like to thank Tom Vettenburg and Claudio Biancotto for the friendly atmosphere in the office and many interesting discussions, as well as Tony Corcoran during the time we also shared an office. I would also like to thank my other colleagues in the Imaging Concepts group; Gonzalo Muyo, Alistair Gorman James Downing and Tushar Choudary for their support and friendship throughout.

I also need mention everybody at Glasgow: Laurence Brewer, Guillem Carles, Javier Fernandez, Lewis McKenzie and Paul Zammit who have made my time there enjoyable and helped create a friendly atmosphere in the office.

I'd be remiss if I didn't thank all my friends, both from home and all the new ones I've made in Edinburgh and Glasgow who helped me along and made me feel at home in Scotland.

Finally I'd like to thank my parents and family for their continual support and encouragement throughout this process.

Declaration

The work presented in this thesis is my own except where otherwise stated. No part of this thesis has been submitted elsewhere for any other degree.

Patrick Kelleher

Chapter 1 – Introduction

1.1 Introduction

Spectral imaging collects spatial and spectral information from a scene in the form of a three dimensional (3D) data-cube, (x, y, λ) . These data-cubes are a rich source of information about the scene and are invaluable in numerous fields: remote sensing depends on spectral imaging for classification of large land areas and rugged terrain, as well as environmental monitoring [59]; disease detection and monitoring are important applications in medical imaging [44]; security applications involving explosive detection are also prevalent [99]. However, spectral imaging is subject to a series of bottlenecks - or design trade-offs - that result in a diverse family of instruments with different applications for which they are suitable.

There are three areas where these bottlenecks come into effect. Firstly, in the mapping of the spatial and spectral elements of the data-cube to the detector, a suitable optical architecture needs to be chosen that allows for separation of the incoming spatial and spectral information; for example dispersion based systems require spatial filters that severely limit the field of view (FOV), a detailed review of different spectral imaging systems is given later in this chapter. Secondly, the detector size can limit the number of data-cube elements that can be mapped in a single measurement; this is related to the first bottleneck and is often considered concurrently. The third bottleneck is the computational processing bottleneck; due to the size and density of the data-cubes, particularly those with high resolution, the complexity of processing increases with the dimension of the data-cube, sometimes referred to as the curse of dimensionality.

As a consequence of the bottlenecks, high resolution is achieved by mapping a subset of the data-cube to the detector and time sequentially constructing the whole cube from a series of measurements. On the other hand, gathering the data-cube in a single measurement requires mapping all the data-cube elements -both spatial and spectral- to detector pixels, resulting in a reduced resolution, such single measurement techniques are generally referred to as snapshot techniques. Due to their acquisition speed, time-sequential methods are best suited to static or slowly changing scenes, whereas snapshot devices can be applied to cases where there is motion present. Different snapshot devices have different spatial-spectral resolution combinations and tend to be matched to applications where the spatial-spectral resolution trade-off is appropriate for the application, for example, devices that acquire relatively few spectral bands can optimise their choice of spectral bands to coincide with the parts of the material spectrum that are the most informative.

This thesis describes a snapshot spectral imaging technique that trades off spatial resolution for spectral, in contrast to most snapshot devices that tend to acquire a full

spatial image at small subset of wavelengths. The motivation for this approach was to exploit the natural spatial characteristics present in a scene, often similar objects will cluster and form distinct regions that have a high degree of local correlation. This is eloquently summarised in Toblers First Law of Geography,

Everything is related to everything else, but near things are more related than distant things [117].

Sampling a subset of spatial points from across the scene made it possible to make inferences about the complete scene and further allowed spatial resolution to be traded for spectral resolution. The resulting device concept could acquire spectra from distinct spatial points, in any order, from across the scene and was referred to as Random-access spectral imaging (RASI).

To implement the RASI concept an optical architecture was designed that built upon ideas from multi-object spectroscopy (MOS), with the enabling technology being a digital micromirror device (DMD), which acted as a light switch. The DMD allowed a two channel architecture to be developed, with one channel being a spectroscopy channel and the other a conventional imaging channel, used to guide the selection of different spatial regions.

Two demonstrations of RASI were performed for this thesis. First, a demonstration with red blood cells undergoing de-oxygenation - resulting in a change in spectrum - were tracked while moving, exploiting the RASI ability to acquire spectra from multiple positions across a scene simultaneously, this was in combination with the image acquisition ability which allowed the positions of the red blood cells to be tracked and the spatial coordinates from which the spectra were measured to be updated according to the tracking algorithm. The second application was to demonstrate alternate sampling methods that are possible when a device can access points across the scene in any order (random-access). A RASI device modified for Raman spectroscopy was used to construct a binary classification scenario as a test case. This test case was used to test statistical random sampling and a systematic sampling method for the application of reconstructing a classification map using only a subset of the scene data. Classification maps of the whole scene were reconstructed using a k-nearest neighbor interpolation algorithm with high fidelity when compared to the reference or ground truth classification map.

The remainder of this chapter is organised as follows: the basics of spectral imaging and the associated bottlenecks will be described; a review of different time-sequential and time resolved techniques will then be presented; an overview of spectral processing methods will be given; the RASI concept will be described in more detail in the context of other spectral imaging instruments; a review of multi-object spectrometers and digital micromirror applications will be given before presenting a final RASI design.

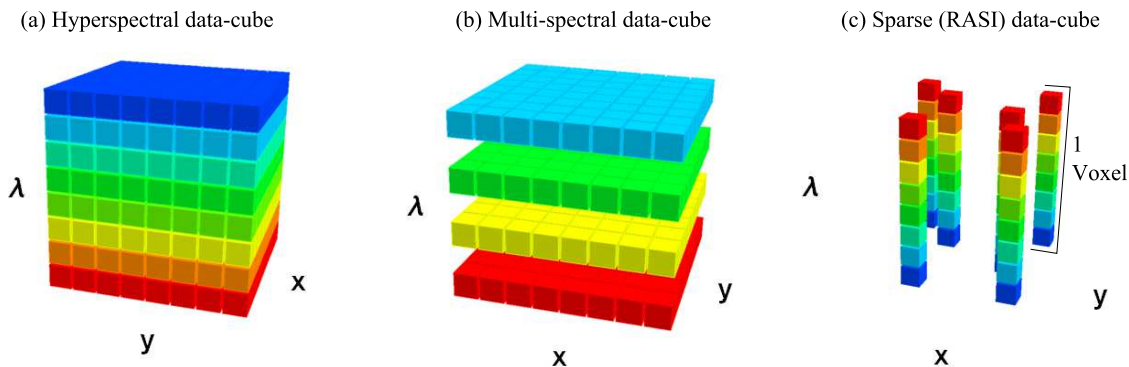


Figure 1.1: Overview of spectral imaging. (a) is a full data-cube, (b) shows a multi-spectral data-cube, which has less spectral bands than in (a). (c) shows a spatially sparse data-cube, the RASI output, it has more spectral bands than (b) but the individual voxels are discontinuous.

1.2 Spectral Imaging Overview

Spectral imaging, also referred to as imaging spectroscopy and hyperspectral imaging were first conceived of as a field in the 1980s; it is often defined “as the acquisition of images in hundreds of contiguous, registered spectral bands such that for each pixel a radiance spectrum can be derived” [63], a given hyperspectral data-cube has two spatial dimensions and one wavelength dimension with N_x and N_y elements in the x and y spatial directions and N_λ elements in the wavelength dimension. When an instrument samples the data-cube at relatively few wavebands (less than 50), it is referred to as a multi-spectral imager, with the resulting data-cube as in Figure 1.1 (b). In this thesis, the RASI approach samples the data-cube at different spatial regions, essentially acquiring a data-cube that is spatially sparse. An example data-cube is shown in Figure 1.1 (c). There is an additional imaging arm that acquires spatial data, which provides the imaging component to RASI as a red-green-blue colour image of the scene.

Since the hyperspectral data-cube consists of both spectral and spatial information, it combines elements of the individual fields of imaging and spectroscopy. In analogy to images, which are said to consist of picture elements known as pixels, data-cubes consist of volume elements that can be referred to as voxels. Each voxel corresponds to one point in space, and is the spectrum of the material at that point in space; the RASI instrument collects voxels from different points in the scene into a sparse data-cube, the image provides context for the positions of different voxels. The spectra themselves have certain properties, the shape of the spectrum can be used to identify materials by comparison with already existing spectral libraries. Each spectrum has a particular spectral resolution which determines the closest adjacent wavelengths that can be distinguished and the spectral range gives the range of wavelengths over which the spectrum is obtained, e.g. the visible portion of the electromagnetic spectrum from 400 –

700 nm, or the spectrum from in-elastically scattered light from Raman spectroscopy.

1.2.1 Spectral Imaging: Limitations and Bottlenecks

When considering the bottlenecks, it useful to consider the first two together, that is the optical architecture and the detector throughput, as many of their issues are inter-related, the spectral resolution as set by the optical architecture can be limited by the number of pixels on the detector for example. In order to help understand the bottlenecks, it is useful to consider a figure of merit that relates the data-cube elements to the detector pixels. This figure is adapted from astronomy, where it was used to compare integral field units, which are a form of hyperspectral imager. The figure of merit function was the Specific Information Density [4], denoted as ρ_I here, and expressed as

$$\rho_I = \eta \frac{n_x n_y n_\lambda}{N_l N_m}, \quad (1.1)$$

where N_l and N_m are the numbers of detector pixels, n_x and n_y are the number of spatial resolution elements and are related to the spatial elements of the data-cube by $N_x = f_s n_x$ and $N_y = n_y f_s$, the term f_s is the oversampling of the detector, the axes of the detector and data-cube spatial dimensions are assumed to be aligned. n_λ is the number of spectral resolution elements and is related to the data-cube spectral elements by $N_\lambda = f_\lambda n_\lambda$ and f_λ is the spectral oversampling by the detector. The term η is the system throughput. In the case of Nyquist sampling the oversampling factors would be 2 ($f_s = f_\lambda = 2$).

The limiting form of Equation 1.1 is

$$N_x \times N_y \times N_\lambda = N_l \times N_m \quad (1.2)$$

which gives the maximum number of data-cube elements for a given detector size in a single measurement. The factors, N_x, N_y, N_λ are set by the optical architecture and dictate how much of the data-cube can be gathered in a single measurement, whereas the N_l and N_m set the throughput by the detector and which also limits the acquisition of the data-cube elements. In the case of time-sequential hyperspectral imaging, when a subset of the data-cube is being collected, the resolution of two of the dimensions of the data-cube can be maximized. This is possible because the whole data-cube is then constructed by stepping through the third dimension of the data-cube; because of this, time-sequential hyperspectral imagers tend to have higher resolution than snapshot approaches. Snapshot devices are more complex in that all the components of the data-cube must be mapped to the detector in a single measurement, resulting in the necessary trade-off between spatial and spectral resolutions. The enabling technology for most modern snapshot systems are large format two dimensional (2D) detector arrays which have become larger and more affordable. Furthermore the advantages of snapshot

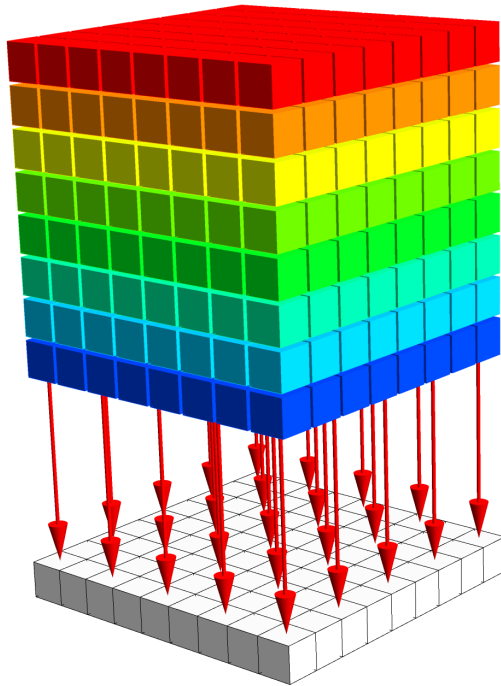


Figure 1.2: Mapping of a 3D cube to a 2D detector.

devices are similar to the Jacquinot and Fellgett advantages in traditional spectroscopy [67].

As an example, consider a spectral image with $N_x = N_y = 1000$ and $N_\lambda = 500$. The total number of elements required by this size data-cube is then $5 \times 10^8 = 500$ Mega Pixels. This is the size of some of the largest array detectors currently in existence. Currently Gigapixel images do exist, but they are generally stitched together from lower pixel count images, rather than being collected using a single detector. The core point being that the difficulty in mapping high-resolution spectral data-cubes to a 2D detector lies with the radical increase in data size, which limits the amount of spatial-spectral information that can be collected in a time-resolved measurement without trading-off the spatial-spectral measurements as described in Equation 1.2.

The final bottleneck is due to the sheer volume of data obtained, high resolution data-cubes often have mega-pixel spatial resolution and hundreds of spectral bands as in the example above. The dimensionality of the dataset increases the complexity of processing, the so called "curse of dimensionality" [101]. The increase in data set size also brings other issues. It can increase the presence of noise, resulting in noisy bands being discarded during processing. Further the larger number of variables can increase the running time, preventing the processing of data in real-time.

Large hyperspectral data-sets are also subject to many of the same drawbacks and issues as other problems in big data [45]. Often they require novel and experimental algorithms to process, also interpretation of the data set can be misleading. The field of big data is still in its infancy and the techniques for meaningful dimension reduction

Resolution trade-offs

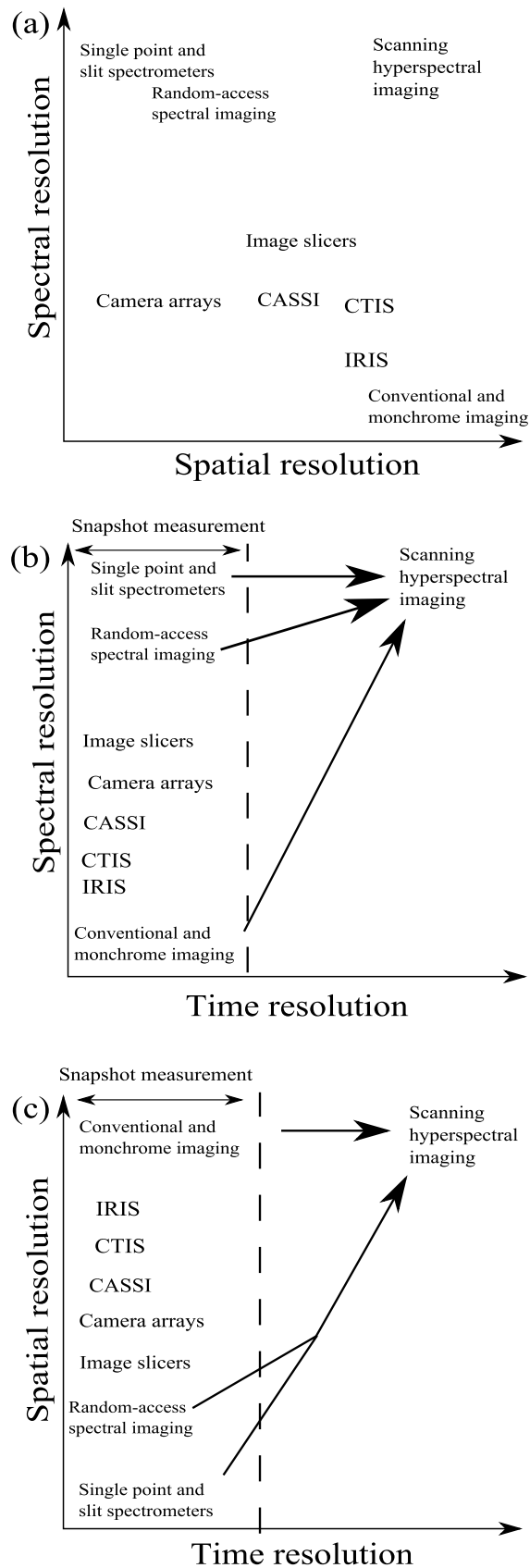


Figure 1.3: (a) shows the trade-off between spectral and spatial resolution for a single measurement or snapshot, (b) and (c) show the time evolution for scanning methods to achieve a full data-cube. The single measurement and snapshot time regime is labelled on (b) and (c).

that allow for convenient interpretation are still being developed. Examples in wrong predictions using big data have occurred, often based on misguided interpretation and overly simple metrics that have been extended from lower dimensional spaces [84]. However the field is rapidly developing and many of these topics are active and fruitful areas of research.

Figure 1.3 gives an overview of the resolution trade-offs in spectral imaging for different spectral imaging devices, both snapshot devices and time-sequential scanning devices, a review of which will be given in Section 1.3. Figure 1.3 (a) shows the trade-off between spatial and spectral resolution for a single measurement, to map the entire data-cube results in a reduced spatial and spectral resolution of the final data-cube for snapshot devices. Figure 1.3 (b) and (c) show the time axis of the trade-offs, which demonstrates how scanning methods achieve high resolution by combining multiple measurements. The result for scanning methods is the potential for both high spatial and spectral resolution in the final data-cube.

The RASI device trades off spatial resolution for spectral resolution in a snapshot device, collecting data from a subset of spatial regions at a large number of spectral bands, unlike most other snapshot devices which sacrifice the number of spectral bands for better spatial resolution in those bands as shown in Figure 1.3 (a). The so-called sparse data-cube collected by RASI helps to avoid the third bottleneck reducing the amount of data collected, data collection is guided using the conventional imaging channel so as to collect spectra from regions of interest rather than every point in the scene. This is particularly advantageous for time-series measurements where, if a full data-cube were collected at each step, not only would it be subject to the lower resolution of snapshot devices but also the volume of data would increase rapidly, which would limit the possibility of processing in real-time. The selection of spatial regions of interest improves the processing and removes the need to search through the whole data-cube, in principle moving some of the processing load to the acquisition phase. With respect to Figure 1.3 (b) and (c), RASI can clearly be used as a scanning hyperspectral imager as well, by combining a series of sparse data-cubes over time it can achieve high spatial and spectral resolution data-cubes, in the same manner as other scanning hyperspectral imagers.

1.3 Hyperspectral Data Acquisition

The various methods of data acquisition (many of which were shown in Figure 1.3) can be used to define the different techniques of spectral imaging and their areas of applicability. Time-sequential methods build up the cube over time, whereas time-resolved take enough data to acquire or reconstruct the cube from a single measurement. Direct spectral imaging techniques acquire the spectral information directly (using dispersive

elements or filters for example), whereas indirect methods extract the spectra via some form of inversion process (Fourier Transform spectroscopy for example). The following section will detail these processes with a particular focus on snapshot spectral imaging.

1.3.1 Time-sequential Spectral Imaging

Time-sequential approaches to spectral imaging are often extensions of standard spectroscopy devices, for example spatial scanning methods pass a slit based spectrometer over a scene and, combine the slices of the data-cube into a complete data-cube. Often they are applied to applications where the scene is static or the scanning motion complements the acquisition process, such as a conveyor belt. Scanning methods also include tunable filters that scan in the wavelength dimension and Fourier Transform Spectrometers.

Spatial scanning

Spatial scanning involves extracting the wavelength information from a spatial subset of the scene. The full data set is then built up in a time sequential manner by scanning over the whole scene. Two relatively common types of spatial scanning are whiskbroom and pushbroom scanning [110]. A whiskbroom sensor scans the scene and acquires a single voxel at time, which is a fraction $\frac{1}{N_x N_y}$ of the total data-cube. Pushbroom scanning acquires a one dimensional slice of the data-cube using a slit, a fraction $\frac{1}{N_x}$ of the total data-cube in a single measurement, both are shown in Figure 1.4. In terms of optical design both approaches are conceptually similar, an objective lens focuses light onto an entrance aperture -slit in the case of pushbroom - after which the light is collimated and passed through a dispersive element (a prism or diffraction grating) used to separate the wavelengths before they are re-imaged onto a detector [65]. Whiskbroom methods require the use of additional moving parts, a scanning mirror, which is a significant drawback compared to other methods, especially when the hyperspectral imager needs to be mounted on a mobile platform.

In remote sensing applications, the natural sweep of the satellite or aircraft provides the necessary scanning motion for time-sequential methods to operate. Various space based observing systems exist [100], also aircraft based sensors, such as the ubiquitous AVIRIS system [102] which provide large amounts of data on mineral, vegetation coverage, forests and urban areas. Numerous spectral processing algorithms have been developed with these data sets which will be discussed later.

Wavelength Scanning

Wavelength scanning takes a slice of the data-cube through the spatial dimensions, essentially a monochromatic image. By stacking these monochromatic images so as to

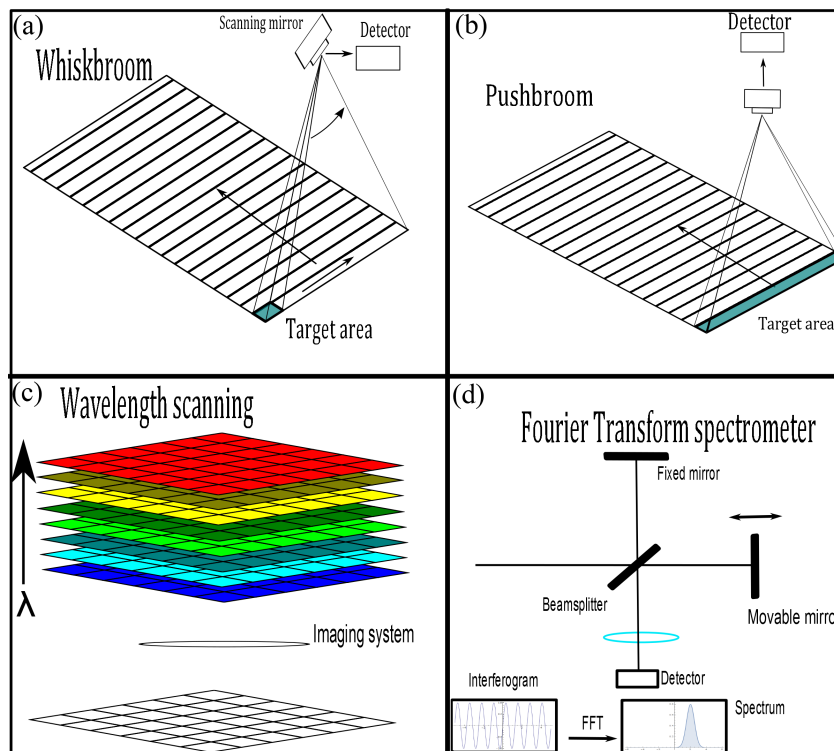


Figure 1.4: (a) and (b) show the operation of a whiskbroom and pushbroom scanner respectively. (c) shows the collection of monochromatic images stacked to form a hyperspectral data-cube as an example of wavelength scanning. (d) is an outline of the operation of a Fourier transform spectrometer.

align their spectra, a hyperspectral data-cube can be formed this is shown schematically in Figure 1.4.

Wavelength scanning approaches tend to be optically simpler than other time-sequential spectral imagers, often being imaging systems with the addition of a filtering mechanism before the detector, or with wavelength selective illumination. The simplest of these methods use a filter wheel and sets of interference filters, more sophisticated approaches employ electro-optical and acousto-optical filters [77]. The latter two options offer the most flexibility in the form of Liquid crystal tuneable filters and Acousto-optical tuneable filters [55]. The incoming radiation can be filtered without the use of moving parts or multiple filters, further simplifying the optical design of these devices. This also allows faster scanning speeds and removes the need for moving parts in the design.

Wavelength scanning approaches allow for all points in a particular field of view (FOV) to be imaged simultaneously at an individual wavelength. The number of measurements required to measure the entire data-cube depends on the number of wavebands being measured. This can lead to high speed data acquisition appropriate for various biological spectral imaging applications, though the optical efficiency is still limited as all light from outside the measurement waveband is necessarily discarded by the filtering process.

Fourier Transform Imaging Spectrometer

Spatial and wavelength scanning determine the spectrum by directly measuring the different components, Fourier transform imaging spectroscopy (FTIS) first measures an interferogram and performs an inversion to calculate the spectrum, a hyperspectral data-cube is obtained by scanning the FTIS across the whole scene.

The principle of operation is similar to that of a Michelson interferometer. Light from the source is passed through a beam-splitter, down one path is a fixed mirror; the other has a movable mirror, as shown in Figure 1.4. The reflected beams interfere with each other causing some wavelengths to be canceled by destructive interference; the intensity for that configuration is then recorded at the detector. Altering the position of one of the mirrors results in a different interference pattern, by measuring the intensity for a series of different positions, an interferogram is built up, Fourier Transforms are used to convert the interferogram into a wavelength spectrum, as obtained by direct spectroscopy. It is worth noting that the detector can be a 2D array detector[109], which removes the need to scan spatially, as the interferogram for each spatial point can be obtained simultaneously.

FTIS has a throughput advantage (Jacquinot advantage) over spatial filter based (i.e. a slit) spectrometers, in that the aperture itself is the limit to optical throughput rather than a slit; though the input beam should fill the entire input aperture for the full improvement. FTIS also has a multiplex advantage as it collects all the wavelengths in a spectrum simultaneously, this advantage is most important when the measurement is limited by detector noise[76].

Despite its advantages, in the context of spectral imaging FTIS still suffers from in-efficient light collection due to its scanning, if a 2D detector is used, it is similar to the efficiency of the wavelength scanning approach.

1.3.2 Time-resolved Spectral Imaging

In contrast to the time-sequential scanning, snapshot spectral imagers acquire the data-cube in a single measurement (a multiplex advantage over scanning methods); the consequences of this are the trade-off in spatial-spectral resolution and, in general, a more complex optical system. The advantages for snapshot systems lie in their application to dynamic, real-time scenes, where the presence of motion artefacts severely limit the applicability of scanning. Further, snapshot devices can have a throughput advantage over traditional scanning methods as they no longer filter out a portion of the data-cube during acquisition; the $\frac{1}{N_x}$ and $\frac{1}{N_\lambda}$ factor for spatial and wavelength scanning respectively [67]. Most snapshot methods are multi-spectral due to their relatively low number of spectral bands, also when acquiring data in real-time, they are subject to the same data

processing limitations.

Computed Tomographic Imaging spectrometer

Computed tomography is a process of reconstructing a 3D space from a series of 2D projections of that space. Sophisticated algorithms used to generate highly accurate reconstructed representations of the 3D space are often referred to as x-ray transforms. In medical imaging, X-Rays are used to image bone structure and human body parts and the term “CT scan” is used to describe a computed tomography scan. The principles of Computed Tomography have been applied extensively in other fields and the estimation of the 3D spectral datacube is a natural application for the x-ray transform.

The Computed Tomographic Imaging Spectrometer (CTIS) is snapshot hyperspectral imaging technique that employs the methods of computed tomography to estimate the spectral imaging data-cube. The system consists of the fore-optics which collects the light, which is then collimated. The dispersing element in the system is the computer generated hologram (CGH), which is similar to a pair of crossed diffraction gratings, indeed crossed gratings were used in early CTIS models [32]. The light from the field

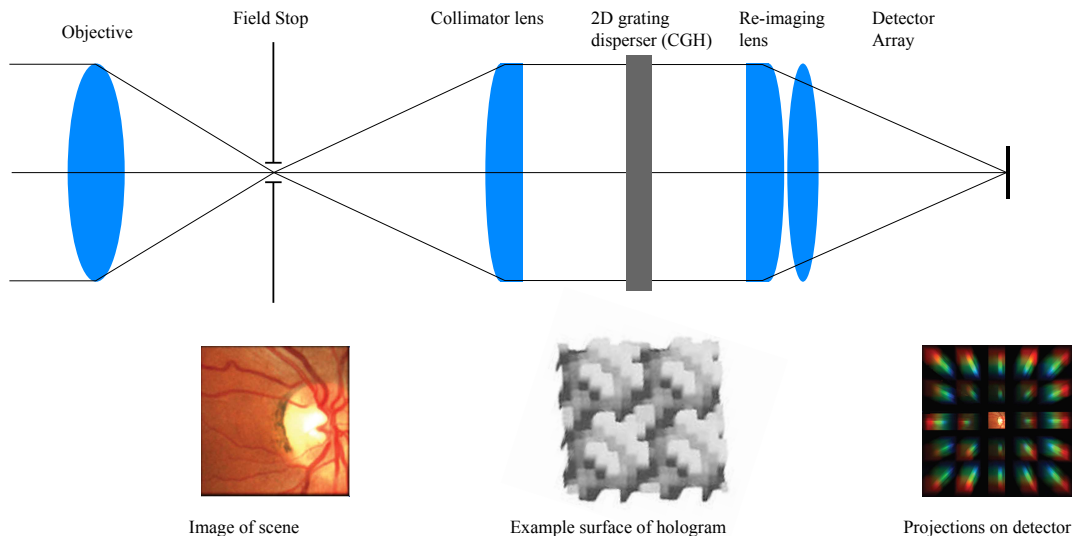


Figure 1.5: Diagram of the optical layout of CTIS; the field stop image of the retina, the example CGH and image of datacube projections are reproduced and modified from [75] for demonstrative purposes.

stop passes through the computer generated hologram element, resulting in a series of projections of the field stop diffracted by the holographic element, the projections are then re-imaged on a 2D detector, as shown schematically in Figure 1.5. The central projection is a panchromatic zero order image of the field stop, the outer orders are 2D spectrally dispersed projections corresponding to different diffraction orders, with the order increasing with distance from the central zero order image. Computer generated

holograms are often designed to redirect light from the zero order to the higher order projections, which are often light starved. Collecting numerous projections simultaneously allows the 3D spectral datacube to be estimated from a single measurement.

The reconstruction process for CTIS considers each of the projections as “parallel projections of a continuous three-dimensional volume onto a plane” [32]. Further, the Central Slice Theorem allows that the Fourier Transform of each of these projections is plane in the 3D frequency space of the (x, y, λ) datacube. These planes pass through the origin of the frequency space datacube. The normals of the different planes in frequency space are tilted at the same azimuthal and projection angle as their spatial inverse. In principle, the 3D frequency space cube can be recovered from the 2D projections in that space. Then a 3D inverse Fourier Transform can be performed to recover the real-space spectral datacube. The details of this aspect are dependent on the imaging properties of the device itself, enough projections must be gathered to estimate the 3D cube.

This leads to some of the natural limitations of CTIS, the number of projections is set by the size of the focal plane array as well as the field stop size and projection angles created by the CGH. It is possible for a sufficiently compact diffraction pattern from CGH to use every pixel on the detector to supply data, though this is an upper bound.

Further, there is a limit on the projection angles allowable in the CTIS design. The result of this is an upper bound on the projection angles available to be sampled. The primary factors in this limit are detector size and efficiencies of higher diffraction orders. This leaves a missing cone in the frequency space datacube, leaving insufficient data for a unique solution to be made. Although in practice the missing cones effect on the reconstruction can be mitigated using physical constraints and a priori knowledge about the scene [66]. The scene itself can affect the reconstruction; the spatial frequency content, spectral properties, brightness and background noise characteristics of the scene are all parameters that need to be considered in the design of recovery algorithms for different imaging tasks.

The CTIS has been used for ophthalmology [75], it has been combined with a microscope for fluorescence [47] microscopy it has also been involved in feasibility studies for astronomy applications [71]. It fulfills a role as a medium spatial/spectral resolution device that offers a snapshot capability. Its requirement for computationally intensive and bespoke algorithms limits its range of application.

Image Replicating Imaging Spectrometer

The Image Replicating Imaging Spectrometer (IRIS) is a snapshot multi-spectral imaging system that cascades a series of birefringent interferometers to spectrally filter and demultiplex multiple spectral images onto a detector array. The birefringent interferometer consists of an input polariser, followed by a wave-plate and then a Wollaston

prism. The incoming light is initially linearly polarised, then the wave plate divides it into two orthogonally polarised components, according to the fast and slow axis of the wave plate. The Wollaston prism causes interference between the orthogonally polarised components such that the ray splits into two divergent rays, with orthogonal polarisation. Each input ray after passing through N of these so-called birefringent spectral de-multiplexors will split into 2^N output rays [68]. The spectral transmission functions of the different rays can be altered to provide different performance. The filter functions provide cyclic transmission peaks, so a bandpass filter is used to control the spectral range of light entering IRIS. The spectral characteristics of the transmission function have a central transmission passband with adjacent significantly weaker side lobes. The filter functions are the same as those described by a Lyot filter.

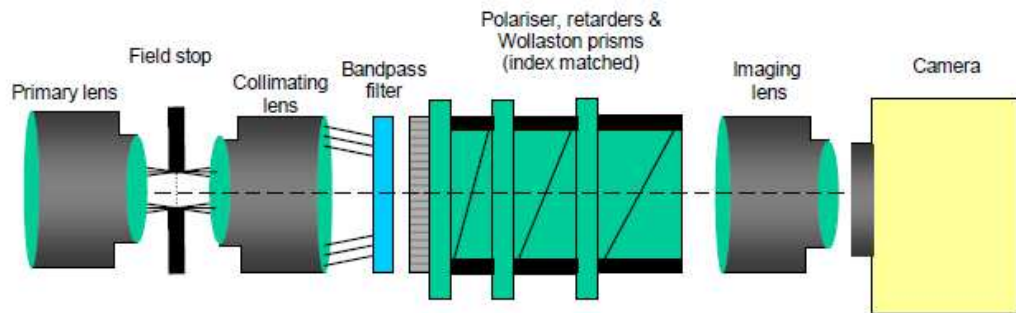


Figure 1.6: Schematic of IRIS reproduced from [68].

This system has been applied to retinal imaging where, considering the constant movement of the eye it offers considerable advantages over time-sequential techniques. It has also demonstrated the ability to record multi-spectral movies, without the need for significant reconstruction algorithms [61]. The number of wavebands is set by the number of cascaded birefringent spectral de-multiplexors. Further, the finite extent of the detector also limits the number of de-multiplexed images of the field stop that can be obtained. Optical throughput for one of the spectral bandpasses of the system is high as a large aperture is used. The transmission efficiency of an individual waveband depends on the form of the transmission function, generally less than 10% of the total light is lost to the side-lobes.

Coded Aperture Snapshot Spectral Imager (CASSI)

Coded aperture techniques have been applied to X-ray phenomenon for a number of years. A coded aperture consists of multiple opaque and transparent regions, this is located in front of the detector to modulate the incident radiation. Then by exploiting the known properties of the coded aperture and the information at the detector, the source distribution can be determined [62]. The coded aperture snapshot spectral imager (CASSI) system combines the principles of coded apertures into a device that is capable of snapshot spectral imaging. It has two reported configurations.

The dual disperser CASSI (DD CASSI) system has a dispersing path both before and after the coded aperture [57]. The layout of DD CASSI is shown in Figure 1.7 (b), the system images a scene, the light from which is dispersed and re-imaged in the first dispersing path. The scene is re-imaged onto the coded aperture, but due to the dispersion, multiple images are formed at different, wavelength dependent locations. These images and their intrinsic mix of spatial and spectral information are then modulated according to the pattern on the coded aperture. The second dispersing path after the coded aperture, counter-acts the effects of the first dispersing path and creates an image of the source at the detector. This process turns the spatial modulation of the coded aperture into a change in both the spectral and spatial information. The DD-CASSI design multiplexes spectral information in a localised spatial region on the detector, the detector image is similar to the scene.

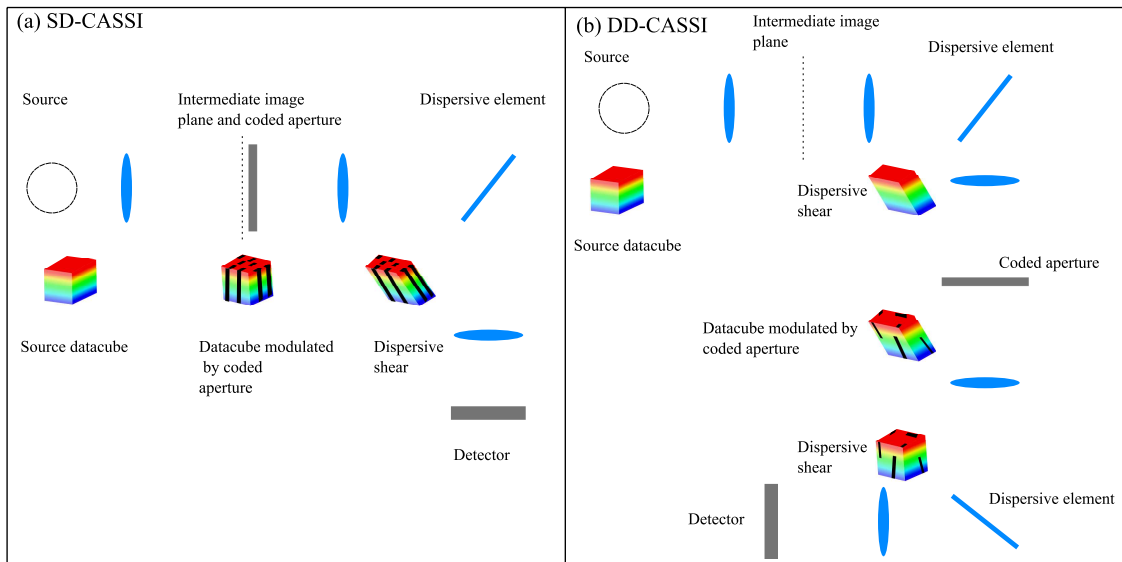


Figure 1.7: (a) shows the SD CASSI layout and (b) the DD CASSI, see text for more detail.

The single disperser CASSI (SD CASSI) model, shown in Figure 1.7 (a), operates with a single dispersion element, its setup is similar to any standard dispersive spectrometer system, except with a coded aperture as the entrance aperture. It has less optical components than DD CASSI, also it is capable of imaging point sources unlike DD CASSI which multiplexes only spectral information in the data-cube. The SD-CASSI design results in spatio-spectral overlap of the dispersed and modulated datacube in the detector plane, effectively multiplexing both spatial and spectral information. SD CASSI has been reported with improved designs, using double Amici prisms for video rate spectral imaging. A scene with lighting birthday candles has been imaged with this system in [123]. A modified SD CASSI system has been reported attached to a Zeiss AxioObserver A1 inverted microscope for fluorescence microscopy applications, in this instance the test case was the tracking of ten fluorescent beads [30].

The two reported designs of CASSI have different limitations. The DD-CASSI

cannot reconstruct the spectrum of a point source as it multiplexes only spectral information, but in general it offers higher spectral resolution. SD CASSI can resolve point sources, provided it maps to an open element of the coded aperture, otherwise the light from the point source would be blocked by the code. It can also provide superior spectral resolution, at the cost of a lesser spatial resolution.

The CASSI architecture seeks to avoid the limitations imposed on other snapshot spectral imaging approaches, by detector sizes and other bottlenecks. The approach, borrowing from compressive sensing ideas, avoids directly measuring the voxels present in the scene datacube. Rather it collects a significantly reduced subset of the datacube and reconstructs the datacube using various algorithms. Numerous algorithmic approaches exist for the two CASSI designs and the design of novel codes and re-constructive algorithms is an ongoing area of inquiry [90]. CASSI offers a throughput advantage over traditional time-sequential designs, without sacrificing resolution, which is one of the key features of coded aperture spectroscopy. Since the coded aperture itself consists of alternating transparent and opaque regions, CASSI blocks half the light from entering the instrument, resulting in a throughput of 50%.

Integral Field Spectroscopy - Fibre reformatters and lenslet arrays

In the field of astronomy, hyperspectral imaging is referred to as integral field spectroscopy. The goal remains the same; the acquisition of a datacube with spatial and spectral information (x, y, λ) . Reformatter techniques divide the scene into sections and re-arrange them via some method to fit the entrance aperture of a spectrometer, essentially reformatting the scene to the form of the entrance aperture shape. Two of the most common methods performing this reformat are fibre reformatters and lenslet arrays [4].

A fibre reformatter approach places a densely packed array of fibres at an intermediate image plane of an imaging system, as seen in Figure 1.8 (a). A lenslet array is used to couple light into the fibres. The scene can be sampled according to how closely the fibres can be packed together. The image of the fibres output is coupled to the entrance slit of a spectrometer, it should be noted that the fibre aperture is round. The light is dispersed by the spectrograph and a spectrum for each spatial area associated with each fibre is obtained. The long slit of the spectrograph needs to be of sufficient length to facilitate all the fibres from the two spatial directions. The fibres themselves can affect performance, the spectral transmission properties of the fibres and the possibility of so called modal noise are all accounted for in fibre reformatter.

The lenslet array approach re-images portions of the scene to a spectrograph entrance, which has its slit removed. The positions of the lenslet array compared to the scene sets the spatial sampling of the scene. The pupil size of a lenslet is set by the

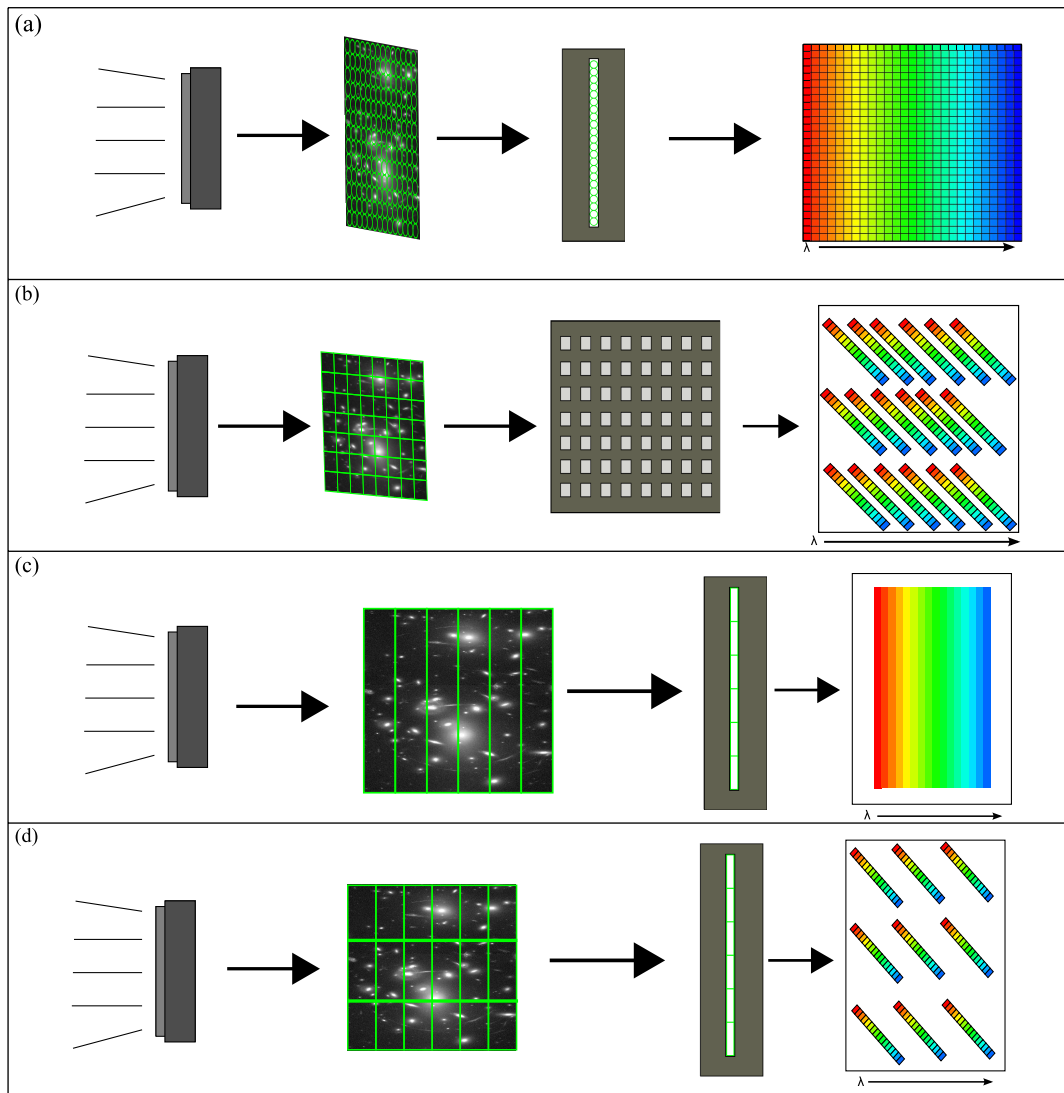


Figure 1.8: (a) shows the scene scene divided up according the fibres and then reformatted to a long slit. (b) is an example of the layout of a reformatter based on a lenslet array approach, the rotated dispersion is shown on the detector plane. (c) is an example of scene divided into a series of slits by an image slicer and re-imaged onto the long slit of spectrometer. (d) shows the scene divided by a micro-slicer, which has smaller slit elements than a standard image slicer.

magnification, which is often the critical parameter in such systems. This is limited by the possibility of spectral overlap in the spectrometer detector plane and short spectral ranges are used to counter this. The dispersion is often rotated to allow larger spectral ranges as well [12], shown in Figure 1.8 (b). Further, the use of a lenslet array improves the fill-factor of the fibre bundle.

Integral Field Spectroscopy - Image Slicers

Image slicing spectrometers (ISS) are another type of integral field spectrograph [27], the approach reformats the scene onto the entrance slit of a spectrometer. This is achieved

by placing a mirror consisting of thin slices at an intermediate image plane in the optical system. The orientation of each mirror slice is such that the individual slices of the input image are laid out end to end to form the input slit of a spectrometer. Figure 1.8 (c) shows a representation of the reformatting process.

The enabling technology for ISS are the image slicers, a range of designs are possible including plane mirrors and fan shaped mirrors [121]. The use of mirrors make the ISS particularly apt for use in the IR spectrum as the whole system can be constructed from mirrors.

Figure 1.8 (d) shows an alternate form of image slicer, that of a so-called micro-slicer. The approach combines a lenslet array to divide the field of view and crossed cylindrical arrays to turn each pupil image into a slice by exploiting the anamorphism present in the optics [28].

ISS were first developed for astronomy and that is where they still see a large degree of application, there have also been examples of applications in remote sensing [29]. Recently in the literature an example of an Image Slicing spectrometer (ISS) for microscopy has been reported [54]. A microscope is used as the fore-optics, the intermediate image plane from the microscope is re-imaged using a telecentric relay to the image slicer, whereupon it is reformatted and redirected so that it passes through a dispersing prism and is subsequently re-imaged via a lenslet array onto a focal plane array. Unlike other image slicing systems the re-imaging array is designed such that images of each slice overlap at the detector, this is to ensure efficient use of the focal plane array.

The image slicing approach allows the whole scene to be spatially and spectrally interrogated in a snapshot. It offers spectral performance on-par with standard single slit spectrometers, albeit with a longer entrance slit, without the loss due to spatial filtering of the scene from pushbroom techniques. Like all snapshot devices it is still subject to the trade-off in spatial and spectral resolution due to the finite size of the detector. Since the data-cube is taken in its entirety with each measurement, the possibility of real-time processing decreases as the data size increases. Other issues with data mining are also possible with the increased data output, though in many cases it is also advantageous to acquire the whole data-cube particularly where the potential regions of interest are unknown beforehand.

Multi-aperture and filter array cameras

An effective approach to time-resolved spectral imaging is to either distribute different wavelength information to different portions of the detector array, or otherwise have a different detector for each waveband being collected; IRIS is a sophisticated example of such an approach. A more straightforward method of achieving this is via filter arrays

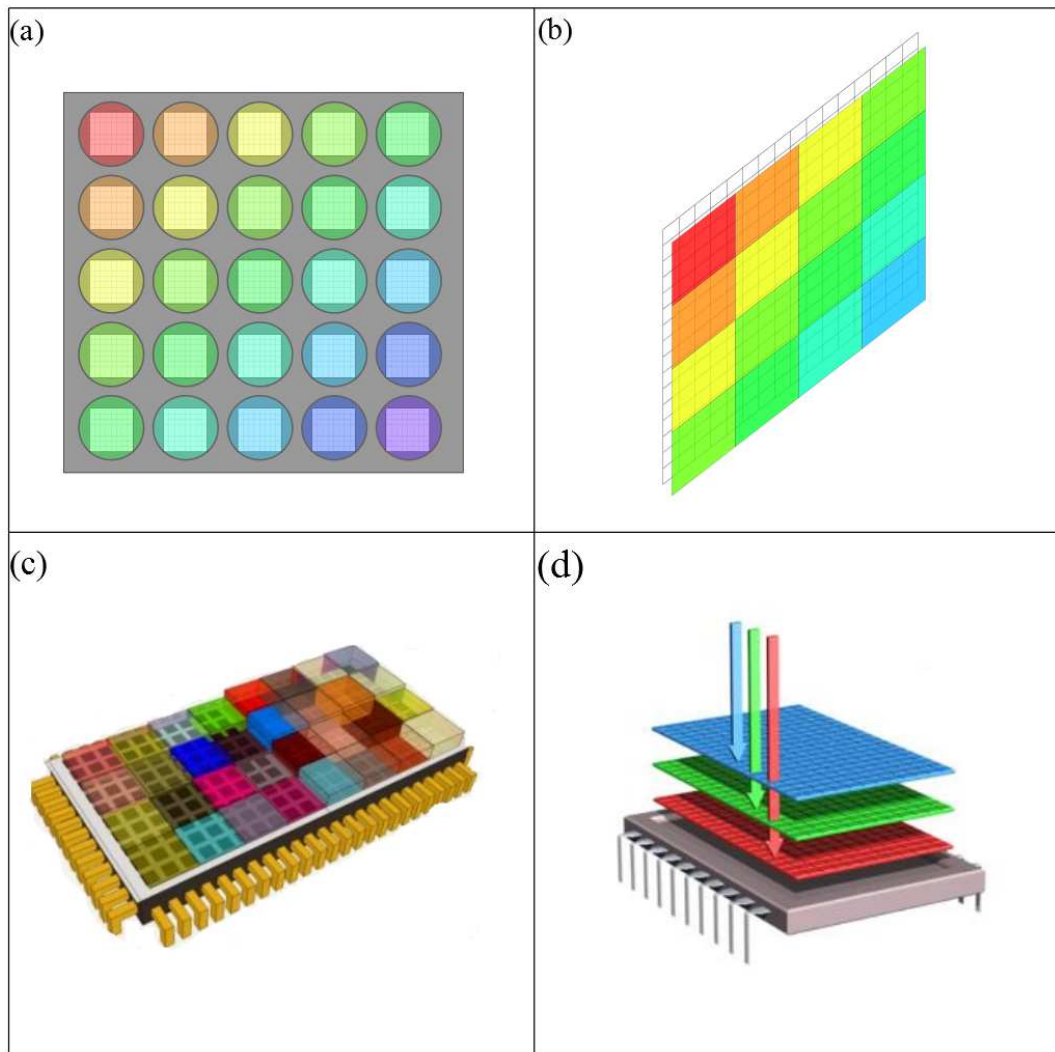


Figure 1.9: (a) is an array of cameras with a different bandpass filter over each separate aperture. (b) is a focal plane array with a mosaic of filters at different wavelengths dividing it up. The diagram in (c) shows the monolithic Fabry-Perot mosaic of filters over a CMOS sensor [113]. Finally (d) demonstrates the basic principle of operation of the FOVEON sensor which relies on the different layers of the detector being sensitive to different parts of the spectrum.

over the detector.

Arrays of cameras with a unique bandpass filter over different cameras is a methodology that offers a robust approach to spectral imaging [38] shown in Figure 1.9 (a). The cost of cameras and filters - in the visible range - in recent years has decreased dramatically and is set to continue its fall. The size of the individual cameras is on the scale of millimetres, though the number of wavelengths is limited to the number of cameras that can be reasonably packed into an appropriate area, making it unfeasible for large numbers of wavelengths. Issues with differing view perspectives also place limitations on the number of cameras that can be tiled in this manner.

Figure 1.9 (b) shows a tiled arrays of filters placed over a 2D detector array with

different wavelength passbands for each filter [94]. A single lens can be used for system, allowing a simple optical layout, though they do require de-mosaicking algorithms which can be demanding [95].

A particularly potent example of such a design is shown in Figure 1.9 (c) and employs a series of Fabry-Perot etalons fabricated monolithically and combined with a CMOS sensor [113]. Fabry-Perots can perform as optical filters, the central wavelength can be tuned according to the distance between the mirrors in the etalon. Other filter characteristics such as the passband FWHM and even the transmission can also be altered. These Fabry-Perot arrays are fabricated and placed over a standard CMOS sensor. The filters can be tiled in a manner similar to a Bayer matrix, allowing for both spectral and spatial information to be obtained, though there is a trade-off between the number of bands and the spatial resolution possible via this layout [56].

Another notable mention are the so-called Foveon sensors, which are a developing technology that show promise for future applications [58]. It is the digital analogue of three-colour chemical films. These films had three layers of photosensitive film, one for each of the red, green and blue necessary to make a colour image, prior to the advent of digital cameras. Foveon sensors have three layers of silicon on top of each other. Each layer is modified to be sensitive in the red, green or blue part of the visible spectrum. The combination of the three layers provides a colour image without the need for a Bayer matrix and the interpolation required to generate a full colour image. As this technology develops it could be possible to directly measure a spectrum at each pixel [40].

1.4 Hyperspectral Data Analysis

Once the data has been obtained, the processing and analysis must be considered. The computational complexity of these approaches depends on the spectral and spatial resolution of the datacube, which relates to the size of the data set, to that end dimension reduction is often a part of the processing. One of the most common and desired outcomes of hyperspectral image processing is the classification of the different spectra into different spatial regions, with each region corresponding to a different spectral class. Traditionally represented as a false colour image, with different colours representing the different spectral classes. This allows for easy visualisation and interpretation of the 3D information present in the dataset. Many implementations of these algorithms exist, providing novel and efficient approaches to solving classification problems in different contexts.

Waveband optimisation is a process whereby the optimal wavebands for measuring a particular phenomenon are determined. It can be quite similar in practice to some dimension reduction approaches, often wavebands that are noisy or contain redundant data are removed.

An important consideration in spectral imaging applications is that the spectra associated with each voxel is not necessarily a pure spectra and may be a superposition of several spectra. To deal with this a process known as spectral unmixing is used.

1.4.1 Hyperspectral Image Classification

Hyperspectral image classification relies on comparing the spectra in a particular dataset to a so-called training set, this training set can be from a spectral library, constructed from ground truth or extracted from the dataset itself. Selecting the training set can be accomplished via supervised, with user involvement, or unsupervised automatic methods. Spectra from the recovered data-cube are compared to exemplar spectra in the training set. A variety of methods are available to perform this, a common metric is the spectral angle mapper, which takes the inner product of two vectors and computes the difference between them as an angle [59].

$$\theta = \cos^{-1} \frac{a \bullet b}{|a| |b|}, \quad (1.3)$$

where a and b are two vectors being compared, other comparison metrics exist that are well described in [59]. By systematically comparing every spectra in the data set to the training set, the voxels can be classified into their respective classes, this then leads to the familiar false colour image commonly produced in hyperspectral imaging post-processing. This systematic approach is time consuming and is a “brute force” approach to the classification problem, it neglects the spatial component of the hyperspectral image. More sophisticated approaches combine spatial and spectral information to make the classification of the scene more efficient [114]. This is achieved by selecting a small number of wavebands to identify spatial regions and distinct objects to cluster the data and reduce the number of calculations required to classify the whole datacube.

Often it is only a small number of objects that are of interest, so the problem becomes efficiently extracting the objects characteristics from the data-cube. Various approaches exist for this, depending on the unique characteristics of the object of interest [114]. The possibility of mixed spectra, the case where the spectra in a given voxel is a combination of multiple basis spectra limits the application of these. Spectral unmixing must be performed before the above techniques can be fully applied.

Dimension Reduction

Generally the size of datasets can be extensive, making processing slow. Dimension reduction and data compression can be used to reduce the size and manageability of these processes, allowing for improvements in processing speed and easier interpretation. The distinction between dimensional reduction and data compression is that the former does

not reduce the dimension of the data with the goal of reconstructing an approximation to the original, which is the goal of data compression. Rather it seeks to present the minimum amount of data required for any processing of the lower dimension data set, without a significant reduction in performance.

The simplest approach to dimension reduction involves removing spectral bands. The removal of these bands depends on the knowledge available about these bands. Often they can contain redundant information or are otherwise known to be unreliable. This approach is dependent on prior knowledge of spectral characteristics, which is often not the case.

Another method of dimension reduction which also involves the optimisation of squared error is the optical real-time adaptive spectral identification system (ORASSIS) [14]. This is a modular data processing system, designed specifically for use with remote sensing hyperspectral imagers based on aerial or space-based platforms. To reduce the dimension of datasets, initially a subset of exemplar pixels are selected. These exemplars represent the different pixel classes present in the scene. Pixels from the scene are compared to each pixel in the set of exemplars, generally using an angle metric. Any new pixel that is sufficiently different from the pixels in the exemplar is then added to the set. The exemplar set is used to create an orthogonal basis, thus creating a reduced dimension dataset, though the reduction depends on the diversity of endmembers present in the scene.

Other approaches to data and dimension reduction exist, it is an active area of research with respect to its application to hyperspectral datasets. As hyperspectral data acquisition improves, the resolution and acquisition speed of data-cubes increases as well. This leads to much greater aggregation of data, as individual datasets are larger and more are collected, thus requiring faster and neater approaches to processing and visualising collected data in a reduced format so as to be interpretable.

1.4.2 Spectral Unmixing

It is possible that the spectrum at the detector is mixed, i.e. a mixture of more than one distinct substance. This can be due to the spatial resolution of the sensor being low enough that numerous spectrally distinct regions being imaged occupy the same voxel, the measured spectrum from the voxel will be some combination of the constituent materials. Otherwise mixed spectra can be the result of mixed materials in the voxel. The term “Spectral unmixing” describes a systematic method by which the mixed output signal is divided into its constituent spectra. These are referred to as endmembers, the proportion of each endmember present in the signal is referred to as the abundances [81].

Linear unmixing model

The most commonly used algorithms in spectral unmixing are based on a linear mixing model (LMM). In this case it is assumed that the spectral abundances of each endmember in the scene are linearly related to the spectral intensity of each endmember in the measured signal. If in a scene M endmembers exist each having L elements this linear relationship can be expressed as:

$$x = \sum_{i=1}^M a_i s_i + w = Sa + w, \quad (1.4)$$

where x is a $L \times 1$ measured voxel spectrum vector, S is the $L \times M$ matrix whose columns are the $L \times 1$ endmembers, $s_i = 1, 2, 3 \dots M$, a is the $M \times 1$ fractional abundance vector. w is a $L \times 1$ additive noise vector. There are two primary physical constraints that can be applied to this, namely that all the abundances are all non-negative,

$$a_i > 0 \quad \forall i, \quad (1.5)$$

and that the sum of all the individual abundances accounts for all the endmembers present, so

$$\sum_{i=1}^M a_i = 1. \quad (1.6)$$

While the linear model is relevant when the endmember distribution on the voxel are in distinct areas of the surface, when the endmembers on the voxel are mixed on spatial scales smaller than the path length of the photons in the mixture, then the LMM no longer holds, as the light scatters off numerous elements and the mixing between these is non-linear. These non-linear effects have been recognised in the literature and numerous techniques can be employed to account for them. Although the LMM model is strictly speaking only applicable in the case where the endmembers are arranged in discrete sub-zones of the entire area of a voxel. Which is rarely the case in nature.

Despite this the LMM is still widely used as the standard spectral unmixing method. Generally this is due to the complex nature of the of calculations required for non-linear unmixing. It is important to have detailed knowledge of particle size, composition and alteration state of the endmembers present to obtain a full solution. Non-linear models are susceptible to errors in these parameters [87].

As it is the most widely used model for spectral unmixing it has numerous different algorithms that exploit it for different situations [80]. Generally it involves a number of common steps. A dimension reduction step to reduce computational costs, this step is optional and not used in all algorithms. The set of constituent endmembers that make up the mixed voxels in the scene are determined. Following this, the abundances for each

mixed voxel are calculated.

Endmember determination

Essentially the goal of endmember determination for LMM is to determine the spectral values that will occupy the columns of S in Equation 1.4. This can be done by interactive or supervised methods which require human involvement and interpretation. Automated or unsupervised methods require no human input.

Supervised approaches to linear unmixing require **a priori** knowledge about the endmembers present in the scene. This can be obtained by selecting a pure voxel from the scene, by comparing mixed to pure voxels information about the mixing relationships can be obtained leading to estimates for the endmember abundances [9]. The greater the number of endmembers obtained from pure voxels the better the estimates. Since it will not always be possible to obtain voxels that are 100% pure it is sometimes beneficial to use an external reference library for comparison. Although this can lead to ambiguous results as many endmembers have similar spectra, distinction is made more difficult when noise from the detector is taken into account, as well as possibly atmospheric effects [53].

Unsupervised unmixing methods avoid human input and try to directly determine endmembers. This has the advantage of avoiding the almost trial and error approach of supervised methods, while also allowing for repeatability of results.

Non-parametric methods try to minimise an objective function using statistical information from the data. Generally this can take the form of squared error, clustering algorithms have been used for this purpose, such as K-means partition algorithms [52] and others like it [16]. These seek to minimise the objective function in a number of iterations to arrive at estimates for the endmembers. This objective function is often of a form such that it can be solved simultaneously for both endmembers and their relative abundances.

Parametric methods use statistical information from the data and optimise towards a particular parametric density function. The performance of these algorithms depends on the approach [3], there exists methods that incorporate the linear mixing model into a stochastic mixing model [111]. Here fundamental endmembers are extracted from the data, they are assumed to be of a Gaussian distribution. Then maximum likelihood estimates of each hard endmembers parameters are determined using an expectation maximisation algorithm. Each voxel in the scene is considered to be either a fundamental endmember or a linear combination of one or more of the fundamental endmembers. Geometrically, each stochastic endmember is a cluster of pixels on the edge of the data cloud. Each hard endmember has an associated mean, covariance and prior probability. The mixed voxel can then be treated as having their own Gaussian parameters. Unmixing

then obtains the set of fundamental endmembers that are the most likely constituents of that voxel.

Abundance Estimates

Calculating the abundance estimates is performed using a group of algorithms classed as inversion algorithms. This class of algorithms are generally dependent on some form of least squares method, that is minimising squared error [22], though in hyperspectral imaging partial least squares are most common [6]. In a non-constrained non-parametric, non-statistical approach the goal is to minimise the error between the approximated spectrum and the real spectrum. Many of the endmember determination algorithms also determine the abundances in conjunction with the endmembers [36], many of the clustering algorithms mentioned previously also provide both S and a .

The least squares minimisation process minimises the function $|x - Sa|^2$. When no constraints are placed on the minimisation this is referred to as an unconstrained least squares method. Physical constraints can be applied to the model, such as the full additivity constraint $\sum_{i=1}^M a_i$, meaning that the sum of all the abundance of each endmember accounts for the entire measured spectrum. The solution to the least squares problem is the same as for the unconstrained case, except with a correction term. Another physical restraint that can be applied is that $a_i > 0$ for $i = 1, 2 \dots M$. However this adds a great deal more complexity to the minimisation procedure. As the minimisation problem then becomes a quadratic programming problem with linear inequalities as constraints. The approaches that utilise this constraint are known as non-negative least-squares [72].

A more statistical approach is to minimise the variance of the estimate of a , so \hat{a}^V . This requires the assumption that the noise vector w is a zero-mean random process with a covariance of Γ_w . The estimator is then given by:

$$\hat{a}^V = (S^T \Gamma_w^{-1} S)^{-1} S^T \Gamma_w^{-1} x. \quad (1.7)$$

This statistical analogue of least squared error has been adapted for attempts at real time processing of AVIRIS data [21]. Variable endmember methods treat each pixel individually, using different endmembers for each voxel. As it is likely that the endmembers present in a single voxel are a much smaller subset of the endmembers present in the entire scene, the challenge then becomes one of selecting which subset of endmembers to apply it to. In [43] an unconstrained linear least squares method is used where abundance values which are negative are removed during a number of iterative steps of the algorithm, as they have no physical meaning.

1.5 Motivation for Random Access Spectral Imaging

The previous sections detailed the various approaches to spectral imaging. What they all have in common is that they all collect a full data-cube, though the wavebands might not necessarily be contiguous, the spatial regions are continuous.

The Random-access Spectral Imaging approach described in this thesis is an example of an extreme trade-off of spectral and spatial resolution; the spatial distribution of spectral components in exchange for the acquisition of a high spectral resolution voxel. This approach is feasible as the RASI device being implemented here includes a conventional imaging channel that acts as a source of spatial information about the scene.

As with all spectral imaging systems, the RASI approach has a particular set of applications for which it is suitable, where RASI fits in the overall context of spectral imaging is shown in Figure 1.3 (a). The higher spectral resolution can improve the performance of spectral unmixing and classification algorithms, as the increased number of spectral features available helps to increase discrimination between different spectra. Also the availability of numerous wavebands allows the use of smoothing algorithms to help reduce the affects of noise. Further certain spectroscopic techniques such as Raman spectroscopy are reliant on high spectral resolution, due to the small linewidth of features present in a Raman spectrum. In conditions where there is a high degree of spatial correlation RASI can be used to measure a subset of voxels and, depending on the distribution of points, the whole classification map can be interpolated.

In general RASI is most useful where only a small number of observations are required; but with each observation having a high dimensionality. In addition to acquiring the sparse data-cube of voxels, the RASI approach in this thesis provides a conventional image that can be used to guide and augment voxel gathering. This is shown in a later chapter where an example of target tracking is used to demonstrate dynamic spectral imaging. In terms of the three design trade-offs prevalent in spectral imaging, exploiting the multi-object spectrometer design enables spatial regions in the scene to be mapped to the detector. Since the requirement of acquiring a “full” data-cube has been relaxed and instead a subset of the data-cube is acquired, the issues of detector throughput and data processing are circumvented. The detector size still limits the number of points that can be measured simultaneously, but the number of points is arbitrary up to that limit.

1.6 Random-access sampling

The term random-access comes from the field of computer science. It is familiar from terms such as Random Access Memory (RAM), though the term direct-access is more commonly used. It refers to accessing an element of a set; with random-access (direct

access), any arbitrary element can be accessed in an equal time. This is as opposed to sequential access where the elements need to be accessed in a particular order and the time taken to access changes with position of the element in the set, the difference between random-access and sequential access is shown in Figure 1.10.

In this thesis, random-access is used in the context of the set of potential measurements from the 3D data present in the scene, in essence any voxel can be collected; this idea is at the core of the instrument design that will be described in this thesis. In general operation this would allow the device to select any spatial region from across the device field of view and extract the full spectra for that region.

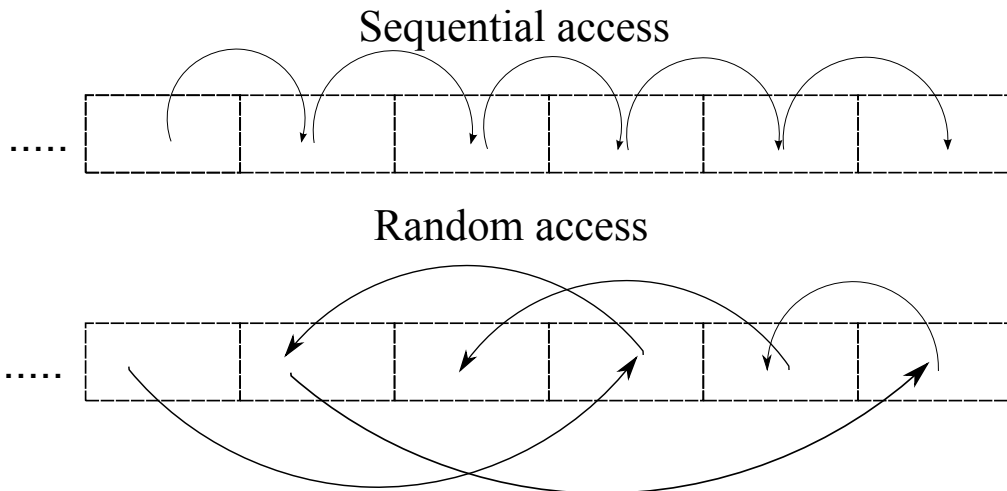


Figure 1.10: *Random-access allows the elements of a set to be accessed in an equal time and in any order; in contrast sequential access can only access components in a particular order. In the context of spectral imaging, each set element would correspond to the voxel of the data-cube and a RASI device would allow the voxels in a scene to be acquired in any order.*

In order to construct an instrument to achieve RASI, ideas from multi-object spectroscopy are coupled with modern micro-electromechanical technology, in this case a digital micromirror device. These will be discussed in the following sections.

1.7 Multi-object spectrometers

As a prelude to discussing the implementation of the random-access concept, the basics of multi-object spectroscopy (MOS) will be described. A MOS device collects spectra from across a FOV, a mask with a series of apertures (generally slits) aligned with the objects of interest is used as the spatial filter for the device entrance aperture, replacing the long slit of traditional spectrometers. This allows numerous objects to be investigated simultaneously across a certain FOV [125].

Historically, MOS devices have been applied extensively in astronomical applications, generally for measurement of the spectral properties of stars and other objects

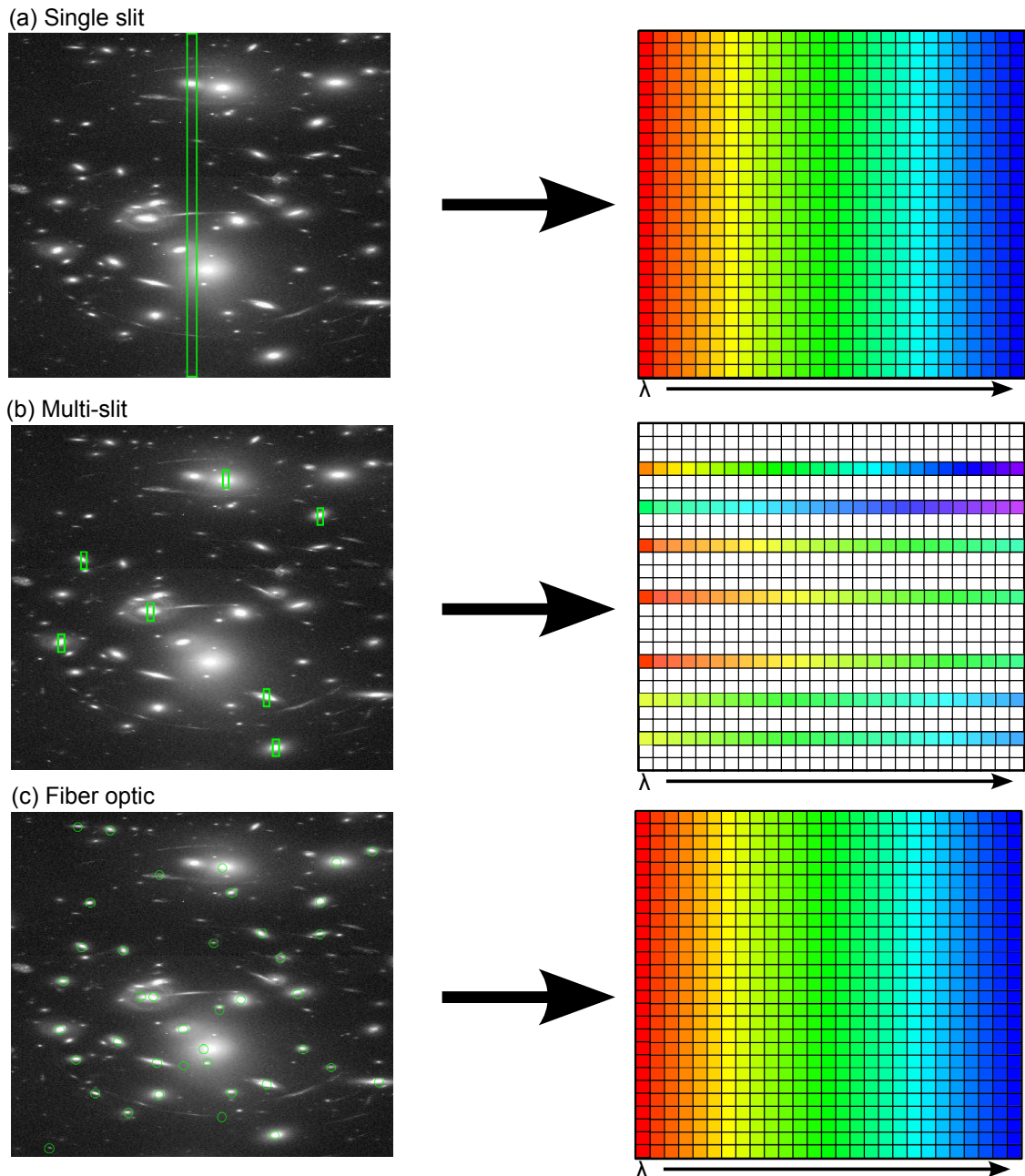


Figure 1.11: (a) shows a single slit projected onto an image, its position is fixed and the spectra on the detector are distributed in the same manner. (b) shows slits from a multi-object spectrometer distributed across the scene, aligned with objects of interest; the dispersed spectra are in different positions on the detector plane and have different spectral ranges depending in the position of the slit. (c) shows the apertures from a fibre MOS device aligned with objects of interest and the reformatted fibre outputs aligned with the input slit of a spectrometer, so similar to (a) in that respect. Image is used for demonstrative purposes only and taken from [128].

in the night sky. This is apt in the case of astronomy as the positions of objects can be predicted and the time-scales over which measurements can be taken is relatively long [31]. In this regard, it is straight forward to see why MOS approaches were first applied in astronomy. Initially, particular masks could be machined for a known configuration

of stars in the sky, this allowed for long integration times that would be an uneconomical use of a telescope's time if they were performed with a standard single slit spectrometer, as the single slit would need to be aligned with each object individually.

The position of the slit in the FOV affects how much of the spectral range is incident on the detector, slits at the edge of the FOV will have a part of their spectrum cut-off, due to the finite size of the detector. This results in an effective change in the spectral range in the observed spectral range of the slit, according to its position on the entrance aperture [31]. Different machined masks are used for different configurations of objects across the FOV. Contemporary MOS devices still use solid masks, so they don't suffer from any transmission loss. The advancement of modern cutting technology also allows masks to be created with high precision in a short space of time. Numerous MOS instruments use this approach, as in [116], [11] and [41]

Other approaches to MOS in astronomy utilise optical fibres. Early systems relied upon rigidly affixing the fibres to plates with holes drilled for the fibres in positions aligned with the objects of interest in the field of view [106] [69]. These early approaches were inflexible but had the advantage of being able to measure a much larger number of objects than the multi-slit approach described above. Improvements in the alignment and positioning by the use of robots has led to the increasing use of optical fibre MOS [112]. The positions on fibres could be re-adjusted in a matter of minutes and, the number of objects was limited by the number of fibres present and the size of the detector CCD. Advances in optical fibres have also expanded the wavelength ranges where this technique can be applied.

Fibre MOS approaches offer the advantage of a larger field of view and a larger number of spectra than can be collected by multi-slit approaches that use machined plates. Slit lengths and widths can be altered to match the characteristics of the source object, while the aperture of fibres are fixed. Fibres also introduce issues due to their transmission characteristics, aperture size and fragility whereas slits are clear apertures without such characteristics [69].

In general, MOS approaches offer many advantages that can be applied in numerous areas other than astronomy. These advantages include:

- **Multiplex advantage:** Multiple spectra can be acquired simultaneously
- **Resolution:** Using a series of slits allows resolution to be function of slit width in the same manner as normal long-slit spectrometers and offer potentially the same resolution as that supplied by any of the most modern spectrograph's.
- **Re-configurability :** Slit configurations can be altered to account for the spatial distributions of objects of interest. This is dependent on the method and technology by which the slit positions are altered.

- **Wide FOV:** MOS allow for information from a large FOV of view to be collected.

The characteristics of a MOS device are key to the implementation of the random access approach to sampling, the possibility of using reconfigurable masks of slits will allow the collection of spectra from any point across the instrument field of view. This, combined with a means of acquiring spatial information gives random access sampling. As mentioned previously, the technology that will be used to enable this approach is the DMD. The following sections will describe the DMD, its uses in general and in particular with respect to MOS applications.

1.8 Digital Micromirror device

The term Digital Micromirror Device (DMD) describes an optical light switch based on a novel micro-electromechanical system. It is an array of mirrors that can be used to modulate light digitally [119]. Each light switch is an aluminum mirror which can flip between two states, effectively steering the light in one of two directions. The mirror is on a single crystal silicon CMOS (complementary metal-oxide semiconductor) substrate. It is rotated using electrostatic attraction from a voltage difference across the air gap between the mirror and the substrate underneath. Mechanical stops are used to limit the rotations of the mirrors, generally $\pm 10^\circ$ or $\pm 12^\circ$. The mechanical switching time including time taken for the mirror to settle and electro-mechanically latch is approximately $16 \mu s$. Recently development kits have been made available by Texas Instruments which can be used for any application. Another extremely important characteristic of DMDs is their reliability, they have been shown to work for 100000 hours with no degradation in quality [37].

The DMD has found many applications in various fields, such as in microscopy. It is often used in a conjugate image plane as a dynamic aperture. The DMD replaces the traditional diaphragm placed at the image conjugate plane in a conventional microscope, or the DMD can replace the variable diameter iris used as a Fourier filter in optical scatter imaging [35].

Despite its many uses, the DMD does pose a number of challenges when being incorporated into an optical design. There are limitations imposed by the angle of tilt of the mirrors on the numerical aperture of the optics. However there are methods of accounting for these limitations in projector systems [15]. For example, using a truncated lens to avoid overlap between incoming and reflected rays, a more elegant solution given is to use a total internal reflection (TIR) prism. When placed in front of the DMD it allows the incident and reflected rays to overlap, but separates them out according to their angles of incidence and reflection. Descriptions of the design and use of prisms and various other DMD based projector optics are given in [130] and [46].

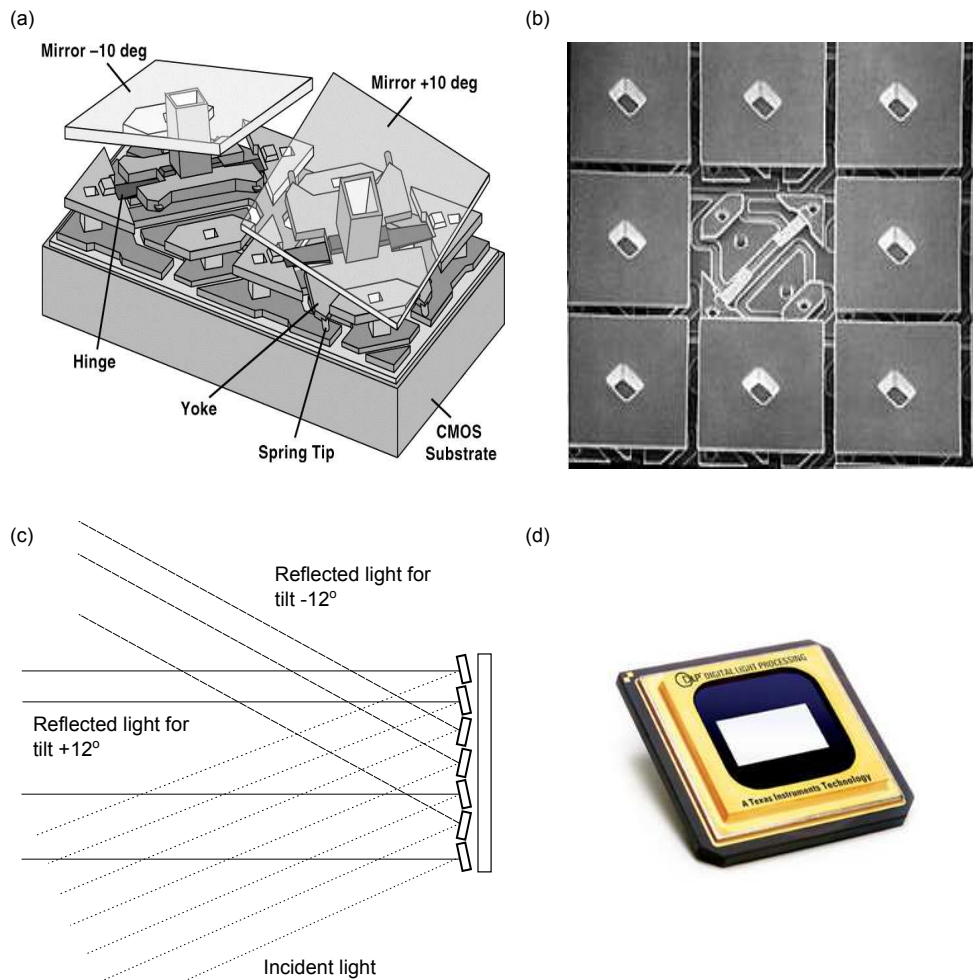


Figure 1.12: Diagrams of the DMD. (a) is a schematic of two tilt mirror and their underlying substrates [37]. (b) is a magnified view of the individual micromirrors with the aluminium removed from the central one [33]. (c) is a schematic of parallel rays of light incident on the micromirrors and being reflected in their respective directions according to the tilt of the individual micromirror. (d) is an image of a commercial DMD chip.

1.8.1 DMD Applications

The broad range of applicability of the DMD to various and diverse applications is represented in the literature. The key element that a DMD can provide is a degree of flexibility without the addition of large moving parts. These are all based on the ability of the micromirrors to be switched at high speeds. This section aims to describe the general flexibility of the DMD and how it is directly relevant to application to the implementation of RASI.

The most common use of DMDs is in so-called Digital light Projection (DLP) systems [119]. These are commercially available projectors and other display applications such as TVs. The basic optical layout uses a light source that is modulated by a Red-Green-Blue colour wheel to illuminate the DMD chip. The image of this chip is

then projected onto a screen or surface. The DMD accepts electrical signals at its input, representing these as gray levels of brightness, then outputs these, which are interpreted as analogue brightness levels by the human eye. Variations exist in quality, optical layout and cost between different projection systems. LEDs can be used to replace traditional light sources and simplify the layout. Limitations imposed by the switching angles of the DMD mirrors require some interesting optical layouts, such as truncated optics and prisms in the optical path to separate the incident and reflected beams. The design and improvement of DLP systems is an ongoing field of research [34].

The DMD has obvious uses in the field of imaging. The ability to switch the micromirrors has been leveraged to enable various forms of programmable imaging. By forming the image of a scene on the DMD and re-imaging it onto a detector, the dynamic range of different parts of the scene are modulated to prevent saturation on the detector. The modulation is achieved by switching the mirrors between the two possible states at different rates, effectively reducing the amount of light reaching the detector at one of the detectors. This is referred to as a DMD camera in some publications [107]. This also allows various calculations to be performed in the optical domain leading to feature detection, appearance matching and edge detection algorithms [96].

The ability to alter the dynamic range of optical signals has also been exploited in the field of spectroscopy in a similar fashion. In a spectrometer, a dispersive element disperses light onto a detector, by replacing the detector with a DMD and placing the detector in a plane conjugate to the DMD it is possible to alter the dynamic range such that weak signals can be detected in the same CCD (charge-coupled device) frame as strong signals. The longer exposure time to detect the weaker signals would otherwise cause the stronger signal to saturate the detector.

Perhaps one of the richest areas of application is in the field of optical encoding. Various approaches to imaging and spectral imaging are based on spatial encoding patterns, such as coded apertures in the CASSI system described previously. The reconfigurability of the DMD is a natural way of implementing this, as it allows multiple masks to be generated and displayed quickly and easily [42]. This has been implemented very successfully in compressive sensing. Compressive sensing is an approach to imaging that allows for a single detector to be used to take a number of measurements in a short space of time and to use the sparsity of the signal to reconstruct an entire image at sub-Nyquist sampling rates [19]. This has been implemented successfully in the visible and infra-red using DMDs. Approaches to encoding the more complex Hadamard masks have also been successfully demonstrated.

The key point here was to demonstrate, in various optical modalities the flexibility of the DMD and how it is the natural contender as the enabling technology for the proposed RASI modality. It has been used as an imaging device successfully and in spectrometers. The utility of its speed and reconfigurability are also apparent for

application to a multi-object spectrometer.

1.8.2 DMD Multi-object spectrometers

The suitability of the DMD for application to multi-object spectroscopy has been well established in the literature [78]. There exist various approaches to constructing a MOS device, depending on the spectral region and application requirements. In the previous section the numerous and varied possible configurations of DMD based applications are mentioned. In this section the implementations of MOS approaches are described and discussed.

The first descriptions of DMD based MOS concepts describe in general the potential of the DMD. These also describe some of the issues associated with using the DMD, such as the diffraction effects of the grating like structure of the micromirror array [79].

One of the earliest attempts at a DMD based MOS is the Rochester Institute of Technology Multi-object spectrometer (RITMOS) [93]. This uses a telescope as a fore-optic and has an imaging and spectroscopy channels. It uses a low numerical aperture (NA) lens to form an image on the DMD which allows increased separation of incident and reflected light rays. The imaging channel has a specifically designed Offner relay to counter the off-axis aberration introduced by the DMD. The spectroscopy channel uses a transmission grating spectrometer to disperse light deflected from the DMD. Effort was made when selecting apertures to avoid their respective dispersion in the detector plane, and thus overlap between spectra. The RITMOS was purpose built for astronomical applications, so its design accounts for the low NA of the telescope. It has been used to spectrally interrogate spectral characteristics in a similar manner to previous astronomical devices.

The design characteristics of an approach to building a DMD MOS device are described in [122]. It has both a spectroscopy and imaging channel. A custom built spectrometer, referred to as a polychromator in the text, is built. Mirrors and a concave grating are used and modified Czerny-Turner design is the result. Much is made of the correction of astigmatism correction in the design. The ability to swap between two gratings gives it two spectral ranges, 395 to 675 and 645 to 905 and resolution of $< 0.8nm$. The final system is demonstrated using a paper stained with dyes and the output of a mercury lamp. It shows that high resolution spectroscopy can be performed in a laboratory environment. It also demonstrated the care required in deciding on a particular approach to designing a DMD MOS, as the decisions on the placement of optics, spectrometer setup and imaging channel can have effects on performance.

A particular advantage of utilising a DMD MOS approach is the ability to select regions of interest, this is particularly useful in cases where there are few objects of interest and a lot of background, natural motion in the scene. The natural wastage in a

datacube that this can correct is considered in [26]. It describes an approach that advocates adaptive control for thermal imagers via electro-optic elements to yield an enhanced sensor, given the acronym ACTIVE-EYES. The approach describes a combination of dynamic range control and spectral measurement. The dynamic range modulation allows the ratio of energy to the spectroscopy channel to be altered to prevent detector saturation. In cases where there exist extremely bright and less luminous objects in a given scene this allows all the spectral information to be obtained in a single frame. The rapid switching of the micromirrors being used to alter the dynamic range of different objects at different rates. This also helped restore spatial detail to the imaging portion of the device.

The application to tracking was explored in [98]. A straight forward DMD MOS setup is used, the DMD is illuminated with a fibre head. The position of this spot was then viewed in the imaging channel and tracked. Pixels in the region of the light source, visible on the imaging detector, are switched and the spectra obtained. One of the key challenges for hyperspectral imaging is dynamic scenes, so the possibility of extracting spectral information from moving objects is of interest. In this instance the simplest setup was used to demonstrate the principle.

1.9 RASI Design Parameters

This thesis describes a DMD based MOS design. The goal of the design is to demonstrate approaches to countering the bottlenecks of time-resolved spectral imaging methods. The previously described implementations of DMD based MOS devices offer a blueprint as to how develop this, using a dual channel architecture with an image of the scene formed on the DMD and imaging camera at a conjugate plane to the DMD in one channel. This provides a reference for selecting regions of interest in the scene. DMD pixels are then nominated and switched to a spectroscopy channel. Here the DMD acts as a dynamic aperture to a spectrometer and the spectral information of these points can be extracted. This provides a suitable architecture for random-access to data in the scene, neatly allowing any point of interest to be selected, while minimising the redundant data collected. This circumvents the issues of data rates of modern detectors and 3D data-cubes, since data collected is based on some criteria of interest this also cuts down the need for large scale data processing of high data density data-cubes.

The design will be based on a consideration of the properties of the DMD and the use of off-the-shelf lenses to implement the design and a commercial, high performance spectrometer. The emphasis is on creating a working prototype without the use of custom optics. Furthermore the particular imaging modality of interest will be on microscopy applications, in particular tracking of dynamic objects. The possibility of using targeted area selection to estimate a full data-cube in a novel manner using the unique sampling

capabilities of the RASI approach is also of interest in certain spectroscopic modalities, such as Raman spectroscopy, where low signal strength can require long integration times or multiple scans. So the possibility of parallel acquisition has potential to increase data collection rates.

1.10 Thesis Outline

The layout of the remainder of this thesis is as follows. Chapter 2 will describe the concept and design factors in detail. Chapter 3 will be a description of the prototype built and experimental appraisal of it. Chapter 4 will describe the core operation of the RASI prototype built. An application of dynamic spectral imaging will be shown, namely the spectral properties of red blood cells undergoing a characteristic change in spectrum while in motion. An approach to mitigating the effect of spectral overlap is also discussed. Chapter 5 demonstrates the system in a different spectral modality, namely using Raman spectroscopy. Novel sampling methods are demonstrated in this chapter. Finally, Chapter 6 contains conclusions and recommendations for future work.

Chapter 2 – Instrument Concept and Design

2.1 Introduction

The previous chapter described the background of hyperspectral imaging and the limitations associated with the current instrumentation, it also proposed an approach to counter these via a Random Access Spectral Imaging (RASI) system. This chapter is concerned with the practical aspects of the concept of RASI and the design of a RASI system, to that end an overview of the implementation of the concept will be given in this chapter. The basic optical parameters of the system and how they relate to the functionality of such a system will be described. These aspects range from a description of the properties of the DMD, the spectrometer and the different possible layouts, as well as their respective merits. Finally a ray trace model of the setup will be shown, the purpose of which is to show the necessary overall system layout prior to the experimental realisation, which will be shown in the following chapter.

2.2 System overview

The basic concept allows direct spatial access to the spectral content of, in principle, any set of voxels in a scene. This allows the acquisition of data based on the distribution of "interesting" points, implicit in this concept is the requirement for an ancillary capacity for observing and identifying the "interesting" points. As was discussed in the previous chapter a convenient method of achieving this is via a conventional imaging channel to observe the scene, the advantages of this is that it provides a readily understood means of identifying points across the field of view (FOV), in effect acting as a source of spatial information about the scene.

A conceptual diagram of the RASI device is shown in Figure 2.1, giving the basic layout of the system architecture. Light from the scene is collected and imaged onto the DMD, from there it is redirected into either the conventional imaging or spectroscopy arm of RASI. As previously stated the DMD is a 2D array of micromirrors, each mirror can be tilted in one of two directions, the spectrometer and conventional imaging channels are aligned so as to collect light from a particular tilt direction, thereby creating the two channel system.

In the design implemented, telecentric lenses are used for the imaging and re-imaging optics of the system; these provide even illumination of the DMD but require extra consideration - in terms of alignment - when used in an off-axis configuration. Alignment of the overall system also needs to be considered, especially in the case of the spectrometer where off-axis effects can severely degrade performance. As a 2D

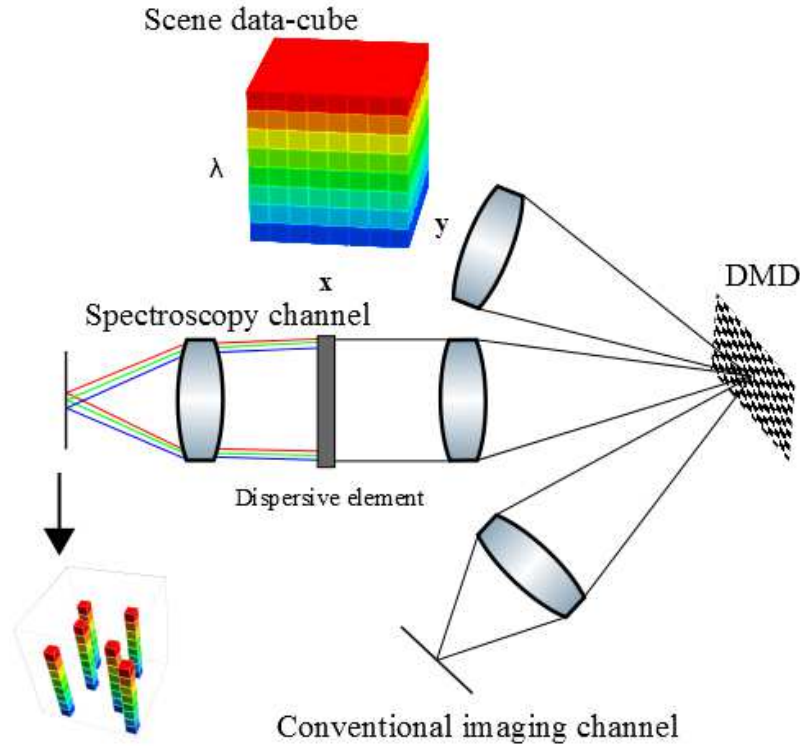


Figure 2.1: *Optical architecture of RASI. The potential data-cube of the scene is imaged onto the DMD, from which selected DMD pixels are switched towards the spectroscopy channel with the remaining pixels being switched towards the conventional imaging channel. The relatively few pixels switched towards the spectroscopy channel are dispersed and the voxels from their positions are recorded while the conventional imaging channel records a standard colour image of the scene.*

array there are also diffraction affects that need to be considered, though the scale of DMD pixels is on the order of tens of microns so it can be used as an imaging device for wavelengths $\leq 1\mu m$ [39], as has been demonstrated by other works described in the previous chapter.

The optical design for the whole system is a series of trade-offs where the limits of the DMD, the lenses, and spectrometer need to be considered; along with the practical considerations of alignment and the space envelope into which all the components need to fit. The primary purpose of this chapter is to describe the parameters of these design decisions and provide the groundwork for a feasible experimental demonstration of RASI.

2.3 Specular reflection properties

The reflective properties of the DMD will set the angles of incidence for any illumination beam, further the limits on the half-angle of the incident beam cone are set by the tilt of the micromirror. Quantifying the limits these impose is important for the choice of lenses in the design.

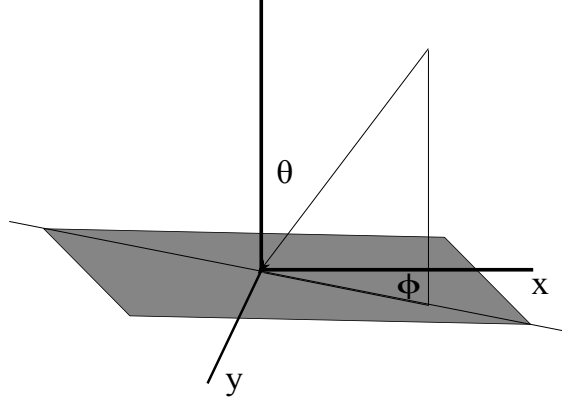


Figure 2.2: Coordinate system of a single micromirror.

A single micromirror is a square, flat surface that tilts an angle $\pm\phi$ along its diagonal, each individual micromirror can be described using a Cartesian coordinate system with an origin at the center of the micromirror; light rays are represented using a unit vector $\vec{d}_i = (a, b, c)$, whose properties in spherical coordinates are:

$$\begin{aligned} a^2 + b^2 + c^2 &= 1, \\ a &= \cos \phi \sin \theta, \\ b &= \sin \phi \sin \theta, \\ c &= \cos \theta, \end{aligned} \tag{2.1}$$

where ϕ is the angle with the x-axis and θ is the angle with the z-axis as shown in Figure 2.2. To understand and describe the incident and reflected rays from a single micromirror, the vectorial form of Snell's law of reflectance [70] is used, which for the incident unit vector \vec{d}_i gives the reflected vector \vec{d}_r from the surface S with surface normal \hat{n}_S as:

$$\vec{d}_r = 2(\hat{n}_S \bullet \vec{d}_i)\hat{n}_S - \vec{d}_i. \tag{2.2}$$

The surface normal in the flat state of the mirror will be the standard $\vec{k} = (0, 0, 1)$, perpendicular to the xy plane. However when the surface is tilted along its diagonal ($x = -y$) by an angle, say ϕ , then the new surface normal, which can be described in terms of spherical coordinates as

$$\vec{d}_S = \cos \phi \sin \phi \hat{i} + \sin \phi \sin \phi \hat{j} + \cos \phi \hat{k}, \tag{2.3}$$

with possible tilt values of $\varphi = \pm 12$, can be simplified to

$$\vec{d}_S = \frac{\sin \varphi}{\sqrt{2}} \hat{i} + \frac{\sin \varphi}{\sqrt{2}} \hat{j} + \cos \varphi \hat{k}. \quad (2.4)$$

Thus for a given incident ray, the direction of the specularly reflected ray can be calculated, for either case of $\varphi = \pm 12$.

To maximise performance as a two channel system and allow the largest separation, the largest divergence between the two possible reflected states - denoted as θ_{div} - is required. θ_{div} is calculated using the dot product of the two reflected vectors, \vec{d}_r^+ and \vec{d}_r^- , corresponding to the values of φ of 12° and -12° . Re-arranging the dot product as

$$\theta_{div} = \arccos \vec{d}_r^+ \bullet \vec{d}_r^- \quad (2.5)$$

gives θ_{div} , which is plotted in Figure 2.3. The maximum divergence angle between the two possible reflections occurs when the ray is incident perpendicular to the tilt axis on the micromirror diagonal, so $\phi = 45^\circ$. The maximum divergence between the two reflected rays is 4ϕ , which only occurs for rays incident with $\phi = 45^\circ$.

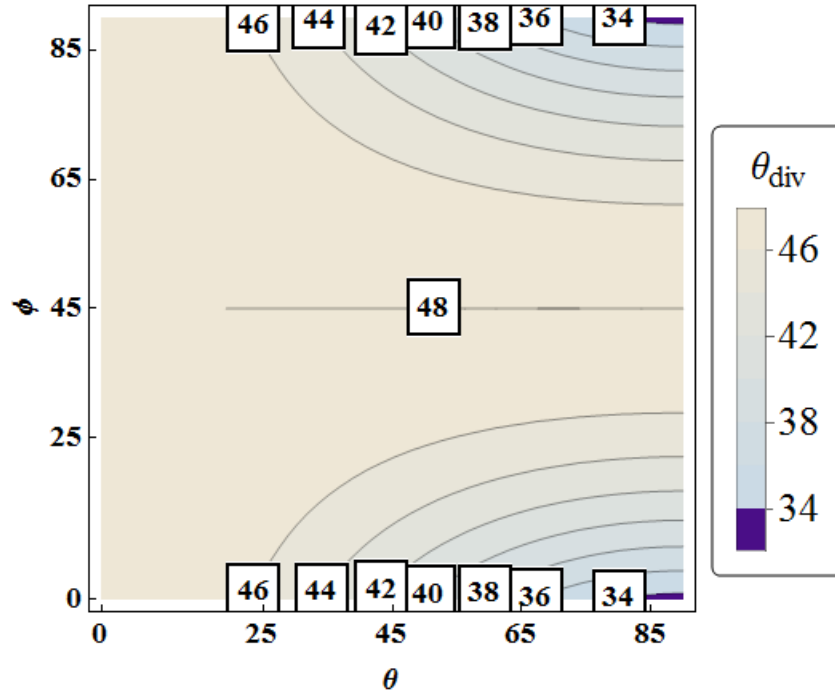


Figure 2.3: Plot of the divergence angle between the two reflected vectors as expressed in Equation 2.5 in terms of the angles of incidence (θ, ϕ) .

The choice of value for the angle θ allows the directions of the reflection for the two channels to be selected. For a ray incident at $\theta = 0$, the two reflected rays will be reflected at $\pm 2\varphi$, creating two off-axis channels for RASI. If the incident ray has $\theta = 2\varphi$, the directions of reflection will be 0° , i.e. in the direction of the plane normal, the other direction will then be $4 * \varphi$ or 48° .

In part, the importance of the reflectance characteristics of the individual micromirrors is that they place certain limitations on the half-angle of any cone of light reflected from the DMD. Practically speaking, this limits the numerical aperture (NA) and f-number (f/n), the f/n is given by

$$f/n = \frac{f}{D}, \quad (2.6)$$

where f is the focal length and D the diameter of a lens, the NA is given by

$$NA = \sin \theta_{NA}, \quad (2.7)$$

where θ_{NA} is the half angle of the cone of light; NA and f/n are both related by

$$f/n = \frac{1}{2NA}. \quad (2.8)$$

The symbol f/n is used as a shorthand for the f-number, where f-number is known it can be incorporated into the expression, for example, for a f-number of 6, the shorthand would be $f/6$, this shorthand will be used throughout this thesis. The limiting f/n is set by the tilt angle, φ , as it limits the NA, if the incident cone angle were larger than φ , then the mirrors would not be able to switch the whole cone into another channel of the setup, defeating the purpose of using the DMD as an optical switch.

2.4 Field of View and Etendue

Field of view (FOV) is a metric that describes the extent of the scene that can be seen by a detector behind a lens, generally it is used in the context of a lens-detector system, but it can also be used to describe the FOV of the DMD. FOV angle, $2\alpha_{FOV}$, is given by

$$2\alpha_{FOV} = 2 \tan^{-1} \frac{d_{det}}{2f}, \quad (2.9)$$

where f is the lens focal length and d_{det} is the detector (or micromirror) length. A FOV can be determined for a more complex lens system using an effective focal length for the entire lens structure. Each pixel in the DMD, or detector, will have an instantaneous field of view (IFOV) which can be estimated according to the size of the pixel.

The radiometric performance of an optical system is described in terms of a geometric quantity known as etendue [24]. Both the aperture area and FOV play a role in determining the light gathering power of an optical system, so etendue is often referred to as $A\Omega$ product, where Ω is the solid angle. The etendue dU is given by:

$$dU = dA \cos \theta d\Omega, \quad (2.10)$$

where dA is the surface area element, θ is the angle with the surface normal and $d\Omega$ is the solid angle. Equation 2.10 can be determined for a single square micromirror to give:

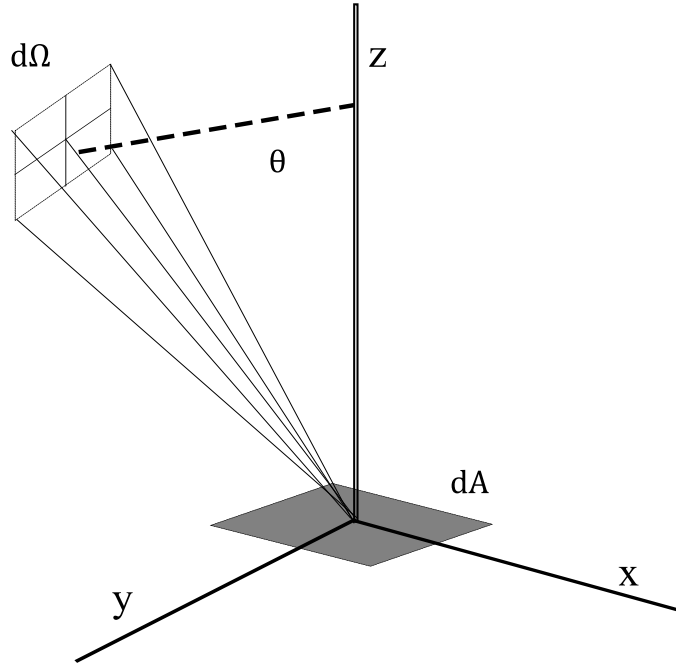


Figure 2.4: Etendue of a single micromirror.

$$dU = \frac{\pi dA}{4(f/n)^2}, \quad (2.11)$$

dA is the area of a single micromirror in this case. For a fixed DMD pixel size the light gathering power of the RASI setup will be set by the f-number of the beam incident on the DMD. In order to improve the energy transfer via the DMD, the beam diffraction limited spot-size should be smaller than a given DMD pixel. In calculating this it is worth noting that etendue is related to the number of states in a single transverse mode in a finite area [18] and is related to the wavelength of that mode by

$$dU = \lambda_{vac}^2, \quad (2.12)$$

where λ_{vac} is the vacuum wavelength of light. Equations 2.11 and 2.12 can then be related to construct a relationship between wavelength, area and f-number, such that

$$f/n = \frac{\sqrt{\pi A}}{2\lambda}. \quad (2.13)$$

It is also worth pointing out that Equation 2.13 can be re-arranged into the form of a diffraction limited spot size expression:

$$d = 1.22\lambda f/n, \quad (2.14)$$

where d is the diameter of the spot. Using the relation in Equation 2.13, an upper bound

for the maximum f-number that will produce a spot that fits on a single micromirror can be calculated using the known value for the micromirror size; each mirror has side length of 10.6 microns, which gives approximately $f/12$ at $\lambda = 800$ nm and $f/16$ at $\lambda = 600$ nm. Smaller spot sizes increase the irradiance on individual DMD pixels, at the cost of image resolution, that is higher spatial frequencies are not sampled sufficiently to be detected, this trade-off is advantageous when the DMD pixels are acting as dynamic apertures for the spectrometer arm of RASI, as it measures spectral frequencies rather than spatial frequencies.

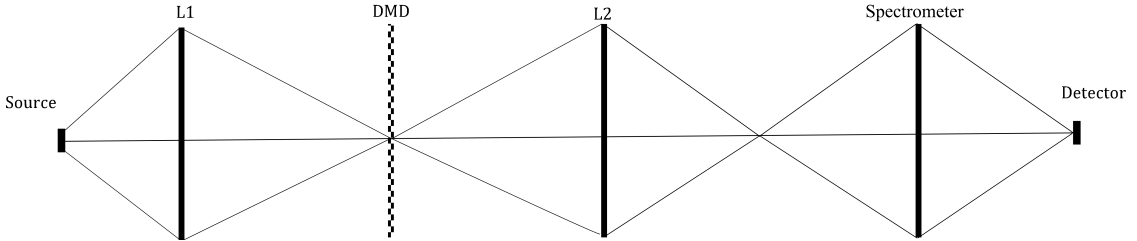


Figure 2.5: Simplified representation of the RASI system from the source to the spectrometer for a single aperture on the DMD. Light from the source is imaged onto the DMD by L1, the DMD aperture is then re-imaged by L2 into the entrance of the spectrometer after which it is focussed onto the detector.

Figure 2.5 shows a simplified diagram of the propagation of light rays from a light source, through a DMD aperture and onto the spectrometer detector; the DMD aperture will consist of multiple pixels organised into a slit with a height and a width. The etendue for this slit will be the sum of the contributions from the number of pixels in both the horizontal and vertical directions of the slit, i and j directions respectively, with the resulting expression being a multiple of the etendue for a single micromirror. Thus the system etendue (U_{sys}) is given as

$$U_{sys} = \frac{\pi N_i N_j A_{DMD}}{4 * f^2 / n_{DMD}} = N_i N_j dU \quad (2.15)$$

where N_i and N_j are the number of DMD pixels in the horizontal and vertical directions of the slit. The form of this equation is similar to the etendue of a standard slit based spectrometer, although since the DMD slit is composed of discrete elements of equal size, the standard slit width and slit height terms have been replaced by a multiplication of the area of a single DMD pixel by the number of DMD pixels. The system etendue should be greater than or equal to the source etendue so as to optimise the system throughput, this can be achieved dynamically by altering the number of pixels used in the DMD slit according to the extent of the source.

2.5 Telecentric lenses, off-axis alignment and system layout

This section describes the use of telecentric lenses to achieve uniform illumination of the DMD to improve the performance of RASI, by ensuring all the light cones incident on the DMD are parallel. Due to the tilt of the micromirrors at least two of the possible three input/output channels will have their conjugate planes tilted with respect to the central optical axis of the imaging lens. This off-axis effect is accounted for with the Scheimpflug condition which can be used to calculate the appropriate conjugate plane tilt to achieve an in-focus image. The Scheimpflug condition must also be modified when used with telecentric lenses. Finally a layout must be chosen that decides which input/output channels will be imaged from an off-axis position.

2.5.1 Telecentric lenses

A telecentric lens is a compound lens which has its entrance or exit pupil at infinity, depending on whether or not it is image or object space telecentric, an example of a non-telecentric and a telecentric lens are shown in Figure 2.6. A compound lens with both its pupils at infinity is said to be doubly telecentric, this thesis uses only doubly telecentric lenses so these will be referred to as telecentric lenses. As a consequence of their configuration, telecentric lenses provide uniform illumination across their FOV, this is as a result of the central rays of all light cones leaving the lens in parallel; this also results in telecentric lenses having a very low tolerance for wide input angles into the compound lens [13] which is visible in the diagram of a telecentric lens in Figure 2.6 (b). Telecentric lenses have a number of other useful properties. Unlike conventional

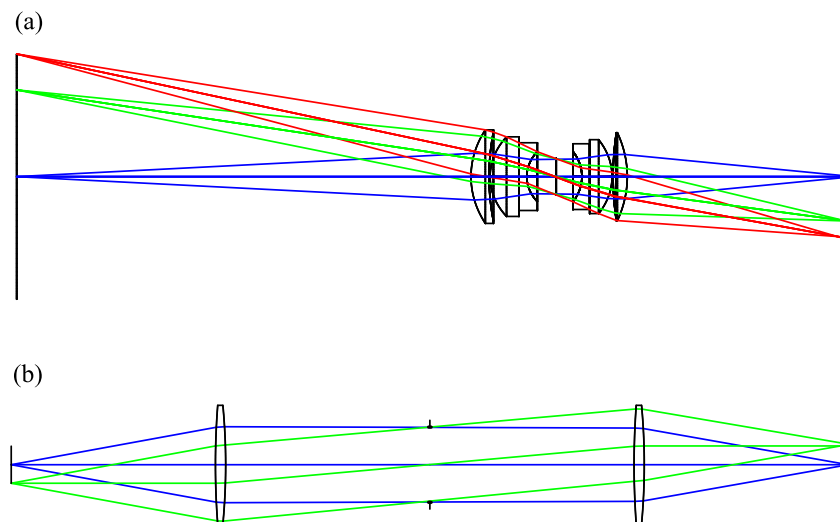


Figure 2.6: (a) shows a Double Gauss type objective and (b) shows a doubly telecentric lens. (a) has an angular FOV from which it collects light whereas the (b) only collects light from a tight angular region (typically $< 1^\circ$ for a good telecentric lens) in front of the objective lens.

lenses, the f-number of telecentric lenses stays constant with de-focus and hence the magnification, which allows for constant brightness at different distances [124].

2.5.2 Off-axis imaging and the Scheimpflug condition

A simplified layout of off-axis imaging is shown in Figure 2.7, the object plane is tilted with respect to the central optical axis of the lens, in cases where the lens cannot be repositioned to account for the object plane tilt, the image plane is also tilted. If the detector (or DMD) in the image plane is not tilted appropriately the result will be an out of focus image; the appropriate tilt angle can be determined using the Scheimpflug condition [89].

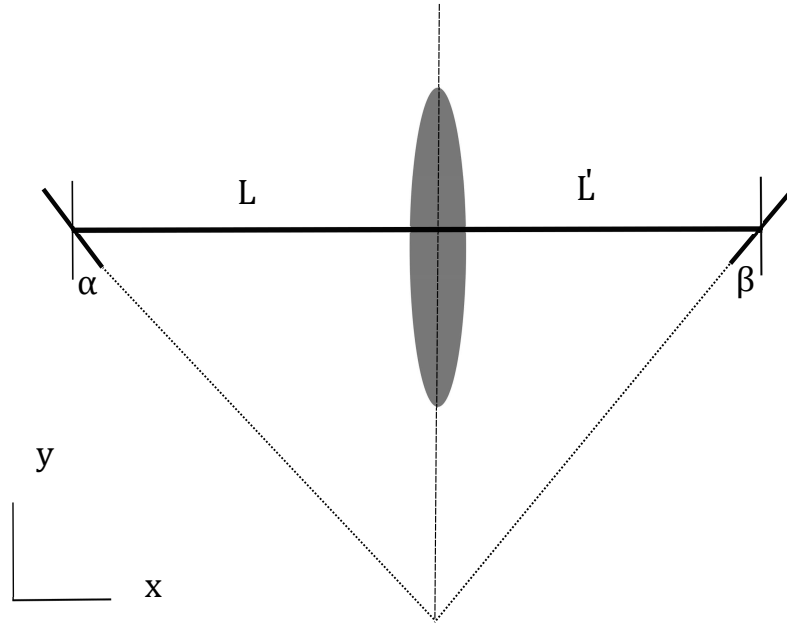


Figure 2.7: Basic Scheimpflug configuration, the image plane and object are aligned according to their tilt with respect a line perpendicular to the lens central point.

The basic Scheimpflug condition is shown in figure 2.7. Using the basic imaging condition and considering that the object plane is tilted by an angle α such that:

$$\frac{1}{x(y)} - \frac{1}{x'(y)} = \frac{1}{f} \quad (2.16)$$

The object tilt is described by:

$$x(y) = L - y \tan \alpha \quad (2.17)$$

and

$$x'(y) = \frac{f(L - y \tan \alpha)}{f + L - y \tan \alpha}. \quad (2.18)$$

The image plane is found at $x'(0)$ and assuming that $L \gg y \tan \alpha$. Which leads to:

$$\frac{1}{f} + \frac{1}{L} = \frac{1}{x'(0)}, \quad (2.19)$$

Equation 2.19 is just a statement of the Lensmakers equation which requires $x'(0) = L'$. The object and image planes intersect when $x(y) = x'(y)$ this leads to

$$y = \frac{L}{\tan \alpha}. \quad (2.20)$$

When this is put back into the expression for the object plane so that $x(\frac{L}{\tan \alpha}) = L - L = 0$ and the image plane to get $x'(\frac{L}{\tan \alpha}) = \frac{fL}{L+f} - \frac{fL}{L+f} = 0$, showing that the object plane and image plane intersect in the plane of the lens. Equation 2.18 can be rewritten as:

$$x'(y) = \frac{fL}{f+L} - \frac{f \tan \alpha}{f+L} y = L' - y \tan \beta, \quad (2.21)$$

where

$$\tan \beta = \frac{f}{L+f} \tan \alpha, \quad (2.22)$$

the magnification of the system is $M = \frac{L+f}{f}$. Equation 2.22 allows the angles for the tilt of the object and image planes to be calculated.

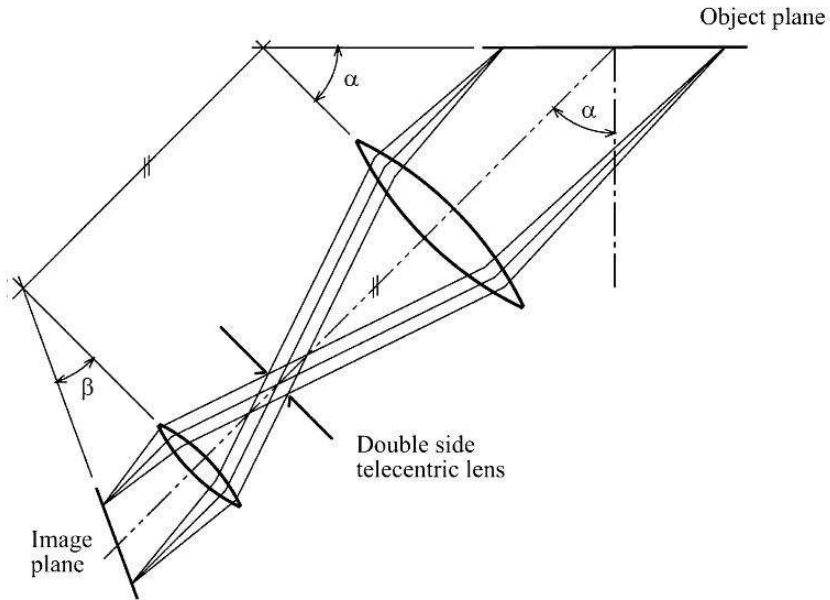


Figure 2.8: Scheimpflug orientation of telecentric lenses; reproduced from [49].

The Scheimpflug condition can be adjusted to account for the telecentric lenses, a schematic of the Scheimpflug condition for telecentric lenses is shown in Figure 2.8. The resulting relationship between angles in the image and object planes of the telecentric lens [49] is:

$$\tan \beta = -M \tan \alpha. \quad (2.23)$$

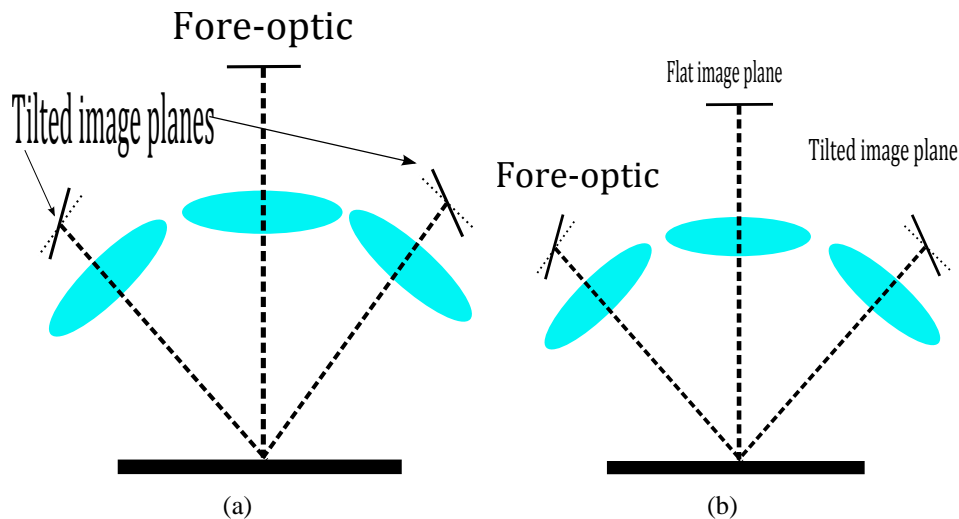


Figure 2.9: Two layouts, the on-axis case and the off-axis.

This is the final equation used when determining the appropriate tilt angles for tilting the image and object planes and allows the implementation of various imaging layouts.

2.5.3 On-axis vs. off-axis illumination layouts

Two illumination options are possible for the DMD layout: on-axis and off-axis. An on-axis imaging configuration has both its image and object plane parallel, whereas off-axis has tilted conjugate planes and requires consideration of the Scheimpflug condition. The two options are shown in Figure 2.9, the question of on-axis or off-axis is a question of which of the imaging and re-imaging channels need to have the Scheimpflug condition accounted for during alignment, it will also affect the angular positions of the different channels.

In the case of on-axis DMD illumination, the scene image is re-imaged directly onto the DMD plane as in Figure 2.9 (a), this enables the fore-optic to be positioned with relative ease. However both the imaging channel and the spectrometer need to be tilted appropriately to account for the Scheimpflug condition. This introduces a number of practical considerations, particularly for aligning the spectrometer, as spectrometers can generally be quite bulky and made with few moving parts for adjustment. Depending on mechanical parameters this can be quite difficult, both of the channels are symmetric about the fore-optic.

The alternative to the on-axis illumination is to use one of the 24° angle of incidence channels, shown as the off-axis illumination option in Figure 2.9 (b). The clear advantage of this configuration is to enable an easier alignment of one of the re-imaging channels. The easiest choice in this case is to place the spectrometer in that channel so that it does not require tilting due to the Scheimpflug condition. Spectrometers already have numerous potential issues such as chromatic aberration that can be exacerbated by

extra-defocus. This significantly reduces the alignment difficulty of this channel, it also makes it easier to potentially exchange one spectrometer with another.

In the comparison of the two layouts, it is clear that simplifying the alignment of the spectrometer offers more advantages than simplifying the fore-optic alignment. The more extreme tilt of the imaging channel with respect to the DMD would also degrade the performance and make alignment more difficult, but the potential loss was deemed acceptable in comparison to the difficulties of tilting the spectrometer detector. In the final implementation the off-axis illumination configuration, Figure 2.9 (b), was chosen; though if custom aberration correction optics were created it could potentially mitigate much of the alignment issues.

2.6 DMD diffraction

Section 2.3 describes the DMD in terms of geometric optics, in this section the diffraction characteristics of the DMD are considered.

The DMD is a periodic array of square mirrors, the mirrors can be treated as apertures of finite extent which are equally spaced in both spacial directions. When the individual mirror facets of the DMD are switched to either of their respective orientations the profile of the apertures is that of a sawtooth formation, commonly referred to as blazed. This alters the phase of the reflected light accordingly. In general the size of DMD pixels is on the order of tens of microns, with the space between micromirrors of approximately 1 micron. Thus the DMD can be described as being a coarse blazed, diffraction grating.

Diffraction gratings split diffracted light at different angles according to the wavelength of the light, angle of incidence and the periodicity of the grating elements. Light of a given wavelength is diffracted into multiple angles, said to be of different orders. In a blazed grating, the standard diffraction pattern is multiplied by an additional blaze function that acts as an envelope, concentrating most of the incident power into diffraction orders within that envelope. The position of these envelopes for the DMD are set by the tilt angle of the micromirrors and the angle of incidence, further the centers of the envelopes align with the predicted reflection angles obtained from the specular reflection analysis in Section 2.3.

In practice, the re-imaging optic can gather the majority of diffraction orders within its solid angle for wavelengths less than one micron [39], the effects of diffraction often being aggregated into a loss term to account for light lost in collected diffraction orders [46]. Typically diffraction needs to be accounted for with the DMD in cases where coherent illumination is used [25], or wavelengths greater than one micron.

2.7 Spectrometer

The Kaiser Holospec f1.8i was the spectrometer used in this setup, it was placed in the reflective channel such that there was no need to tilt it due to the Scheimpflug condition. It had unity magnification and it contained a volume phase holographic grating as the dispersive element, so it was subject to distortions. In normal operation a curved slit is placed in the entrance aperture, to correct for the distortion. However in this case the slit is removed and the DMD acts as the entrance aperture. The distortion is dependent on the slit position in the entrance aperture and will vary with distance from the central optical axis.

The grating equation for this spectrometer is [10]

$$\lambda v = \cos \gamma [(\sin \theta_1 + \phi_1) + \sin(\theta_2 + \phi_2)], \quad (2.24)$$

where λ is the wavelength, v is the spatial frequency of the grating, γ is the vertical angle made by an off-axis ray. θ_1 is the angle of incidence at the optical axis θ_2 is the angle of refraction at the central wavelength, θ_1 and θ_2 are constants for a fixed geometry of the gratings position. ϕ_1 is the angle between the lateral slit position and the input lens optical axis and ϕ_2 is the lateral angular position between the output lens optical axis and the image position on the detector, shown in Figure 2.10. The horizontal position from the optical axis in the entrance plane is given by x_1 and, x_2 in the image plane. y_1 is the vertical distance in the entrance/object plane, y_2 in the image plane. These quantities are related by

$$\begin{aligned} \tan \phi_1 &= \frac{x_1}{f1} \\ \tan \phi_2 &= \frac{x_2}{f2} \\ \tan \gamma &= \frac{y1}{f1} \\ \tan \gamma &= \frac{y2}{f2}. \end{aligned} \quad (2.25)$$

The attributes of the grating can be determined using Equation 2.24, and certain known parameters of the grating. Using the centre or design wavelength, λ_0 , of the grating and setting $x_1 = 0, y_1 = 0$ so $\phi_1 = \phi_2 = 0$ and $\gamma = 0$; the relation between the spatial frequency of the grating and the design wavelength is given by:

$$v = \frac{\sin \theta_1 + \sin \theta_2}{\lambda_0}. \quad (2.26)$$

The linear reciprocal dispersion is calculated from Equation 2.24 by differentiating

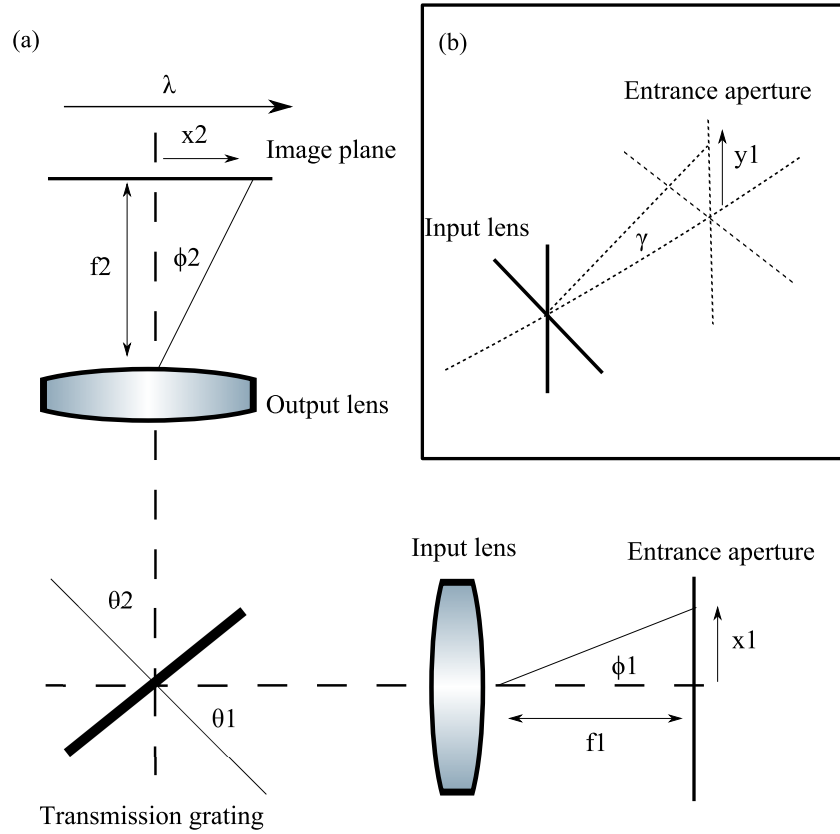


Figure 2.10: Spectrometer schematic relating the input position to the resulting position in the detector plane.

with respect to x_2 and using Equation 2.26 to get

$$\frac{d\lambda}{dx_2} = \frac{\lambda_0 \cos \gamma \cos(\theta_2 + \phi_2) \cos^2 \phi_2}{f_2 (\sin \theta_1 + \sin \theta_2)}, \quad (2.27)$$

which is typically expressed in nm/mm. The linear reciprocal dispersion is used in combination with the entrance slit width to calculate the spectral linewidth ($\Delta\lambda_{BP}$) for a given slit width, by multiplying Equation 2.27 by a slit width w , the linewidth can be estimated as

$$\Delta\lambda_{BP} = w \frac{d\lambda}{dx_2}. \quad (2.28)$$

The slit width, w , corresponds to a discrete number of DMD pixels, decreasing the width improves the spectral resolution at a cost of optical throughput, however it does allow the flexibility of dynamically altering the spectral linewidth to accommodate measurement conditions.

Smile and keystone are two distortions common in dispersive spectrometers and involve the bending of light rays in the spatial and spectral directions. This can be seen with the variation of the parameter x_2 with respect to the input positions in the entrance aperture and how it varies with wavelength for a fixed input position. This is described

by re-arranging Equation 2.24 into the form

$$x_2 = -f_2 \tan \left[\theta_2 - \sin^{-1} \left[\sqrt{\frac{f_1^2 + y_1^2}{f_1^2}} \lambda \nu - \sin \left[\theta_1 + \tan^{-1} \left(\frac{x_1}{f_1} \right) \right] \right] \right], \quad (2.29)$$

which allows the curvature in the image plane to be calculated as a function of input plane position, (x_1, y_1) .

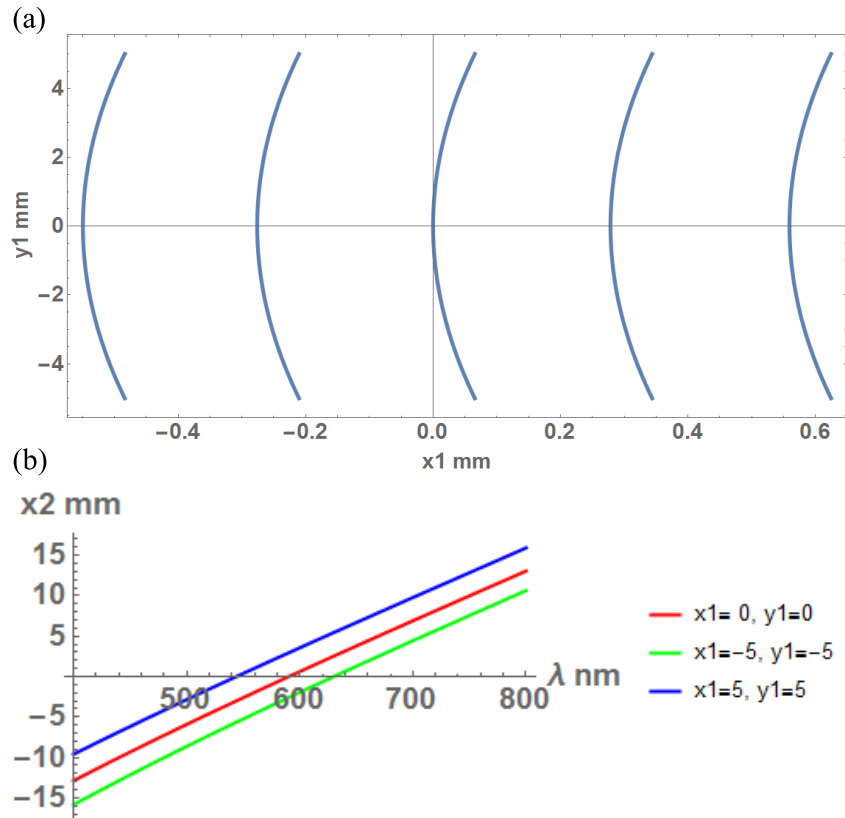


Figure 2.11: (a) shows the bending of light rays in the detector plane as a function of input position (x_1, y_1) for a single wavelength of 590 nm. (b) shows the change in spectral curvature for different input positions. A grating with $\lambda_0 = 590 \text{ nm}$ and $\nu = 660.695 \text{ mm}^{-1}$ was assumed.

Figure 2.11 (a) plots the curvature in the image plane as a function of the slit input position. The resulting smile distortion is visible from the curving of the line across aperture positions for a wavelength of 590 nm. This is important when long slits are used with the spectrometer, though for short slits it has less affect so long as it is appropriately calibrated.

Of particular interest is the behaviors of x_2 for a given input position at a number of wavelengths, as this will affect the wavelength calibration of the spectrometer for each unique slit the DMD can generate as an input to the spectrometer. Equation 2.29 is plotted for fixed input positions to explore the relationship between wavelength and x_2 , which is shown in Figure 2.11 (b) . The resulting plots exhibit low curvature across the

wavelength range, indicating that in the ideal case, spectral keystone distortion should be minimal.

2.8 Optical throughput

Equation 2.15 gives the etendue for a slit of width $N_m d_{DMD}$, this can be expanded to incorporate the spectral linewidth (Δ_{BP}) and reciprocal linear dispersion ($D = \frac{d\lambda}{dx_2}$) by relating the width in Equation 2.28 to the number of DMD pixels as

$$w = N_i d_{DMD} = \frac{\Delta\lambda}{D}, \quad (2.30)$$

which allows the etendue for the DMD slit to be related to the linewidth of the slit by substituting into Equation 2.15 to get

$$U_{sys} = \frac{\pi N_j d_{DMD}}{4 * (f/n)_{DMD}^2} \frac{\Delta\lambda}{D}. \quad (2.31)$$

Increasing the spectral linewidth increases the etendue and hence the power collected from the source, the power collected from a source of radiance L is

$$P = L \times U_{sys}. \quad (2.32)$$

In order to improve the power collected by the system the etendue must be matched to - or greater than - the etendue of the source. Spectral linewidth can be traded off against etendue by increasing the number of DMD pixels in the slit, the same as increasing the slit size in a traditional spectrometer.

2.9 Zemax model

The previous sections have discussed the various aspects of the components needed to assemble the device. This section extends this premise by considering a Zemax model of the system. The model will consist of the illumination and re-imaging channels as described in the previous sections, further the Scheimpflug condition and how it relates to the tilts in the input and re-imaging channels will be modeled. Telecentric lenses will be used in the model to help understand their behavior, further, an objective lens will be placed before the input telecentric lens to help understand the details of coupling light into the system while also accounting for the Scheimpflug condition. The goal of the model is to help corroborate the choice of illumination and the advantages it will confer as well as to help inform the choices of components that will need to be made to build an experimental prototype.

Zemax itself is a commercial ray tracing program that allows optical systems to be modeled in a realistic physical environment. It can perform sequential ray tracing using geometrical optics for standard lens components and employs a non-sequential mode for portions that require physical models to describe the optical propagation. It is used extensively in the optical design industry and appears in academic literature for optical design. It contains a model for a general MEMs device that can be adapted to fit the description of a DMD [34]. This used to create the model of the system.

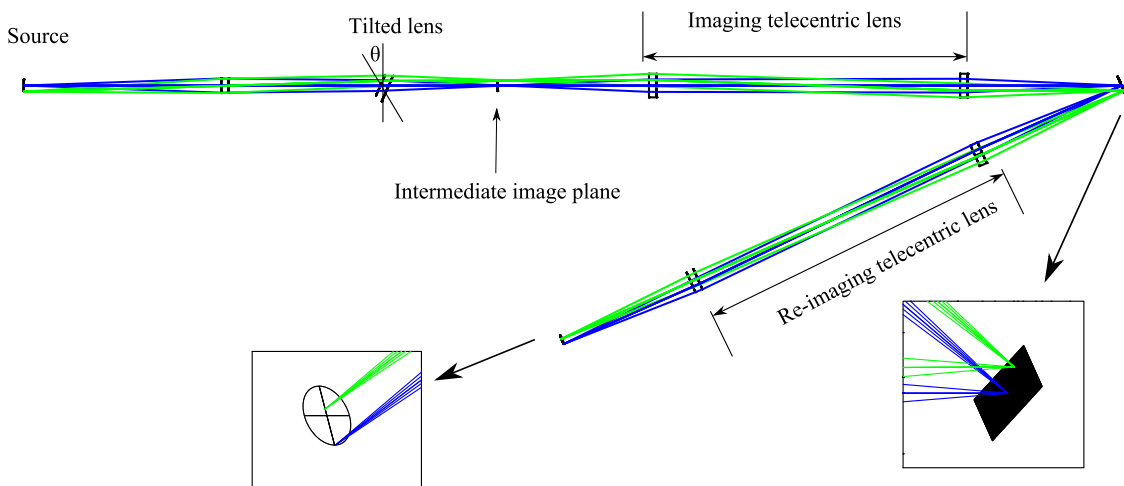


Figure 2.12: The path of light rays from the source, through the first lens and the tilted lens to an intermediate image plane that is re-imaged onto the DMD, which is tilted with respect to the optical axis of the incoming light rays. A close up of the rays incident on the DMD is shown. The reflected ray bundles are re-imaged by another telecentric lens onto the final image plane. A close up is shown to indicate that this image requires no tilt to form an in-focus image. This will be aligned with the entrance aperture of the spectrometer, which simplifies the alignment as it removes the need to tilt the spectrometer image plane according to the Scheimpflug condition.

The model was created using paraxial lenses in sequential mode, combined with the DMD in non-sequential mode. These can be combined into a single model in Zemax. The DMD is illuminated from an off-axis angle as described in a previous section. A telecentric lens was used for the illumination, also an example objective is placed before the telecentric lens to help simulate the coupling of light into the system in a real system. The objective portion consists of two paraxial lens, one that images a source at a finite distance and collimates the light from the source. A second lens then focuses the collimated beam to create an intermediate image plane, the telecentric lens then re-images this to the DMD. Since the DMD is illuminated from off-axis, the image will not be in focus on the DMD. The Scheimpflug condition is used to correct for this by tilting the input image, this is achieved by tilting the second lens in the imaging objective. The form of the objective is chosen to mimic the principles of an infinity corrected microscope, the second lens corresponding to the tube lens of such a microscope.

The model of the DMD constitutes a non-sequential component in Zemax. The

size of the micromirror array can be specified and the number of DMD pixels in the two dimensions. The size of each micromirror in each direction is given by dividing the length of the array in that direction by the number of pixels. To simplify the calculation time it was chosen to have an array 64 DMD pixels and array size of 10.8×8.6 mm. This is the same size as an 1024×768 DMD array with pixel length of 10.6 microns, but with DMD pixels a factor of 64 times larger. The micromirror tilt angles were set to $\pm 12^\circ$ and the mirrors were orientated so as to tilt along their diagonals. The above-mentioned parameters correspond to the characteristics of the DMD available for this device.

Once an in focus image has been successfully formed on the DMD it can be redirected to one of the two possible possible directions allowable by the switching angle of the individual micromirrors. One of these directions will be normal to the DMD plane, such that when it is re-imaged there will be no need to tilt the image plane. This is a consequence of tilting the input image. It is in this channel the spectrometer will be placed, as this makes aligning the spectrometer much simpler. A telecentric lens is used for re-imaging the DMD. The other direction into which light is switched is similarly constructed however it is rotated through 48° and it requires its image plane to be tilted according to the Scheimpflug condition so as to form an in-focus image. This is where the panchromatic camera will be placed.

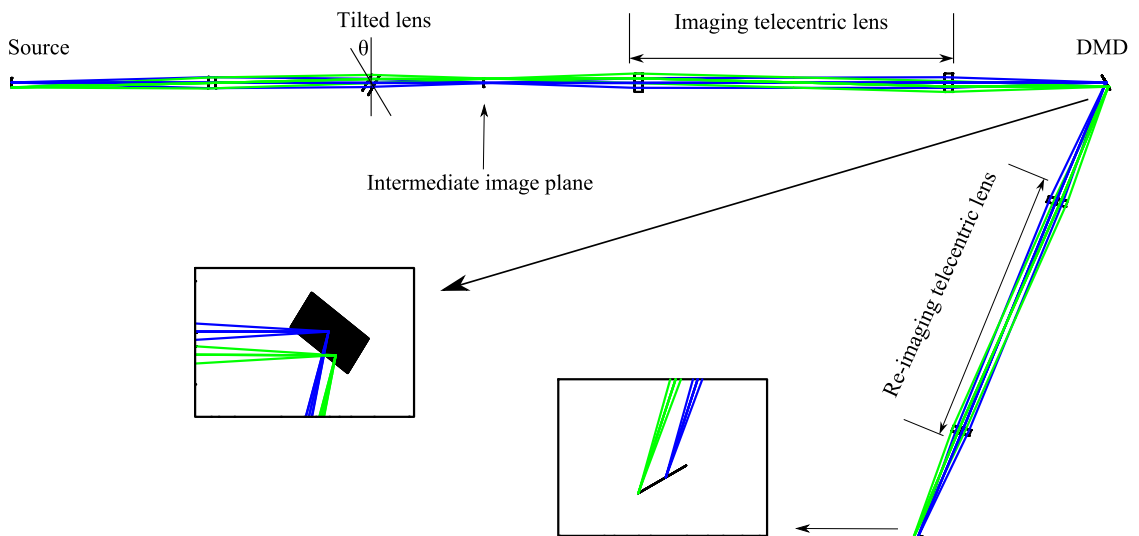


Figure 2.13: Similar to the previous diagram, but for the case where the micromirrors are switched in the other direction. Here the DMD is re-imaged using a telecentric lens again, but this time the image plane needs to be tilted according to the Scheimpflug condition to form an in-focus image. A close up is shown of the tilted image plane.

Figures 2.12 and 2.13 show the two possible paths light rays can travel as given by the ray tracing software. The aim of this model was to combine the various aspects discussed in the previous sections into a single, complete design for the whole system. This complete design will be used to help select components for the experimental realisation of the device. Since the paraxial approximation is used for the lens components

in this model it circumvents some of the real issues relating to the use of physical optics, these issues include distortion of various kinds, vignetting and scattered light in the system. However the system will be built with stock components, the model itself merely offering a guide for the placement of the optics and to help account for issues such as the Scheimpflug condition.

2.10 Chapter Summary

This chapter provided an overview of the principle of operation of the RASI device. The basic principles of the application of Random-access spectral imaging were discussed and how, in conjunction with a DMD, the random-access approach would be implemented.

The specular reflective properties of an individual micromirror were described, further the etendue of a single micromirror and how it scales with the number of micromirrors was shown. Different layouts of the device for imaging and re-imaging components were shown and a design that minimised the alignment issues of coupling a spectrometer to the system was chosen. Further the diffraction behaviour of the DMD as a coarse grating was described and how it relates to the specular behaviour already described. Distortion behavior of the spectrometer was also shown as a prelude to coupling it to the DMD. Finally a Zemax model showing a simplified paraxial model of the illumination and re-imaging lenses for the DMD was shown, including the necessary tilts to account for the Scheimpflug condition and an objective lens in preparation for the inclusion of a microscope as the input objective for the RASI device, which will be discussed in the next chapter. This was in preparation for the following chapter wherein the construction, experimental realisation and calibration of the system will be discussed.

Chapter 3 – Experimental realisation

3.1 Introduction

Chapter 2 described the basics of the Random Access Spectral Imager (RASI) layout that will be implemented experimentally in this chapter. The constructed system used off-the-shelf telecentric lenses to image and re-image the DMD onto the spectrometer entrance aperture and the imaging camera, additionally a microscope was coupled to the RASI system entrance aperture to provide an imaging modality for demonstrating the system. In contrast to most other imaging systems - spectral or otherwise - which have fixed apertures, RASI uses the DMD as a dynamic aperture; as a result, an extensive geometric calibration was required to relate the DMD pixels to the pixels of both the spectrometer and imaging cameras. Since the entrance aperture width to the spectrometer could be altered via the DMD, spectral resolution and signal-to-noise could be altered by changing the number of pixels in a particular slit, which will be quantified. A further consequence of using a DMD was the presence of scattering from the backplane of the DMD; this effect was characterised and a means of countering it proposed.

3.2 System overview

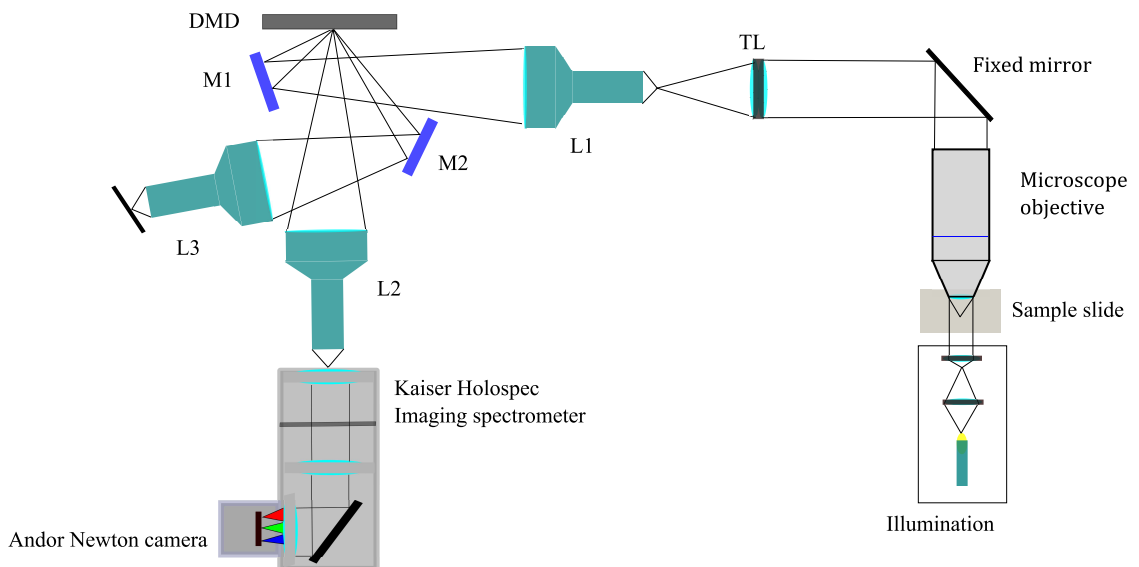


Figure 3.1: Overview of the RASI system layout: L1, L2 and L3 are the telecentric lenses; TL is the microscope tube lens; M1 and M2 are turning mirrors to help direct the incident and reflected rays from the DMD.

Figure 3.1 shows an overview of the whole system, light collected by the microscope objective is coupled into the central RASI system which consists of the telecentric lenses and the spectrometer and conventional imaging arms of the system. Mirrors are

used to simplify alignment of the spectrometer and make the system more compact. Prior to a more detailed discussion of the overall system setup the particulars the DMD, the telecentric lenses and the spectrometer need to be expanded upon as they affect the construction and alignment.

3.2.1 Digital micromirror device

The properties of the DMD as an optical switch and the diffraction properties are described in the Sections 2.3 and 2.6; here the peculiarities relating to the construction of the DMD used in this thesis are discussed. The model of DMD used was a Texas Instruments D4100 0.55' with XGA (1024×768 pixels) resolution.

The first point to consider is the tilt of individual micromirrors along their diagonals; even though the mirrors are laid out in a rectangle, resulting in a diamond shaped aperture when viewed off-axis. Furthermore the DMD needed to be aligned with the spectrometer entrance aperture so the sides of the DMD array were parallel with the detector pixel sides, or else any slits generated on the DMD would also have a diamond shape on the spectrometer detector. To achieve this, mirror M1 in Figure 3.1 was used to illuminate the DMD while maintaining the alignment of the DMD with the spectrometer entrance aperture. This required the imaging and re-imaging channels all to be offset vertically; this configuration is shown in the 3D system representation in Figure 3.4, which shows a computer aided design (CAD) model of the system.

A second point is that extra micromirrors surround the central array of 1024×768 controllable micromirrors. These extra micromirrors are a consequence of the manufacturing process and have the direction of their tilt fixed and are referred to as a ‘pond’ of micromirrors. The light reflected from the ‘pond’ of fixed micromirrors can contaminate one of the system channels, it was purposefully directed towards the imaging channel to avoid contaminating the spectrometer channel.

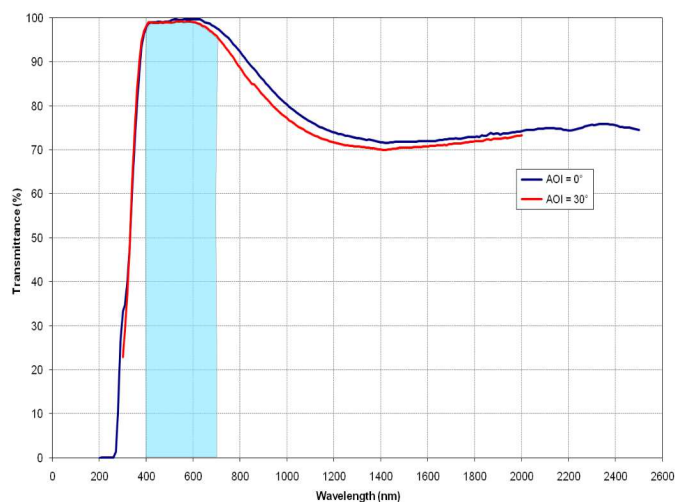


Figure 3.2: Transmission of the DMD window [1].

The DMD used was fitted with a window designed for the visible, the transmission spectrum for this window is shown in Figure 3.2.

The DMD is interfaced via an electronic driver board and is addressed in blocks, the blocks are subsets of the whole array, to which a state command is loaded. Then, a reset command is given which causes the state to change, effectively resulting in the micromirror switching its position. Individual blocks can be addressed if it is known that only a small subset require a change, though this does require keeping track of the addresses. The DMD can also be addressed globally, i.e. sending a command to every micromirror, though this does not require a change in state for a given micromirror. In general to address the DMD a binary sequence is uploaded to the DMD where the given value (0 or 1) at a point in the sequence sets the position of its corresponding micromirror, the primary challenge in this regard was generating the appropriate binary sequence. Software was provided that converts monochrome bitmaps to the appropriate binary format automatically as well as some Labview functions that were used to integrate the operation of the DMD into a larger setup.

3.2.2 Telecentric lenses

As discussed in the previous chapter, telecentric lenses are required for the illumination, they are also used to maintain the telecentric condition of the reflected light bundles from the micromirrors. The telecentric lenses (three were acquired) that were obtained for this prototype were 0.5x *Silver Series* telecentric lenses from *Edmund Optics*. A summary of their characteristics are shown in Table 3.1.

Magnification	0.5X
Front Working Distance (mm)	120
Back Working Distance (mm)	60
Working Distance Tolerance (mm)	± 3
Depth of Field (mm)	± 2.1
Front Aperture	$f/6$
Back Aperture	$f/3$
Telecentricity ($^{\circ}$)	< 0.1
Distortion (%)	< 0.3
Mount	C-Mount

Table 3.1: *Silver Series Telecentric lenses parameters.*

To ensure that the incident and reflected rays did not overlap, the lens side with aperture of $f/6$ was used to illuminate and re-image the DMD, this is shown in Figure 3.1. The larger f-number allowed for the system to be constructed in a reasonable amount of space without the use of large optics to accommodate all the reflections from the DMD, though as a consequence the etendue of the DMD-lens system is much lower than the maximum allowed by the use of lenses with aperture of $f/2.4$.

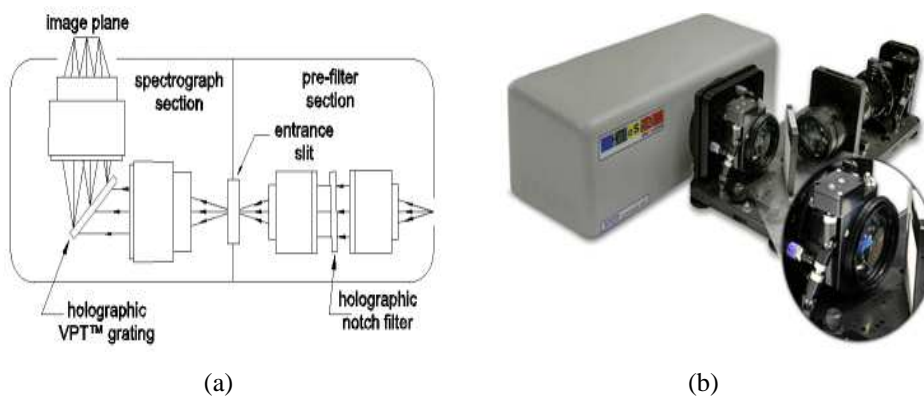


Figure 3.3: (a) is the diagram of the internal optics of the Kaiser Holospec and (b) is a view from the outside.

3.2.3 Spectroscopy components

One of the key aspects of the RASI device was its ability to collect high-resolution spectra from across the FOV of the device. To that end it was necessary to have a spectrometer with a removable slit, otherwise the slit would spatially filter the light reflected from the DMD. Furthermore the performance of the spectrometer in positions away from the normal slit position needed to be sufficient to allow spectral measurements to be performed. Since the DMD was re-imaged by a telecentric lens with magnification of 0.5X, the size of the open entrance of the spectrometer need only have had dimensions of 5.4×4.1 mm, which was smaller than the actual size of the Kaiser Holospec entrance aperture.

The Kaiser Holospec is a dispersive spectrometer using a plane holographic grating and 1 : 1 magnification between the entrance and exit apertures of the spectrometer. It is a modification on a general purpose spectrometer, but with an additional holographic notch filter for Raman spectroscopy using a 785 nm laser. Two gratings were obtained with the spectrometer: one for broadband spectroscopy, the other for Raman spectroscopy. Their parameters are listed in Table 3.2. The dispersion values given in Table 3.2 are

	Spectral coverage	Dispersion
HSG-785-LF	-34 to 1894 cm^{-1}	2 $cm^{-1}/pixel$
HVG-590	384.5 to 795.5 nm	0.42 nm/pixel

Table 3.2: Table of grating parameters, the pixel size referenced is 26 microns.

with respect to pixels 26 microns in size, the same as the camera used in conjunction with the spectrometer in this setup. The two gratings were interchangeable, so it was possible to change from a broadband spectral mode to Raman spectroscopy mode with relative ease.

The *Andor Newton* conveniently comes with an adapter specifically for the *Kaiser Holospec*, which makes them easier to use together. The camera also has a cooling abil-

Specification	Value
Array	1024 × 255
Pixel Size	26 × 26 microns
Read noise	as low as 2.5 e^-
Dark current	as low as 0.0001 $e^-/pixel/sec$

Table 3.3: Table of camera parameters.

ity, down to -100°C , allowing it to reduce some aspects of noise. Other useful elements were the extensive *Labview* library which allowed for integration and coordination with other devices.

3.3 Core RASI construction

The opto-mechanic layout of the optical breadboard system that was constructed for RASI is shown in Figure 3.4, the layout follows the approach described in Section 2.5, in that the DMD was illuminated from an off-axis angle of 24 degrees, through the lens L1 and redirected onto the DMD via M1. The issues raised in Section 3.2.1 with regard to the projection of a diamond aperture onto a square detector were accounted for by rotating the DMD so that it was parallel to the entrance aperture of the spectrometer. As a consequence the imager channel needed to be directed into the lens L3 with a mirror, as it was switched at an angle of 48 degrees, which required a more complex opto-mechanical solution which can be seen in a 3D representation of breadboard layout in Figure 3.4. A light-tight enclosure was placed around the whole breadboard once the system was constructed.

As a consequence of this construction, the alignment of the spectrometer was greatly simplified, as the DMD was imaged directly onto the spectrometer entrance aperture. This was important as due to its bulk, it was the most difficult component to mount and align. Other designs either keep the imaging and re-imaging planes in the same horizontal plane [98] and use specialised optics to correct for any distortions in the spectrometer [93].

3.3.1 Custom Microscope for RASI

An infinity corrected microscope was created and coupled to the core RASI setup, as shown in Figure 3.1. The tube lens of the microscope was tilted to account for the Scheimpflug condition for the imaging lens, as described in Section 2.9 in the previous chapter, also shown in Figure 3.7 (b). The microscope objective was a 60X, 0.85 NA Nikon Plan Fluorite Objective used with an infinity corrected tube lens (ITL200), both sourced from Thorlabs. The microscope slide mount, where the microscope objective object plane was located, was attached to a motorised (stepper motors) translational

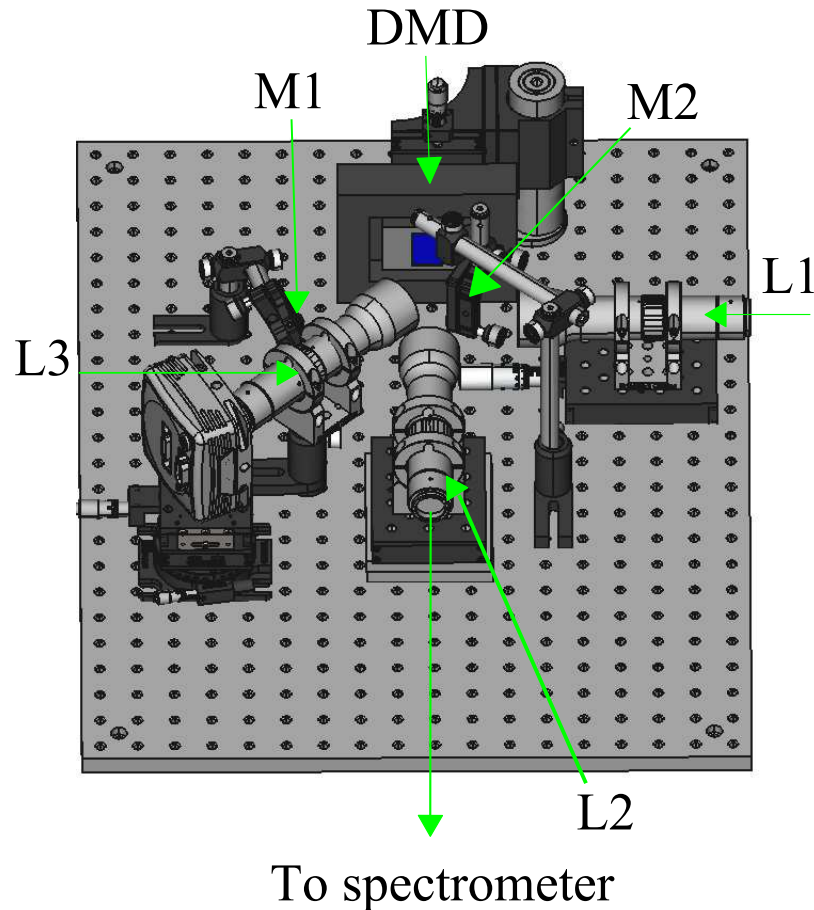


Figure 3.4: 3D CAD model of RASI experimental system. The positions of the imaging and re-imaging lenses are shown, along with the mirrors M1 and M2 which are used.

stage with three degrees of freedom (Nanomax, MAX343), which provided a convenient focussing mechanism for the microscope.

A visible light (Perkin Elmer, Xenon) source was used to illuminate the microscope sample in a Koehler configuration. A schematic of the Kohler illumination layout is shown in Figure 3.6, the source and the aperture stop, as labelled, are at conjugate planes, the condenser projects a completely out of focus image of the aperture stop onto the microscope object plane, thereby achieving even illumination in the microscope object plane. A field stop is placed conjugate to the microscope object plane to control the illumination area of the Koehler illumination.

The purpose of the microscope was to provide an imaging modality by which the RASI system could be demonstrated on a range of targets, other imaging modalities involving macroscopic imaging have been explored in other work.

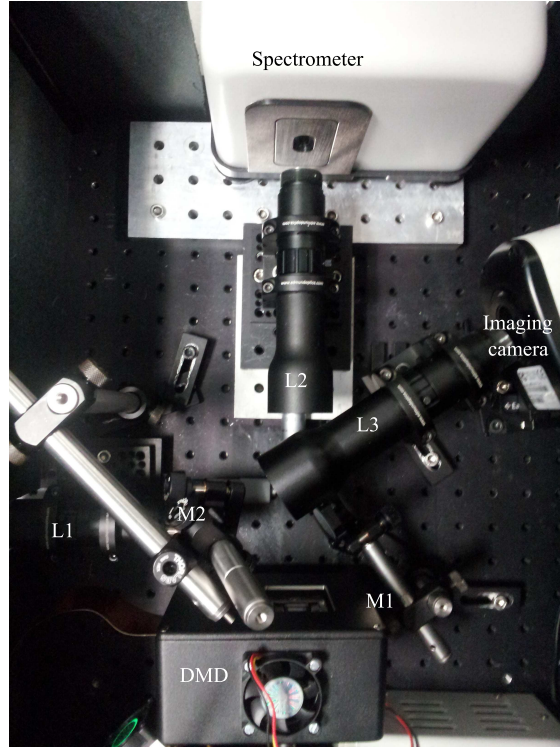


Figure 3.5: Breadboard view of setup.

3.4 Imaging arm parameters

The imaging channel re-images the microscope object plane via the DMD onto a detector; effectively acting as a bright field microscope. The camera used was a Lumenera Infinity colour camera with a 1280×1024 array of 5.5 micron pixels. The primary purpose of the imaging channel was as a reference by which to identify regions of interest across the RASI FOV and re-direct them to the spectrometer channel. This required a geometric calibration relating the camera pixels to DMD pixels. Two other parameters were of particular interest, the actual RASI FOV and Full-On-Full-Off (FOFO) contrast of the channel, a common measure for DMD based imaging systems.

3.4.1 Geometric calibration

The purpose of the geometric calibration of the imaging channel was to determine relations between the DMD pixels of index (i, j) and camera pixels, of index (X, Y) . Since for each (i, j) there exists a unique (X, Y) , then the relations

$$\begin{aligned}
 i &= f_i = f_i(X, Y) \\
 j &= f_j = f_j(X, Y) \\
 X &= g_X = g_X(i, j) \\
 Y &= g_Y = g_Y(i, j)
 \end{aligned} \tag{3.1}$$

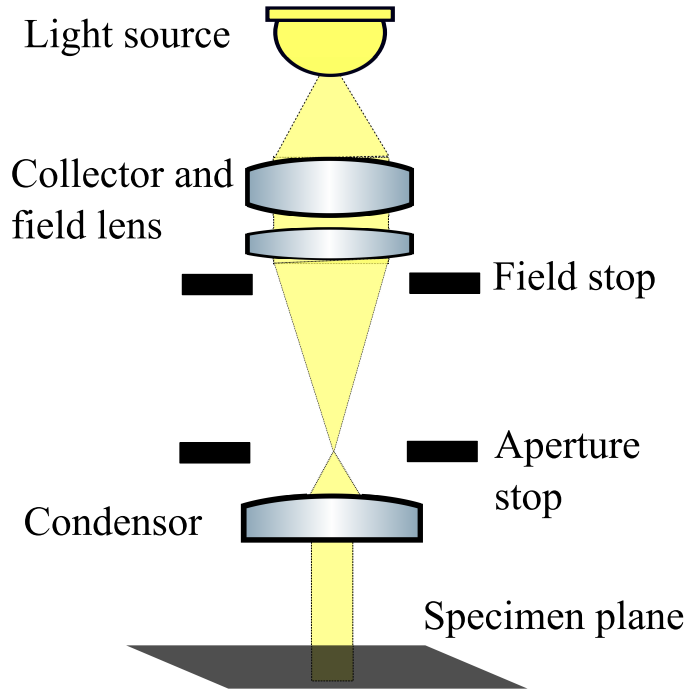


Figure 3.6: Koehler illumination layout.

can be used to describe this mapping between DMD and camera pixels. The relations in Equations 3.1 were generated directly by systematically switching individual DMD mirrors towards the imaging channel and recording the position of the bright spot on the imaging camera. One issue with this approach was the pond of mirrors, mentioned in Section 3.2.1, which could contaminate the acquired images, this was solved by simply subtracting a second frame with just the pond of mirrors illuminated, that is all the micromirrors pointed away from the imaging channel. These pairs of DMD and camera pixel coordinates were acquired for an evenly spaced grid of DMD pixels, a spacing of 64 DMD pixels was found to be sufficient.

The acquired data was used to create interpolating functions for f_i and f_j , these functions were of the form:

$$\begin{aligned} f_i &= a_1X + a_2X^2 + a_3Y + a_4Y^2 + a_5 \\ f_j &= b_1X + b_2X^2 + b_3Y + b_4Y^2 + b_5, \end{aligned} \quad (3.2)$$

where a_1, a_2, a_3, a_4, a_5 and b_1, b_2, b_3, b_4, b_5 are fitting parameters. Equations and fit parameters were also determined for the g relationship, this fitting was done with *Mathematica*. The RMS error for the polynomial fit to f_i was 0.5 DMD pixels and it was 0.4 DMD pixels for the fit to f_j . Example values for the fit parameters are shown in Table 3.4, the quadratic terms in the fit are on the order of 10^{-6} and 10^{-7} leaving the linear fit parameters as the dominant terms. This is a consequence of the low distortion in the system, pincushion and barrel distortions are radial distortions that bend straight lines towards and away from the system optical axis; both can be modeled and corrected using quadratic and higher polynomials.

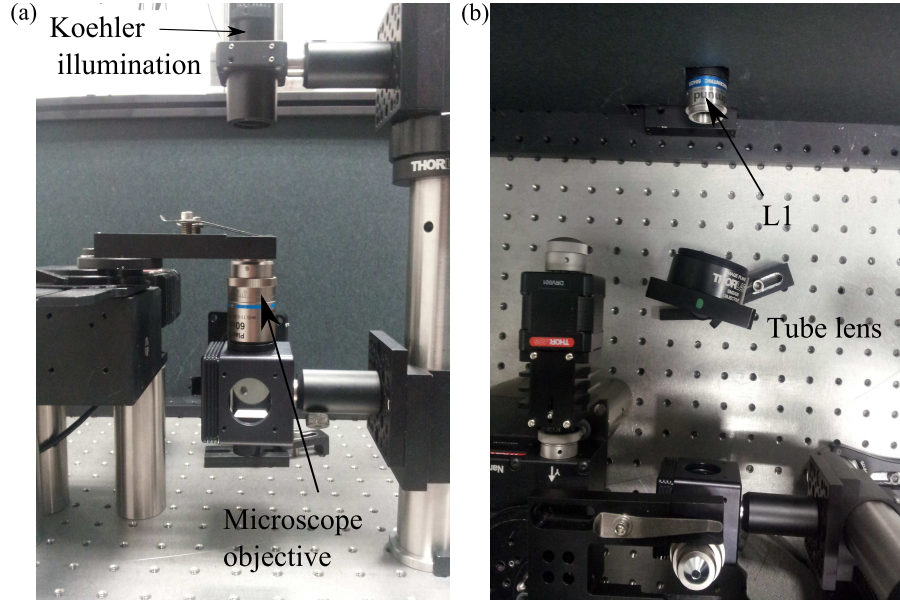


Figure 3.7: (a) Microscope objective and (b) infinity corrected tube lens coupling light to core RASI, the lens tilt corrects for the Scheimpflug condition.

	a_l	b_l
$l = 1$	0.413	0.891
$l = 2$	4.548×10^{-6}	6.920×10^{-7}
$l = 3$	1.014	0.658
$l = 4$	-7.58062×10^{-6}	-3.174×10^{-7}
$l = 5$	128.561	-390.466

Table 3.4: Table of fit parameters for an example imager channel geometric calibration, the fit parameters have units of DMD pixel per CCD pixel.

3.4.2 Image orientation, correction and contrast

Due to the orientation of the camera with respect to the DMD, the image of the DMD is rotated on the camera, this can be corrected to recover a 1024×768 array using the geometric calibration data. The rotated image is not a debilitating issue and could be corrected by rotating the camera, but it was decided to correct this issue in software, the primary motivation for transforming the camera image from a trapezoid shape to a rectangular image was to simplify visualisation of the scene. An example of the correction is shown Figure in 3.8, a regular grid of squares is displayed on the DMD and the raw image is transformed into a rectangular image.

Three other examples of DMD images are shown in Figure 3.9, the first shows a checkerboard pattern that was generated on the DMD itself and was transformed using the image correction procedure. Figure 3.9 (b) and (c) show images of microscope slides in the object plane of the microscope. In all cases it possible to see that the images in the centre are in focus and become more blurry in the top right and bottom left of the images, this was due to the camera not being tilted sufficiently for the Scheimpflug

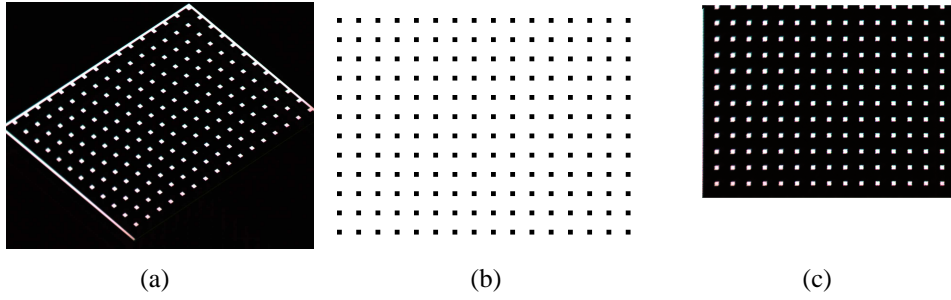


Figure 3.8: (a) is the raw image as seen on the detector, (b) is the mask pattern uploaded to the DMD and (c) is the corrected version of the raw image.

condition to be fulfilled, though performance was deemed acceptable; this blurring could be improved upon using a camera mount with a more robust rotation mechanism.

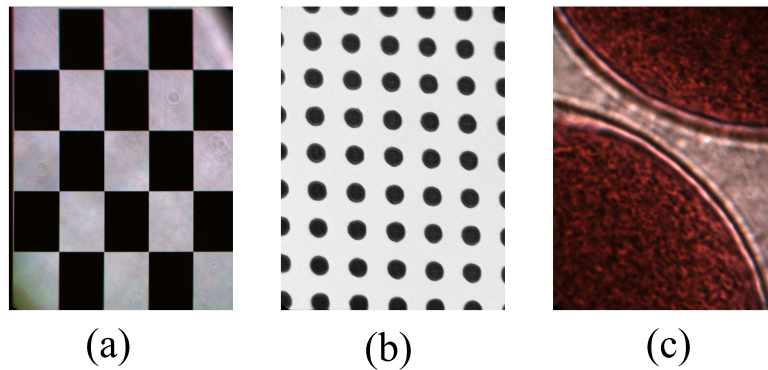


Figure 3.9: (a) is a corrected checkerboard pattern that has been displayed on the DMD. (b) is a microscope slide with 5 micron diameter dots that has been corrected. (c) is also an image of a microscope slide, this time of a Pumpkin Pollen histological slide.

A particular metric for contrast in DMD systems is the Full-On-Full-Off (FOFO) comparison [92], which measures the difference between all the DMD pixels switched towards a channel and all the pixels switched away from the same channel; the FOFO contrast was measured to be 0.98; contrast was defined as

$$C = \frac{S_{on} - S_{off}}{S_{on} + S_{off}}, \quad (3.3)$$

where S_{on} was the pixel signal value from the DMD pixels switched on and S_{off} the value from the pixels switched away from the channel. Camera frames in the two states were captured, converted to grayscale and a region of 20 by 20 pixels in the centre of the image was chosen, the pixel values of which were averaged to determine the S_{on} and S_{off} values. FOFO contrast was important because it measures affect of scattering from the backplane of the DMD on the imaging channel which reduces the contrast present in any image acquired. The closer the value of C to 1, the smaller the affects of scattering on the overall performance of the imaging channel. It is visible in the images shown

in Figure 3.9 that the affect of scatter is less significant in the imaging channel than the affects of alignment and the Scheimpflug condition.

3.5 Spectroscopy channel parameters

The spectroscopy arm of RASI uses the DMD as a dynamic aperture to the spectrometer, as a consequence there are some key differences between RASI and a normal dispersive spectrometer system. An extensive spectral calibration needed to be performed similar to the geometric calibration of the imaging arm, but including the wavelength dependence between DMD pixel and spectrometer camera pixels, this calibration was performed using Matlab. Another consequence of the dynamic aperture is that the spectral linewidth and signal can be varied by the changing the number of pixels in a slit.

3.5.1 Geometric and wavelength calibration

Each DMD pixel of index (i, j) acted as an aperture to the dispersive spectrometer, the image of the aperture was dispersed on the spectrometer camera which had coordinates of (x, y) , as such each DMD pixel was related to a set of camera pixels. This transform between DMD and camera pixels can be summarised mathematically as

$$(i, j) \xrightarrow{\tau} (x, y, \lambda).$$

In practice it was necessary to generate a series of functions that would allow the prediction of the (x, y) coordinates of a particular wavelength for a given DMD pixel.

$$\begin{aligned} x &= \tau_x = \tau_x(i, j, \lambda) \\ y &= \tau_y = \tau_y(i, j, \lambda) \end{aligned} \tag{3.4}$$

The two different gratings required different calibrations, since they had different spectral ranges (Visible and IR) and different light sources were used for each grating. For each grating calibration, a grid of points across the FOV needed to be gathered at multiple wavelengths, these grids of points were used to interpolate the spectral calibration across the whole DMD, as exhaustively gathering data for each DMD aperture would be excessively time consuming. A super-continuum source was used as the calibration source for the visible grating and a commercial Neon lamp was used for the IR grating, different data gathering strategies were used for the different sources.

The super-continuum output was a white light spectrum in the visible and it could be coupled to an acousto-optic tunable filter to allow control over the output wavelength. The output from the super-continuum source was coupled to the entrance port of the system and the DMD was illuminated evenly. Using the AO filter, a single wavelength

was selected, this was done in steps of 10 nm from 480 nm to 690 nm, and individual micromirrors were switched towards the spectrometer. For each micromirror, a measurement was taken at a number of different integration times, so there was a number of different measurements of the same location on the DMD, this helped counter any variance of the light intensities at different wavelengths, which gave the wavelength dependent position of the light reflected from the micromirror. The data from the multiple frames was used to extract the centroid in each case, these values were averaged, and a standard deviation taken, points with high standard deviations were removed from consideration as the high variance indicated some error in the data acquisition, caused by either light from an outside source interfering with the calibration experiment or fluctuations in the output from the super continuum source. In this way a grid of points across the FOV at a given wavelength was built up. This process was then repeated over a number of wavelengths to build up an array of data describing a grid of points on the DMD array. The output from the calibration was then formatted into series of arrays combining the DMD coordinate, CCD coordinate and wavelength.

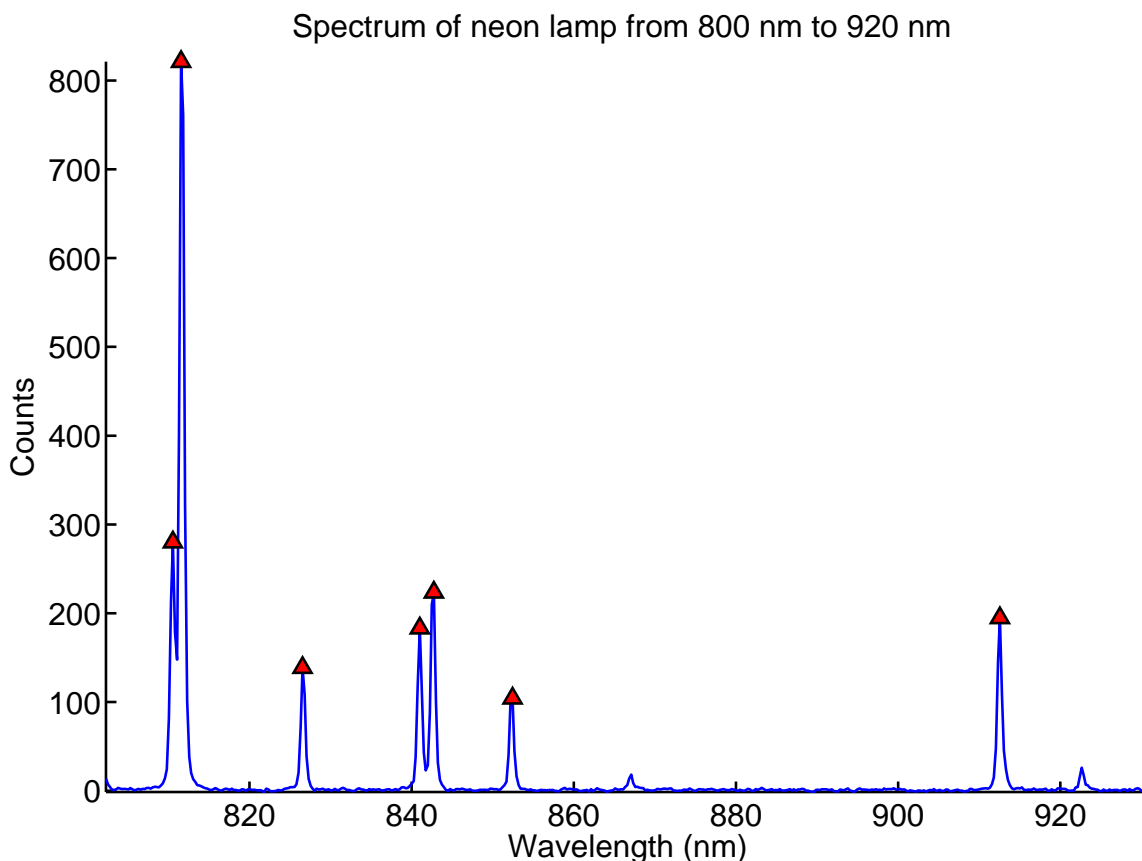


Figure 3.10: *The reference spectrum used to characterise the neon lamp and for comparison with the spectrum obtained by the RASI system for calibration.*

An alternative approach for gathering data was used in the case of the infrared sensitive grating, a neon light source was used to provide the spectral lines for calib-

Wavelength (nm)
810.58
811.58
826.56
841.01
842.75
852.44
912.54

Table 3.5: Wavelengths from the Neon light source

ration. To facilitate this, the neon lamps spectrum was measured with an independent spectrometer (Ocean Optics HR4000) in the spectral region 800 nm to 960 nm. The reference spectrum is shown in Figure 3.10 and a list of the wavelengths of the spectral lines is given in Table 3.5. It should be noted that the Neon lamp used was a commercial Neon lamp, not a calibration standard, the Neon lines measured do not match up with the positions of standard Neon lines and other, expected spectral lines are missing, indicating that the lamp used was not a pure source. The lamp still provided a useful calibration source as it provided numerous spectral lines over the necessary spectral range of the IR grating.

The light from the Neon lamp was coupled into the front optic of the RASI setup and the DMD was illuminated. DMD pixels were then systematically switched towards spectrometer, the spectral lines appearing on the detector, resulting in multiple wavelengths being captured at once, unlike the approach using the super continuum source where a single wavelength was captured at a time. As such extra steps were required to extract the correct relations between DMD pixels and the centroid positions of different wavelengths on the CCD frame. The strongest spectral line was the 811.58 nm line, this was used as a reference to label the other known spectral lines according to their positions relative to the 811.58 nm peak. The last wavelength, 912.53 nm was at the edge of the spectral range of the camera, so as the DMD pixels were scanned across the input aperture the final spectral peak would "walk off" of the frame, as demonstrated in Figure 3.11. Once the peak positions were extracted the data was tabulated in the same manner as the results obtained using the super continuum source. The outputs from the calibration process were then formatted into a series of grids of coordinates of the DMD and CCD frame at the wavelengths of the Neon lamp. Similar to the output from the process using the super-continuum source, once the calibration data was obtained and formatted, the same calibration procedure could be applied to both cases. The DMD contains 786432 individual micromirrors, so of necessity the grids for each wavelength, which was a small subset of this, was an evenly spaced grid with points spaced every 64 DMD pixels. This reduced the time taken to collect the calibration data as the values in between the collected points were interpolated.

The first step once all the points were gathered was to generate an interpolated

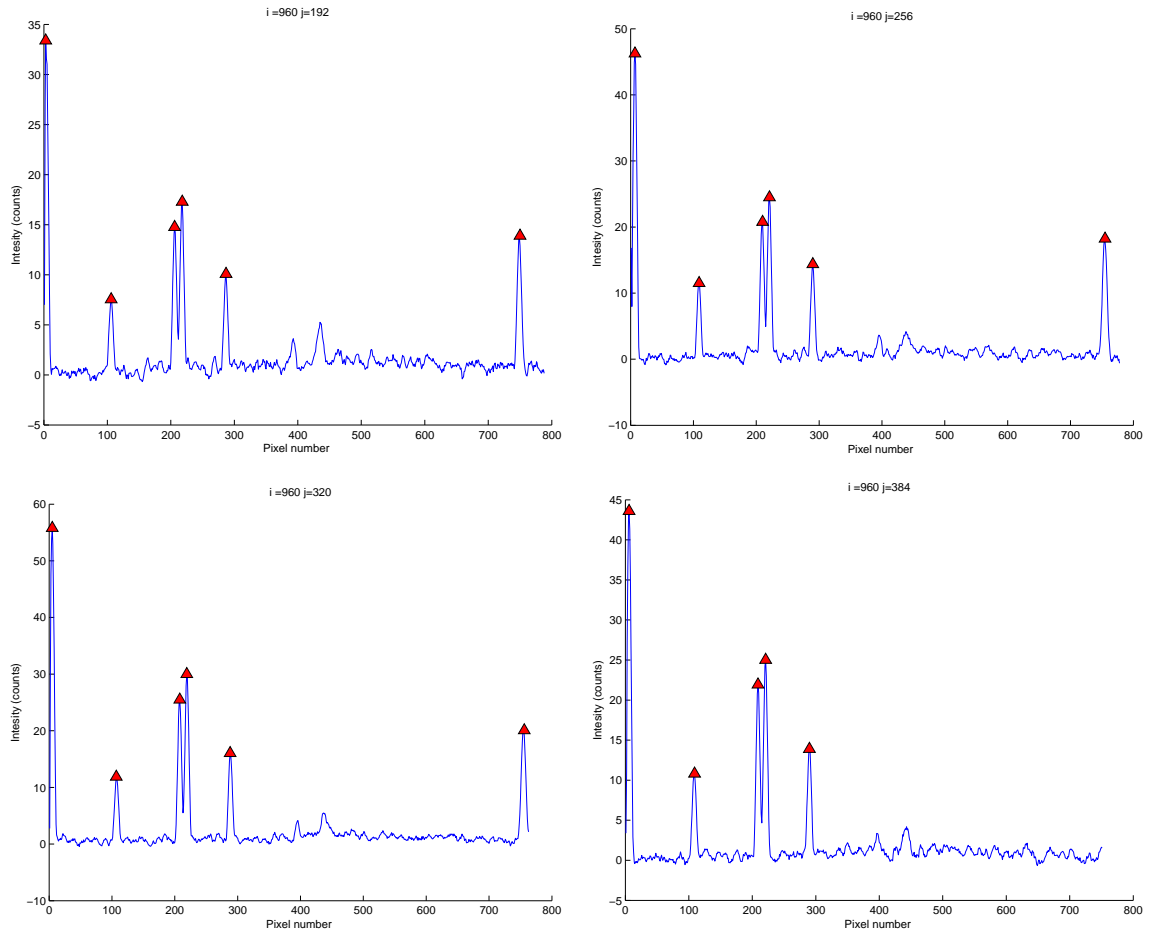


Figure 3.11: Example of sets of spectral lines on the detector and how the 912 line is shifted off the detector as the DMD scans across the entrance aperture of the spectrometer

1024×768 array for each wavelength collected, in order to fill in the blank spaces between the collected data points. This was achieved by creating a lattice of size 1024×768 and using the collected data points as nodes in the lattice, the points in between were interpolated using a triangle nearest neighbor interpolation. Two arrays were constructed for each wavelength, consisting of (i, j, x) and (i, j, y) . Each of these grids contained the relationship between DMD pixel coordinates and either the x or y pixel coordinate of the camera.

Once the grids had been populated it was then possible to generate the wavelength calibration for a large subset of the possible DMD pixels. The wavelength calibration related wavelength to the CCD pixel coordinates and was generated - for both x and y coordinates - by fitting the wavelength and camera pixel data contained in the interpolated

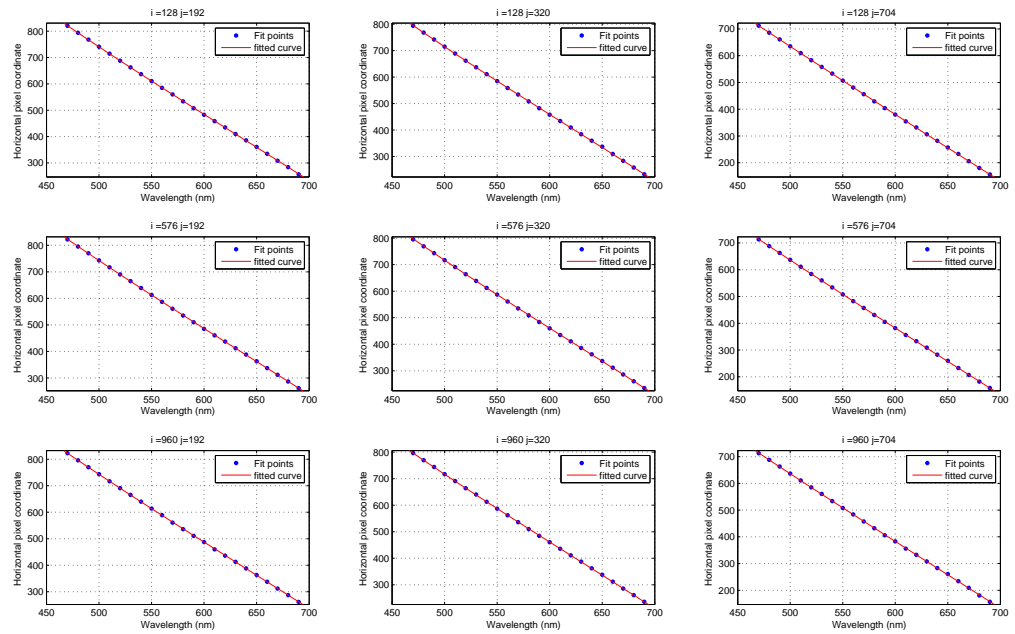


Figure 3.12: Fits to the horizontal coordinates of the camera and wavelength, each fit is associated with a particular DMD pixel of coordinates (i,j) .

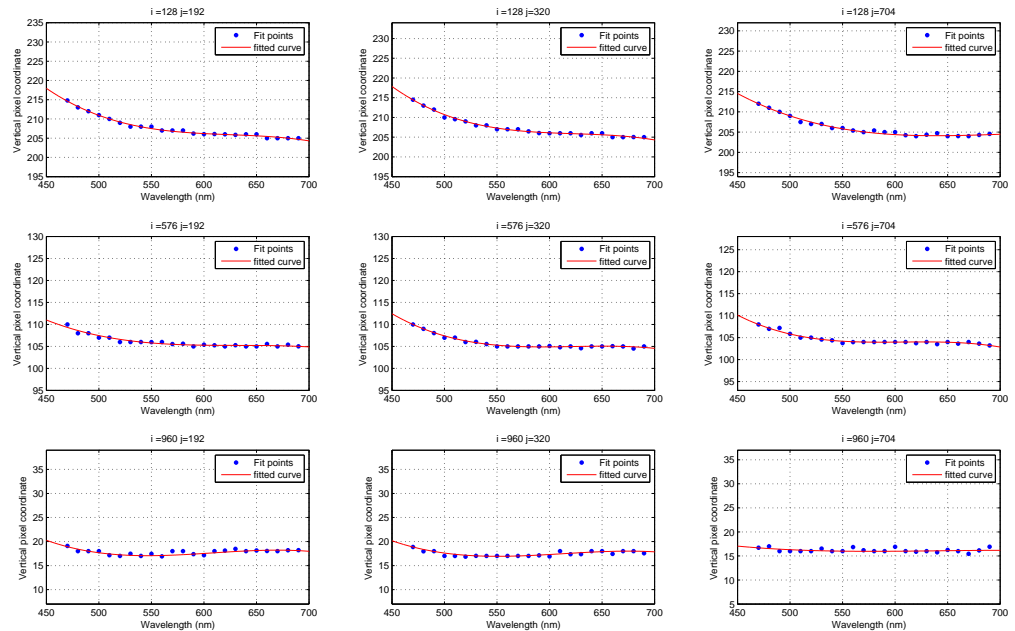


Figure 3.13: Fits to the vertical coordinates of the camera and wavelength, each fit is associated with a particular DMD pixel of coordinates (i,j) .

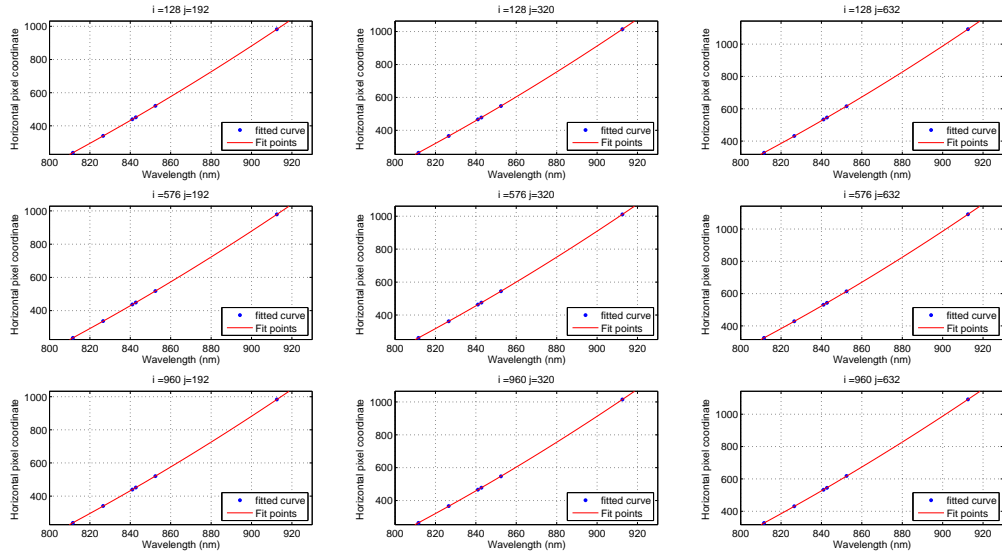


Figure 3.14: Fits to the horizontal coordinates of the camera and wavelength, each fit is associated with a particular DMD pixel of coordinates (i, j) for the infrared grating.

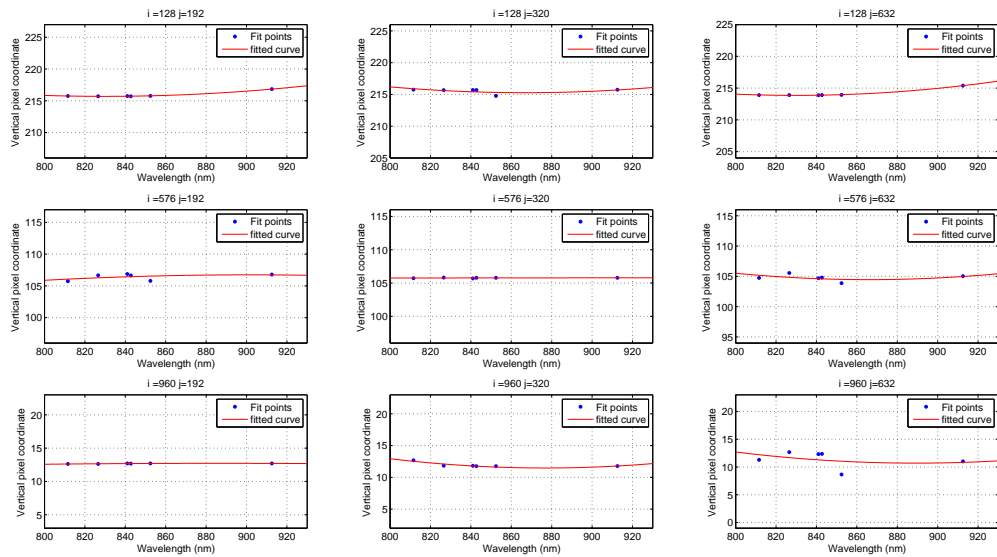


Figure 3.15: Fits to the vertical coordinates of the camera and wavelength, each fit is associated with a particular DMD pixel of coordinates (i, j) for the infrared grating.

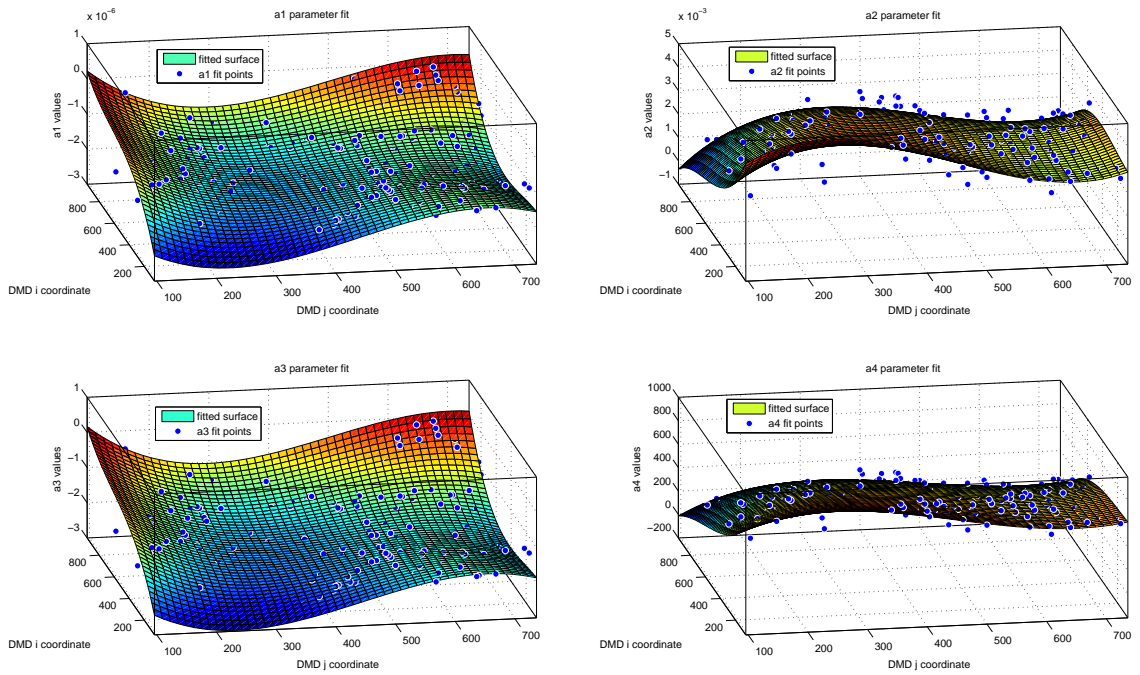


Figure 3.16: The fitting parameters fit to a third order polynomial for the broadband grating calibration in the horizontal direction.

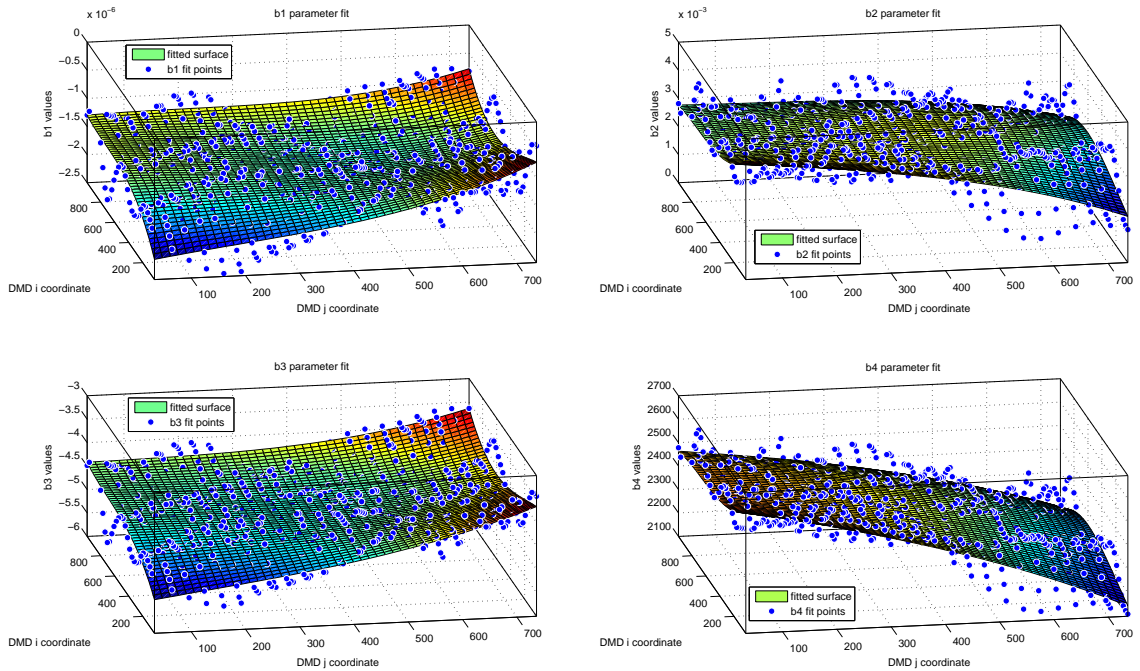


Figure 3.17: The fitting parameters fit to a third order polynomial for the broadband grating calibration in the vertical direction.

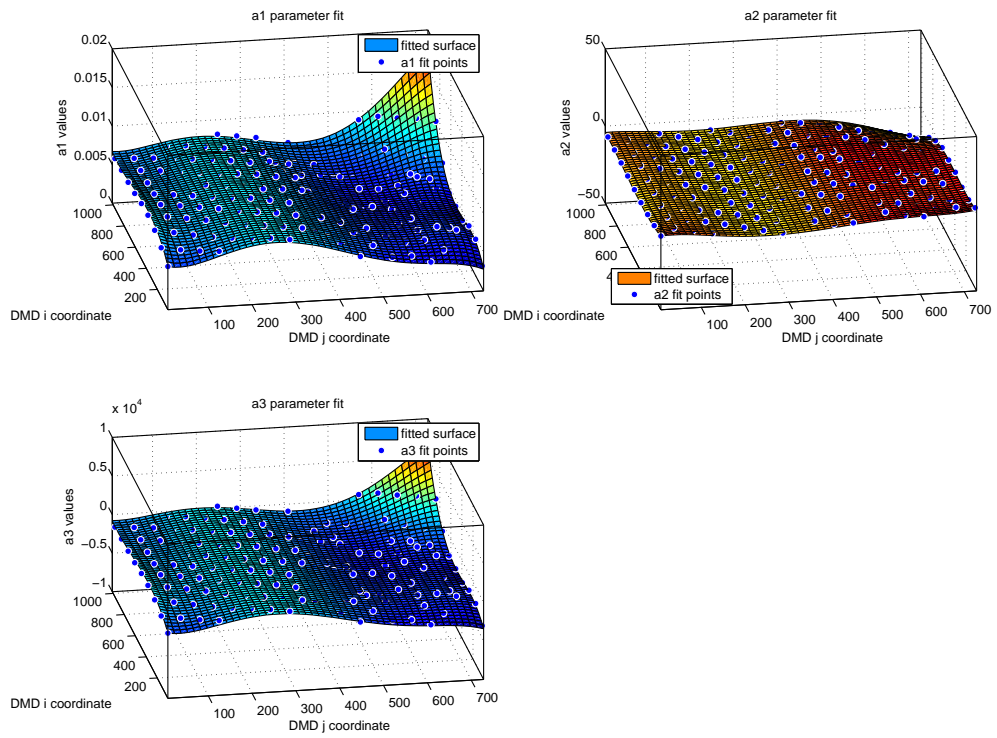


Figure 3.18: The fitting parameters fit to a third order 2D polynomial for the infrared grating calibration in the horizontal direction.

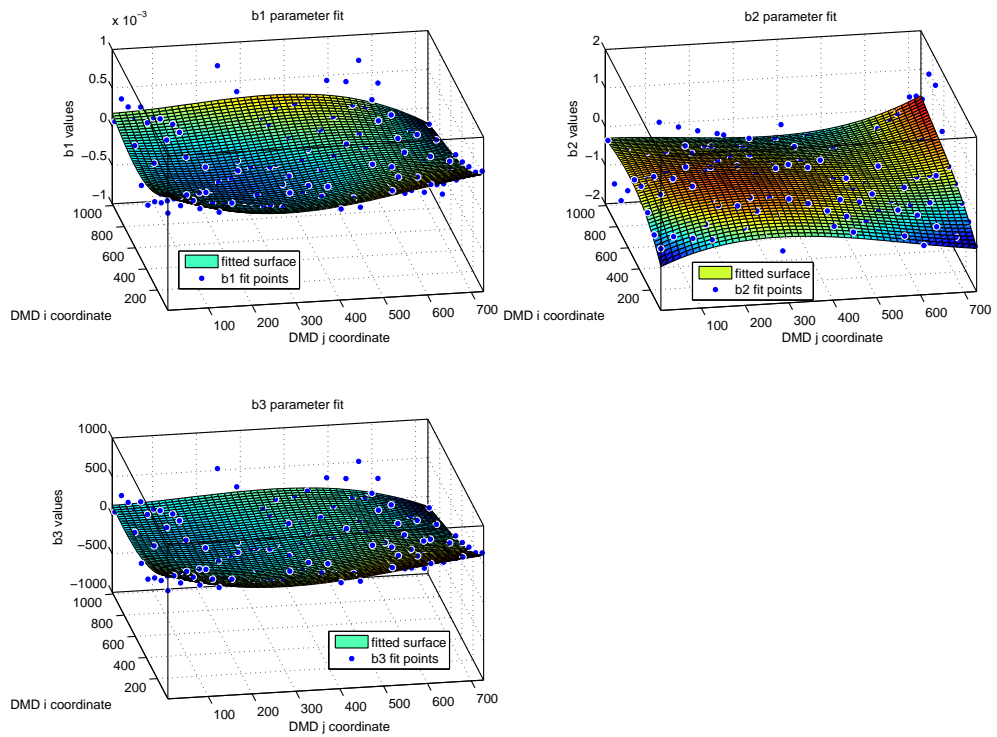


Figure 3.19: The fitting parameters fit to a third order 2D polynomial for the infrared grating calibration in the vertical direction.

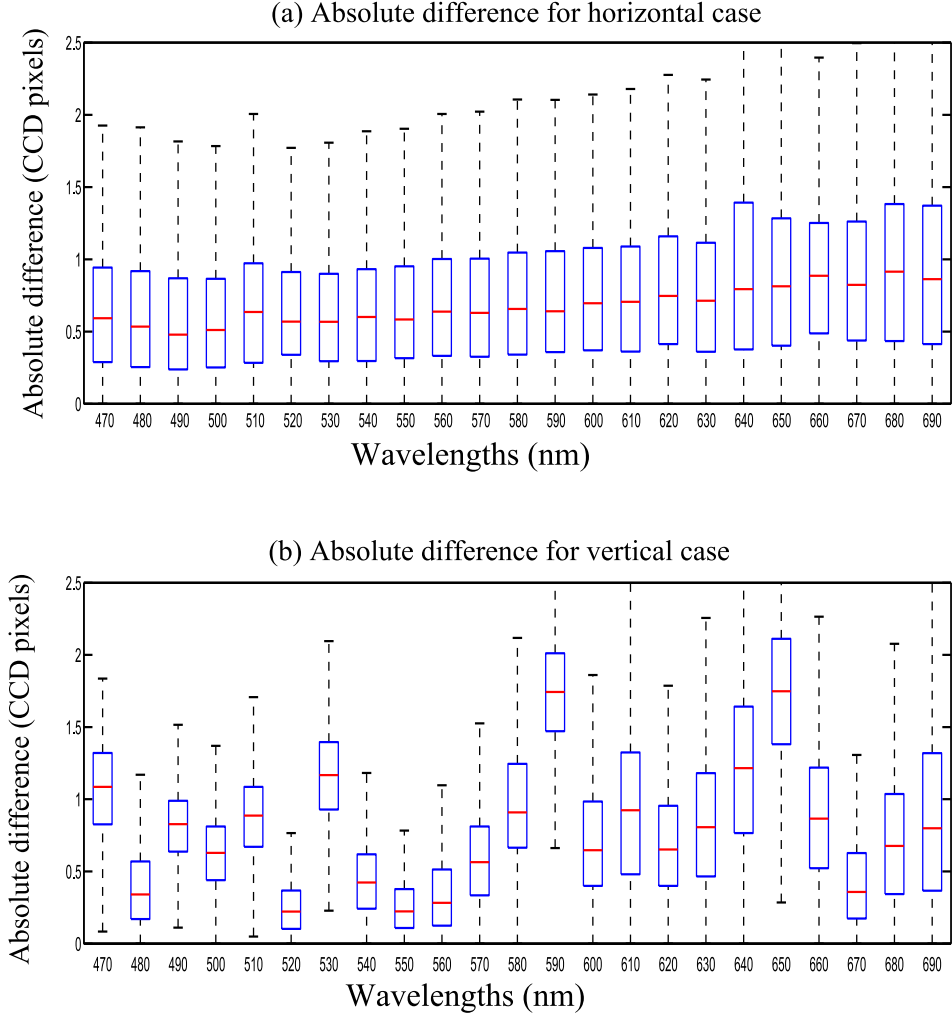


Figure 3.20: The box plots show the mean and upper and lower quartiles for the difference the coordinate values and the coordinate values recovered by the calibration relations. This is shown for each wavelength at which data was collected and for both cases of calibration relation, the vertical (y) and horizontal (x) directions.

grids to polynomial equations of the form

$$\begin{aligned} x &= \sum_{l=0}^L a_l \lambda^l \\ y &= \sum_{l=0}^L b_l \lambda^l, \end{aligned} \tag{3.5}$$

where a_l and b_l parameters are fit parameters. Examples of the fits of the equations from various points are shown in Figures 3.12 and 3.13 for the broadband spectroscopy grating and in Figures 3.14 and 3.15 for the IR Raman grating. These parameters are unique for a given value of DMD pixel (i, j), so each is a function of DMD index such that $a_l(i, j)$ and $b_l(i, j)$, where l is the subscript of the fit parameter, the number of fit parameters

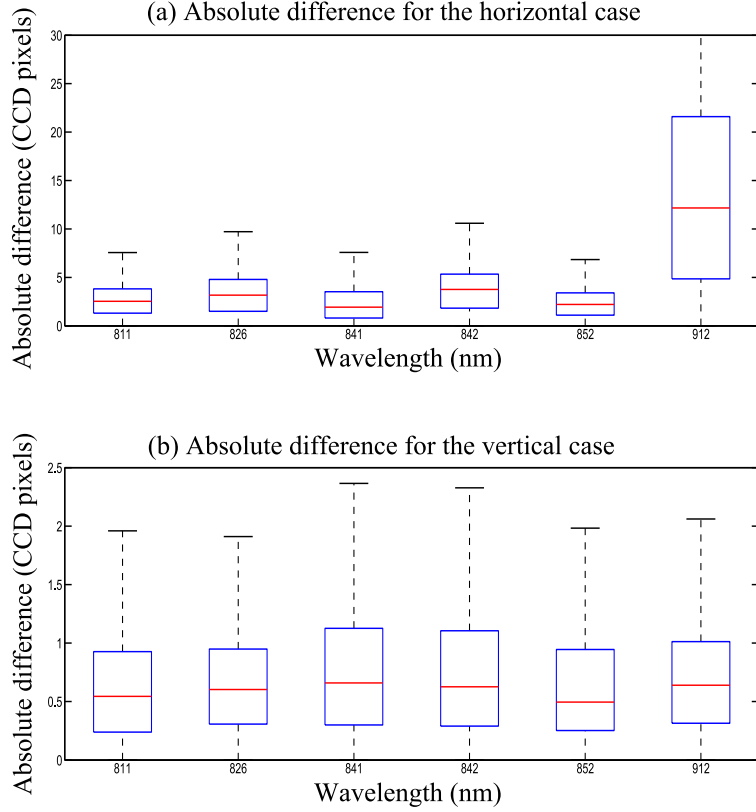


Figure 3.21: Box plots for the Infrared grating calibration, similar to the box plot in Figure 3.20. The error for the 912 nm data is much higher than other wavelengths, most likely due to the smaller number of points available to generate the calibration relations, which is a result of the “walk off” of that wavelength, demonstrated in Figure 3.11.

was set by the order of the polynomial used for the fit, given as L in Equations 3.5. The parameters a_l and b_l were determined over (i, j) by interpolating their values using a 2D polynomial with the DMD indices as the variables. The polynomial used was

$$\begin{aligned}
 a_l(i, j) &= \sum_{p=0}^K \sum_{k=0}^K \alpha_{pk} i^p j^k \\
 b_l(i, j) &= k \sum_{p=0}^P \sum_{k=0}^K \beta_{pk} i^p j^k.
 \end{aligned} \tag{3.6}$$

. This was calculated for every value of l , the results of the fit are shown graphically for the broadband grating in Figures 3.16 and 3.17 and for the IR Raman grating in Figures 3.18 and 3.19, which shows how the different parameters vary over the DMD surface, four fit parameters ($L = 4$) were used for the wavelength calibration in the case of the broadband grating, values of $P = 3$ and $K = 3$ were used for interpolating each of the four wavelength calibration parameters over the whole 1024×768 DMD array. For the IR grating $L = 3$ was used and they were interpolated using $P = 5$ and $K = 5$ polynomials.

It was found that using multiple fit parameters improved the overall accuracy of the interpolation process, when looking at the fits in the horizontal directions, it seems like a simple linear fit would suffice to describe the wavelength calibration. However when fitting over the whole DMD array having smoother variations as a result of higher order polynomials was preferable to the concentrating all the variation in two fit parameters.

Using Equations 3.6 it was then possible to incorporate all the calibration data into a pair of equations, given as

$$\begin{aligned} x(i, j, \lambda) &= \sum_{l=0}^L a_l(i, j) \times \lambda^l \\ y(i, j, \lambda) &= \sum_{l=0}^L b_l(i, j) \times \lambda^l \end{aligned} \tag{3.7}$$

which were dependent on DMD pixel and wavelength. Given those values, which were, in principle, always within the users ability to know, the position of the spectrum for any DMD pixel switched towards the spectrometer could be calculated.

Figures 3.20 and 3.21 show box plots of the absolute difference between the values for camera pixels calculated in the final form of the calibration relations in Equations 3.7 and the original values from which the interpolations were generated. The box plots were calculated for each wavelength that was collected, the central line in each “box” of the box plot shows the median value - the second quartile - while the top and bottom show the 25th - the first quartile - and the 75th - the third quartile - percentiles. Both the horizontal and vertical (x and y) fit results are shown for each grating calibration. Most noticeable is the large error for the 912 nm horizontal coordinate in Figure 3.21 (a), this is due to the “walk off” of that wavelength across the FOV, resulting in less points available for the interpolation, however since the wavelength is only present for a portion of the FOV of RASI, its higher error has less affect on the overall performance of the calibration relations. The results are expressed purely in terms of CCD pixels, as that is what was necessary for extracting spectral data from the CCD, the results can be converted to distance values by multiplying by the CCD pixel size, of 26 microns.

It is noticeable in the plots of the vertical fit parameters for the interpolation, shown in Figure 3.17, that the data points vary with a higher-order pattern than the interpolation function used. This affect is most noticeable at the edges of the field where the deviation between the interpolation function and the data points is most visible. As a consequence the interpolation function smooths out this feature of the data, which could contribute to the measured error between to data points and final interpolation functions. The absolute error between data points and interpolation function shown in the box plots in Figure 3.20 (b) show the scale of any error introduced to be less than 2 CCD pixels. The affects of higher order aberrations are more pronounced at the edge of the system FOV, as is the

case in the plots in Figure 3.17, which is the likely cause of such variances.

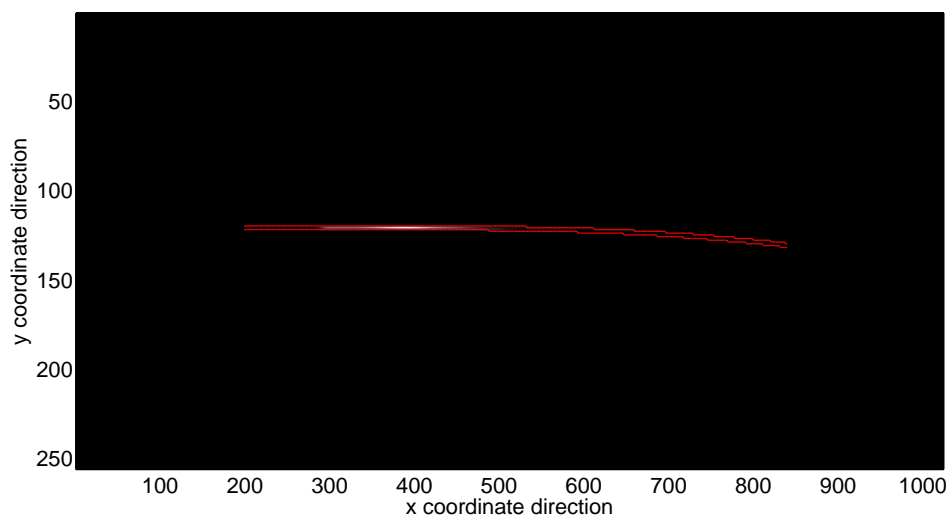


Figure 3.22: Demonstration of using the calibration data to show the region illuminated by DMD pixels.

As a demonstration of the calibration relations, the DMD was illuminated and some micromirrors were turned towards the spectrometer. Then, using the calibration relations the position of the light on the CCD was predicted. The extent of the light is marked on Figure 3.22. The red lines were drawn onto the CCD frame using the values predicted using the calibration equations.

The calibration relations determined in this section form the core of using RASI, any practical attempt to perform spectroscopy requires knowledge of these relations. The approach employed is used to ensure that the calibration can be applied across the field of view, hence the focus on creating grids of parameters and using them to create interpolating functions that can be used to easily extract data from anywhere in the CCD frame. The processing of data was handled by Matlab and the final calibration relations were written as Matlab functions.

A spectral extraction algorithm was written which takes the known information, DMD slit position, slit length and slit width and uses the calibration relations in Equations 3.7 to return, depending on the length of the slit, an array containing the CCD counts values for every wavelength along the rows and the spatial information in the columns. The rows and columns were aligned so as to correct for any curvature in the spectral positions. This information could then be stored and processed without storing the whole CCD frame.

3.5.2 Spectral linewidth

Spectral resolution is a measure of the ability of a spectrometer to resolve spectral features into their separate components. The definition of spectral resolution in the

optical regime is given as “Wavenumber, wavelength or frequency difference of two still distinguishable lines in a spectrum” [91]. The resolution is governed mainly by the slit width and the reciprocal linear dispersion as given in Equation 2.28, which gives the theoretical spectral linewidth. As an example, the linear reciprocal dispersion of the IR grating used for Raman spectroscopy was $2 \text{ cm}^{-1}/\text{pixel}$, which could be converted to nanometres to give $0.137 \text{ nm}/\text{pixel}$, where the pixel size was 26 microns. In order to compare the estimated value, the spectral linewidth was measured directly.

A peak from the Neon lamp was chosen, 826.5 nm, and was measured for different slit widths. The measured peaks for different slit widths are shown in Figure 3.23 (a), where the width of the peaks is seen to increase with the increase in slit width. By fitting a gaussian function to the peaks it was possible to estimate the full-width half maximum of the peaks and therefore measure the actual spectral linewidth for a given slit width. The measured spectral linewidth (FWHM) is shown on Figure 3.23 (b), where the estimated and measured spectral linewidth are shown. The measured values for the FWHM align with the estimated spectral linewidth, the slightly unstable behaviour of the measured linewidth is likely due to fluctuations in the output from the Neon lamp. Since each input slit to the spectrometer consisted of a discrete number of DMD pixels, the different slit widths were expressed in terms of the number of DMD pixels used in the slit, the physical width of a slit could be calculated by multiplying the number of DMD pixels by the length of a DMD pixel, 10.6 microns, and the magnification between the DMD spectrometer entrance aperture, which was 0.5X.

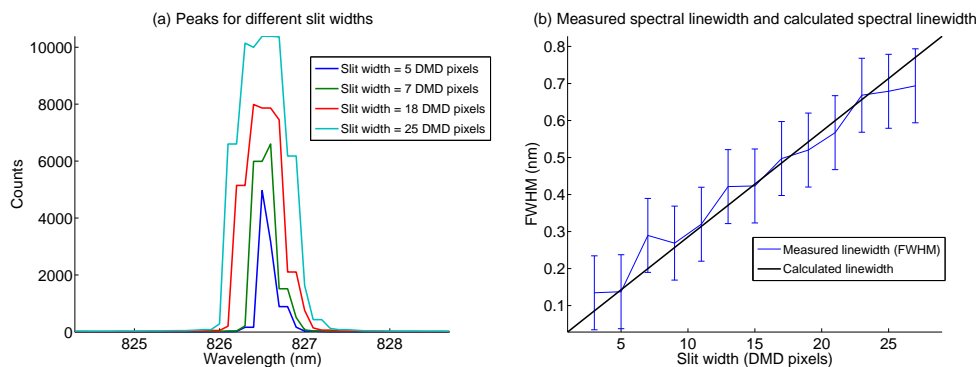


Figure 3.23: (a) are the 826.5 nm peak from the Neon lamp for different possible slit widths, the peaks become broader with increased slit width. (b) shows the measured FWHM of the peaks for different slit widths, the expected spectral linewidth is also plotted on the graph.

For the case of the broadband diffraction grating, Equation 2.28 also applies and the spectral linewidth can be similarly estimated for different slit widths. Slit widths of 5 and 10 DMD pixels give spectral linewidth values of 0.43 nm and 0.85 nm, using the dispersion data from Table 2.28.

When selecting a slit width, the two primary considerations are how the width affects the spectral linewidth of measurement and how the slit width affects the amount

of light collected. In the case of discrete spectral features such as emission lines it is important that the image of the slit on the CCD occupies three CCD pixels to resolve the peak fully, the slit width can be chosen to accommodate this. When a continuous, broadband light source is present the spectral resolution is the smallest element of the spectrum that can be isolated. The system throughput increases with increasing linewidth as expressed in Equation 2.31, as the larger the slit the more light can enter the spectrometer, improving the signal to noise, which will be discussed further in Section 3.7.

3.6 Stray light analysis

Stray light is often defined as any unwanted light present in an optical system. The sources of stray light are many and varied, ranging from unwanted diffraction orders generated by unintentional gratings to scatter from rough surfaces or surface contaminants. Numerous other causes of unwanted light can also occur, depending on the circumstance. Most imaging devices suffer from stray light. Often the signal-to-noise of spectrometers can be limited by the presence of stray light. All these sources occur in the RASI system, with the addition of light scattering from the DMD itself. The goal of this section is to describe the stray light in the system and to help quantify the effect it has, while also demonstrating methods to help mitigate its effects. The other issue that will be discussed is the issue of spectral crosstalk; which arises from the stray light that occurs outside the boundaries defined by the calibration relations.

3.6.1 Sources of scatter

In this section some of the sources of scatter are identified and discussed, the steps taken to reduce their effects are also described.

To help eliminate environmental lights such as from room lights, computer monitors and other erroneous sources of light a light tight enclosure was built around the core RASI setup. Any LEDs (light emitting diodes) on the imaging camera or the DMD driver electronics board were blocked as well, as they would be inside the enclosure. One of the primary sources of scatter was from the DMD itself.

The DMD was much smaller than the maximum FOV of the telecentric lenses, or the microscope that was coupled to it. As a result the telecentric lenses illuminated the DMD active area, including the pond of fixed micromirrors which were permanently switched towards the imaging channel. The telecentric lenses also illuminated the metallic casing around the DMD which caused further unwanted reflections inside the system enclosure. Though since telecentric lenses were used, only light rays which fulfilled the telecentric condition were able to pass through. This helped reduce the affects of any

diffuse reflection from the DMD and stray reflections that did not arrive at the appropriate angles.

Behind the micromirrors was a backplane on which the micromirrors were mounted, this was also a source a source of stray light. Light rays which were incident between micromirrors could scatter under the micromirrors before propagating into the FOV of the re-imaging lens [51]. Light could also scatter from the edges of the micromirrors. Unwanted rays hitting the detector cause a reduction in contrast, which is a phenomenon common to DMD-based systems[23] [92].

3.6.2 Stray light analysis

To help understand the effect of the stray light, a measure of the change in background was recorded at numerous different intensities and integration times and compared to the non-illuminated values. The DMD background was measured by turning all the pixels away from a channel and measuring the values recorded by the detector, a mean value of the whole CCD was calculated to show the dependence of the background on the illumination intensity and to demonstrate that even when all the pixels were switched away from a channel, light scattered from the DMD was still reaching the detector. The results of this are shown in Figure 3.24, the blue dots indicate the background in the absence of all light, that is the light source to the system was switched off. The data was taken at numerous integration times, so the increase was due to the increase in noise associated with the detector for the no-light case. In the ideal case when all the DMD pixels were switched away from the channel, the result should be the same with the light source switched on, as the channel would be effectively switched 'OFF', though with the affects of scatter from the DMD this was clearly not the case. When the light entering

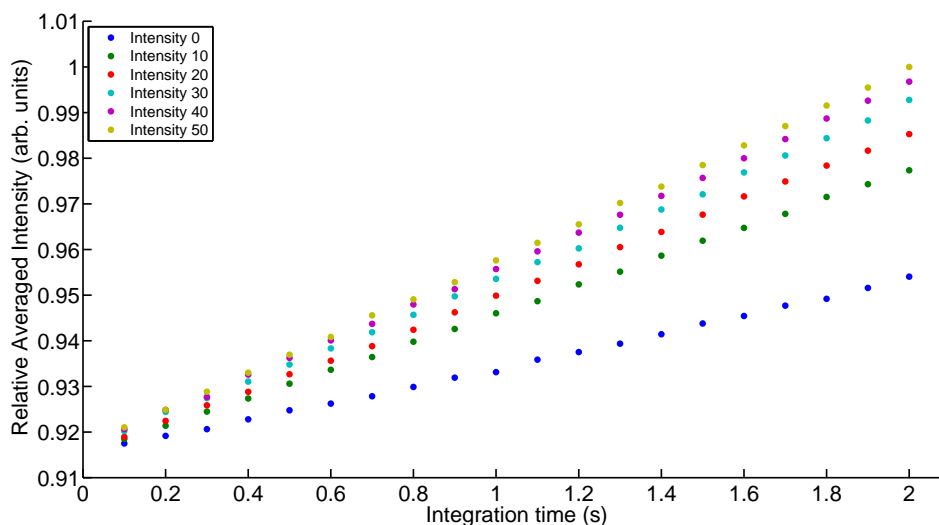


Figure 3.24: Demonstration of the increase in background as the amount of light incident on the DMD increases.

the system was increased, the value of the background increased, clearly showing the amount of scattered light was dependent on the input light, as can be seen from Figure 3.24.

3.6.3 Spectral crosstalk

Another cause for concern was the possibility of crosstalk between adjacent spectra. Crosstalk was light from the one slit affecting the measurement in a nearby slit. The crosstalk was investigated experimentally by opening a single slit, then extracting the spectral information from the spectral track associated with that slit. The spectral track, is shown in Figure 3.25, the counts from inside the track have been removed in software so only counts on the detector that have extended beyond the spectral track are shown. The crosstalk extends at least two CCD pixels above and below the spectral track and is on the order of 0.1% of the number of counts in the spectral track. The extra counts would appear in any spectral track opened adjacent to the track shown in Figure 3.25, and would be ambiguously mixed with the true spectral information from the slit. The scale of the problem is minor and can be easily avoided by allowing vertical space between DMD slits.

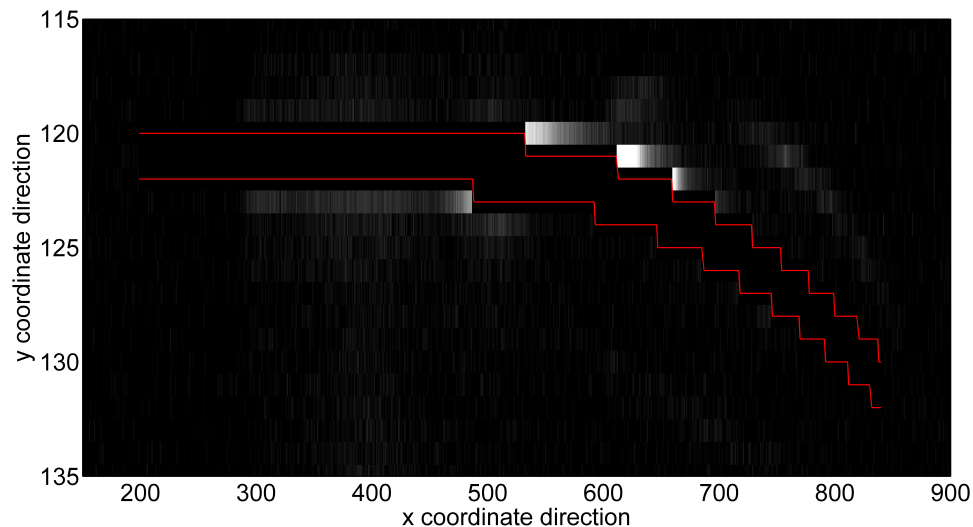


Figure 3.25: Region surrounding a spectral track, the values between the red lines have been set to zero so as to show the spreading of light beyond the lines predicted by the calibration.

3.6.4 Stray light correction

Section 3.6.2 discussed the issue of stray light in the system, demonstrated in Figure 3.24, as a background affect that increases in proportion to the incident light intensity. Since there were no moving parts in the system and the only aspect that changed from measurement to measurement was which directions the micromirrors were switched, it

was possible to treat the stray light as a constant background. In order to correct the background a correction frame could be acquired separately and subtracted from the measurement frame to account for the stray light.

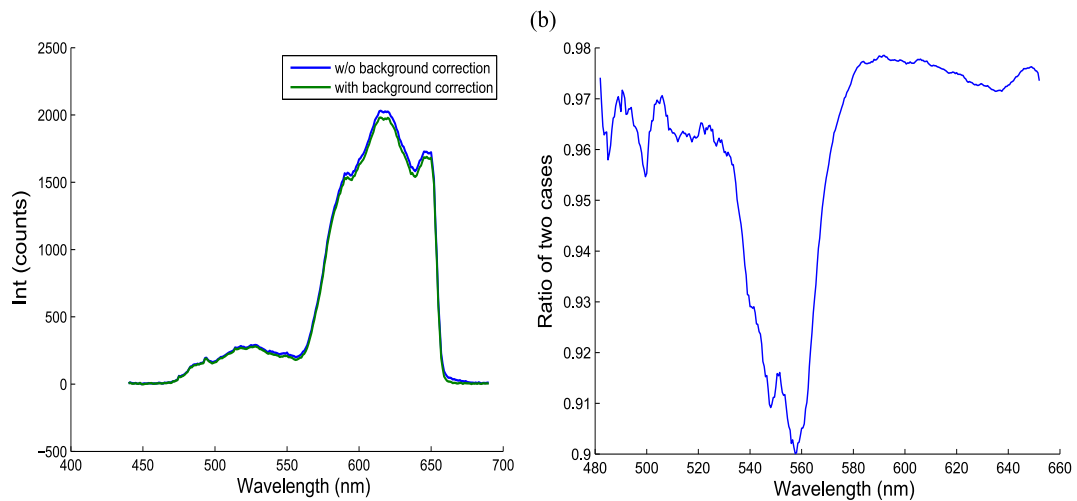


Figure 3.26: (a) shows the spectrum of the light source without the background subtraction and with the background subtracted (b) is the ratio of the two cases, while the difference is relatively small, it is still appreciable.

An example correction is shown in Figure 3.26 (a) where the spectrum of the illuminating light source is shown without a background subtraction correction and with the background subtraction. A ratio of the two is shown in Figure 3.26 (b), showing that there is a noticeable difference caused by the background noise and that it can be corrected, subtracting dark frames is of course a normal procedural element in most spectroscopy so this approach requires no extra processing or steps when determining spectra from the CCD frame.

Background subtraction has been used successfully in other applications where DMDs are used in imaging and spectral imaging systems [85] to mitigate the effects of background scatter from the DMD. More sophisticated methods of quantifying the scatter from DMDs have been employed in the literature for creating a scattering model, though this is still an active area of research [50].

3.7 Signal to noise considerations

The signal-to-noise (SNR) ratio compares the signal to the noise present. Signal in this context are the photons from the object of interest being investigated, whereas photons from stray and scattered light such as those described in the previous sections are considered as noise. Regardless, all photons also contribute Poisson or shot noise, which was why limiting stray light was important. In a CCD other noise sources are the read noise and dark-current noise, which are both intrinsic to the camera.

Read noise is the noise of the on-chip amplifier which converts the electrons to an analog voltage. It can be quantified as

$$\sigma_{RN} = \sqrt{RN^2 n_{pix}} \quad (3.8)$$

where $(RN)^2$ is the readout noise per pixel and n_{pix} is the number of CCD pixels in the measuring aperture. Read noise can be reduced by averaging frames together, which results in an improvement by a factor of the square root of the number of frames averaged.

The other intrinsic noise component is the dark noise, which is a consequence of the generation of thermal electrons termed as dark current, this is described by

$$\sigma_{DN} = \sqrt{DN \times n_{pix} \times t}. \quad (3.9)$$

where DN is the dark current in $e^-/second/pixel$ and t is the exposure time. The dark current can be reduced by employing cooling, which the *Andor Newton* allows, down to -100° C.

The remaining noise characteristic, is the intrinsic photon or "shot" noise of the signal itself. This is described by Poisson statistics. The incident photon flux, say, P given in units of *photons/pixel/second* for convenience where pixel refers to detector pixel not DMD pixel even though the aperture is set by the number of DMD pixels, shot noise is calculated from

$$\sigma_{shot} = \sqrt{n_{pix}(P+B)Qt}, \quad (3.10)$$

where Q is the quantum efficiency which gives the conversion between optical power and electron current generated, B is the unwanted background light including the stray light scattered from the DMD.

The overall signal-to-noise combining the three different noise sources is then

$$SNR = \frac{n_{pix}PQt}{\sqrt{n_{pix}(P+B)Qt + Dn_{pix}t + RN^2 n_{pix}}}. \quad (3.11)$$

The power collected by the system given in the previous chapter was in terms of the numbers of DMD pixels in the aperture, which will set the number of CCD pixels which light will be incident upon, n_{pix} , used in the SNR equation. n_{pix} itself gives the number of pixels in the area of the CCD under consideration, so $n_{pix} = n_x n_y$, which can be related to the number of DMD pixels by the magnification between the DMD CCD camera and the relative sizes of the pixels, which gives 1 CCD pixel as 4.9 DMD pixels in terms of the ratio of lengths. n_{pix} is then given as

$$n_{pix} = n_x n_y = (4.9N_i)(4.9N_j) = 24N_i N_j, \quad (3.12)$$

Combining Equations 3.12 and 3.11 gives

$$SNR = \frac{4.9\sqrt{N_i N_j P Q t}}{\sqrt{(P + B) Q t + D t + R N^2}}, \quad (3.13)$$

which shows the SNR expressed in a discrete form, which can be increased with the number of DMD pixels switched towards the spectrometer. Considering also Equation 2.31 where the etendue and consequently the power are expressed in terms of spectral linewidth, the trade-off in a given measurement between spectral linewidth and SNR can be related.

3.8 Chapter summary

This chapter has given an overview of the experimental realisation of RASI. A summary of the critical components was given, including various key parameters. The construction of RASI was detailed, with a 3D CAD representation of the layout shown and the various construction aspects discussed. Furthermore the construction of a custom microscope was outlined including a description of the Koehler illumination that was made for the microscope. The parameters of the complete imaging arm of RASI, including the geometric calibration process and sample results were discussed, these were used to show a corrected image of the imaging arm. The spectral geometric calibration was laid out in detail, with results from steps in the procedure shown and the accuracy of the approach demonstrated. The system stray light and the issues surrounding it were considered, with an approach for correcting the background demonstrated. Finally the signal to noise of the system was discussed.

Chapter 4 – Demonstration of RASI

4.1 Introduction

The previous chapter described the RASI instrumentation and the calibration procedure for it, this chapter gives examples of spectral imaging using RASI; with a first example showing the basic operating principle, that of a multi-object spectrometer on a static scene. The primary focus of this chapter is on a novel example of dynamic spectral imaging where the evolution of the absorption spectrum (due to de-oxygenation) of moving red blood cells (RBCs) is monitored. A description of the problem background and the experimental method are given, along with the details of spectral unmixing techniques used to quantify the change of the RBC spectrum.

A further consideration in this chapter will be countering the affects of spectral overlap in the spectrometer detector plane. Examples of correcting the overlap are given using modified linear spectral unmixing methods; potential methods of removing the overlap physically are also discussed.

4.2 Core operation

The basic operation of the RASI device involves the switching of individual pixels or groups of pixels, in the form of slits, towards the spectrometer, based on the reference information obtained from the imaging channel; all applications of RASI can be described as variations in the distributions and size of the slits across the DMD and between time-sequential frames.

This section describes a static example where a microscope slide with a histological sample was imaged; the slide contained a stained sample of a section of tongue taste-buds (Histological slide number: H0505). The purpose of this section is to give an example of the operation of RASI as a multi-object spectrometer, before describing the more complex example of dynamic spectral imaging in the sections that follow.

The DMD modulation frame and the image of the scene, with a line connecting the areas switched towards the spectrometer are shown in Figure 4.1 (a) and (b) respectively. The DMD modulation frame contains the slit sizes and positions, it represents the input aperture to the spectrometer, the slit positions were chosen so as to follow the contour of the white portion of the image. A CCD frame with the dispersed spectra from the different apertures is shown in Figure 4.2 (a); example line profiles for the transmitted and reference spectra are shown in Figure 4.2 (b), which were extracted using the calibration relations developed in the previous chapter. In order to calculate the transmission spectrum for each slit the dispersed spectrum was recorded at each point with the sample

in place and a reference spectrum for the illumination was taken with the slide removed, the transmission was then calculated using

$$T(\lambda) = \frac{I_{tr}}{I_{ref}}, \quad (4.1)$$

where I_{tr} was the spectra measured passing through the sample and I_{ref} the reference measurement without the sample present. Equation 4.1 was used to determine the transmission profile for each slit positions, four of which are shown Figure 4.3.

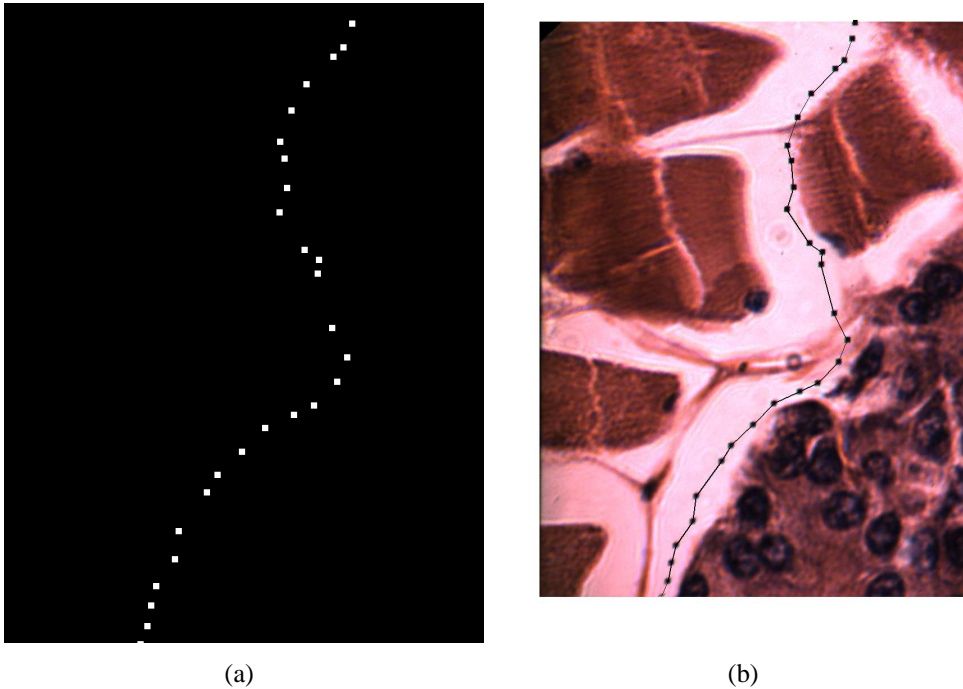


Figure 4.1: (a) is the modulation mask on the DMD (b) is the resultant, corrected image frame with a line drawn between the various apertures corresponding to the switched DMD pixels, the physical size of the sample shown is $80 \times 60 \mu\text{m}$, the same size as the RASI FOV.

This section provides a basic example of the operation of RASI, any arbitrary DMD modulation frame can be created and used to extract spectral information from a given scene. In this case, points were chosen so as to avoid spectral overlap, which will be considered later. It is also possible to recreate the affects of spatial scanning hyperspectral imaging instruments, a long slit approach can be taken where a slit the length of the DMD array can be created, then by scanning its position across the DMD the effect of a pushbroom scanner can be created. Potentially, it could scan the whole device field of view in $\frac{768}{W}$ measurements, where W is the width of the slit and 768 is maximum width of the DMD itself in terms of DMD pixels. The slit sizes can be downsized to suit different applications as well, so multiple smaller slits could be scanned across the FOV in different directions and in parallel. In situations where the

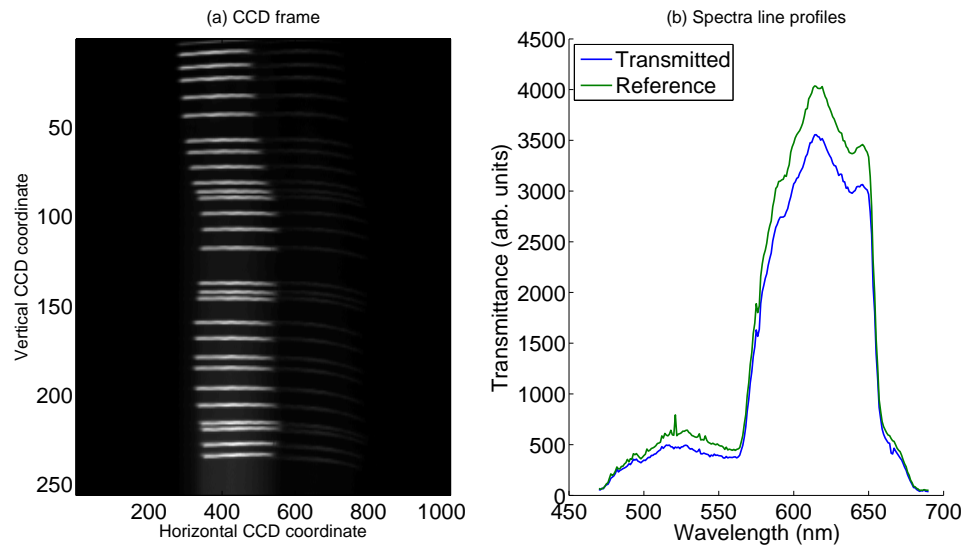


Figure 4.2: *The dispersed spectra on the CCD and the line spectra from a case of the reference spectra and the transmittance spectra*

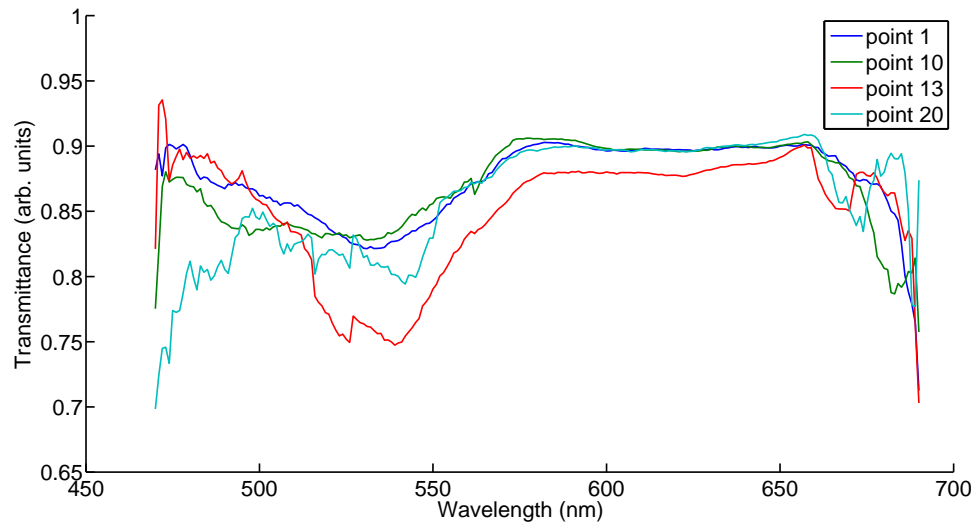


Figure 4.3: *Transmission profiles from four of the slit positions from which spectra were collected and calculated using Equation 4.1.*

scene is static, statistical sampling methods can be used to extract a subset of voxels from the scene to make inferences about the whole scene by exploiting the similarity between groups of pixels, two examples of this will be discussed in the next chapter for examples of random sampling and grid based sampling.

4.3 Red blood cell experiment

Prior to spectral imaging of the red blood cells (RBCs) it is appropriate to introduce some of the background elements and to motivate the study of RBCs. This section will describe previous work investigating the optical properties of RBCs and describe the advantages spectral imaging could offer to help improve upon current methods.

Additionally the absorption spectrum of oxygenated and de-oxygenated blood will be shown, further the change of RBC absorption spectrum will be derived in the form of a linear unmixing problem.

4.3.1 Red blood cell background

RBCs (also referred to as erythrocytes) are the means by which human and other mammal bodies transport oxygen around the circulatory system. The RBCs collect oxygen in the lungs and deposit it in tissue and other organs while being squeezed through capillaries, resulting in de-oxygenation of the RBCs. Whole blood consists of a mix of RBCs, plasma and platelets, the term hematocrit refers to the percentage of RBCs present in a sample of whole blood. The RBCs themselves are biconcave in shape with an approximate diameter of $7\ \mu\text{m}$ and an approximate thickness ranging from $2.5\ \mu\text{m}$ at their edges to $1\ \mu\text{m}$ at the centre. The RBCs have a flexible membrane, which allows them to squeeze through capillaries - which can often have diameters of $3\ \mu\text{m}$ - and allows the diffusion of oxygen into and out of the RBC. Inside the cell, oxygen binds to a protein called hemoglobin (*Hb*), resulting in oxygenated hemoglobin (*HbO₂*), the ratio of *Hb* to *HbO₂* determines the optical absorption of the cell [60].

The characteristics of blood can be used as a means of investigating the health of a patient. A measure of the hematocrit for example can be used as an indicator of health, a low hematocrit count is a sign of poor health though the number of possible causes are many. The optical properties of blood can be used to help in this regard, and can provide many useful insights as the spectra of a bulk sample is a combination of the spectra of all the constituents. This principle is often employed in clinical applications for the detection of drugs, disease monitoring and assessing the health of a patients RBC count. In particular the oxygenation of the blood is of interest as a metric that has been employed in characterising the health of blood. Blood oxygenation can be calculated from spectral measurements and can be measured quite readily in patients using a pulse oximeter, which uses two wavelength oximetry [127].

In microscopic studies of blood samples, the properties of the individual cells can be considered. The morphological features of the cells, such as the size, can indicate vitamin deficiencies, for example larger RBCs can indicate a vitamin B12 deficiency and smaller sized RBCs can indicate an iron deficiency [97]. Abnormalities in the shape of RBCs are also a useful indicator; crescent shaped RBCs are characteristic of sickle cell anemia [82] and teardrop shaped cells can indicate myelofibrosis and thalassemia [48]. These morphological deviations in the individual cells provide extra information over testing on bulk samples, this is exploited using observations of the blood smears under high magnification and is common practice in many clinical settings. Such observations are made possible by the ubiquitousness of imaging microscopes and the relative ease

with which the shape of RBCs can be identified. The spectral properties of individual RBCs are not employed to the same extent, as the means of determining the spectra of a small microscopic regions of a sample is rare in clinical settings, standard spectrometers are used on bulk samples more frequently.

The advantages of spectral imaging have been studied in the literature and various systems have been applied to cases where static RBCs were investigated. Standard hyperspectral approaches that use a series of monochromatic wavelengths to build up a full hyperspectral datacube time-sequentially are used in [86]. Here, the spectrum of various RBCs were studied under different conditions, including being infected with *Plasmodium falciparum* parasites resulting in an observably different spectrum. The use of optical tweezers has also been used to facilitate the spectroscopy of individual cells [5]. This has been applied very successfully in combination with Raman spectroscopy [8]. However, with optical tweezing, there is a possibility of causing damage to live biological samples due to the power or wavelength of the trapping lasers [126]. These approaches are all enabled by controlling the position of the cell. However, limiting the motion of cells by physical or chemical means can change the spectral properties of the sample [129].

The goal of applying RASI to the problem of microscopic RBC spectral imaging is to combine the advantages of spectroscopy with the dynamic imaging advantages already enjoyed by standard microscopes, while also avoiding the problems of approaches described above. Other spectral imaging devices are limited by the trade-offs that limit spectral-spatial resolution and the need for time-resolved spectral imaging as already described. RASI can be used to simultaneously measure the spectrum of multiple RBCs and track their positions visually across the FOV of RASI. In the experiment that will be described in the following sections the oxygenation of RBCs will be changed and the evolution in the characteristic absorption spectra shown, using spectral unmixing techniques.

4.3.2 RBC absorption

The calculation of the absorption spectrum of a single RBC requires consideration of the Beer-Lambert law, which describes the absorption of light in a heterogeneous non-turbid medium with a wavelength dependent absorption coefficient, given as

$$I(d) = I_0 10^{-\epsilon dc}, \quad (4.2)$$

where $I(d)$ is the optical power at depth d and I_0 is the optical power incident on the medium. ϵ is absorption per unit volume per unit distance, d is the depth of the measurement and c the concentration per unit volume. The ratio $\frac{I(d)}{I_0}$ is the transmission

as defined in Equation 4.1. Absorbance (A) can then be determined from

$$A = -\log(T) = -\log\left(\frac{I(d)}{I_0}\right). \quad (4.3)$$

Figure 4.4 shows the characteristic spectrum of hemoglobin in the range from 500 nm

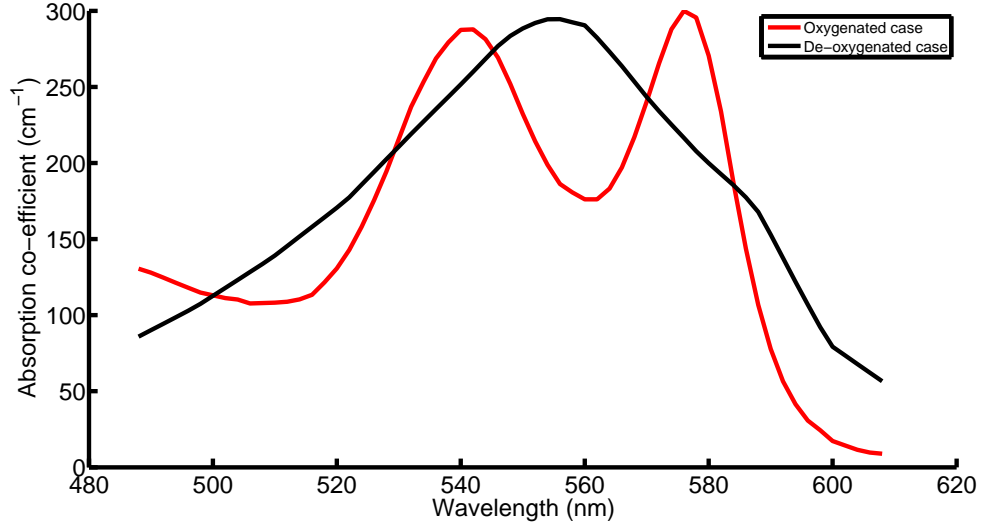


Figure 4.4: Spectral absorption profile of blood from 500 to 630 nm [103]

to 630 nm, the data is taken from an online source [103] that is commonly used as a standard for the absorption spectra of blood. The spectrum of hemoglobin shows two strong absorption features in its absorption spectrum in this region in the oxygenated state, which transition to a single feature during de-oxygenation. This spectral range is the focus of the experiments performed in this thesis, as the light source used for illumination has a spectral output that covers this region.

The absorption spectrum of the RBC corresponds to the oxygenated spectrum in Figure 4.4 when the RBC contains only HbO_2 , when it contains only Hb its spectrum corresponds to the deoxygenated spectrum, the red and black curves respectively. Combining Equations 4.2 and 4.3 the absorbance can be written in general as

$$A = \epsilon dc, \quad (4.4)$$

where the parameters are as before.

Given that a RBC has a mix of Hb and HbO_2 , the total concentration of the two components can be expressed as the sum of the relative concentrations of oxygenated (c_o) and de-oxygenated (c_{do}) hemoglobin multiplied by the total weight per volume of Hb present, de-noted as W . The relative concentrations have the sum-to-one property

$$c_o + c_{do} = 1, \quad (4.5)$$

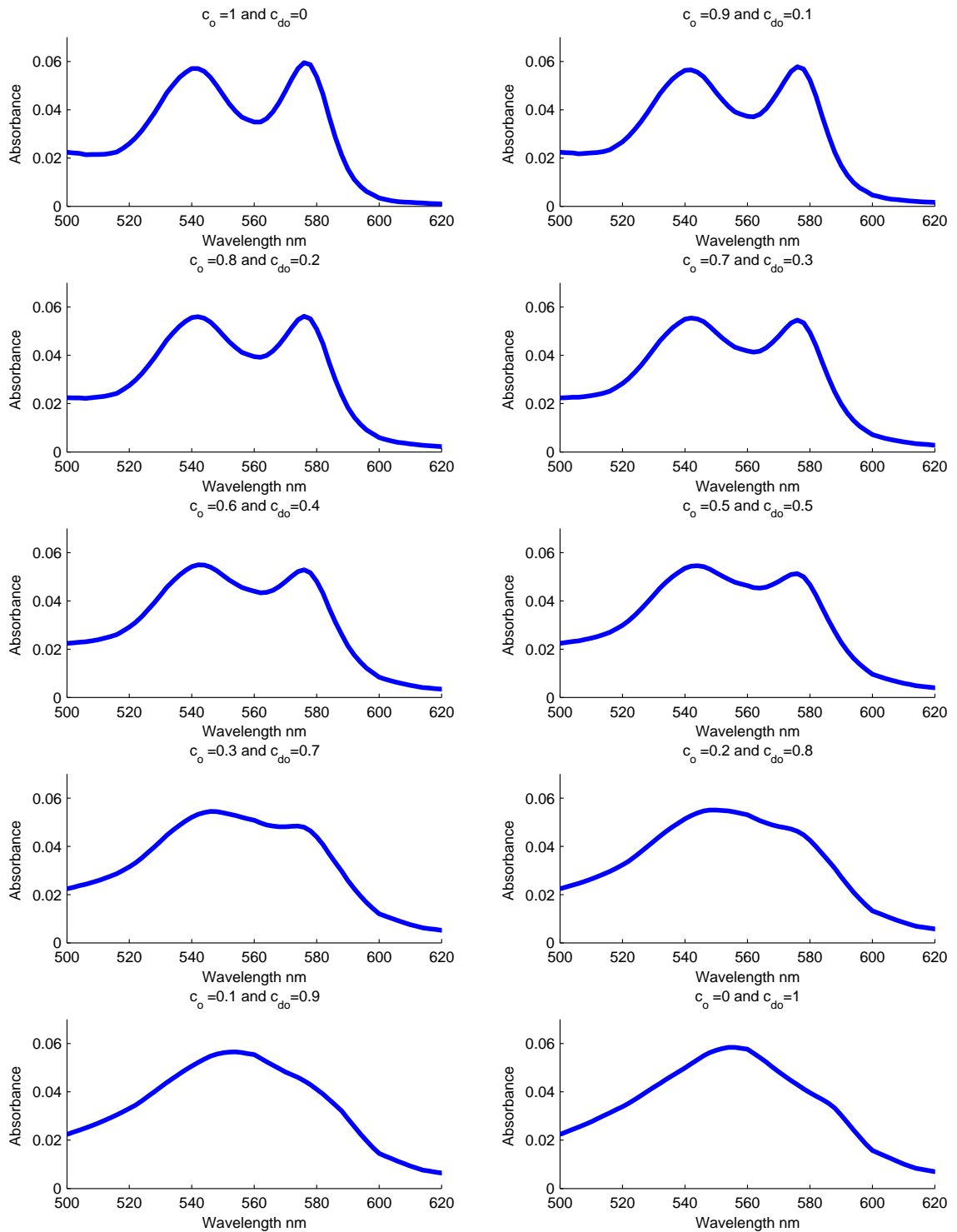


Figure 4.5: Change in spectra with different concentrations of Hb and HbO₂

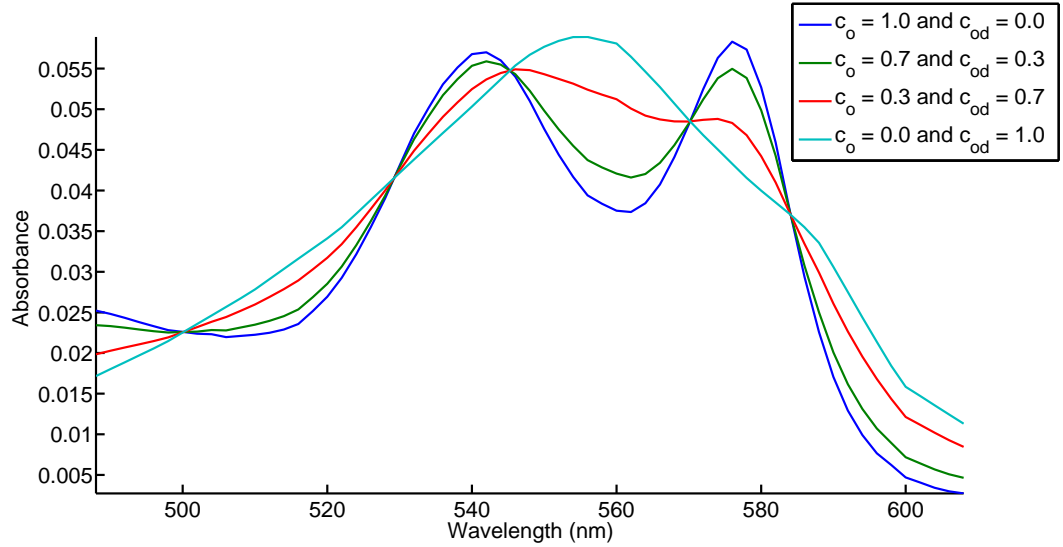


Figure 4.6: Various concentrations plotted on the same graph

and the two constituents have different absorptive co-efficients ϵ_o and ϵ_{od} . Considering these factors the Beer Lambert law can be re-written as

$$\frac{I(d)}{I_0} = 10^{-(c_o W \epsilon_o + c_{od} W \epsilon_{od})d} = 10^{-W(c_o \epsilon_o + c_{od} \epsilon_{od})d}, \quad (4.6)$$

with the absorbance then becoming

$$A = W(c_o \epsilon_o + c_{od} \epsilon_{od})d. \quad (4.7)$$

Then considering the form and noting that ϵW can be combined into a single absorption coefficient $\alpha = \epsilon W$, the fully oxygenated absorbance case can be written as $A_o = W \epsilon_o d$, with $c_o = 1$, which can be generalised as

$$A_o = c_o W \epsilon_o d = c_o \alpha_o d. \quad (4.8)$$

Similarly the de-oxygenated case can be represented as

$$A_{do} = c_{do} W \epsilon_{do} d = c_{do} \alpha_{do} d. \quad (4.9)$$

Equations 4.8 and 4.9 then allow the absorption spectrum of a single RBC, or other mix of Hb and HbO_2 to be written as a linear sum of the two constituents in the form

$$A = c_o \alpha_o d + c_{do} \alpha_{do} d = c_o A_o + c_{do} A_{do}. \quad (4.10)$$

Equation 4.10 describes the problem of determining the concentration of Hb and HbO_2 as a problem of linear spectral unmixing. The effects of change of the relative concentrations are emulated in Figure 4.5, the absorbance is plotted with an assumed thickness of $d = 2 \mu m$, modeling the expected change in oxygenation spectrum. The spectra

associated with different concentrations are also shown in Figure 4.6, clearly visible are the so called isobestic points where values of $\alpha_o = \alpha_{od}$. The mixed model of Hb and HbO_2 have historically been used in the field of blood oximetry. The system of equations is solvable with only two wavelengths, though in principle a better solution should be possible with more wavelengths. Two wavelength oximetry forms the basis of various devices that determine oxygenation such as the pulse oximeter that has been mentioned previously.

4.4 Dynamic spectral imaging of RBCs

The previous section discussed the interest in the optical characteristics of blood and the works described in that section refer to the study of bulk samples or microscopic static or trapped RBCs. The absorbance was also described using the Beer-Lambert law and expressed in a manner amenable to the application of linear spectral unmixing techniques. This section describes the experiment where RASI is applied to the spectral imaging of RBCs. The experiment performed imaged a dilute solution of blood cells, a tracking algorithm was used to determine the positions of the RBCs and the calibration functions related the image coordinates to DMD pixel indices (i, j) . Slits were created on the blood cells at these coordinates to act as apertures to the spectrometer. The spectral information from these was recorded on the spectrometer camera and saved, along with the output from the imaging channel. The dilute solution was also mixed with a chemical called sodium dithionite. This is a reagent commonly used to de-oxygenate HbO_2 , as a consequence the spectrum of the RBCs changed over time, similar to the change in spectrum shown in Figure 4.5. The following sections explain the various aspects of the experiment in more detail.

4.4.1 Tracking algorithm

One of the key elements of this experiment was the ability to track the positions of the blood cells on the imaging channel, as the positions of the slits generated to extract the spectral information needed to be adjusted according to the motion of the blood cells. While tracking algorithms consist of a large body of work, they are often difficult to implement and require the use of efficient coding paradigms, such as C or C++. Tracking of blood cells has often been implemented in post processing scenarios after a video has been taken [64][74], not during acquisition as in this case.

In this application the process required the position of the RBC to be constantly updated in real-time, while also allowing for the other hardware that comprise the RASI system to be updated as well. Another source of overhead in the approach was updating the DMD. The array was controlled by sending black and white *.bmp* images of $1024 \times$

768 pixels to the DMD, each colour corresponding to a DMD mirror tilt state, which had to be generated for every set of updated coordinates. This was a significant source of overhead, as due to the speed of transfer across the USB and subsequent display on the DMD itself the actual rate at which frames were displayed was 1 frame per second. It was possible to speed this up by a factor of 10 by converting the *.bmp* files to binary (*.bin* format) prior to transfer. This could be accomplished by use of a function that was part of the ActiveX library controls on the DMD control board, however the conversion itself was also quite time consuming. So while this was a viable approach if it was possible to have a set of pre-generated patterns to convert prior to uploading to the board, it was not particularly useful when rapid pattern generation and upload was required.

To assuage this issue it was decided to create a piece of custom code to generate the necessary *.bin* files. A blank *.bin* file of size 128 columns and 768 rows was created. This was used as the template *.bin* file. Noting that $1024/8 = 128$, each position in the *.bin* contained a symbol representing an 8 bit number. Each bit corresponded to a single micromirror and the value placed there, either a 1 or 0, determined the direction the corresponding micromirror was switched. The goal of the code was to take DMD micromirror indices (i, j) , use them as a reference to insert the appropriate bit value in the correct position in the *.bin* file. Using this approach, a slit or multiple slits could be created, each with a set length and width and one of the slit corners corresponding to the input DMD indices. The details of the code represent a rather tedious problem of indexing an array, but are otherwise straight forward. Once the indexing was completed, the edited template file was saved, this was what was uploaded to the DMD and displayed. Part of the display overhead was converting the *.bmp* to a *.bin*, this approach sped up the process, furthermore it removed the need to generate a large 1024×768 array and turn it into an image file, instead it directly turned coordinates into a *.bin* files to upload. This custom script was written in Matlab and integrated into a larger Labview program that controlled the overall process.

The hardware that comprised RASI was all controlled via Labview, once the custom script for generating DMD display patterns was created and it was deemed feasible to perform this experiment at a reasonable frame rate it was decided to develop a tracking algorithm within the Labview environment. Attempts were made at a rigorous tracking algorithm, that would target a particular blood cell and track its motion as long it remained in the field of view. While this was achieved it required the user to set initial conditions to be effective. Also, as the blood cells were in motion they often quickly passed from the field of view, the algorithm then required a new target and set of initial conditions. A more free form approach was finally taken, using the pattern matching functionality of Labview. Template images of blood cells were obtained, then an algorithm was created that searched each frame for a number of best matches to the template. Due to the similarities between blood cells, most of the RBCs in a given frame

constituted a good match to the template image. So by searching for the ten best matches, it was possible to extract spectral information from the various blood cells in a scene. The approach had limitations, but these could be accounted for by making adjustments to the number of best matches required. Also by diluting the solution of blood so as to reduce the likelihood of a large number of blood cells in the field of view at any time it was possible to perform the experiment with ten blood cells moving across the FOV without it being overcrowded with RBCs.

The approach employed in the tracking algorithm allowed a large amount of data to be collected, also it required very little user interaction. Once the experiment was completed it was then possible to process all the data from the tracking to construct a coherent overview of the spectra of all the spectrally interrogated blood cells.

4.4.2 *De-oxygenating RBCs*

In this experiment the conversion of HbO_2 to Hb in RBCs was achieved via the use of sodium dithionite, ($Na_2S_2O_4$). The use of sodium dithionite as a de-oxidising agent for HbO_2 is well established, certainly in the case of bulk blood sample measurements. The interaction of sodium dithionite with whole blood and subsequent oxygen release is quite complex, however it does not affect the integrity of the cell. The de-oxygenation occurs as a result of the diffusion of oxygen through the layers of the cell membrane, the rate of de-oxygenation has been shown to be dependent on the concentration of external sodium dithionite present, the pH of the solution is also a factor. The half life, that is the time taken for the concentration of oxygen to decrease to half its initial value has been shown to be on the order of hundreds of milliseconds for high concentrations [120]. A linear relationship between sodium dithionite concentration and change in oxygen saturation over a time scale of sixty minutes has been shown to exist [17].

The previous descriptions of interactions of sodium dithionite relate to bulk measurements, it has been studied similarly as a reducing agent [115]. It has also been successfully used as a de-oxygenation agent in microscopic scale spectroscopy experiments [105], in a manner similar to what was applied in this experiment.

4.4.3 *Aperture consideration*

Due to the biconcave structure of the RBC, the path length of light through the RBC was different at different points along the slit, this resulted in a different value of d associated with different positions along the slit. To improve the spectra, the slit was averaged along the spatial direction, however due to the different thickness at each point in the slit, the interpretation of the resulting averaged spectrum needed to be considered.

The absorption for a given row along the slit is given by Equation 4.4. A repres-

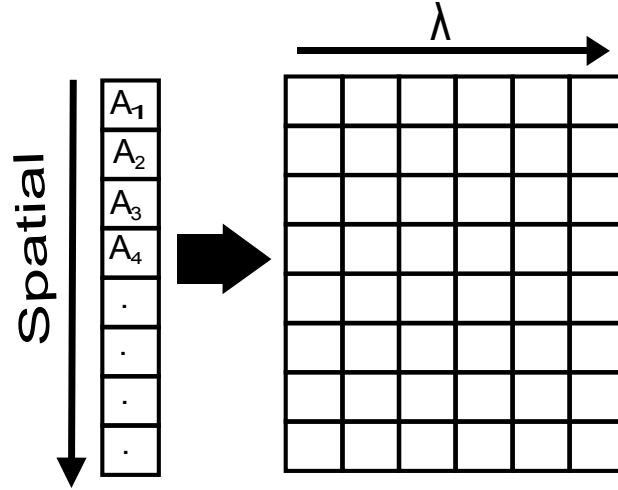


Figure 4.7: Slit overview; absorption spectra are average along the spatial direction of the slit to improve performance.

entation of the slit is given in Figure 4.7, averaging the slits along the columns for a slit of length N gives

$$\langle A \rangle = \frac{1}{N} (c_1 \varepsilon_1 d_1 + c_2 \varepsilon_2 d_2 + \dots + c_N \varepsilon_N d_N) \quad (4.11)$$

where c_i is the concentration, d_i is the depth and ε_i associated with a pixel i . Then relating the averaged absorbance to the relative concentrations:

$$\langle A \rangle = \frac{1}{N} \sum_{i=1}^N c_i \varepsilon_i d_i \quad (4.12)$$

$$\langle A \rangle = \frac{1}{N} \sum_{i=1}^N (c_{oi} + c_{odi}) W_i \varepsilon_i d_i \quad (4.13)$$

$$\langle A \rangle = \frac{1}{N} \sum_{i=1}^N (c_{oi} + c_{odi}) \alpha_i d_i \quad (4.14)$$

where $\alpha_i = W_i \varepsilon_i$ is associated with a pixel i , c_{oi} and c_{odi} describe the relative concentrations of Hb and HbO_2 associated with a given pixel i . Equation 4.15 can be re-written as

$$\langle A \rangle = \frac{1}{N} \alpha_o \sum_{i=1}^N c_{oi} d_i + \alpha_{od} \sum_{i=1}^N c_{odi} d_i. \quad (4.15)$$

Which, by considering that in each case the maximum value of c_{oi} and c_{odi} is 1. The maximum possible value of $\sum_{i=1}^N c_{oi} d_i$ and $\sum_{i=1}^N c_{odi} d_i$ occurs where all the values of $c_o = 1$ or $c_{od} = 1$, respectively $\forall i$. This then allows these summations to be expressed as a fraction of the maximum value so that:

$$\sum_{i=1}^N c_{oi} d_i = k_o \sum_{i=1}^N d_i \quad (4.16)$$

$$\sum_{i=1}^N c_{odi}d_i = k_{od} \sum_{i=1}^N d_i \quad (4.17)$$

where k_o is the fraction associated with oxygenated concentration and k_{do} is the fraction associated with the de-oxygenated concentration. Rearranging Equations 4.16 and 4.17 above allows the values of k_o and k_{do} to be interpreted as

$$k_o = \frac{\sum_{i=1}^N c_{oi}d_i}{\sum_{i=1}^N d_i} \quad (4.18)$$

and

$$k_{od} = \frac{\sum_{i=1}^N c_{odi}d_i}{\sum_{i=1}^N d_i}. \quad (4.19)$$

The values k_o and k_{od} represent the weighted sum of the contribution of the individual concentrations associated with each individual depth. The concentrations are weighted according to depth of each measurement, so a shorter path lengths have a smaller contribution than a longer one. Using these values the averaged absorption can be expressed in the form

$$\langle A \rangle = k_o \frac{\sum_{i=1}^N d_i}{N} \alpha_o + k_{od} \frac{\sum_{i=1}^N d_i}{N} \alpha_{od}. \quad (4.20)$$

The term $\frac{\sum_{i=1}^N d_i}{N}$ is the average of all the path lengths along the slit, denoting it as d_{avg} , a convenient equation is achieved such that

$$\langle A \rangle = k_o d_{avg} \alpha_o + k_{od} d_{avg} \alpha_{od} = k_o \langle A \rangle_o + k_{od} \langle A \rangle_{od}, \quad (4.21)$$

this has the same form as Equation 4.10 and represents a weighted oxygen concentration for an average path length through the blood cell. The utility of Equation 4.21 is that it has a form amenable to a linear unmixing model, which is required for applying linear spectral unmixing algorithms to the data acquired.

4.4.4 Sample preparation

A buffer solution was used to dilute whole blood taken from a large mammal, a horse in this case. The container with the blood was mixed by inverting it numerous times before blood was extracted. The blood was then diluted 40:1 with the buffer solution. A separate solution of a mix of sodium dithionite and buffer solution was also prepared. The concentration of sodium dithionite was chosen so as to de-oxygenate the blood sample over the course of a few minutes.

4.4.5 *Experimental procedure*

The experimental procedure was automated as much as possible with Labview. Once the samples were prepared, sodium dithionite was mixed with the blood solution. Then a pipette was used to place a sample on a microscope slide and placed in the microscope sample holder. The tracking algorithm then tracked the motion of the RBCs as they moved across the field of view of the system. Once 5 minutes had passed and the sample could be reasonably expected to be de-oxygenated, the tracking process was ended and a number of dark frames were taken to account for background illumination effects. The sample of blood was then removed and another microscope slide was placed in the image plane, this held a sample of the buffer solution used to dilute the blood and sodium dithionite solutions described previously. The next part of the experiment involved extracting the reference values to be used to determine the transmission values and subsequent absorbance, supplying the I_0 term from Equation 4.3. During the course of the tracking the positions on the DMD were recorded, so the references were determined by repeating all the measurements from the tracking algorithm with the buffer solution slide in the microscope object plane. This also accounted for any potential local variations in the uniformity of the illumination system; by having the buffer solution sample in the reference measurement the transmission effects of the solution and glass slide were also accounted for, simplifying the calculation. Once this process was completed further background dark frames were taken for the reference measurements.

4.4.6 *Data post processing*

The tracking data collected extends over the course of minutes, however in this time numerous RBCs pass in front of the device FOV, as when the sample is placed in the microscope sample holder the RBCs are in motion due to being mixed and moved. It is necessary to select from the large data set periods when RBCs were successfully tracked crossing the FOV. The conditions for this merely required that blood cells to be moving at a speed that the software could keep up with and slits were successfully generated on the RBCs. The selection was done in a supervised manner to determine time periods which correspond to these conditions. Once a time period was selected, the spectral data was extracted for the tracked RBCs and their paths mapped out, the paths of motion for the individual cells are shown in Figure 4.8.

In the time period selected ten RBCs were successfully tracked and their spectra recorded as they underwent de-oxygenation, the spectra from each of the tracked RBCs was averaged along the slit and the resulting averaged absorbance was obtained, as expressed in Equation 4.11. Averaging along the slit improved the signal to noise of the spectra and also allowed the spectra from each RBC to be expressed as a line profile which simplified representation and analysis. The resulting line spectra were also

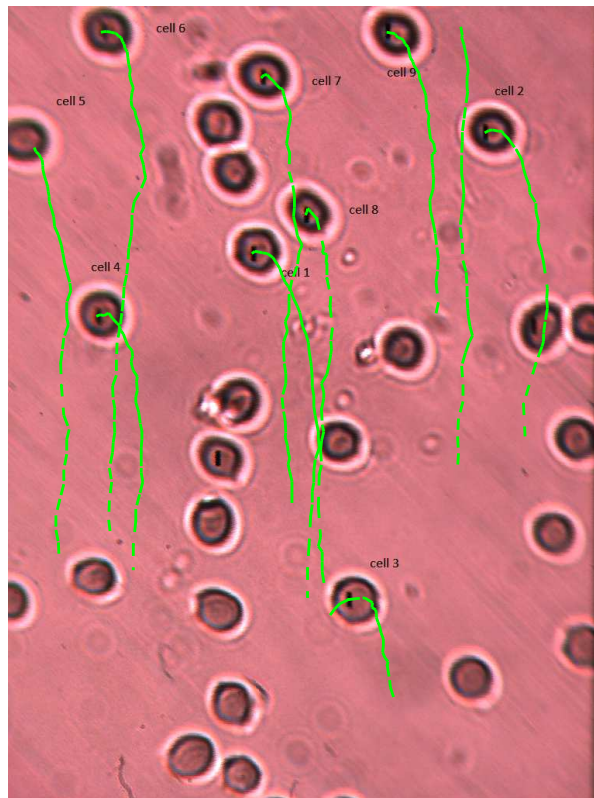


Figure 4.8: Initial frame of the tracking process, the paths followed by the individual cells that were track are plotted over the image in green. The image is the size of the RASI FOV, so $80 \times 60 \mu\text{m}$.

smoothed using a moving average filter to further improve the spectra. An example of the calculated absorbance (optical density) for one of the tracked cells, referred to as cell 1, is shown in Figure 4.9, the absorbance for different times in the de-oxygenation process is plotted, it can be compared to the expected absorbance previously calculated for Figures 4.5. The shape of the spectrum changes in line with expectation, though the baseline of the spectra does fluctuate over the course of evolution, resulting in the offsets between the spectra seen in the graph. The full evolution of cell 1 over time is shown Figure 4.10, where the change in the spectrum from the two distinctive peaks in the oxygenated spectrum to the single peak of the de-oxygenated spectrum is observable, verifying the de-oxygenation of the RBC.

The spectra of the 9 other tracked cells are shown in Figure 4.11, each graph shows a subset of the spectra obtained at different points in the tracking process, sufficient spectra were chosen to show the different steps in the spectral evolution of each cell. The spectra have the shape of the RBC absorption spectra, though each undergoes a different degree of de-oxygenation, which is visible from the different final spectra for the different cases, for example cell 10 has final spectrum with the single peak de-oxygenated peak while spectra for cell 3 changes from the 2 peak oxygenated case to a flat spectrum, indicating some intermediate de-oxygenated state.

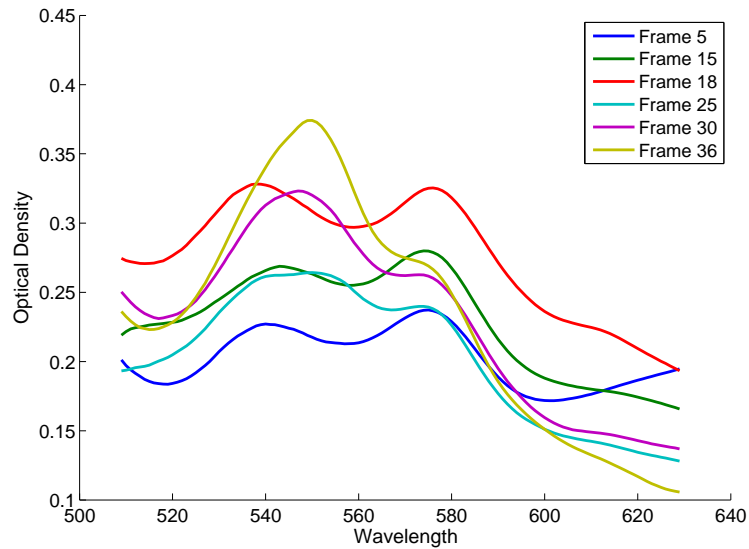


Figure 4.9: The averaged absorption (Optical density) spectra from various frames in the tracking of cell 1. The spectrum evolves from the two distinctive absorption peaks of an oxygenated RBC to the single peak of a de-oxygenated RBC, demonstrating the de-oxygenation of the RBC.

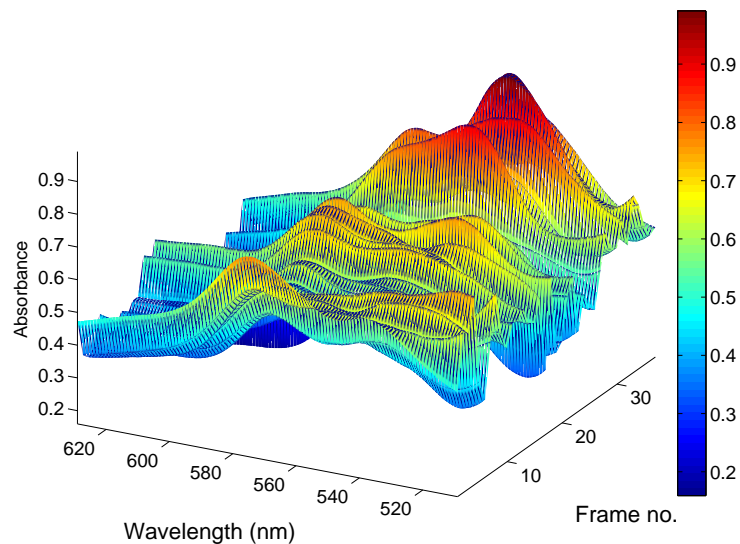


Figure 4.10: 3D representation of the change in absorption spectra over time from cell 1, showing the spectrum from each frame obtained in the tracking process, including those shown in Figure 4.9 above.

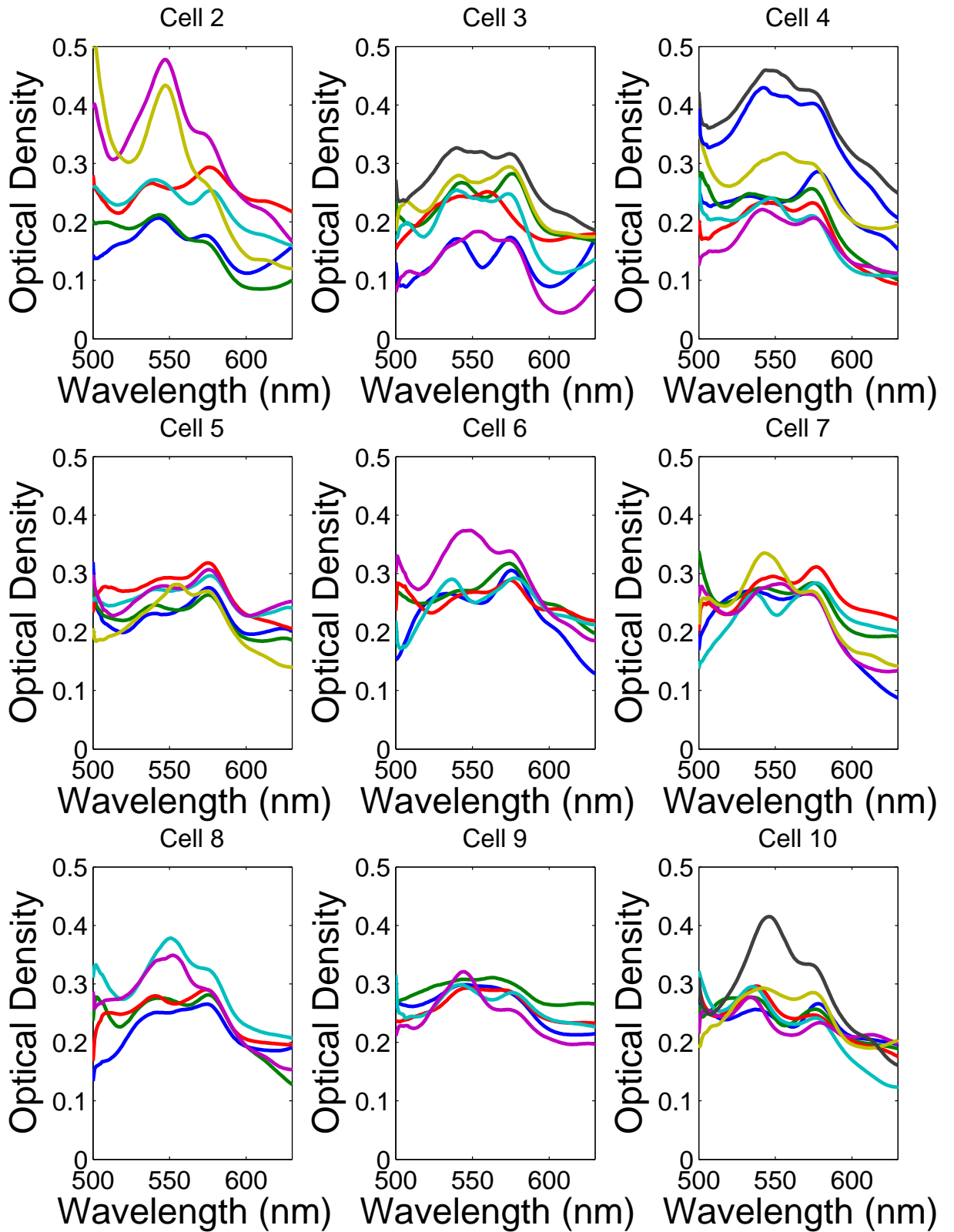


Figure 4.11: Averaged line spectra from numerous frames for each of the 9 other cells tracked. Each of the different cells spectra change, though by the end of the tracking process the degree of deoxygenation is different for each of the cells, as is evident from the shape of the spectra in each case.

4.4.7 Spectral unmixing analysis

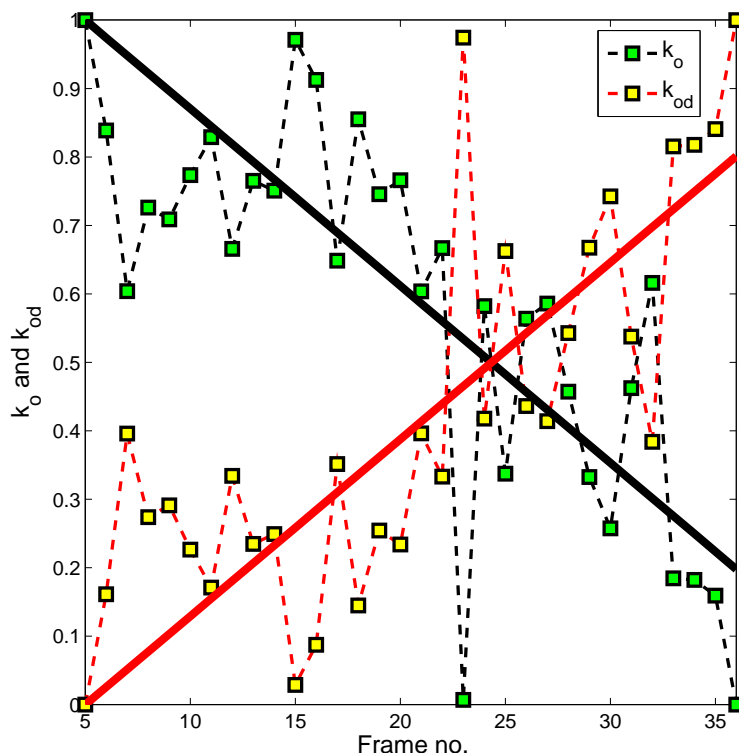


Figure 4.12: Unmixing results from cell 1, showing the de-oxygenation of the RBC from a state of oxygenation to the de-oxygenated state. Two trend lines are plotted over the change in values for the two co-efficients, k_o and k_{od} . A single erroneous point is present in the evolution, representing a spectra with a higher degree of de-oxygenation than the points before and after.

The background and underlying principles of spectral unmixing were described in Section 1.4.2, this section will describe the necessary steps to unmix the spectral data acquired from the RBCs and comment on the results. Spectral unmixing of the spectra in Figures 4.9 and 4.11 requires solving Equation 4.21 for the values of k_o and k_{do} . This required two exemplar or endmember spectra to substitute for the values of $\langle A \rangle_o$ and $\langle A \rangle_{od}$, the spectra acquired from frame 5 and frame 36 in the tracking of cell 1, visible in Figure 4.9, were set as the fully oxygenated and fully de-oxygenated cases, respectively. The spectra from the two frames were chosen as they were sufficiently similar to the expected form of the two states, which were shown in Figure 4.5, and thereby provide suitable start and end points for mapping the evolution of each cell.

The matrix notation form of Equation 4.21 allows the absorbance (or optical density) to be written as

$$\hat{a} = Ak, \quad (4.22)$$

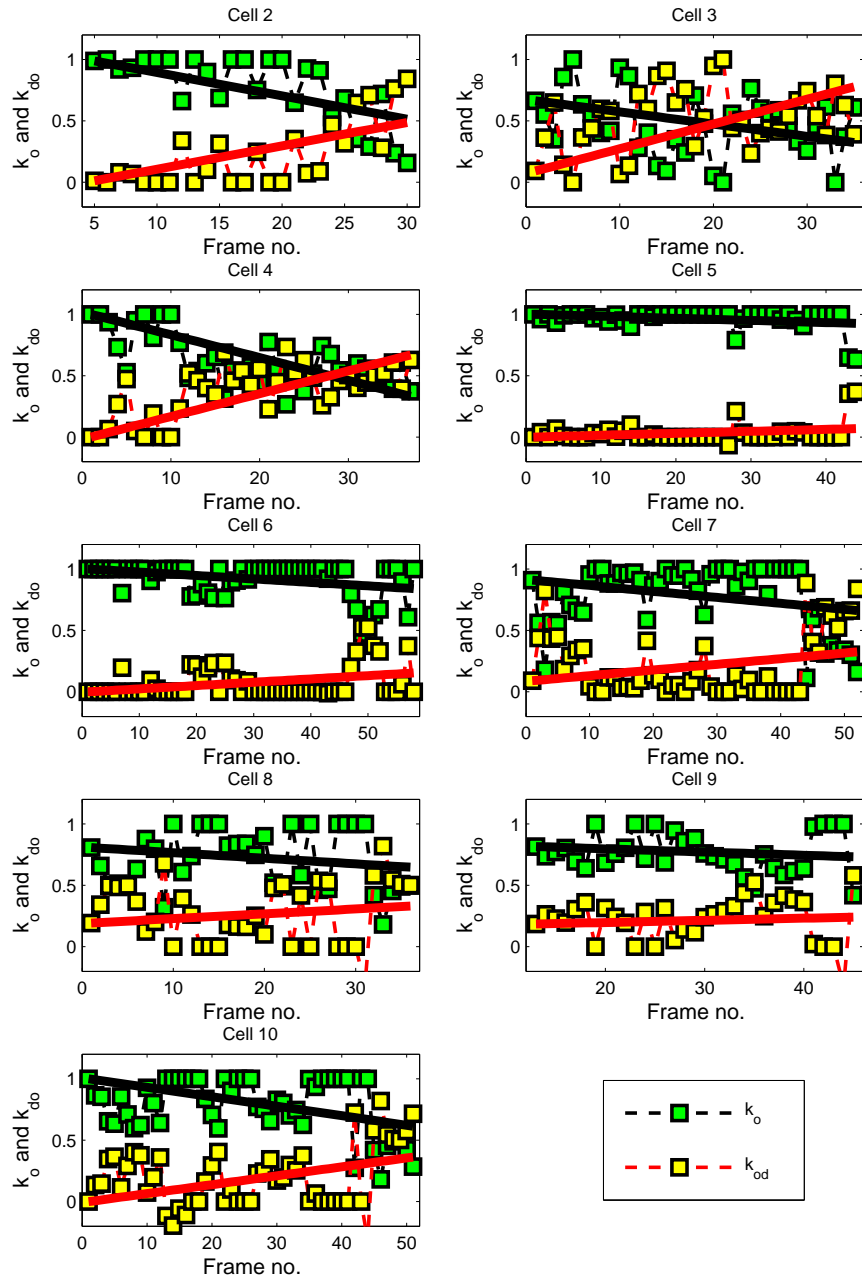


Figure 4.13: Spectral decomposition results from the other nine cells that were tracked, trend lines are plotted in each case for the two coefficients.

where \hat{a} was the absorbance, A a matrix containing the two exemplar spectra as

$$A = [\langle A_o \rangle, \langle A_{od} \rangle], \quad (4.23)$$

k similarly represented the two weighted concentration parameters such that

$$k = [k_o, k_{od}]. \quad (4.24)$$

The problem was then cast as a linear minimisation problem of the form

$$\min \frac{1}{2} \|Ak - \hat{a}\|, \quad (4.25)$$

this minimisation was solved for spectrum of each frame subject to the sum-to-one constraint, so as to make the recovered values physically interpretable as relative concentrations of oxygenated endmember and de-oxygenated endmember,

$$k_o + k_{od} = 1. \quad (4.26)$$

The concentrations were constrained as

$$0 < k_o < 1, \quad (4.27)$$

and

$$0 < k_{od} < 1. \quad (4.28)$$

This was solved in Matlab as a constrained linear least squares problem, using the function *lsqlin* and the constraints given in Equations 4.26, 4.27 and 4.28. The algorithm recovered the values of the concentration, k , which can be referred to as the abundances in more general spectral unmixing terminology. The approach describes the variation in the measured spectrum in terms of the two endmembers, because of this each spectrum is normalised to be between 0 and 1. When a spectrum is fully oxygenated, all the variation in the spectrum should be explained by the shape of the oxygenated endmember, resulting in $k_o = 1$, similarly for the de-oxygenated case. Intermediate states will then be a combination of the endmembers as well, described by some combination of the k_o and k_{od} , within the constraints placed on them in the unmixing algorithm.

The change in the relative concentrations for the case of cell 1 are shown in Figure 4.12, the cell starts from the oxygenated state and changes to the de-oxygenated state over the course of a few seconds. The graph shows the corresponding decrease in the value of k_o and increase in k_{od} , two trend lines are plotted on the graph, each taking the initial k value as the intercept for the linear line. The trend lines show the complementary changes in the two concentrations and the almost linear change in the oxygenation of the

cell. A single erroneous point is noticeable at frame 23 which is outside the trend of the overall time series, it corresponds to a more heavily de-oxygenated spectrum, possibly due to another RBC in the shadow of the tracked RBC while it was moving across the RASI FOV.

The spectral decomposition behaviour of the 9 other cells was calculated as well, using the same method and the same two endmembers for the reference oxygenated and de-oxygenated spectrums. The concentration parameters for each cell are shown in Figure 4.13. Each cell undergoes a different de-oxygenation process, cells 5 and 7 remain oxygenated for the majority of the experiment, though experience a significant drop in their final frames, cell 6 also experiences a sudden change in oxygenation partway through, but it recovers to its initial values. Cells 2 and 4 transition relatively smoothly towards a de-oxygenated state, whereas the remaining cells experience more oscillatory behaviour in their evolutions, but the overall trend was still towards a decreased oxygenation level in each cell. On the microscopic scale it is probable that the distribution of the sodium dithionite within the solution of RBCs is non-uniform, the differing concentrations around the RBCs can alter the de-oxygenation rate, further since the RBCs are in motion they likely pass through regions with different densities of sodium dithionite, which would alter the rate of oxygen diffusion from the RBCs. Another possible source of variation in the measurements was out of focus blood cells passing in planes above or below the visible RBCs, since the light would have to pass through both cells this would alter the resulting spectra.

4.4.8 Discussion of red blood cell experiment

The use of the spectral unmixing method here takes advantage of the relatively high spectral resolution of RASI, more points in the spectrum makes smoothing more effective, which is used to improve the performance of spectral unmixing by decreasing the variance in the spectrum. Smoothing also helped to reduce peculiar spectral effects due to variation in illumination and the topology of the RBCs, as an alternative to smoothing an extra endmember can be constructed and added to the spectral unmixing problem to account for the extra variations present. The high resolution also helps to resolve more features of the constituent spectra which improves unmixing performance by making the unique features of different spectra more apparent. Further, the large number of points in the spectrum allows the problem to be cast as an overdetermined system of equations.

The unique aspect of this experiment was the monitoring of the spectral characteristics of RBCs while in motion. The spectral evolution was shown to be different for each RBC, though the spectra obtained were consistent with the expected shape for the absorption spectrum of blood cells.

4.5 Spectral overlap in the spectrometer detector plane

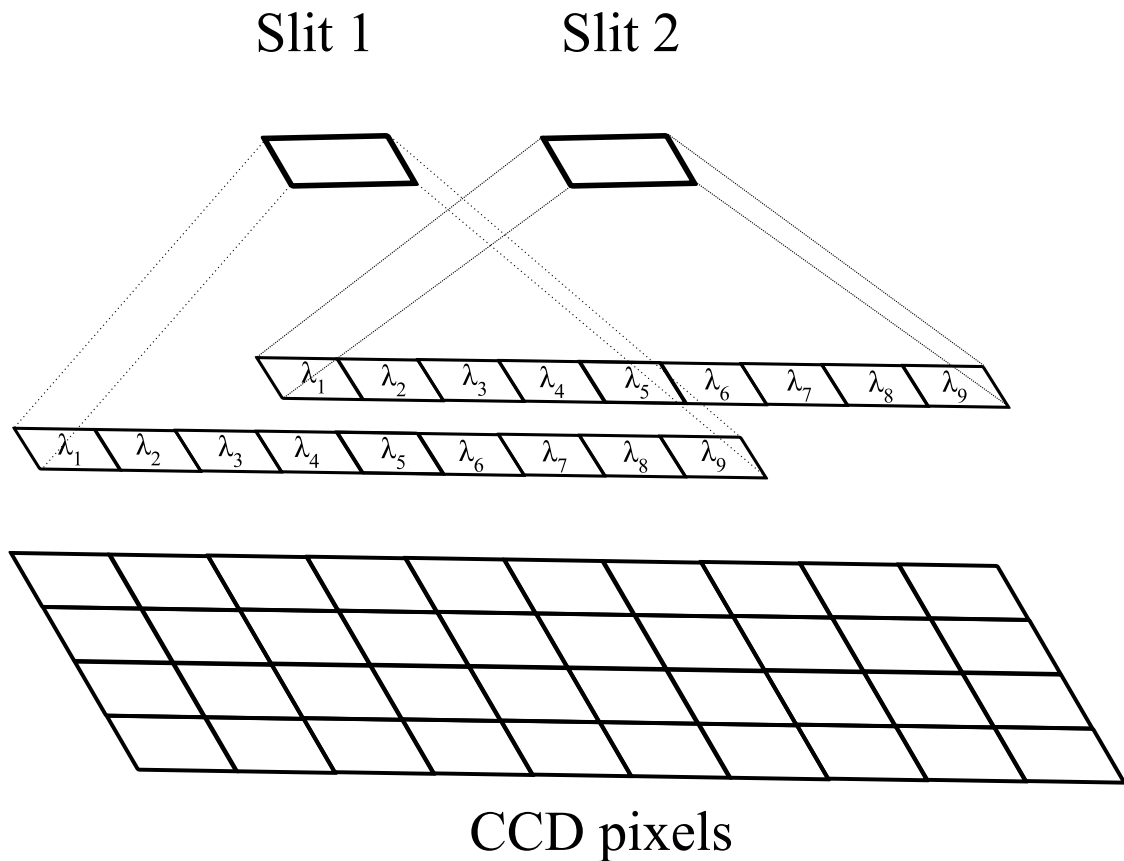


Figure 4.14: *The light from the entrance slits is dispersed by the spectrometer and light of different wavelengths is incident on the same CCD pixels.*

The dispersed light from laterally offset slits on the DMD can overlap on the spectrometer detector plane, shown in Figure 4.14. This limits the number of slits that can be created and used unambiguously per DMD pixel row to a single slit per row, without limiting the spectral range of the spectrometer. The inherent ambiguity that arises from the presence of multiple slits occurs because the detector CCD pixels cannot distinguish between incident photons of different wavelengths. The measured intensity is additive

$$I_{meas} = I_{\lambda_1} + I_{\lambda_2},$$

as the response of CCD pixels is linear, though the quantum efficiency of the CCD is a function of wavelength.

The wavelength calibration data discussed previously provided the positions on the CCD where the wavelengths from each slit were incident, so the task of accounting for the spectral overlap was to determine the contribution from each slit to each CCD pixel.

Considering two slits on the same DMD row such that their dispersed spectrums overlap, the measured spectrums associated with each respective slit are denoted by

$\hat{S}_1(\lambda)$ and $\hat{S}_2(\lambda)$ and a pure spectra denoted as $S_1(\lambda)$ and $S_2(\lambda)$ which gives the spectra that would be measured if only a single slit was open in each case. Since the contributions from the slits are superimposed, the measured overlapping spectra can be described in terms of the addition of the pure, non-overlapping spectra. The measured spectrum for a slit will consist of the pure spectrum of that slit and the pure spectrum of the other open slit, though the second spectrum will be shifted in wavelength to coincide with the wavelength of the slit in question. This can be expressed as

$$\hat{S}_1 = S_1 + A_{12}S_2 \quad (4.29)$$

and

$$\hat{S}_2 = A_{21}S_1 + S_2. \quad (4.30)$$

The matrices A_{nm} simply multiply the pure spectra so the resulting vector corresponds to the same CCD pixels as the wavelengths from the measured spectra. This is done by shifting the values in the vector representing the secondary pure spectra along the column so they occupy the appropriate positions. This can be more conveniently represented as

$$\hat{S}_1(\lambda) = S_1(\lambda) + \bar{S}_{12}(\lambda), \quad (4.31)$$

and

$$\hat{S}_2(\lambda) = \bar{S}_{21}(\lambda) + S_2(\lambda). \quad (4.32)$$

The terms $\bar{S}_1(\lambda)$ and $\bar{S}_2(\lambda)$ represent the shifted pure spectrum associated with each slit that overlaps with the primary slit. In principle these can be measured directly, but the shifting matrices A_{nm} can be used to determine them from the pure spectra themselves. The shifting matrices can be determined from the calibration data and the relative differences between the spectral tracks of each open slit from which the measured spectra are taken; the shifting matrices are used to calculate the $\bar{S}_1(\lambda)$ and $\bar{S}_2(\lambda)$ vectors as

$$\bar{S}_{12}(\lambda) = A_{12}S_2(\lambda) \quad (4.33)$$

and

$$\bar{S}_{21}(\lambda) = A_{21}S_1(\lambda). \quad (4.34)$$

These equations can then be used as a method of mitigating the effects of spectral overlap, with the goal of determining the value of the pure spectra from the measured spectra in the case of each slit. The above expressions can be easily extended to accommodate overlap from more than two slits.

4.5.1 Subtraction

The simplest approach to removing the effects of the overlap would be to subtract the values of the extra overlapping light and therefore determine the values of the pure spectrum, though this approach is dependent on sufficient prior knowledge of the constituent spectra to perform the operation. In the case of two slits described above at least one of the pure spectra needs to be known exactly.

This has limitations as often it is only the distinctive spectral shape that is known about a particular materials characteristic spectrum. The subtraction approach requires the known values of intensity, essentially the correct number of counts from the measured values to then determine the obscured spectrum. Various factors can effect this, such as variances in the illuminations, as such this approach is of limited applicability in solving issues associated with spectral overlap.

4.5.2 Linear mixing model

Often linear spectral unmixing approaches use *a priori* knowledge of the potential set of endmembers present in the datacube. The LMM approach to spectral unimxing determines the relative abundances of this set of endmembers in a given mixed spectra. This approach can be applied in creating a more robust approach to correcting the spectral overlap issue, rather than trying to directly calculate the contribution of each wavelength from each slit and thereby determining the intensity contributed by each slit. By concentrating on identifying the constituent spectra in the measured overlapping spectrum, by explaining the variation in the measured spectral shape in terms of possible candidate spectra, the LMM approach can be sufficiently modified to help solve the overlap issue. Equations 4.33 and 4.34 can be modified into an appropriate format to achieve this by normalising the measured spectrum to be between 0 and 1, which is achieved by dividing across by the maximum value present. So

$$\frac{\hat{S}_1}{\hat{S}_{1max}} = \frac{S_1}{\hat{S}_{1max}} + \frac{\bar{S}_2}{\hat{S}_{1max}} \quad (4.35)$$

and

$$\frac{\hat{S}_2}{\hat{S}_{2max}} = \frac{\bar{S}_1}{\hat{S}_{2max}} + \frac{S_2}{\hat{S}_{2max}}, \quad (4.36)$$

then the pure and shifted spectra can be written in normalised form, as a product of the maximum value times the normalised spectrum, $S = S_{max} \times M$, where M represents the normalised candidate spectrum, given as

$$\frac{\hat{S}_1}{\hat{S}_{1max}} = \frac{S_{1max}M_1}{\hat{S}_{1max}} + \frac{\bar{S}_{2max}\bar{M}_2}{\hat{S}_{1max}} \quad (4.37)$$

and

$$\frac{\hat{S}_2}{\hat{S}_{2max}} = \frac{\bar{S}_{1max}\bar{M}_1}{\hat{S}_{2max}} + \frac{S_{2max}M_2}{\hat{S}_{2max}}, \quad (4.38)$$

putting these values into Equations 4.35 and 4.36 the ratios of maximum values can be treated as co-efficients, with values between 0 and 1, which allows the overlap to be represented as

$$\hat{S}_1 = a_1M_1 + a_2\bar{M}_2 \quad (4.39)$$

and

$$\hat{S}_2 = b_1\bar{M}_1 + b_2M_2. \quad (4.40)$$

The two equations represent a linear sum that can be solved in the LMM manner and approaches can be imported from standard algorithms to implement this. While the non-negativity constraint still applies, the standard sum to one constraint however is not applicable, as the parameters a, b in Equations 4.39 and 4.40 are the ratios of maximum values in the spectra. The constraints are then

$$a_i \geq 0 \quad \forall i, \quad (4.41)$$

the other constraint on the values of the abundances is due to the ratio of the maximum values, the maximum value in the overlapping spectra must be at least the same value as the largest maximum value in the constituent endmembers

$$0 \leq a_i \leq 1 \quad \forall i. \quad (4.42)$$

The general case of the spectral overlap linear problem can be represented as

$$S = \sum_{l=1}^{2L} a_l M_l, \quad (4.43)$$

which is the same form as standard unimxing problems, but due to the lack of a sum-to-one constraint the most feasible approach to solving this constrained least squares problem is the non-negative least squares approach (NNLS). The solution to the NNLS is a subset of the constrained least squares problems, the approach to solving the NNLS minimises

$$\min \|Ma - S\|, \quad (4.44)$$

an algorithm is implemented in Matlab using the *lsnonneg* function, which implements the algorithm according to [2].

4.5.3 Demonstration of spectral overlap correction

The approaches described above offer solutions to dealing with spectral overlap, here these ideas will be demonstrated for a particular example. Simply, a neon light was used to illuminate the system input aperture, and three slits were opened on the DMD, the dispersed light from these slits was then collected and the spectrum determined, the positions of the slits were chosen so as the spectrum from each would all overlap. The slits were opened in various combinations allowing the collection of the three spectra in the absence of overlap and the various possible combinations of having two and three slits open, with the purpose of using the collected data to demonstrate the above mentioned methods of correcting the overlap.

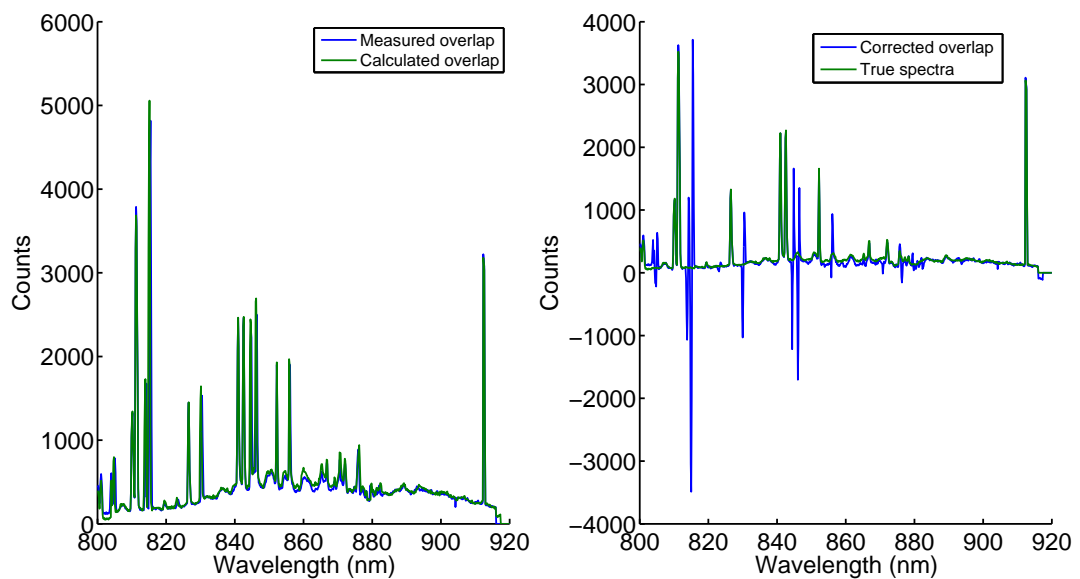


Figure 4.15: (a) The measured overlapping spectra and the overlapping spectra calculated using Equation 4.29. (b) The results of the subtraction compared with known spectra.

An example of the subtraction is shown in Figure 4.15, to determine the subtracted version, the spatially offset spectra were calculated and subtracted from the overlapping versions. The results of this subtraction are shown, while it is successful in removing some of extra features present due to the overlap, differences in intensity result in some portions of the new spectrum being negative. Which of course makes using the so-called corrected spectrum difficult for the purposes of comparison. The differences can be due to numerous things, variations in the light source output, uneven illumination or other experimental parameters. In more complicated cases these problems will be further complicated, demonstrating the limited utility of an approach to correcting spectral overlap based on the subtraction approach.

The second approach using LMM was applied as well, the key step was generating the appropriate set of candidate spectra to apply to the problem, in this case using the

data from the Neon light source, the candidate true spectra were already known. The candidate list consisted of the possible full spectra and the shifted spectra calculated using the approaches in Equations 4.33 and 4.34. The true spectra associated with the slit were calculated using the recovered co-efficients and the relations expressed in Equations 4.37 and 4.39. Figure 4.16 shows the overlapping spectra and the recovered

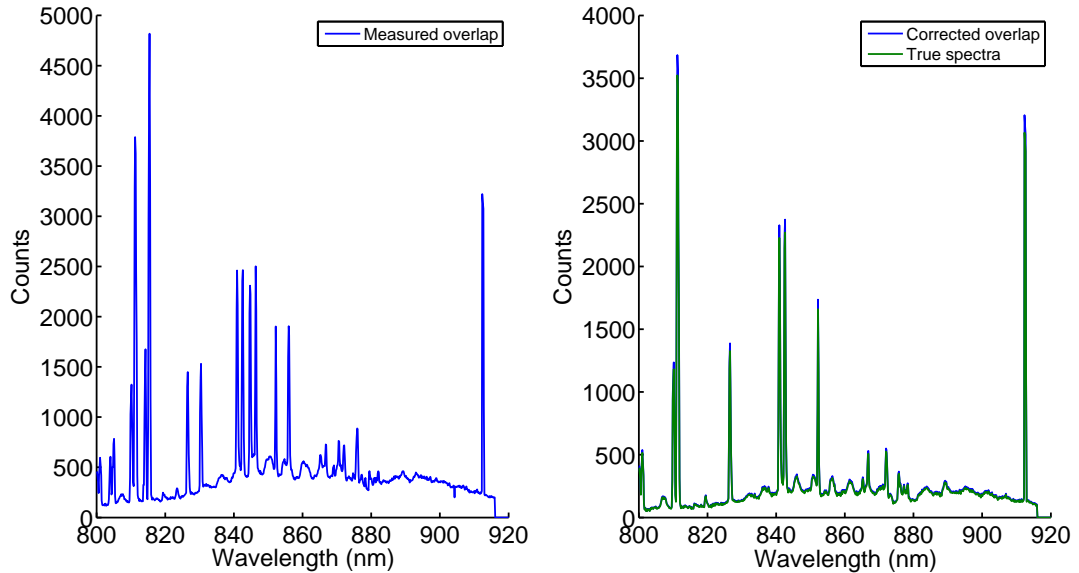


Figure 4.16: (a) shows the overlapping spectra in a single spectrum and (b) shows the spectrum recovered using the LMM method compared to the known spectra for that slit

true spectra, which is compared to the independently measured spectra for that slit. As is visible, the recovered spectra matches the true spectra, this approach is dependent on sufficient knowledge of the possible spectra that can be present and the number of overlapping spectra present from adjacent slits.

4.5.4 Spectral Overlap discussion

The problem of spectral overlap introduces an ambiguity into the spectra recovered from the CCD, the resulting measurement constitutes an ill-posed problem where there are more unknowns than knowns. The knowns being the sum of the contributions from the different overlapping spectra and the unknowns the values associated with the different spectra. This can be solved using prior knowledge or assumptions about the constituents themselves, the above approaches use knowledge of the spectral shapes, however in the case of subtraction this is hampered by the variation in the spectra, resulting in negative values in the recovered spectrum. The approach based on spectral unmixing provides a more manageable approach as it tries to explain the features present in the overlapping spectra in terms of other known spectra. As long as the possible constituents are known this approach can be applied, oftentimes in spectral processing tasks the goal is to detect

the presences of certain spectral signatures, which can be done more easily than exact reconstruction of the spectra itself. Other numerical approaches exist that potentially could be altered from other current spectral unmixing techniques, for example approaches that are based on “blind source separation” such as independent components analysis would not require the use of prior knowledge of the spectra involved.

The alternative to a numerical approach as described above would be to incorporate a hardware solution that helps mitigate the problem physically. One possible approach to this would be to use a so-called Foveon sensor that has been described previously in Section 1.3.2. The Foveon has three layers of pixels that have different pass band characteristics. Essentially a red, green and blue layer. The positions of slits could be positioned upon the DMD so as the blue and red portions of the spectra overlap, but are then collected by different layers of the Foveon sensor. This could be effective for a sufficiently broad spectral range, but it also requires that the slits have sufficient spatial separation to cause the offset of different portions of the spectrum. This approach could help improve the number of spectra collected simultaneously in a single row, but it mitigates the problem rather than solving it entirely.

One of the key disadvantages of spectral overlap is that it reduces the number of spectra that can be unambiguously collected in a single snapshot. This is principally limited to one per row of the CCD camera, but more realistically it is limited by the length of the DMD slit and the size of the object being measured. The number of spectra obtained can still be on the order of hundreds. The spatial distribution of slits across the field of view is also limited as slits cannot be on the same DMD row; if enough prior knowledge of the scene is available, then methods described above could be used to increase the number of points collected.

Avoiding the problem of overlap is the best course to avoiding the potential errors associated with the spectral overlap and that is the course that has generally been taken in the work presented in this thesis.

4.6 Chapter summary

The utility of the RASI system that was built was demonstrated on a simple example, showing the core MOS capabilities of the device. As an example of the application to a more complex problem, an experiment involving the measurement of the spectrum of RBCs undergoing de-oxygenation while in motion was described. The background and motivation for the experiment were given and the technical details of the tracking were given, the methods of de-oxygenation were also described. The experiment tracked ten RBCs across the RASI FOV and measured their change in spectrum, from the characteristic spectrum associated with oxygenated RBCs to that of de-oxygenated RBCs. This change was characterised using a spectral unmixing approach based on a LMM. Finally

the problem of spectral overlap in the detector plane of RASI was discussed and some approaches to solving and mitigating it were demonstrated. A potential solution based on novel multi-layer CCD cameras was also discussed.

Chapter 5 – Raman spectroscopy and alternative spatial sampling methods

5.1 Introduction

The previous chapter discussed broadband spectroscopic applications. In this chapter the focus will be on extending the functionality of RASI to Raman spectroscopy. The previous approaches were based on transmission and absorption, whereas Raman spectroscopy is a phenomenon of the inelastic scattering of light [73]. The goal of this chapter is to introduce and describe the Raman effect, and its underpinnings as a form of inelastic scattering, a short survey of the literature on Raman spectroscopy in the context of hyperspectral imaging are presented. The necessary modifications to the RASI system are described, including the addition of an illuminating laser and filters required to help separate the Raman scattered light.

The modified Raman RASI was used to demonstrate examples of alternate sampling methods that are enabled by the random-access approach and not possible with other spectral imaging systems. Two standard sampling methods are demonstrated: selecting points at random from the scene and a grid based sampling approach. A test case was created by scanning a large region of the FOV and applying the two sampling methods to it; classification maps of the whole scene were constructed from the sampled subsets and compared to the results from the entire test case, which was used as reference to gauge the performance of the different methods.

5.2 The Raman effect

The Raman effect is a phenomenon of inelastic scattering that is exemplified by its low efficiency and high chemical specificity. A brief overview of the historical development of Raman spectroscopy and the underlying physical processes are provided in this section, in order to provide insight into the various challenges and applications of Raman spectroscopy.

5.2.1 Background of the Raman effect

The Raman effect is a phenomenon of the in-elastic scattering of light in matter, it was initially predicted theoretically by Brillouin in 1922 and then, independently again in 1923. The first experimental demonstration was performed by C.V. Raman in 1928, for whom the effect was named. Interestingly, the experimental setup consisted of a focused and filtered beam of sunlight and an unmixed liquid sample, the results were observed

with the human eye. Due to the low efficiency of the inelastic scattering process, the Raman effect was of limited use in spectroscopy until the invention of the laser, which provided a monochromatic, high power source of light. Development in holographic gratings and improvements in detector technology also accelerated the development of Raman spectroscopy as a standard laboratory technique.

5.2.2 Description of the Raman effect

Scattering of light involves the interaction of light and matter. The energy, E , of a photon of frequency ν is given by Planck's law as

$$E = h\nu, \quad (5.1)$$

where h is Planck's constant and the frequency, ν is related to the wavelength, λ , by

$$\nu = \frac{c}{\lambda}, \quad (5.2)$$

where c is the speed of light. When a photon interacts with a molecule, the photons are either elastically or inelastically scattered. Elastic scattering by particles much smaller than the wavelength of light is called Rayleigh scattering. In this phenomenon, when the molecule interacts with a photon of energy, $h\nu_0$, it is excited from its ground state, E_0 , to an excited state of energy $E_0 + h\nu_0$. The molecule then returns to its initial state and emits an identical photon, so the energy of the molecule and photon remain the same after the interaction. Inelastic scattering results in a net change of the energy, which can be seen as a change in frequency (or wavelength) of the scattered photons.

The energy of the Raman scattered photons can be shifted either up or down, this is shown in Figure 5.1, along with the Rayleigh (elastic) scattering change. When the frequency is shifted down (to a longer wavelength), the scattered photon is less energetic relative to the incident photon; this is referred to as Stokes scattering. When the scattered photon is more energetic the scattered photon will have a frequency that is increased (shifted to a shorter wavelength) with respect to the incident photon, which is called anti-Stokes scattering. The spectrum of scattered photons will be symmetric about the incident frequency, ν_0 , though the intensities of the different Raman peaks corresponding to the different states of the molecule will differ. This is due to the initial populations of the states in the molecule which is dependent on the temperature. In a state of equilibrium, the higher energy state will be less populated than the lower, which results in the number of transitions from the upper to lower state being less than those from the lower to the upper state, resulting in the Stokes peaks being stronger than the anti-Stokes. It is worth noting that Raman spectra are commonly represented in terms of the relative frequency or wavelength shift from the incident photon. The relative shift in

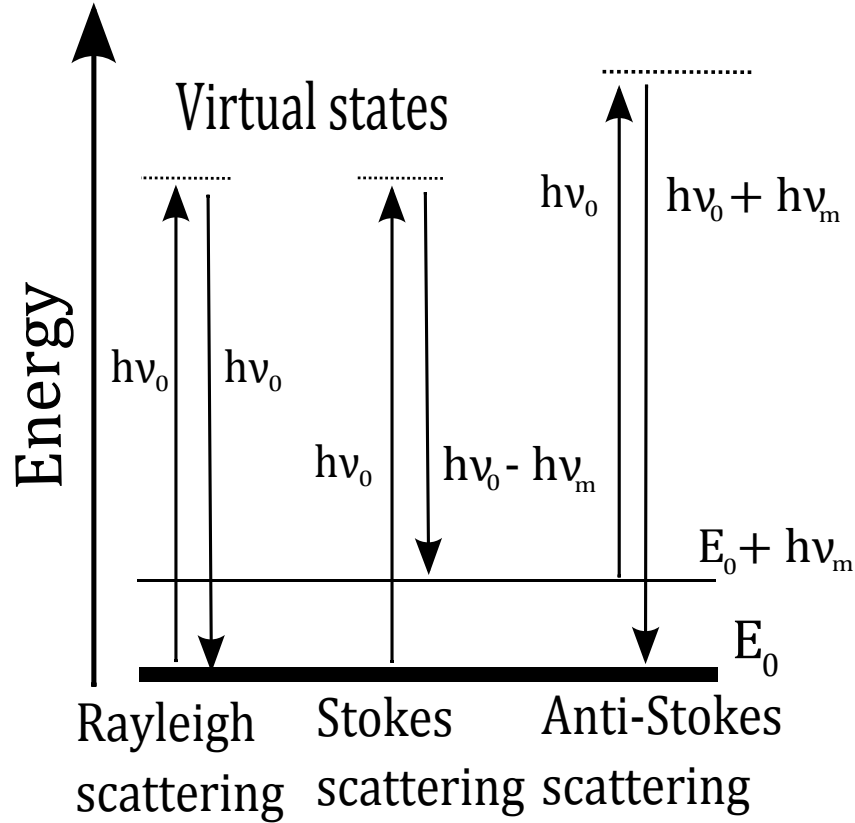


Figure 5.1: Rayleigh and Raman excitation

wavenumber for incident photons of wavelength λ_0 is

$$\Delta w = \frac{1}{\lambda_0} - \frac{1}{\lambda_1}, \quad (5.3)$$

where λ_1 is the wavelength in the spectrum. This formulation allows the incident wavelength to be placed at the origin of the spectrum and the scattered light intensities to be placed at $\pm\Delta w$, referred to as the Raman shift.

Fundamentally, the positions of the spectral lines in a Raman spectrum are dependent on the properties of the molecule from which the photons are scattered. The oscillating electric field of the photon induces a polarisation in the molecule. This holds for atoms as well, however the polarisation is isotropic in atoms and so the atom only experiences Rayleigh scattering. In molecules where the induced polarisation can be anisotropic, Raman scattering is possible [88]. Measurement of the intensity of scattered light allows the rotational and vibrational modes of the molecule to be probed by Raman spectroscopy.

A semi-classical description of Raman spectroscopy gives the intensity of the scattered light as [118]:

$$I = \Phi K |\mathbf{e}_e \alpha \mathbf{e}_s|^2 d\Omega, \quad (5.4)$$

where $K = 4\pi^2 a^2 \frac{1}{\lambda_1^4}$ and $a = \frac{1}{137}$ and λ_1 is the wavelength of the scattered light. $d\Omega$ is the solid angle into which the light scattered. I is energy per unit time into solid angle

$d\Omega$. Φ is the energy per unit area per unit time of the incident beam. The unit vectors \mathbf{e}_e and \mathbf{e}_s define the directions of the electric fields of the incident and inelastically scattered light. Finally, α is the scattering tensor and contains the information on the vibrational and rotational energy levels of the molecule. The parameter K shows that the intensity of Raman scattered light increases inversely with the fourth power of wavelength and directly with the irradiance of the incident beam. The literature on interrogating the scattering tensor is extensive and will not be further explored here.

Above has been a brief and simplified description of some of the key aspects of the basic Raman effect. There are other kinds of Raman spectroscopy, to date an estimated 25 kinds. Some examples are listed below

- Resonance Raman spectroscopy
- Surface enhanced Raman spectroscopy
- Spontaneous Raman spectroscopy
- Optical Tweezer Raman spectroscopy
- Stimulated Raman spectroscopy
- Coherent anti-Stokes Raman

Generally the goal is to enhance the sensitivity of the Raman effect, however they are beyond the scope of this thesis and are listed here only to demonstrate what a broad categorisation Raman spectroscopy is.

5.2.3 Raman spectrometers

The basic requirements for the parts of a Raman spectrometer have not changed since the initial experimental demonstration by Raman, though the various parts have of course been drastically improved by modern technology. The basic layout requires an excitation source, a sampling system and a detector. Lasers provide a highly monochromatic, high power excitation source, whose choice of wavelength is key with regard to the application. The sampling system merely refers to the method of collecting the Raman scattered light and depositing it on the detector, it will include the collection optics and the means of separating out the different wavelengths in the scattered light, examples include confocal microscopes, dispersive spectrometers and acousto-optical devices for filtering. Finally the detector is where the gathered light is measured, it can range from a single photodiode in the case of a monochromator layout to, as is more often the case, an array detector. Generally the detector is an integrated part of the sampling system. In modern systems the use of dichroic mirrors, edge pass filters and laser line filters further augment the performance of Raman spectrometers.

The excitation source in modern Raman spectrometers is a laser, as it provides a high power, monochromatic source of photons. The behaviour of the laser source can have dramatic effects on the measured Raman spectrum. Any side lobes can overpower the Raman spectrum and add unwanted background to the measurement, this is usually counteracted with the use of laser line filter. Wavelength stability can also be a factor as the Raman shift in wavenumbers is measured relative to the laser wavelength as explained in Equation 5.3. Another key parameter is the wavelength of the laser, Equation 5.4 shows this can affect the intensity of the scattered light, with longer wavelengths reducing the intensity of Raman scattering and shorter wavelengths increasing it. Fluorescence is also a cause for concern; it tends to occur with higher energy, shorter wavelength photons and can easily overwhelm any Raman signal. As such visible and UV wavelength lasers are rarely used with organic molecules.

The sampling system is often matched to the particulars of the sample being evaluated and can also be designed to include the excitation source. When the collecting optics and excitation laser are on the same optical axis it is the back scattered Raman light that is collected, in microscopes this is referred to as an epi-illumination configuration and is achieved using dichroic mirrors to couple the laser beam to the optical path of the system. This approach is one of the most common in microscopy applications of Raman spectroscopy, as it provides a straight-forward approach to illuminating the sample and collecting the back-scattered light. The RASI system described in the previous chapters of this thesis provides the sampling system and the calibration and properties of the diffraction grating used in the spectrometer are also previously described. The details of the addition of the laser illumination components to the setup will be described in the following section.

5.3 Raman hyperspectral imaging

Like other spectroscopic techniques, Raman spectroscopy can be used for hyperspectral imaging. It is often referred to as Raman imaging. The motivation for incorporating Raman spectroscopy into hyperspectral imaging is that it provides a high degree of specificity for identifying compounds based on their spectrums, due to the relationship of the peaks in the Raman spectrum and the vibrational energy levels of the molecules, the spatial distribution of different materials can then be determined from the Raman image.

In order to construct a Raman image, each point in the sample being imaged must be illuminated with the laser to produce the Raman scattered light. Each point in the sample can be illuminated in sequence with the laser beam or the whole sample can be illuminated in a global illumination configuration.

Scanning methods generally focus a laser spot onto a point on the sample and

collect the signal from this point. Then the sample is moved and the process repeated until an area has been scanned, the Raman data-cube is constructed from the data at each point. The time taken for acquisition is a key factor here, as imaging a large area can be time consuming, to acquire an 128×128 pixel image at a 1 second integration time for each pixel would take ≈ 4.5 hours. The beam can be shaped into the form of a line and scanned across the sample, thereby decreasing the number of measurements that need to be taken to acquire the whole Raman image [108]. Also methods exist where multiple laser spots are incident on the sample, to decrease the number of measurements as well. This can be done using multiple lasers simultaneously, or by using a spatial light modulator[104]. The advantage of focusing the laser comes from the increase in the incident power at that point, which increases the signal of the Raman scattered light. The increase in laser power brings its own concerns though as there is a possibility of burning the sample in the case of biological samples, thermal expansion has also been noted to be an issue [73].

Distinct from the scanning approaches mentioned above, a global approach does not use point or shaped illumination, instead the whole area of interest is illuminated, then a tunable filter is used to build up a stack of monochromatic images [20]. In certain cases it should also be possible to choose an optimised subset of wavelengths to measure and further reduce the time taken for data collection. The global approach allows for a large area to be monitored simultaneously, this area illumination is commonly achieved by defocusing the laser beam to cover the whole region, which is an advantage when used with the RASI system which needs to be able to extract a Raman spectrum from each point in the scene, without adjusting the laser illumination. The trade-off for this approach is the reduction of incident power at a given pixel in the Raman image, resulting in a lower Raman signal at each point in the scene.

5.4 Raman RASI

This section describes the necessary additions to the RASI experimental layout, namely the choice of laser, including the wavelength and the reasons for the choice of wavelength. The necessary filters chosen are also described, as well as their uses and positions in the setup. The global illumination system designed and implemented for the system will also be described, including a description of the laser propagation through the setup and various considerations when expanding the beam to illuminate the FOV of RASI.

The implementation of Raman spectroscopy in the RASI system required the addition of an excitation source to the setup. The source used was a 785 *nm* laser, named a “Luxxmaster MiniRaman Boxx”, supplied by Laser Components, with power output up to 500 *mW*. The wavelength was chosen as a compromise between the reduced efficiency of the Raman effect at longer wavelengths versus the reduced potential for

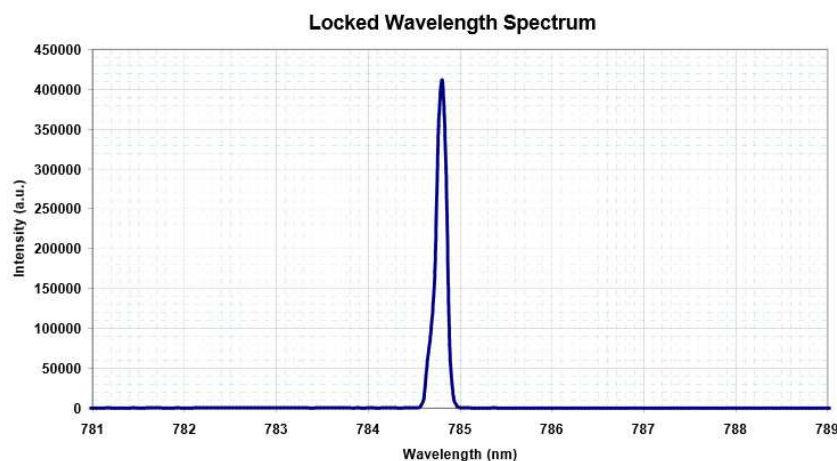


Figure 5.2: Spectral output of Raman laser

background fluorescence, which is common in organic samples. The output spectrum from the laser is shown in Figure 5.2. The key issue when deciding how to illuminate the sample was to enable the RASI setup to be able to collect light from any points across the FOV simultaneously, this required multiple regions to be illuminated with the laser to produce the Raman effect at these points, the two primary approaches for illumination are described in Section 5.3. Any scanning technique would be too limiting, as scanning a single laser spot or line would be too slow. In principle, if multiple laser spots were generated and could be coordinated with the apertures of the RASI system that would be desirable, this could be achieved with multiple laser beams and galvo-mirrors used to direct them, or otherwise an SLM could be used to generate a spot pattern on the sample. These approaches would require careful consideration of the design of the illumination, as well as adding extra calibration procedures, instead it was decided to implement a global illumination setup.

One of the main advantages of using a global illumination layout was that the entire FOV was illuminated simultaneously. This allowed the RASI system to be used without any further calibration steps or considering the alignment of a laser spot with a point of interest. The laser was coupled to the back-aperture of the microscope objective and the beam was defocussed to implement the global illumination. A dichroic mirror was used to couple the laser light into the optical path of the system. The primary disadvantage of using the global illumination was that the power of the laser was distributed over a relatively large area, thereby reducing the maximum signal to noise possible. The loss in signal was compensated for by increasing the integration time of the camera and averaging frames. Only in the case of tracking in a dynamic scene would the time delay between acquisitions become an issue, but the fundamental inefficiency of the Raman effect prohibits such high speed acquisition in any case.

5.4.1 Modeling of the global illumination

The goal of the global illumination was to create a defocused laser beam in the object plane of the microscope objective to illuminate the sample in the RASI FOV (which was $\approx 80 \times 60 \mu\text{m}$). The defocused laser beam was to be slightly larger than the FOV of RASI in the same object plane so as to use the optical power from the laser efficiently. If the laser beam was too large, any part of the intensity distribution incident outside the RASI FOV would be wasted, as no Raman spectra could be collected from these areas, also it would reduce the amount of optical power available to the regions in the RASI FOV. If the laser beam was smaller than the RASI FOV, Raman scattering would not occur in regions with no incident laser light, reducing the useful area of the RASI FOV unnecessarily. The additions to the RASI setup to achieve the required beam size are shown in Figure 5.8, the divergent output from the 785 nm diode laser was collimated by a simple lens, this collimated beam was collected by a tube lens and coupled into the primary optical path using a dichroic mirror. The beam entered the back aperture of the microscope objective and a divergent beam was output to the object plane, the extent of the divergence and area of illumination could be altered by adjusting the distance between the tube lens and the back aperture of the microscope objective, thereby achieving the necessary coverage of the RASI FOV.

A model of the global illumination was created using the equations of Gaussian optics. This was used to determine the behaviour of the laser beam as it passed through the simple lens, this model was then extended using the physical propagation calculation capacity of Zemax to further model the behaviour of the beam as it passed through the more complex elements in the setup, such as the tube lens and microscope objective. The purpose of the modeling was to demonstrate that the experimental layout given in Figure 5.8 for the illumination could provide suitable coverage of the whole RASI FOV.

Gaussian optics uses a complex radius of curvature composed of the wavefront curvature $R(z)$, and the transverse size of the beam, $w(z)$. This so called “q-factor” is given by the relation:

$$\frac{1}{q(z)} = \frac{1}{R(z)} + i \frac{\lambda}{\pi w(z)^2}, \quad (5.5)$$

wherein z is the distance the beam has traveled and λ is the wavelength, also, $R(z)$ and $w(z)$ are defined as

$$R(z) = z \left(1 + \left(\frac{\pi w_{00}^2}{z\lambda} \right)^2 \right), \quad (5.6)$$

and

$$w(z) = w_{00} \left(1 + \left(\frac{\lambda z}{\pi w_{00}^2} \right)^2 \right)^{\frac{1}{2}}, \quad (5.7)$$

where w_{00} is the minimum value of the beam waist.

The properties of a Gaussian beam are dependent almost entirely on w_{00} , as well

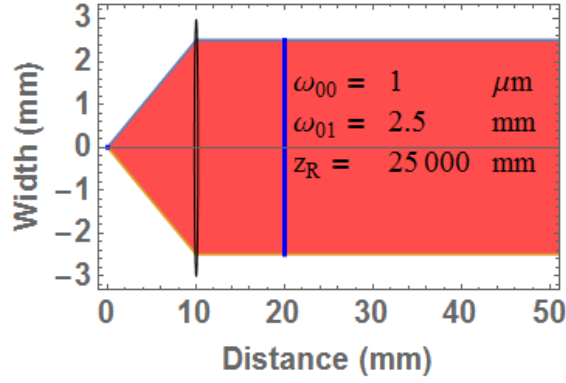


Figure 5.3: Collimation optic overview; the lens used had a focal length of 10 mm, the blue line represents the position of the new beam waist after passing through the lens, its value was $w_{01} = 2.5 \text{ mm}$. The new Rayleigh range, z_R , based on w_{01} was 250 cm.

as the wavelength, once w_{00} is known, then it is possible to calculate the beam size for a given distance z . The far field divergence of a Gaussian beam is given by the relation:

$$\theta = \frac{w(z)}{z} = \frac{w_{00}}{z_R}, \quad (5.8)$$

which is useful for determining the minimum beam waist of a laser from the given divergence. Further, another useful quantity is the Rayleigh distance z_R ,

$$z_R = \frac{\pi w_{00}^2}{\lambda}, \quad (5.9)$$

which is the distance over which a beam will remain collimated. It is also useful to note that the “q factor” can be expressed as

$$q(z) = z + iz_R, \quad (5.10)$$

and which has the useful property that at the beam waist minimum, when $z = 0$, that

$$q(0) = iz_R. \quad (5.11)$$

When a thin lens is placed in the beam path the properties of the beam are transformed, the relationship between the beam before and after a lens of focal length f , with the q factor just before, say q_1 , and after q_2 the lens is given by

$$q_2 = \frac{q_1 f}{f - q_1}. \quad (5.12)$$

The distance from the lens to the new beam waist, z_m and the new beam waist minimum, w_{01} are given respectively by

$$z_m = \text{Re}(q_2) \quad (5.13)$$

and

$$w_{01} = \frac{\sqrt{Im(q_2)}}{\sqrt{Im(q_1(0))}}. \quad (5.14)$$

The equations described above are used to help model the first portion of the illumination layout, the collimation of the diode laser output.

To collimate the diode laser it was necessary to calculate the minimum beam waist of the beam as it emerged from the laser. The value for the divergence was twenty degrees, using Equation 5.8 the value for w_{00} was calculated to be roughly one micron. This value of w_{00} was used with Equation 5.7 to determine the beam waist at a distance of $z = 10$ mm, which was the focal length of the collimating lens. Equation 5.10 was used to determine the q-factor at the lens, then the q-factor after the lens was determined using Equation 5.12, following this the new beam waist minimum, w_{01} , was calculated to be 2.5 mm, and the new Rayleigh range from this beam waist was $z_R = 25000$ mm, which was the range over which the beam would remain collimated. The change in beam waist size from the initial w_{00} to the lens position and the beam waist change after the lens are plotted in Figure 5.3. The collimated beam waist then used as the starting point for the Zemax simulation.

The calculated beam waist of the collimated beam was used as the starting point of the Zemax model, this beam size was verified by measurement which confirmed the calculated value. The Zemax model consisted of the tube lens and a microscope objective. Since the exact parameters of the microscope objective used in the setup were unavailable in a Zemax format a similar microscope objective was used in the model, as the aim of the model was to demonstrate that by adjusting the distance between the tube lens and microscope objective the size of the divergent beam in the object plane could be altered in a controlled manner. The ray diagram of the Zemax simulation is shown in Figure 5.4, the dichroic mirror used in the main setup shown in Figure 5.8 was omitted to simplify the model. In the model, the collimated beam is collected by the tube lens and begins to converge between the tube lens and microscope objective resulting in a divergent beam in the object plane, which is a reversal of the normal usage of an infinity corrected microscope, where the beam would be collimated between the two lenses and, brought to a focus behind the tube lens to form a magnified image of the object plane.

The result of the convergent beam entering the back aperture of the microscope objective was a divergent beam at the output, which is also shown in Figure 5.4. The size of the divergent beam needed to match that of the RASI FOV, also the intensity distribution needed to be such that the distribution across the RASI FOV was sufficient to produce a Raman spectrum at each point. In order to achieve this, most of the power needed to be within the RASI FOV, since the intensity distribution was Gaussian, then the percentage laser energy within the beam waist, $w(z)$ at a given z was 86.4% and the percentage at the Full Width Half Maximum (FWHM) point was 69.2%. An example

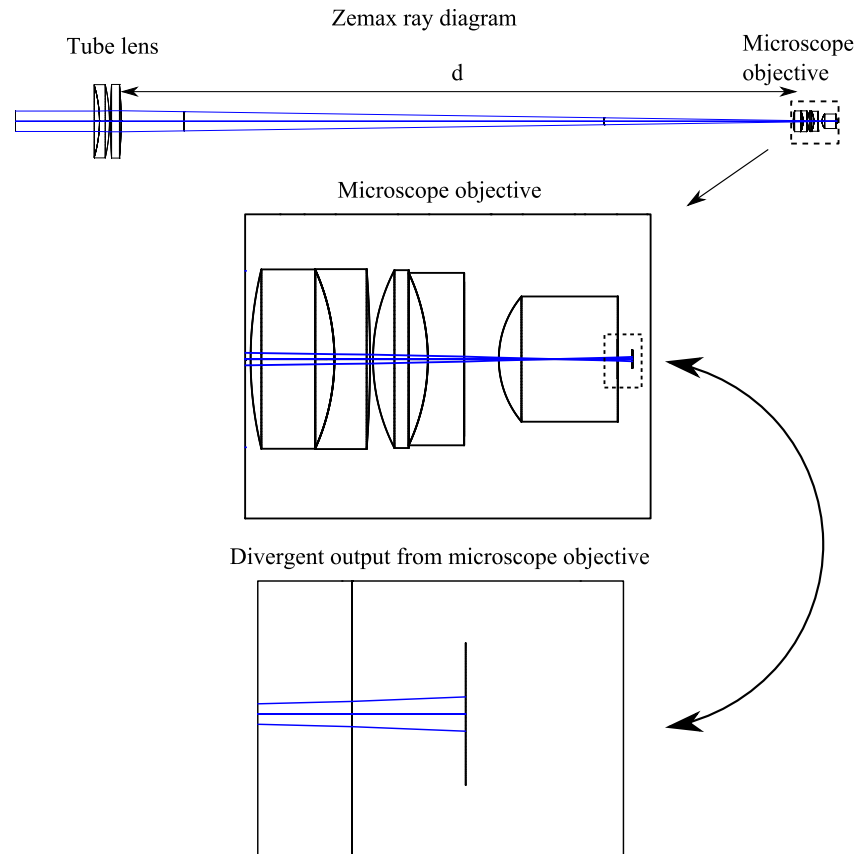


Figure 5.4: This figure shows the ray trace diagram from the Zemax simulation, the first diagram shows the beam propagation, through the tube lens and the microscope objective, to the object plane. The first enlarged diagram shows a close up of the beam path through the microscope, the second shows the divergent rays output from the microscope objective, the result of which is a defocused spot in the object plane of the system.

of the intensity distribution for a distance of $d = 171$ mm between the tube lens and microscope objective is shown in a contour plot in Figure 5.5 (a), three line profiles for different values of d are shown in Figure 5.5 (b). By adjusting the parameter d , the FWHM could be modified so as to cover the RASI FOV, by making the beam larger the coverage of the RASI FOV became more uniform, but more power was deposited outside, making the beam smaller resulted in more power being concentrated in the center of the distribution resulting in less uniform illumination. A stack of three contour plots of the intensity distribution for different values of d are shown in Figure 5.6 to demonstrate the change in size and distribution with a change in distance, d .

The model demonstrates that the layout for the global illumination shown in Figure 5.8 can be used to produce a laser beam of sufficient width to cover the whole RASI FOV. While the model contains differences from the layout, such as the use of a different microscope objective, these differences were compensated for experimentally, for example by adjusting the distance d between the tube lens and microscope until the required beam width was achieved.

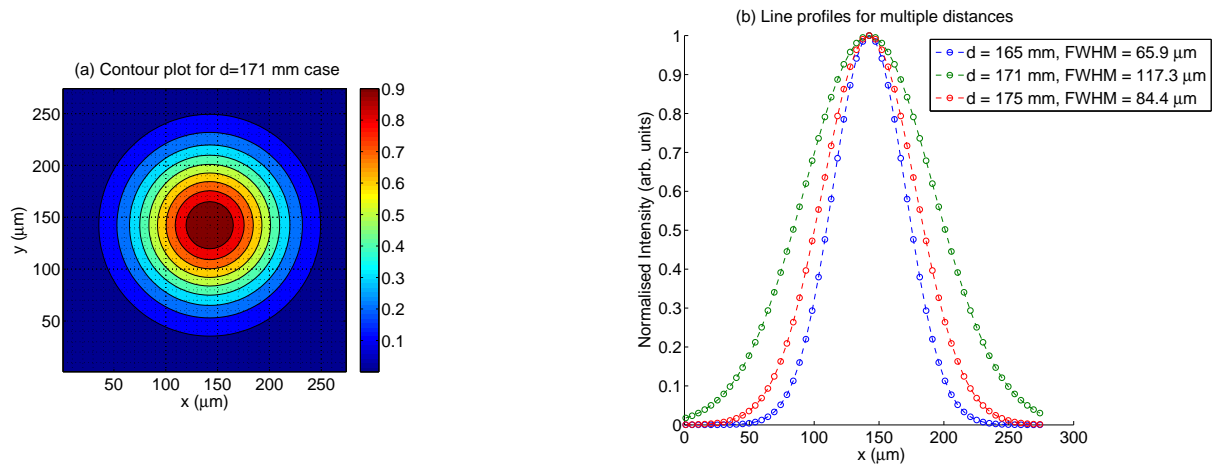


Figure 5.5: (a) Contour plot of the normalised intensity distribution at the object plane of the microscope objective for distance 171 mm between the tube lens and the objective. (b) Line profiles of the intensity distribution for three different distances between the tube lens and objective, the change in FWHM of the Gaussian intensity distributions demonstrates that the laser beam can be expanded to the size of the RASI FOV by altering the distance between the tube lens and microscope objective.

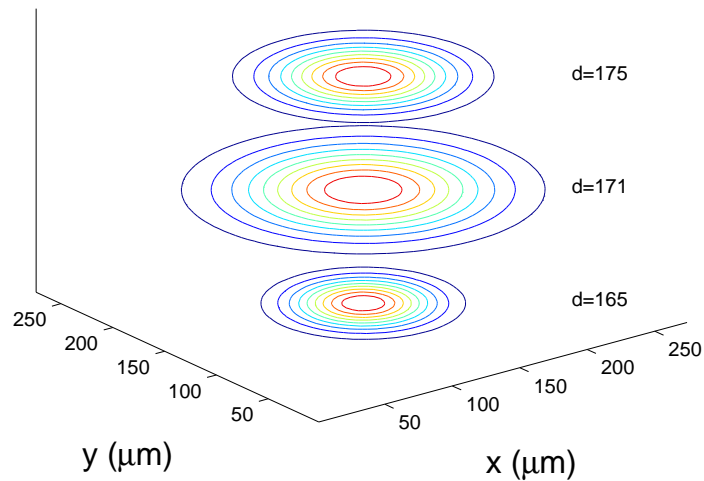


Figure 5.6: Stack of three contour plots of the intensity distribution at the microscope object plane for different distances between the microscope objective and the tube lens in the Zemax model. The three contour plots correspond to the three line profiles given in Figure 5.5 (b).

5.4.2 Filters

The other major change to the RASI setup was the addition of a laser line filter and an edge pass filter to the layout, their purpose was to improve the performance of the system by blocking background or stray light, as well as elastically scattered photons from the laser, from entering the spectrometer. Furthermore a dichroic mirror was used to couple the laser into the RASI optical path, though it also acted as a filter in the optical path. Each filter had a specific purpose and needed to be positioned according to their transmission profiles in order to operate effectively, which will be described in this section, the locations of the filters are noted in Figure 5.8.

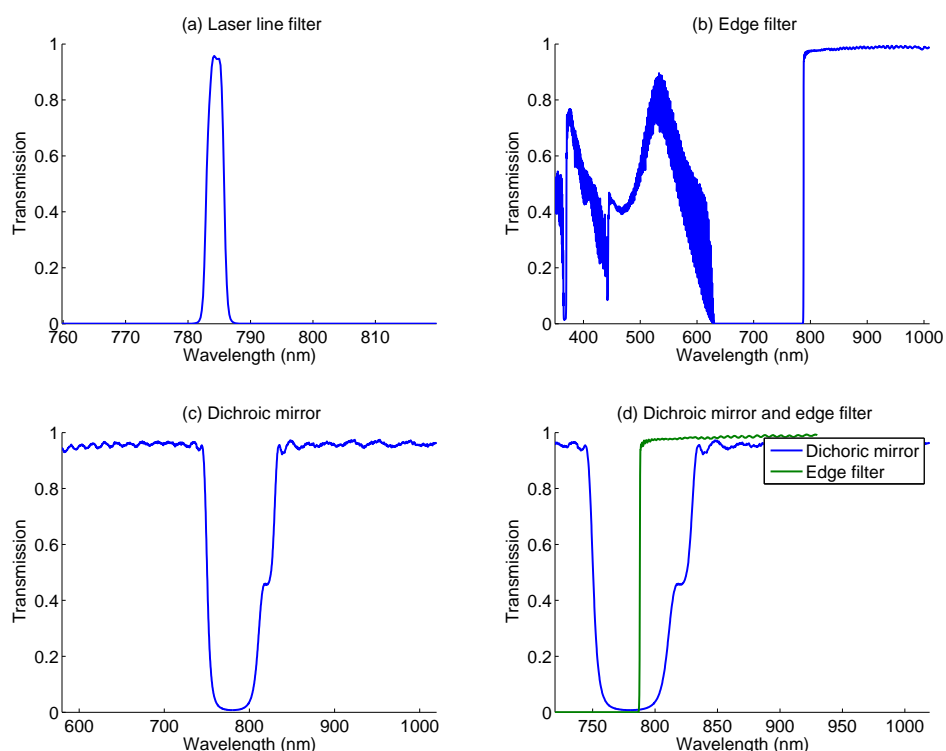


Figure 5.7: Plots of the filter added to RASI system; (a) is the transmission profile of the laser line filter, (b) the edge filter, (c) the dichroic mirror and (d) plots the edge filter and dichroic mirror around 785 nm.

The spectral profile of the laser is shown in Figure 5.2. The purpose of the laser line filter (labelled as F1 on Figure 5.8), whose transmission curve is shown in Figure 5.7, was to attenuate the extra light generated by the diode laser at wavelengths away from the central peak, which diode lasers are known to generate; the spectral profile of the laser is shown in Figure 5.2. The extra light was a source of background noise that could have easily contaminated, or potentially overwhelmed any Raman signal gathered by the spectrometer. The filter was placed in the collimated beam of the laser, before it combined with the primary RASI optical path, this was to reduce the amount of extraneous light entering the system.

The edge filter, shown in Figure 5.7, was placed before the entrance of the spectrometer, it is labelled as F3 in Figure 5.8. It blocked any light at a wavelength lower than the cut-off wavelength of 785 nm. This had the effect of removing stray light at shorter wavelengths, including any Stokes scattered Raman signal. It also helped to prevent any elastically scattered light from the laser from entering the spectrometer. The transmission spectrum at wavelengths lower than 640 nm is erratic and allows visible wavelengths to pass, which was a problem for the illumination system of the RASI system, though easily solved by using a bandpass filter at a higher wavelength to filter the illumination or otherwise switching off the light source while collecting data.

A dichroic mirror was used to couple the laser beam into the RASI optical path, the beam was incident on the mirror at 45° and was reflected into the back aperture of the microscope objective. Light of other wavelengths that were incident on the dichroic were transmitted according to the transmission curve shown in Figure 5.7 (c), resulting in any light from the laser that was back reflected from the sample being attenuated. The transmission profiles of the edge filter and dichroic mirror are compared in Figure 5.7 (d), it is noticeable how far the dip in transmission of the dichroic extends into the longer wavelength region, almost to 830 nm, resulting in decreased signal in this region of the spectrum.

Finally, the Kaiser Holospec spectrometer includes a laser line blocker that blocks the elastically scattered laser light, this filter is denoted as F4 in Figure 5.8. In summary the filters added to the system improved performance by helping to prevent elastically scattered light from the laser entering the spectrometer, though at the cost of a reduced photon count in a portion of the spectrum, up to 830 nm, due in particular to the dichroic mirror. Furthermore they removed background and scattered light from the system which could have degraded the quality of the Raman spectra obtained by the spectrometer.

5.4.3 *Experimental alignment*

In what follows the necessary experimental alignments to finish coupling the laser into the RASI system are described. While the Zemax model and the system diagram in Figure 5.8 show the positions of the various parts added to the optical system, the distance between the tube lens and microscope objective needed to be set experimentally, also since the beam width was much smaller than the microscope FOV the position of the beam had to be moved until it overlapped with the RASI FOV. Otherwise, a region of the sample would be illuminated where no signal could be collected from.

A mineral sample which was a strong Raman scatterer was placed over the microscope objective so that it filled the RASI FOV. Then, multiple slits were opened on the DMD, the tube lens distance and position of the mirror, M3, were adjusted until the intensity measured at the slits was optimised. The mineral used was called Crocoite,

supplier of minerals and crystals, while the reference spectrum was taken from an online database of mineral spectra [7].

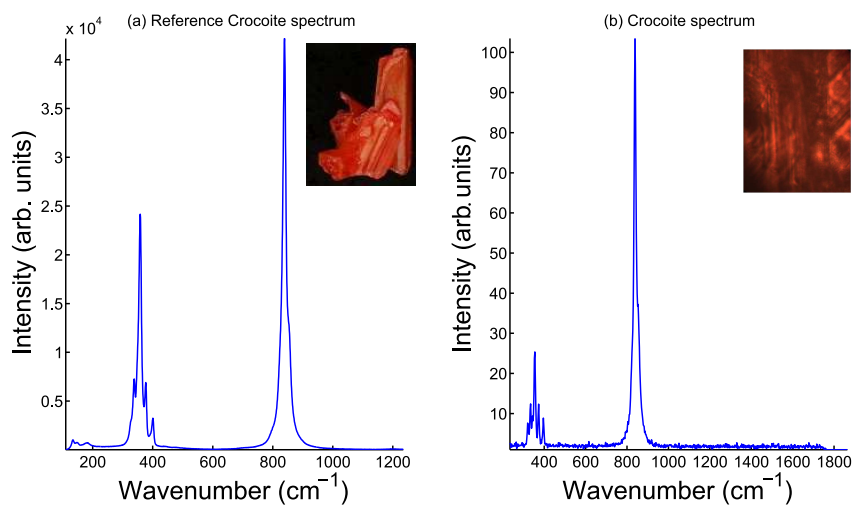


Figure 5.9: (a) shows the reference spectrum obtained, in the top right corner is an image of the Crocoite crystal from the reference data. (b) is the Raman spectrum measured directly with RASI, in the top right corner of the spectrum is the image of the crystal obtained via the RASI microscope.

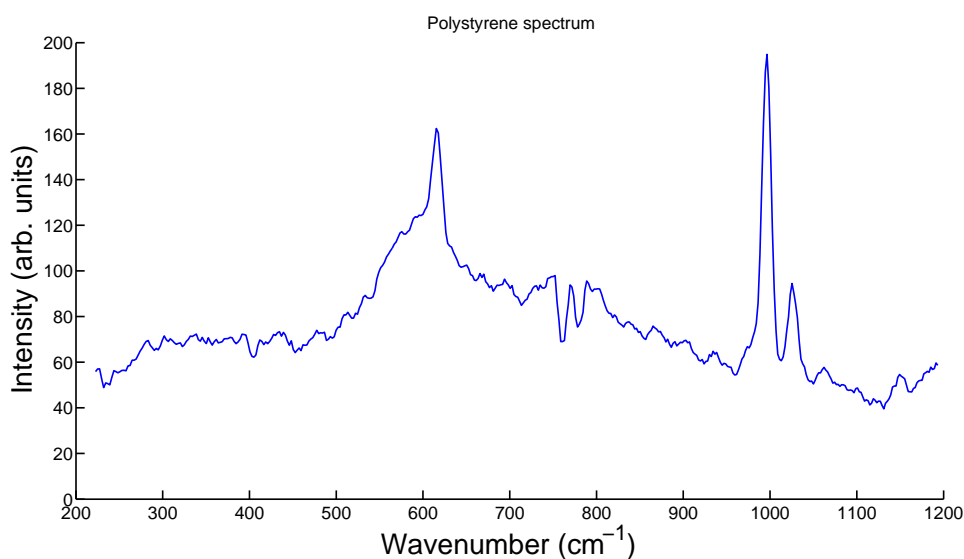


Figure 5.10: The Raman spectrum of polystyrene with characteristic peaks at 618, 997 and 1027 cm^{-1} . The spectrum is smoothed with a moving average filter.

Figure 5.9 shows a reference spectrum of Crocoite and the spectrum acquired from the Crocoite sample used in this experiment. Essentially, the Raman spectrum of Crocoite has two distinct sets of features, a group of peaks near 385 cm^{-1} and a single at 838 cm^{-1} , which are present in both the reference and measured spectra, though the relative intensities between the peaks of the reference spectrum and those of the measured spectrum are different. The Raman signal at shorter Raman shifts will be less than expected due to the transmission profile of the dichroic filter which attenuates

up to 830 nm, as shown in Figure 5.7, 830 nm is 678 cm^{-1} for a 785 nm laser. A second Raman spectrum is shown in Figure 5.10, in this example a small piece of polyethylene was placed in the microscope sample plane and the Raman spectrum acquired. The resulting spectrum shows three features expected of a polystyrene spectrum, peaks at approximately 616, 997 and 1027 cm^{-1} .

5.6 Different Sampling approaches

The remainder of this chapter concentrates on describing approaches to sampling a scene with RASI that exploit its unique architecture, namely the ability to acquire voxels in any almost any order from the scene, which enables a representative subset of regions of the total scene to be collected and thereby reducing the collection of unnecessary or unwanted voxels. Similar sampling approaches are often employed during the post processing of hyperspectral datacubes acquired by other means (sequential scanning or snapshot), that is only a subset of the collected data ends up being used for understanding the properties of the entire datacube [83]. The goal here is to describe such alternate hyperspectral sampling approaches, though implemented in the acquisition phase rather than the post processing phase. To that end, a full dataset of a scene was acquired and used as a test case for different approaches.

A single test case was used for all the sampling methods tried, this had the advantage of simplifying the process of acquiring the data as it only needed a single dataset to be collected. Also, this allowed the different techniques to be compared to each other and to the complete set more easily.

In this example, the case considered is that of a so called binary classification, with the scene consisting of two distinct spectral classes distributed over different spatial regions. This was constructed by using a sample of Crocoite that only partially covered the whole RASI FOV and then scanning the whole FOV, with the result being two regions where the Crocoite spectrum was “present” or “not present”. The particulars of the binary classification will be described in more detail in a following section.

While more complex, multi-class problems can be considered the focus here is on determining an approximation to the spatial distribution of the two classes. Binary classifications also correspond to a number of useful classifications scenarios that are important in their own right, e.g. “healthy” or “unhealthy” and “present” or “not present”. Furthermore, binary classification can be extended to multi-class problems, which is the case in various hyperspectral classification algorithms.

The reason for estimating the spatial distribution directly, rather than after collecting the whole dataset is that it shortens the acquisition time and the amount of data collected. Most meaningful spatial distributions of a given quantity will consist of a

region with borders, the purpose of any approximation is to reconstruct the borders, thereby accurately dividing the scene into its distinct regions accurately. The approaches to sampling can be based on some blind random sampling or grid based method, though these ignore the spatial information available from the imaging channel of RASI. Using the imaging channel as a reference, regions to sample can be selected directly, or via some basic image processing method. After the sampling, the structure of the scene was reconstructed using a nearest-neighbor interpolation.

In what follows, the details of the test case used to demonstrate the various sampling methods will be given, then examples of the different sampling methods will be shown, the results of each will be compared with the full test case results. Finally there will be some discussion of extending the results to more complex cases.

5.6.1 Test case overview

To obtain the data for the test case, a fragment of Crocoite crystal was placed such that it partially obscured the RASI FOV. Then, the FOV was scanned sequentially using apertures consisting of 10 by 10 DMD pixels, the result of this scan was a 100 by 30 data set of Raman spectra. Each vertical column of the resulting data set contained 100 elements, with 30 elements in the horizontal direction, it was taken from the central region of the image of the RASI FOV shown in Figure 5.11 (a). Most of the spectral information was contained in the two peaks of the Crocoite spectrum, the intensity distributions of the two peaks across the spatial region are shown in Figure 5.11 (b) and (c), with (d) showing the intensity from a peak-less region. The distribution at these wavenumbers broadly matches the image, with the intensity being higher on the regions with Crocoite and effectively null on the empty region.

Using the spectral information, two spectral classes were generated for the purpose of labeling every pixel in the data set. The classes were the Crocoite class and an empty class, essentially a flat spectrum. A large degree of variation was present in the spectrum collected at various points; to account for all this variation numerous spectra were combined into a single training set for the Crocoite class. Spectral variability can be caused by non-uniform illumination, differences in surface texture or the presence of impurities in the sample, it is an ever present issue in spectral classification and, in this case is countered by creating a robust training set for the classification. Similarly for the empty training set, numerous spectra were used in the training set. In total 18 and 14 spectra were used in the Crocoite and empty training sets, respectively, these can be seen in Figures 5.12 (a) and (b). Further a plot of the intensity values at the two Crocoite peak wavenumbers for all the spectra in both training sets is shown in Figure 5.12 (c), the values from the different spectra can be easily separated visually, showing that both classes are distinct.

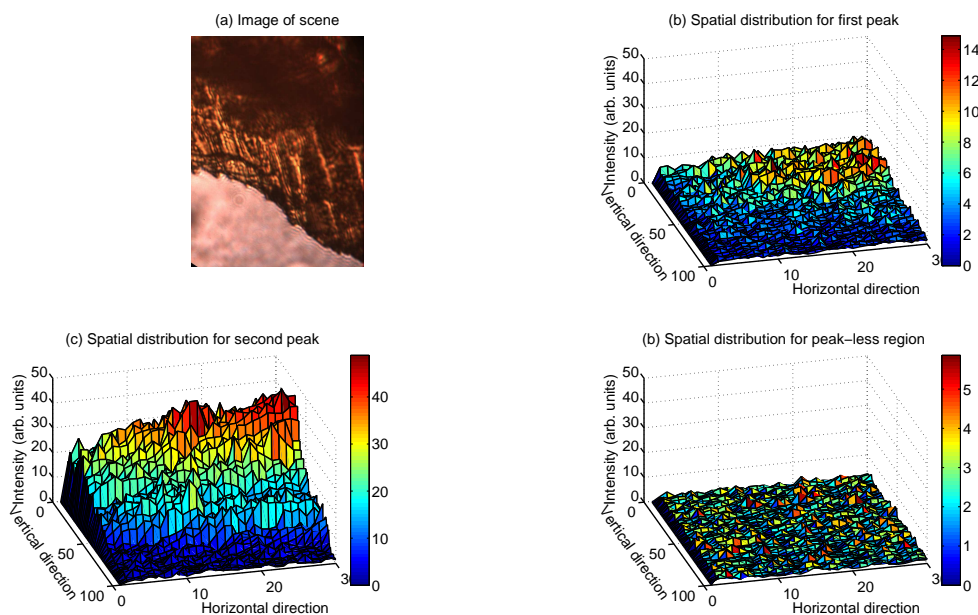


Figure 5.11: (a) shows the image of the Crocoite fragment as seen through the imaging camera. (b), (c) and (d) show the intensities at three different wavenumbers across the scene as measured by the spectrometer

The purpose of using these two robust spectral classes was to set up a binary classification problem. In later sections where alternate spatial sampling methods will be described, the same spectral classification approach will be used, the focus will be on approximating the spatial distribution of the classes, which for the full test case is shown in 5.12 (d).

The most salient spatial structure in the test case was the border between the two different classes, it can be seen to correspond to the visual difference between the parts of the scene image (Figure 5.12 (a)) where Crocoite is, and is not present. Though there are clearly small regions that are intermingled with the Crocoite region which contain the empty class spectrum, this was likely due to some impurity present in the crystal or other contamination that resulted in the null Raman spectra. For the purpose here, the physical reason had little significance, except in so far as these small outlier regions added complexity to approximating the overall spatial distribution.

Various approaches to sampling the scene will be discussed in the following sections that will reconstruct the test case to varying degrees. Only a single structure in the data set will be concentrated on, the border between the two classes, focusing on this aspect of the reconstruction makes the process more straightforward, however the results from this binary classification can be extended to more complex multi-class problems, though that will not be examined in this thesis. These approaches were demonstrated using the test case described here; by indexing the full array using the same method as the sampling method under test, a real experiment was simulated, it was then possible to

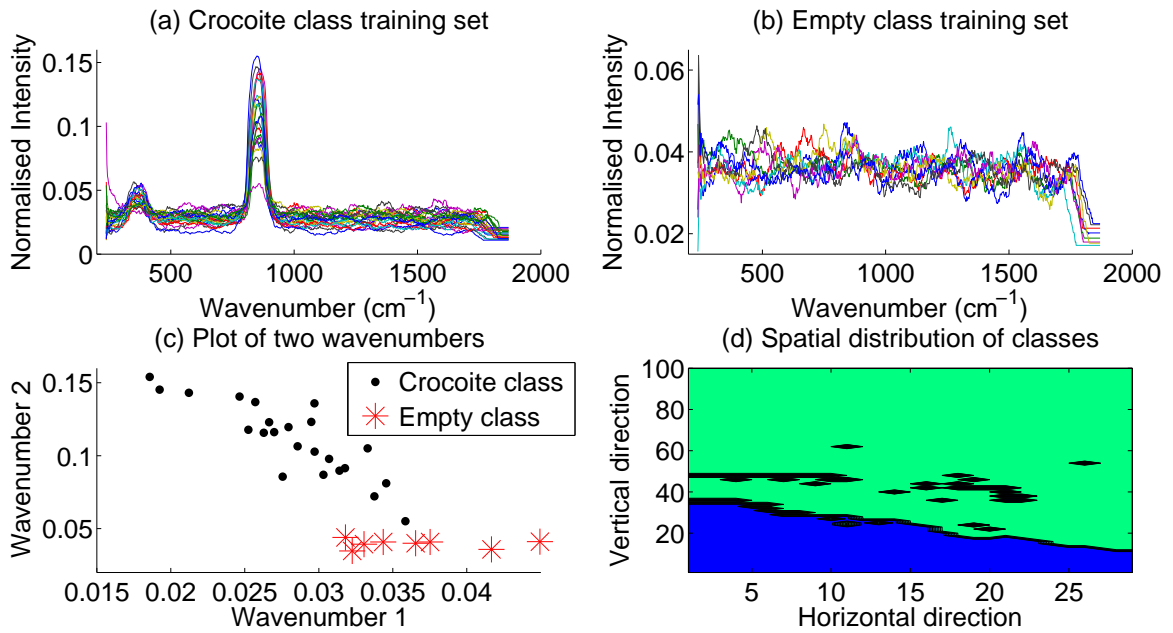


Figure 5.12: (a) and (b) show the spectra used in the training sets for the Crocoite class and the empty class, respectively. (c) is a plot of the wavenumbers of the two Crocoite peaks against each other, for the spectra in the training set, (d) is a contour plot of the classification result with the line showing the border between the two classes. Green represents the Crocoite class and blue the null class.

compare the results from the different approaches to the full data set, which acted as a reference.

5.6.2 Blind random sampling

As a first example, the scene was randomly sampled without replacement, this approach relied completely on the spectroscopy channel of RASI, ignoring any information from imaging channel. Random sampling is a common sampling method where, each point in the scene has an equal chance of being selected. An extra condition was added to the sampling process that limited the number of samples per row to 1, so as to simulate the limitation imposed by the possibility of spectral overlap in the actual RASI instrument.

The random sampling strategy generally provides each subject in a population set with an equal probability of being selected. As a result of this, it provides a fair way of selecting representative samples, though it is subject to a degree of luck, But, so long as the subset extracted is representative of the total dataset, then it is still reasonable to use random sampling.

In the context of the test case, at most 100 points could be selected in a given measurement set. To randomly select points, subject to the constraint, firstly the vertical index was selected at random without replacement, this stopped vertical indices being selected twice in a measurement set and, thereby preventing spectral overlap. Then,

the possible horizontal values for that vertical index were listed - values that had been selected in a previous list were removed from this list - and an index selected at random. A Matlab function, *datasample* was used for the randomised selection, for repeatability all the random values and the order they were generated, were stored in an array. Index coordinates were generated and stored until each coordinate in the test case was sampled, this set of random points were used to sample the test in varying amounts and subsequently reconstruct the classification map.

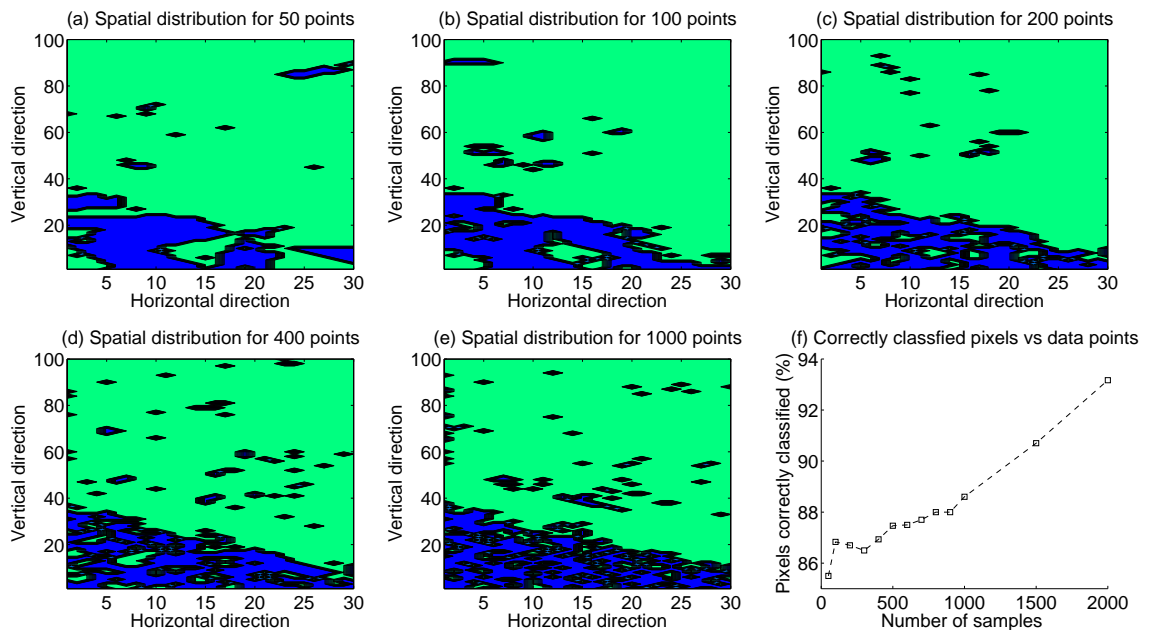


Figure 5.13: Here, Figures (a) - (e) show the reconstructed spatial distribution of the two classes for different amounts of samples, the green represents the Crocoite class and blue the null class. (f) shows a plot of the percentage of correctly classified pixels for different numbers of samples, even for the lowest then number is above 85%.

Shown in Figure 5.13 are the results from the classification reconstructions for various numbers of points in the scene sampled. Once a subset was collected, a classification map was generated using a “k Nearest Neighbour” (k-NN) approach. At each point in the 100 by 30 array of potential points, the k nearest measured pixels were determined, the distance to the nearest points was calculated using a Euclidean distance metric. A majority vote of the k points was used to determine the class of the data point in question, for example with $k = 5$, a data point which had of its 5 closest known points, 3 which were the Crocoite class and 2 which were the empty class, then that point would be set as the Crocoite class. Since in the examples here a binary classification was used, then selecting k to be an odd number ensured no vote would be tied.

Results of the k-NN reconstructions are shown in Figures 5.13, Figures 5.13 (a)-(e) show the classification maps for the spatial distribution for different numbers of points collected. As the number of points collected increases the accuracy increase, this

is shown in Figures 5.13 (f), where the number of correctly classified points for different numbers of points is shown. The reconstructed classification maps were compared to the full map from the test case shown Figure 5.12 (d) to determine the number of correctly classified pixels. As the number of points collected increases the reconstruction accuracy increases, though this can be dependent on the distribution of collected points, as the accuracy decreases slightly for the values in the graph in Figures 5.13 (f), before increasing again. But even for the initial case, where only 50 points were collected, more than 85% of the pixels were correctly classified, though that is less clear from the visual representation in Figures 5.13 (a) for that case. The overall number of correctly classified pixels does not increase much with an increase in the number of samples collected over the initial 50 sample set, for 1500 points the accuracy is roughly 91% a 6% change for a 30 fold increase in the number of points collected.

The classification reconstruction results indicate, in this case at least, it was sufficient to sparsely sample a scene to effectively represent the majority of the information present. Indeed, only 50 randomly selected points were required to reconstruct the classification map of the whole scene using a k-NN algorithm to within 85% accuracy of the fully sampled classification map. This is consistent with statements earlier in the thesis that in most cases, spatial features are highly correlated, which implies that it is possible to predict the value at one location from a nearby location via an interpolation method, as has been demonstrated here.

5.6.3 Systematic sampling approach

Systematic sampling methods acquires samples in an ordered way from the overall population. Other spectral imaging systems, such as the spatial or wavelength scanning based methods, use a systematic sampling approach, however due to their fixed apertures the form of that approach is limited. RASI has the option of generating any aperture or distribution of apertures so it can implement systematic sampling approaches other methods cannot. Here, will be discussed an example of grid based sampling, that is where a regular grid is placed across the FOV, grids of different densities will be shown. The k-NN method for interpolation used previously was used here as well.

Compared to random sampling, systematic methods can provide better coverage of the area, avoiding the possibility of sample points clustering. Providing the grid samples the features present in the data it can be used as representative of the population. If the different spatial regions are not sampled sufficiently this could introduce a bias in the collected data, this can be avoided with a sufficiently dense grid of points.

Grids with 30, 50 and 100 points were constructed to demonstrate the systematic sampling of the test case, the sampling points were chosen so as to form a grid across the whole scene. For a given number of samples, the number of points in the horizontal

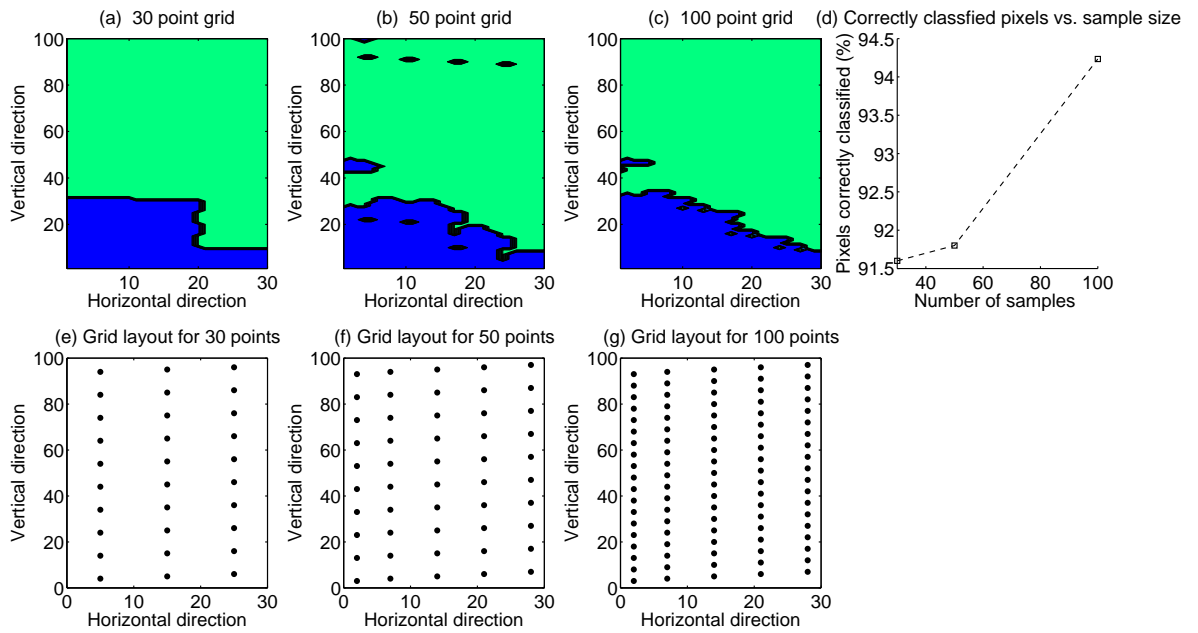


Figure 5.14: This figure shows the reconstructed classification maps for different grids in parts (a) - (c), green represents the Crocoite class and blue the null class, part (d) shows the number of correctly classified pixels for each grid size. (e) - (g) show the positions of the sampling points used for each grid with respect to each other. A value of $k = 1$ was in the kNN algorithm for the 30 point grid and $k = 3$ was used for the 50 and 100 point grids, the accuracy of the reconstruction increases, as before, with the increase in number of points used in the reconstruction.

and the vertical directions were chosen, then the points were placed in a grid equidistant with respect to each other. The points were staggered in the vertical direction so as to account for the avoidance of spectral overlap, these distributions of points with respect to each other are shown in Figures 5.14 (e) - (g), for the three different grid sizes.

The classification maps were reconstructed for the different grids, these are shown in Figures 5.14 (a) - (c), the k-NN approach was used with $k = 1$ for the 30 point grid and $k = 3$ for the other two grids, due to the number of points present. The classification accuracy is shown in Figure 5.14 (d), even for the sparsest grid - with 30 points - the accuracy was above 90%, higher than the accuracy obtained for the random sampling used previously.

Using a grid based sampling pattern exploited, in this case, the high degree of spatial correlation for the two classes, essentially that the two classes occupied continuous spatial regions. This made it possible to get improved reconstruction results for smaller numbers of points than used in the random sampling method. Finer grids could be used for cases with different spatial distributions, though as with any systematic approach the form of the sampling pattern would need to be tailored to the actual spatial distribution present.

5.6.4 Overview of sampling methods

Random sampling and grid based sampling are both examples of taking a subset of a larger population and using the subset to make inferences about the total population. In the examples above a classification map of the whole image (whole population) was generated from the data acquired from the sampling processes. While overall classification accuracy for the interpolated classification was high in both cases, differences between the two results can be seen in the representations of the maps, random sampling resulted in more small variations scattered about the map, whereas the grid sampling approach created a smoother result. Small spatial variations were also present in the true data set, so in that regard the random sampling reproduces that aspect better than the grid sampling, but, the overall accuracy of the grid sampling is consistently higher for lower number of points.

The importance of reproducing the small, local variations in the spatial distributions of the classes depends on the analysis being performed, methods that are interested in the spatial distribution over a large area - a significant portion of the total image area - often smooth out small variations. In other cases, these small variations can be of interest as indicators, of say impurities present in a sample, which can be a useful metric in quality control assessment.

Numerous other ways of extracting a subset from a population are possible, the methods described here are a simple and robust approach to sampling that are commonly employed in statistical sampling in general. Other methods can take account of prior knowledge, which in the case of RASI could be estimated from the colour image measured. Indeed, many current hyperspectral imaging classification algorithms combine spatial parameters in their classifiers. These measure the degree of spatial correlation between adjacent pixels and neighbourhoods of pixels and have been shown to improve classification performance. In principle, RASI could determine spatial correlation parameters using the colour image and then combine these parameters to help construct a more general type of classifier that would be unique to RASI.

An iterative approach could adapt the sampling distribution to the changing content in a scene, thereby combining some of the elements of dynamic spectral imaging discussed in the previous chapter with the capacity to reconstruct full spatial distributions of characteristics demonstrated in this chapter.

5.7 Chapter summary

This chapter described the background to Raman spectroscopy and the underlying aspects that affect the performance of Raman spectroscopic instruments, such as laser illumination wavelength. Methods that combine hyperspectral imaging and Raman spec-

troscopy were discussed in the context of the illumination method, comparing point based and global illumination layouts. The necessary changes to incorporate Raman spectroscopy into the RASI system were described: a ray trace model of the illumination and the necessary optical filters was presented. Example spectra of a mineral called Crocoite and a sample of Polystyrene were also shown.

Alternate spatial sampling methods were demonstrated using a test case that was generated using the Raman spectra of Crocoite. To that end, a binary classification problem was created, using a Crocoite sample in an image, such that there were two regions where Crocoite was “present” or “not present”. This scene was scanned by RASI to create a test case, this test case was then used to simulate different sampling methods. Two methods were tested: a random sampling approach and a grid based method. A full classification map was constructed for different numbers of samples in each case using a k-Nearest Neighbour interpolation algorithm, the results show that the original dataset could be estimated with high fidelity. Finally, other potential sampling approaches that could be used with RASI were discussed.

Chapter 6 – Conclusions

This thesis has explored an alternate approach to spectral imaging, where a spatially sparse subset of the whole hyperspectral image is recorded, which was termed Random access spectral imaging (RASI). This approach helps to overcome some of the common bottlenecks in high-resolution dynamic spectral imaging and opens up new possible approaches in sampling a hyperspectral scene. The enabling technology used to achieve RASI is the digital micromirror device (DMD) which allowed the acquisition of spatial and spectral information to be de-multiplexed into different optical paths of the same optical system. This thesis contains a description of the development of the idea of RASI; the concept and construction of a RASI device with a DMD; and demonstrations of applications of RASI. In what follows a summary of each chapter will be given followed by some possibilities for future work leading from this thesis.

6.1 Thesis Summary

This section provides a brief summary of the thesis on a chapter by chapter basis, of which there were 5 excluding the current.

Initially, in Chapter 1, the basics of spectral imaging and by extension hyperspectral and multispectral imaging were described, this was followed by a review of different time-sequential and time-resolved spectral imaging devices, the purpose of which was to show the merits and limitations of the different approaches and, that spectral imaging devices consist of a series of performance trade-offs or bottlenecks, which must be considered for a given application. Random-access spectral imaging was then introduced fully, by describing the meaning of the term and the bottlenecks in achieving dynamic, high resolution spectral imaging and how a RASI approach could overcome or circumvent the bottlenecks. A survey of relevant multi-object spectroscopy devices and DMD based optical systems were also described, so as to lay the basis for the construction of the RASI system.

The optical design of RASI was introduced in Chapter 2, the concept for the device was shown and how it would be implemented with the DMD was explained. The geometrical optical properties of the DMD were discussed and the limits they set on the overall design described, the use of telecentric lenses in the system was also discussed. The Scheimpflug condition, which was required to keep the different conjugate planes of the optical system in focus, for the off-axis design was explained and extended to describe telecentric lenses. The potential illumination options were detailed and an off-axis illumination of the DMD was selected to allow easier alignment of the spectrometer. Distortion from the spectrometer was also considered, and the inclusion of the Kaiser

Holospec f1.8 spectrometer in the system was described. The system throughput and by extension the etendue relations were derived for a DMD limited system. Finally, a ray trace model (using ray trace software Zemax) of a potential system was used to demonstrate the optical design, including demonstrating the Scheimpflug condition for the different optical paths in the RASI system.

Chapter 3 described the experimental components, layout and construction of the RASI system, followed by calibration and stray light characteristics. The basic layout was given, as well as details about the components: the DMD, the telecentric lenses and the Kaiser Holospec spectrometer. The completed layout was shown in a computer aided design (CAD) drawing and images of the breadboard system were shown. Additionally, a microscope coupled to the RASI was also built and the details of the Koehler illumination and the microscope were shown. Methods were developed for the geometric calibration of the DMD with the imaging arm and spectroscopic arm of RASI, for the spectroscopy arm the results were shown at a range of different wavelengths. The resolution of the system for different apertures sizes was calculated for the IR grating. The presence of background scattering from the backplane of the DMD was shown, and a means of removing it was devised, spectral crosstalk was also discussed. The signal to noise relation for a given DMD aperture was also given.

The focus of Chapter 4 was to demonstrate RASI, first a simple example where a number of points from across the field of view were selected and the spectrum from those points was extracted, as in a multi-object spectrometer. To demonstrate dynamic spectral imaging, an experiment to measure the change of spectrum for red blood cells undergoing de-oxygenation was performed. The background motivation and necessary theoretical considerations for calculating the absorbance of a red blood cell were presented, the results show the expected change in spectrum which was calculated for intermediate stages in the process using linear spectral unmixing, measurements were taken from ten red blood cells simultaneously. The issue of spectral overlap and examples of overcoming it using some techniques from linear spectral unmixing were presented as well.

As a demonstration of the adaptability of the RASI system, it was modified for Raman spectroscopy and alternative spatial sampling schemes for hyperspectral imaging were investigated in Chapter 5. The background and practical considerations of implementing Raman spectroscopy were discussed and a global illumination method was designed and added to the RASI layout. The Raman spectrum of a mineral, Crocoite, was collected and compared to a reference spectrum to show the collection of Raman spectrum, a spectrum of polyethylene was also shown. A binary classification problem was constructed and used to simulate different sampling schemes; both random sampling and a systematic grid sampling methods were tested for different numbers of samples and, were shown to reconstruct a classification map with high fidelity.

6.2 Recommendations for future work

This thesis has shown a practical design for the construction of a RASI device and demonstrated dynamic spectral imaging of red blood cells. RASI has been extended to collect Raman spectra and this has been used to show alternate spatial sampling methods that are not possible for other spectral imaging devices, and were used to construct classification maps with high accuracy.

The optical design of the RASI system used in this system, while functional, could be improved upon. Primarily the imaging and re-imaging optics of the DMD could be improved with the use of custom optics to increase the numerical aperture and hence the etendue of the system, bringing the incident f-number from $f/6$ to close to the limit of $f/2.4$ for the DMD. This would lead to an overall improvement in the performance of RASI, though it should be noted designing low f-number for telecentric lenses is difficult and they are currently expensive to manufacture.

The dynamic spectral imaging would benefit from an increase in optical throughput; also the development of a bespoke tracking algorithm for tracing the positions of red blood cells could improve the performance of that experiment.

In terms of applications in Raman spectroscopy, the implementation of a point illumination to complement the DMD apertures could improve performance over the current global illumination. This could in principle be achieved using a spatial light modulator to create a pattern of spots over the FOV.

Beyond the practical improvements mentioned above, it should be possible to implement numerous approaches to spatial sampling that are not possible with other spectral imaging systems due to their fixed apertures. Building upon the sampling methods used in this thesis, sampling grids with point densities could be tested, further they could be constructed based on information from the imaging channel of RASI. This is potentially a rich area of exploration, as numerous statistical sampling methods could be potentially imported from other fields, where they have already been developed for making inferences about different, large population structures.

Another potentially novel area to explore would be the combination of data from the imaging channel and the spectroscopy in the manner of data fusion. Examples exist in the literature of the fusion of panchromatic images and hyperspectral images to improve spatial resolution or fill in blank areas in the hyperspectral image. Approaches such as these could be built upon to create a data fusion paradigm based on the information provided by RASI.

References

- [1] *Wavelength transmittance considerations for DLP® DMD window*, tech. report, Texas Instruments Incorporated, 11 2012.
- [2] C.] LAWSON AND R. HANSON, *Front Matter*, ch. 0, pp. i–xiv.
- [3] N. ACITO, G. CORSINI, AND M. DIANI, *Statistical analysis of hyper-spectral data: a non-gaussian approach*, EURASIP J. Appl. Signal Process., 2007 (2007), pp. 13–13.
- [4] J. ALLINGTON-SMITH, *Basic principles of integral field spectroscopy*, New Astronomy Reviews, 50 (2006), pp. 244 – 251.
- [5] A. ALRIFAIY AND K. RAMSER, *How to integrate a micropipette into a closed microfluidic system: absorption spectra of an optically trapped erythrocyte*, Biomed. Opt. Express, 2 (2011), pp. 2299–2306.
- [6] J. M. AMIGO, C. RAVN, N. B. GALLAGHER, AND R. BRO, *A comparison of a common approach to partial least squares-discriminant analysis and classical least squares in hyperspectral imaging*, International Journal of Pharmaceutics, 373 (2009), pp. 179 – 182.
- [7] T. ARMBRUSTER AND R. M. DANISI, *Highlights in Mineralogical Crystallography*, 2015.
- [8] A. BANKAPUR, E. ZACHARIAH, S. CHIDANGIL, M. VALIATHAN, AND D. MATHUR, *Raman tweezers spectroscopy of live, single red and white blood cells*, PLoS ONE, 5 (2010), p. e10427.
- [9] A. BATESON AND B. CURTISS, *A method for manual endmember selection and spectral unmixing*, Remote Sensing of Environment, 55 (1996), pp. 229 – 243.
- [10] R. E. BELL, *Exploiting a transmission grating spectrometer*, Review of Scientific Instruments, 75 (2004).
- [11] B. C. BIGELOW, A. M. DRESSLER, S. A. SHECTMAN, AND H. W. EPPS, *Imacs: the multiobject spectrograph and imager for the magellan i telescope*, in Astronomical Telescopes & Instrumentation, International Society for Optics and Photonics, 1998, pp. 225–231.

- [12] A. BODKIN, A. SHEINIS, A. NORTON, J. DALY, C. ROBERTS, S. BEAVEN, AND J. WEINHEIMER, *Video-rate chemical identification and visualization with snapshot hyperspectral imaging*, in SPIE Defense, Security, and Sensing, International Society for Optics and Photonics, 2012, pp. 83740C–83740C.
- [13] M. BORN AND E. WOLF, *Principles of Optics*, Cambridge University Press, 1998, 1998.
- [14] J. H. BOWLES, J. A. ANTONIADES, M. M. BAUMBACK, J. M. GROSSMANN, D. HAAS, P. J. PALMADESSO, AND J. STRACKA, *Real-time analysis of hyperspectral data sets using nrl's orasis algorithm*, in Optical Science, Engineering and Instrumentation'97, International Society for Optics and Photonics, 1997, pp. 38–45.
- [15] J. W. BOWRON AND R. P. JONAS, *Off-axis illumination design for dmd systems*, in Optical Science and Technology, SPIE's 48th Annual Meeting, International Society for Optics and Photonics, 2003, pp. 72–82.
- [16] G. BRAGATO, *Fuzzy continuous classification and spatial interpolation in conventional soil survey for soil mapping of the lower piave plain*, *Geoderma*, 118 (2004), pp. 1 – 16.
- [17] K. BRIELY-SABO AND A. BJORNERUD, *Accurate de-oxygenation of ex vivo whole blood using sodium dithionite*, in Proc. Intl. Sot. Mag. Reson. Med, vol. 8, 2000, p. 2025.
- [18] G. BROOKER, *Modern Classical Optics*, Oxford University Press, 2008.
- [19] E. CANDÉS AND M. WAKIN, *An introduction to compressive sampling*, *Signal Processing Magazine, IEEE*, 25 (2008), pp. 21 –30.
- [20] J. C. CARTER, J. SCAFFIDI, S. BURNETT, B. VASSER, S. K. SHARMA, AND A. . S. S. MICHAEL ANGEL”, *Stand-off raman detection using dispersive and tunable filter based systems*, *Spectrochimica Acta Part A: Molecular and Biomolecular Spectroscopy*, 61 (2005), pp. 2288 – 2298. Georaman 2004: Sixth International Conference on Raman Spectroscopy Applied to the Earth and Planetary Sciences Georaman 2004: Georaman 2004: Sixth International Conference on Raman Spectroscopy Applied to the Earth and Planetary Sciences.
- [21] C.-I. CHANG, H. REN, AND S.-S. CHIANG, *Real-time processing algorithms for target detection and classification in hyperspectral imagery*, *Geoscience and Remote Sensing, IEEE Transactions on*, 39 (2001), pp. 760–768.

- [22] C.-I. CHANG, X.-L. ZHAO, M. ALTHOUSE, AND J. J. PAN, *Least squares subspace projection approach to mixed pixel classification for hyperspectral images*, *Geoscience and Remote Sensing, IEEE Transactions on*, 36 (1998), pp. 898–912.
- [23] C.-M. CHANG AND H.-P. D. SHIEH, *Design of illumination and projection optics for projectors with single digital micromirror devices*, *Appl. Opt.*, 39 (2000), pp. 3202–3208.
- [24] J. CHAVES, *Introduction to Nonimaging Optics*, Taylor Francis Group, 2008.
- [25] X. CHEN, B. BIN YAN, F. JUN SONG, Y. QUAN WANG, F. XIAO, AND K. ALAMEH, *Diffraction of digital micromirror device gratings and its effect on properties of tunable fiber lasers*, *Appl. Opt.*, 51 (2012), pp. 7214–7220.
- [26] M. P. CHRISTENSEN, G. W. EULISS, M. J. MCFADDEN, K. M. COYLE, P. MILOJKOVIC, M. W. HANEY, J. VAN DER GRACHT, AND R. A. ATHALE, *Active-eyes: an adaptive pixel-by-pixel image-segmentation sensor architecture for high-dynamic-range hyperspectral imaging*, *Appl. Opt.*, 41 (2002), pp. 6093–6103.
- [27] R. CONTENT, *New design for integral field spectroscopy with 8-m telescopes*, in *Optical Telescopes of Today and Tomorrow*, A. L. Ardeberg, ed., vol. 2871 of *Society of Photo-Optical Instrumentation Engineers (SPIE) Conference Series*, Mar. 1997, pp. 1295–1305.
- [28] R. CONTENT, *Transparent microslicesIFUs: From 200,000 to 5 millions spectra at once*, *New Astronomy Reviews*, 50 (2006), pp. 267 – 270. *Integral Field Spectroscopy: Techniques and Data Production* *Integral Field Spectroscopy: Techniques and Data Production*.
- [29] R. CONTENT, S. BLAKE, C. DUNLOP, D. NANDI, R. SHARPLES, G. TALBOT, T. SHANKS, D. DONOGHUE, N. GALIATSATOS, AND P. LUKE, *New microslice technology for hyperspectral imaging*, *Remote Sensing*, 5 (2013), p. 1204.
- [30] C. F. CULL, K. CHOI, D. J. BRADY, AND T. OLIVER, *Identification of fluorescent beads using a coded aperture snapshot spectral imager*, *Appl. Opt.*, 49 (2010), pp. B59–B70.
- [31] R. L. DAVIES, J. R. ALLINGTON-SMITH, P. BETTESS, E. CHADWICK, R. CONTENT, G. DODSWORTH, R. HAYNES, D. LEE, I. LEWIS, J. WEBSTER, ET AL., *Gmos: the gemini multiple object spectrographs*, *Optical telescopes of today and tomorrow*, 2871 (1997), pp. 1099–1106.

- [32] M. R. DESCOUR AND E. L. DERENIAK, *Nonscanning no-moving-parts imaging spectrometer*, in SPIE's 1995 Symposium on OE/Aerospace Sensing and Dual Use Photonics, International Society for Optics and Photonics, 1995, pp. 48–64.
- [33] R. A. DEVERSE, R. R. COIFMAN, A. C. COPPI, W. G. FATELEY, F. GESHWIND, R. M. HAMMAKER, S. VALENTI, F. J. WARNER, AND G. L. DAVIS, *Application of spatial light modulators for new modalities in spectrometry and imaging*, in Biomedical Optics 2003, International Society for Optics and Photonics, 2003, pp. 12–22.
- [34] D. S. DEWALD, *Using zemax image analysis and user-defined surfaces for projection lens design and evaluation for digital light processing™ projection systems*, *Optical Engineering*, 39 (2000), pp. 1802–1807.
- [35] A. L. DLUGAN, C. E. MACAULAY, AND P. M. LANE, *Improvements to quantitative microscopy through the use of digital micromirror devices*, in BiOS 2000 The International Symposium on Biomedical Optics, International Society for Optics and Photonics, 2000, pp. 6–11.
- [36] N. DOBIGEON, S. MOUSSAOUI, M. COULON, J.-Y. TOURNERET, AND A. HERO, *Joint bayesian endmember extraction and linear unmixing for hyper-spectral imagery*, *Signal Processing, IEEE Transactions on*, 57 (2009), pp. 4355–4368.
- [37] M. DOUGLASS, *Dmd reliability: a mems success story*, in *Micromachining and Microfabrication*, International Society for Optics and Photonics, 2003, pp. 1–11.
- [38] J. DOWNING, A. A. MURRAY, AND A. R. HARVEY, *Low-cost multi-spectral imaging camera array*, in *Imaging and Applied Optics Technical Papers*, Optical Society of America, 2012, p. JW1A.6.
- [39] D. DUDLEY, W. M. DUNCAN, AND J. SLAUGHTER, *Emerging digital micromirror device (dmd) applications*, (2003), pp. 14–25.
- [40] A. EL GAMAL, *Trends in cmos image sensor technology and design*, in *Electron Devices Meeting, 2002. IEDM '02. International*, Dec 2002, pp. 805–808.
- [41] S. M. FABER, A. C. PHILLIPS, R. I. KIBRICK, B. ALCOTT, S. L. ALLEN, J. BURROUS, T. CANTRALL, D. CLARKE, A. L. COIL, D. J. COWLEY, ET AL., *The deimos spectrograph for the keck ii telescope: integration and testing*, in *Astronomical Telescopes and Instrumentation*, International Society for Optics and Photonics, 2003, pp. 1657–1669.

- [42] W. FATELEY, R. HAMMAKER, AND R. DEVERSE, *Modulations used to transmit information in spectrometry and imaging*, Journal of Molecular Structure, 550–551 (2000), pp. 117 – 122.
- [43] K. C. FEELY AND P. R. CHRISTENSEN, *Quantitative compositional analysis using thermal emission spectroscopy: Application to igneous and metamorphic rocks*, Journal of Geophysical Research: Planets, 104 (1999), pp. 24195–24210.
- [44] B. FEI, H. AKBARI, AND L. V. HALIG, *Hyperspectral imaging and spectral-spatial classification for cancer detection*, in Biomedical Engineering and Informatics (BMEI), 2012 5th International Conference on, IEEE, 2012, pp. 62–64.
- [45] C. FERRARI, G. FOCA, AND A. ULRICI, *Handling large datasets of hyperspectral images: Reducing data size without loss of useful information*, Analytica Chimica Acta, 802 (2013), pp. 29 – 39.
- [46] J. M. FLORENCE AND L. A. YODER, *Display system architectures for digital micromirror device (dmd)-based projectors*, (1996), pp. 193–208.
- [47] B. K. FORD, C. E. VOLIN, S. M. MURPHY, R. M. LYNCH, AND M. R. DESCOUR, *Computed tomography-based spectral imaging for fluorescence microscopy*, Biophysical Journal, 80 (2001), pp. 986 – 993.
- [48] J. FORD, *Red blood cell morphology*, International Journal of Laboratory Hematology, 35 (2013), pp. 351–357.
- [49] T. FOURNEL, S. COUDERT, C. FOURNIER, AND C. DUCOTTET, *Stereoscopic particle image velocimetry using telecentric lenses*, Measurement Science and Technology, 14 (2003), p. 494.
- [50] K. D. FOURSFRING, Z. NINKOV, AND J. P. KERKES, *Scattered light in a dmd based multi-object spectrometer*, in Proc. SPIE, vol. 7739, 2010, pp. 77393X–9.
- [51] ———, *Subpixel scatter in digital micromirror devices*, in MOEMS-MEMS, International Society for Optics and Photonics, 2010, pp. 75960J–75960J.
- [52] C. FUNK, J. THEILER, D. ROBERTS, AND C. BOREL, *Clustering to improve matched filter detection of weak gas plumes in hyperspectral thermal imagery*, Geoscience and Remote Sensing, IEEE Transactions on, 39 (2001), pp. 1410–1420.
- [53] B.-C. GAO, M. J. MONTES, C. O. DAVIS, AND A. F. GOETZ, *Atmospheric correction algorithms for hyperspectral remote sensing data of land and ocean*,

- Remote Sensing of Environment, 113, Supplement 1 (2009), pp. S17 – S24.
;ce:title;Imaging Spectroscopy Special Issue;/ce:title;.
- [54] L. GAO, R. T. KESTER, AND T. S. TKACZYK, *Compact image slicing spectrometer (iss) for hyperspectral fluorescence microscopy*, Opt. Express, 17 (2009), pp. 12293–12308.
- [55] N. GAT, *Imaging spectroscopy using tunable filters: a review*, in AeroSense 2000, International Society for Optics and Photonics, 2000, pp. 50–64.
- [56] B. GEELLEN, M. JAYAPALA, N. TACK, AND A. LAMBRECHTS, *Low-complexity image processing for a high-throughput low-latency snapshot multispectral imager with integrated tiled filters*, in SPIE Defense, Security, and Sensing, International Society for Optics and Photonics, 2013, pp. 87431E–87431E.
- [57] M. E. GEHM, R. JOHN, D. J. BRADY, R. M. WILLETT, AND T. J. SCHULZ, *Single-shot compressive spectral imaging with a dual-disperser architecture*, Opt. Express, 15 (2007), pp. 14013–14027.
- [58] M. S. R. GEHRKE AND A. GREIWE, *Multispectral image capturing with foveon sensors*, ISPRS-International Archives of the Photogrammetry, Remote Sensing and Spatial Information Sciences, 1 (2013), pp. 151–156.
- [59] A. GHIYAMAT, H. Z. M. SHAFRI, G. A. MAHDIRAJI, A. R. M. SHARIFF, AND S. MANSOR, *Hyperspectral discrimination of tree species with different classifications using single-and multiple-endmember*, International Journal of Applied Earth Observation and Geoinformation, 23 (2013), pp. 177–191.
- [60] T. GORDON-SMITH, *Structure and function of red and white blood cells*, Medicine, 37 (2009), pp. 119 – 124. Haematology Part 1 of 2.
- [61] A. GORMAN, D. W. FLETCHER-HOLMES, AND A. R. HARVEY, *Generalization of the lyot filter and its application to snapshot spectral imaging*, Opt. Express, 18 (2010), pp. 5602–5608.
- [62] S. R. GOTTESMAN, *Coded apertures: past, present, and future application and design*, in Society of Photo-Optical Instrumentation Engineers (SPIE) Conference Series, vol. 6714 of Society of Photo-Optical Instrumentation Engineers (SPIE) Conference Series, Oct. 2007.
- [63] R. O. GREEN, M. L. EASTWOOD, C. M. SARTURE, T. G. CHRIEN, M. ARONSSON, B. J. CHIPPENDALE, J. A. FAUST, B. E. PAVRI, C. J. CHOVIT, M. SOLIS, M. R. OLAH, AND O. WILLIAMS, *Imaging spectroscopy and the airborne visible/infrared imaging spectrometer (aviris)*, Remote Sensing of Environment, 65 (1998), pp. 227 – 248.

- [64] D. GUO, A. L. VAN DE VEN, AND X. ZHOU, *Tracking and measurement of the motion of blood cells using optical flow methods*, IEEE journal of biomedical and health informatics, 18 (2014), p. 991.
- [65] R. GUPTA AND R. HARTLEY, *Linear pushbroom cameras*, Pattern Analysis and Machine Intelligence, IEEE Transactions on, 19 (1997), pp. 963–975.
- [66] N. HAGEN AND E. L. DERENIAK, *Analysis of computed tomographic imaging spectrometers. i. spatial and spectral resolution*, Appl. Opt., 47 (2008), pp. F85–F95.
- [67] N. HAGEN, R. T. KESTER, L. GAO, AND T. S. TKACZYK, *Snapshot advantage: a review of the light collection improvement for parallel high-dimensional measurement systems*, Optical Engineering, 51 (2012), pp. 111702–1–111702–7.
- [68] A. R. HARVEY, D. W. FLETCHER-HOLMES, S. S. KUDESIA, AND C. BEGGAN, *Imaging spectrometry at visible and infrared wavelengths using image replication*, in European Symposium on Optics and Photonics for Defence and Security, International Society for Optics and Photonics, 2004, pp. 190–198.
- [69] W. D. HEACOX AND P. CONNES, *Optical fibers in astronomical instruments*, The Astronomy and Astrophysics Review, 3 (1992), pp. 169–199.
- [70] E. HECHT, *Optics (4th Edition)*, Addison Wesley, 4 ed., Aug. 2001.
- [71] E. K. HEGE, D. O’CONNELL, W. JOHNSON, S. BASTY, AND E. L. DERENIAK, *Hyperspectral imaging for astronomy and space surveillance*, in Optical Science and Technology, SPIE’s 48th Annual Meeting, International Society for Optics and Photonics, 2004, pp. 380–391.
- [72] D. HEINZ AND C.-I. CHANG, *Fully constrained least squares linear spectral mixture analysis method for material quantification in hyperspectral imagery*, Geoscience and Remote Sensing, IEEE Transactions on, 39 (2001), pp. 529–545.
- [73] R. HOLZE, *E. smith and g. dent (eds): Modern raman spectroscopy—a practical approach*, wiley, chichester, united kingdom, 2005, 210 + xi p., 24.95 £; isbn 0471497940, Journal of Solid State Electrochemistry, 11 (2007), pp. 558–558.
- [74] A. JOAO AND A. GAMBARUTO, *Image processing in the tracking and analysis of red blood cell motion in micro-circulation experiments*, in Visualization and Simulation of Complex Flows in Biomedical Engineering, Springer, 2014, pp. 133–149.

- [75] W. R. JOHNSON, M. HUMAYUN, G. BEARMAN, D. W. WILSON, AND W. FINK, *Snapshot hyperspectral imaging in ophthalmology*, Journal of Biomedical Optics, 12 (2007), pp. 014036–014036–7.
- [76] J. KATON, *Infrared microspectroscopy. a review of fundamentals and applications*, Micron, 27 (1996), pp. 303 – 314.
- [77] J. KATRAŠNIK, M. BÜRMEIN, F. PERNUŠ, AND B. LIKAR, *Spectral characterization and calibration of aotf spectrometers and hyper-spectral imaging systems*, Chemometrics and Intelligent Laboratory Systems, 101 (2010), pp. 23–29.
- [78] K. J. KEARNEY, M. A. CORIO, AND Z. NINKOV, *Imaging spectroscopy with digital micromirrors*, Proc, SPIE, 3965 (2000), pp. 11–20.
- [79] K. J. KEARNEY AND Z. NINKOV, *Characterization of a digital micromirror device for use as an optical mask in imaging and spectroscopy*, (1998), pp. 81–92.
- [80] N. KESHAVA, J. P. KERESKES, D. G. MANOLAKIS, AND G. A. SHAW, *Algorithm taxonomy for hyperspectral unmixing*, in AeroSense 2000, International Society for Optics and Photonics, 2000, pp. 42–63.
- [81] N. KESHAVA AND J. MUSTARD, *Spectral unmixing*, Signal Processing Magazine, IEEE, 19 (2002), pp. 44–57.
- [82] Y. KIM, J. M. HIGGINS, R. R. DASARI, S. SURESH, AND Y. PARK, *Anisotropic light scattering of individual sickle red blood cells*, Journal of Biomedical Optics, 17 (2012), pp. 040501–1–040501–3.
- [83] E. KOVÁCS, A. SZALÓKI, P. BURAI, J. TAMÁS, ET AL., *Airborne mapping of water retention capacity of light sandy soil*, Analele Universitații din Oradea, Fascicula: Protecția Mediului, 14 (2009), pp. 160–166.
- [84] D. LAZER, R. KENNEDY, G. KING, AND A. VESPIGNANI, *The parable of google flu: Traps in big data analysis*, Science, 343 (2014), pp. 1203–1205.
- [85] J. Y. LEE, M. CLARKE, F. TOKUMASU, J. LESOINE, D. ALLEN, R. CHANG, M. LITORJA, AND J. HWANG, *Absorption-based hyperspectral imaging and analysis of single erythrocytes*, Selected Topics in Quantum Electronics, IEEE Journal of, 18 (2012), pp. 1130 –1139.
- [86] —, *Absorption-based hyperspectral imaging and analysis of single erythrocytes*, Selected Topics in Quantum Electronics, IEEE Journal of, 18 (2012), pp. 1130 –1139.

- [87] S. LIANGROCAPART AND M. PETROU, *Feasibility study on the use of nonlinear spectral unmixing*, in Remote Sensing, International Society for Optics and Photonics, 1999, pp. 159–168.
- [88] D. A. LONG AND P. A. CURRAN, *BOOK TOOLS*, vol. 1, Wiley Online Library, 2002.
- [89] H. LOUHICHI, T. FOURNEL, J. M. LAVEST, AND H. B. AISSIA, *Self-calibration of scheimpflug cameras: an easy protocol*, Measurement Science and Technology, 18 (2007), p. 2616.
- [90] R. F. MARCIA, Z. T. HARMANY, AND R. M. WILLETT, *Compressive coded apertures for high-resolution imaging*, in SPIE Photonics Europe, International Society for Optics and Photonics, 2010, pp. 772304–772304.
- [91] A. D. MCNAUGHT AND A. D. MCNAUGHT, *Compendium of chemical terminology*, vol. 1669, Blackwell Science Oxford, 1997.
- [92] Y. MEURET AND P. DE VISSCHERE, *Contrast-improving methods for digital micromirror device projectors*, Optical Engineering, 42 (2003), pp. 840–845.
- [93] R. D. MEYER, K. J. KEARNEY, Z. NINKOV, C. T. COTTON, P. HAMMOND, AND B. D. STATT, *Ritmos: a micromirror-based multi-object spectrometer*, Proc. SPIE, 5492 (2004), pp. 200–219.
- [94] L. MIAO, H. QI, AND W. SNYDER, *A generic method for generating multispectral filter arrays*, in Image Processing, 2004. ICIP '04. 2004 International Conference on, vol. 5, Oct 2004, pp. 3343–3346 Vol. 5.
- [95] Y. MONNO, M. TANAKA, AND M. OKUTOMI, *Multispectral demosaicking using guided filter*, in IS&T/SPIE Electronic Imaging, International Society for Optics and Photonics, 2012, pp. 829900–829900.
- [96] S. NAYAR, V. BRANZOI, AND T. BOULT, *Programmable imaging using a digital micromirror array*, in Computer Vision and Pattern Recognition, 2004. CVPR 2004. Proceedings of the 2004 IEEE Computer Society Conference on, vol. 1, 2004, pp. I–436–I–443 Vol.1.
- [97] N. C. C. NETWORK ET AL., *Myelodysplastic syndromes. clinical practice guidelines in oncology.*, Journal of the National Comprehensive Cancer Network: JNCCN, 1 (2003), p. 456.
- [98] J. G. NEUMANN, *Dmd based hyperspectral augmentation for multi-object tracking systems*, in SPIE MOEMS-MEMS: Micro-and Nanofabrication, International Society for Optics and Photonics, 2009, pp. 72100B–72100B.

- [99] M. ÁNGELES FERNÁNDEZ DE LA OSSA, J. M. AMIGO, AND C. GARCÍA-RUIZ, *Detection of residues from explosive manipulation by near infrared hyperspectral imaging: A promising forensic tool*, Forensic Science International, 242 (2014), pp. 228 – 235.
- [100] J. PEARLMAN, P. BARRY, C. SEGAL, J. SHEPANSKI, D. BEISO, AND S. CARMAN, *Hyperion, a space-based imaging spectrometer*, Geoscience and Remote Sensing, IEEE Transactions on, 41 (2003), pp. 1160–1173.
- [101] M. Z. PESENSON, I. Z. PESENSON, AND B. MCCOLLUM, *The data big bang and the expanding digital universe: High-dimensional, complex and massive data sets in an inflationary epoch*, Advances in Astronomy, 2010 (2010).
- [102] W. M. PORTER AND H. T. ENMARK, *A system overview of the airborne visible/infrared imaging spectrometer (aviris)*, in 31st Annual Technical Symposium, International Society for Optics and Photonics, 1987, pp. 22–31.
- [103] S. PRAHL, *Molar extinction coefficients of oxy and deoxyhemoglobin compiled by scott prahl*, 1999.
- [104] J. QI AND W.-C. SHIH, *Parallel raman microspectroscopy using programmable multipoint illumination*, Opt. Lett., 37 (2012), pp. 1289–1291.
- [105] K. RAMSER, J. ENGER, M. GOKSOR, D. HANSTORP, K. LOGG, AND M. KALL, *A microfluidic system enabling raman measurements of the oxygenation cycle in single optically trapped red blood cells*, Lab Chip, 5 (2005), pp. 431–436.
- [106] J. RASILLA, S. ARRIBAS, E. MEDIAVILLA, AND J. SEBASTIAN, *Two-dimensional spectroscopy by optical fibres at the wht telescope*, Astrophysics and Space Science, 171 (1990), pp. 301–303.
- [107] S. RI, Y. MATSUNAGA, M. FUJIGAKI, T. MATUI, AND Y. MORIMOTO, *Development of dmd reflection-type ccd camera for phase analysis and shape measurement*, in Optomechatronic Technologies 2005, International Society for Optics and Photonics, 2005, pp. 60490I–60490I.
- [108] S. SCHLÜCKER, M. D. SCHAEBERLE, S. W. HUFFMAN, , AND I. W. LEVIN*, *Raman microspectroscopy: a comparison of point, line, and wide-field imaging methodologies*, Analytical Chemistry, 75 (2003), pp. 4312–4318. PMID: 14632151.
- [109] L. W. SCHUMANN AND T. S. LOMHEIM, *Infrared hyperspectral imaging fourier transform and dispersive spectrometers: comparison of signal-to-noise-based*

- performance*, in International Symposium on Optical Science and Technology, International Society for Optics and Photonics, 2002, pp. 1–14.
- [110] R. G. SELLAR AND G. D. BOREMAN, *Classification of imaging spectrometers for remote sensing applications*, Optical Engineering, 44 (2005), pp. 013602–013602–3.
- [111] A. D. STOCKER AND A. P. SCHAUM, *Application of stochastic mixing models to hyperspectral detection problems*, in AeroSense'97, International Society for Optics and Photonics, 1997, pp. 47–60.
- [112] A. H. SZENTGYORGYI, P. CHEIMETS, R. ENG, D. G. FABRICANT, J. C. GEARY, L. HARTMANN, M. R. PIERI, AND J. B. ROLL JR, *Hectochelle: a multi-object echelle spectrograph for the converted mmt*, in Astronomical Telescopes & Instrumentation, International Society for Optics and Photonics, 1998, pp. 242–252.
- [113] N. TACK, A. LAMBRECHTS, P. SOUSSAN, AND L. HASPELAGH, *A compact, high-speed, and low-cost hyperspectral imager*, in SPIE OPTO, International Society for Optics and Photonics, 2012, pp. 82660Q–82660Q.
- [114] Y. TARABALKA, J. BENEDIKTSSON, AND J. CHANUSSOT, *Spectral x2013;spatial classification of hyperspectral imagery based on partitional clustering techniques*, Geoscience and Remote Sensing, IEEE Transactions on, 47 (2009), pp. 2973–2987.
- [115] N. TATEISHI, Y. SUZUKI, I. CICHA, AND N. MAEDA, *O₂ release from erythrocytes flowing in a narrow o₂-permeable tube: effects of erythrocyte aggregation*, American Journal of Physiology-Heart and Circulatory Physiology, 281 (2001), pp. H448–H456.
- [116] C. G. TINNEY, S. D. RYDER, S. C. ELLIS, V. CHURILOV, J. DAWSON, G. A. SMITH, L. WALLER, J. D. WHITTARD, R. HAYNES, A. LANKSHEAR, ET AL., *Iris2: a working infrared multi-object spectrograph and camera*, in SPIE Astronomical Telescopes+ Instrumentation, International Society for Optics and Photonics, 2004, pp. 998–1009.
- [117] W. TOBLER, *A computer movie simulating urban growth in the detroit region*, Economic Geography, 46 (1970), pp. 234–240.
- [118] G. TURRELL AND J. CORSET, *Raman microscopy: developments and applications*, Academic Press, 1996.
- [119] P. VAN KESSEL, L. HORNBECK, R. MEIER, AND M. DOUGLASS, *A mems-based projection display*, Proceedings of the IEEE, 86 (1998), pp. 1687–1704.

- [120] K. VANDEGRIFF AND J. OLSON, *The kinetics of o₂ release by human red blood cells in the presence of external sodium dithionite.*, Journal of Biological Chemistry, 259 (1984), pp. 12609–12618.
- [121] S. VIVÈS AND E. PRIETO, *Original image slicer designed for integral field spectroscopy with the near-infrared spectrograph for the james webb space telescope*, Optical Engineering, 45 (2006), pp. 093001–093001–6.
- [122] E. S. VOROPAI, I. M. GULIS, A. G. KUPREEV, K. N. KAPLEVSKII, A. G. KOSTYUKEVICH, A. E. RADKO, AND K. A. SHEVCHENKO, *Multi-object spectrometer with micromirror array*, Journal of Applied Spectroscopy, 77 (2010), pp. 285–292.
- [123] A. A. WAGADARIKAR, N. P. PITSIANIS, X. SUN, AND D. J. BRADY, *Video rate spectral imaging using a coded aperture snapshot spectral imager*, Opt. Express, 17 (2009), pp. 6368–6388.
- [124] M. WATANABE AND S. NAYAR, *Telecentric optics for computational vision*, in Computer Vision — ECCV '96, B. Buxton and R. Cipolla, eds., vol. 1065 of Lecture Notes in Computer Science, Springer Berlin Heidelberg, 1996, pp. 439–451.
- [125] F. G. WATSON, *A wide-field multi-object spectroscopy (mos) system*, in 1986 Astronomy Conferences, International Society for Optics and Photonics, 1986, pp. 787–796.
- [126] B. WOOD, P. CASPERS, G. PUPPELS, S. PANDIANCHERRI, AND D. MCNAUGHTON, *Resonance raman spectroscopy of red blood cells using near-infrared laser excitation*, Analytical and Bioanalytical Chemistry, 387 (2007), pp. 1691–1703.
- [127] M. WUKITSCH, M. PETTERSON, D. TOBLER, AND J. POLOGE, *Pulse oximetry: Analysis of theory, technology, and practice*, Journal of Clinical Monitoring, 4 (1988), pp. 290–301.
- [128] WWW.FREEIMAGES.CO.UK, *Freeimages*, 2012.
- [129] C. XIE, C. GOODMAN, M. DINNO, AND Y.-Q. LI, *Real-time raman spectroscopy of optically trapped living cells and organelles*, Opt. Express, 12 (2004), pp. 6208–6214.
- [130] J. M. YOUNSE, *Projection display systems based on the digital micromirror device (dmd)*, in Micromachining and Microfabrication, International Society for Optics and Photonics, 1995, pp. 64–75.